Doctoral Dissertation.
Interuniversity Doctoral Program in
Urban and Regional Development (XXXVIII Cycle)

Rational Design and Synthesis of Epitaxial Nano-Heterostructures for Photocatalysis

Anna CABONA

Supervisor(s):
Prof. Liberato Manna, Supervisor
Prof. Ilka Kriegel, Co-Supervisor

Politecnico di Torino - Università degli Studi di Torino
January 31, 2026

I hereby declare that the contents and organisation of this dissertation constitute my own original work and does not compromise in any way the rights of third parties, including those relating to the security of personal data.

Anna Cabona Turin, January 31, 2026

Summary

Photocatalysis represents a promising approach for the sustainable conversion of solar energy into valuable chemical products, enabling green energy storage in the form of chemical bonds. In the search for efficient and cost-effective photocatalysts, colloidal nano-semiconductors have emerged as attractive candidates due to their tunable electronic properties, size control, and favorable charge-carrier dynamics upon illumination. However, these nanomaterials also present significant challenges in design and synthesis, and several improvements are required to achieve efficient photocatalytic performances. One open challenge is enhancing the accessibility of photoinduced charge carriers that drive photochemical reactions. One possible strategy to address this issue is to employ heterostructures composed of two different materials connected at an interface. In such systems, suitable band alignment can promote charge separation, increase carrier lifetimes, and improve their availability for surface reactions.

This thesis aims to explore the rational design, synthesis, and application of selected heterostructures. Particular attention is given to metal halides, which are currently at the forefront of colloidal chemistry research. Heterostructures based on these materials are promising due to the appealing optoelectronic properties of the metal halide domains. However, these hybrid architectures pose significant design and synthetic challenges. Within this framework, three case studies are presented, each defined by distinct design, synthetic, and photocatalytic challenges.

Chapter 4 evaluates the feasibility of forming an epitaxial $CsPbBr_3$@AgBr core@shell heterostructure by first assessing structural compatibility at the interface. This analysis was performed with Ogre, a python-based package for predicting epitaxial interfaces between ionic materials. The workflow generated atomistic models of several interface configurations, verifying that the two materials are epitaxially compatible along multiple lattice directions, a key requirement for core@shell architectures. Guided by these predictions, we developed a hot-injection synthesis protocol. Unexpectedly, this approach produced the inverse architecture, consisting of an AgBr core and a $CsPbBr_3$ shell. Nevertheless, this outcome is consistent with the epitaxial predictions, with the difference likely originating from chemical reactivity considerations.

Chapter 5 evaluates the practical advantages of epitaxial semiconductor-semiconductor heterostructures for photocatalysis. Although $CsPbX_3/Pb_4S_3Y_2$ heterostructures have been reported previously, we optimized a two-step direct synthesis to improve the reaction yield, which is crucial for enabling systematic photocatalytic testing. Different halide combinations were made accessible by post-synthesis halide exchange reactions, allowing access to a broader range of band alignments, which were characterized by spectroscopic techniques. Photocatalytic performances were demonstrated using thiophenol coupling as a model reaction. For this specific process, we found that the type II $CsPbBr_3/Pb_4S_3Br_2$ heterostructure delivered the highest product yield, outperforming stand-alone nanocrystals of the two materials. This enhanced activity is attributed to effective charge separation at the heterojunction upon illumination.

Finally, Chapter 6 presents a novel heterostructure, $Bi/Bi_{13}S_{18}Br_2$, that was obtained by introducing a mild reducing agent during the synthesis of the semiconductor chalcohalide $Bi_{13}S_{18}Br_2$ to achieve the in-situ reduction of metallic bismuth. These heterostructures adopt a distinctive bell-like morphology, which motivated an investigation of the growth mechanism using a combination of X-ray diffraction and advanced electron microscopy techniques. The proposed growth mechanism indicates that the initial nanorods play a dual role, acting first as heterogeneous nucleation templates for metallic Bi nucleation, and then as a material reservoir for the further growth of the chalcohalide domains via Ostwald ripening. Finally, the photo(electro)catalytic performance of the resulting nanobells was evaluated in dye degradation and CO_2 reduction reactions. Consistently with the $CsPbX_3/Pb_4S_3Y_2$ heterostructures discussed in Chapter 5, the enhanced activity is attributed to the intimate coupling between the two domains, which promotes effective charge separation under illumination.

Overall, this thesis demonstrates how the rational design of epitaxial heterostructures, guided by interfacial compatibility and chemical tunability, can enhance photocatalytic performance through effective multi-domain coupling. At the same time, the work highlights the synthetic and mechanistic challenges that naturally emerge when translating interface design into the experimental realization of complex, functional nanomaterials.

Acknowledgment

I would like to acknowledge my supervisors Prof. Liberato Manna and Prof. Ilka Kriegel for the guidance and the support provided during my PhD research.

I would like to acknowledge the technicians of the nanochemistry lab and of the electron microscopy facility for the support during the analysis.

I would like to acknowledge Prof. Raquel Galian, Prof. Julia Perez-Prieto, Dr Alejandro Cortes-Villena, Dr Ignacio Rosa-Pardo, Dr Delia Bellezza, Alessandro Ciccone from the Institute of Molecular Science in Valencia for the support provided during my period abroad.

To my grandparents, who hold a very special place in my heart

Contents

List of Figures

List of Tables

CHAPTER 1

Photocatalysis: an introduction

1.1 Photocatalysis

Global energy demand is expected to grow exponentially in the coming decades due to the rapid population growth and the surge of artificial intelligence, which requires large data centers that consume significant amounts of electricity for both processing and cooling systems.[1,2] Furthermore, climate change and environmental problems, primarily driven by the extensive use of fossil fuels, impose urgent challenges to human beings. In this context, the development and employment of renewable energy have become essential to decrease and mitigate the emission of toxic and greenhouse gases.[3,4,5]

Among these sources, solar energy is particularly attractive since it is clean, abundant and renewable, offering a sustainable alternative that could decrease our strong dependence on fossil fuels.[6,7] Finding a clean way to exploit and store solar energy would be crucial and the first step towards a greener and more sustainable world. One possible avenue is represented by photocatalysis. Photocatalysis employs a suitable light-absorbing material, the photocatalyst, to drive reactions that are otherwise exceedingly slow or thermodynamically unfavorable, ultimately transforming light into stored chemical energy.[8,9] In this context, the fundamental principle of photocatalysis lies in the interaction between light and matter, involving complex energy-transfer processes that are typically described in terms of charge transfer.[10]

The most relevant example of storing solar energy that has inspired photocatalysis is photosynthesis.[11,12] Indeed, photosynthesis is a natural process that the plants exploit to produce sugar from light, water and CO_2. This process is not a simple energy conversion since it enables the storage of solar energy in the form of chemical bonds. The mechanism of photosynthesis is based on photo-induced electron transfer. More specifically, chlorophyll pigments absorb light and are promoted to electronically excited states. This excitation triggers a series of

redox reactions. The first step is photolysis, which consists in water oxidation and the energy input (light) is used to split water molecules.[13] The second step generates a transmembrane proton gradient thanks to the charge separation, whereby the electrons are transferred along an electron-transport chain. Finally, the resulting electrochemical potential is used to drive the synthesis of carbohydrates. Mimicking photosynthesis in the laboratory to produce valuable chemicals from sunlight represents a promising way to exploit renewable green energy.[14,15,16] Indeed, one of the major advantages of photocatalysis is the ability to promote reactions under particularly mild conditions, often at ambient temperature and pressure. This reduces the use of energy-intensive thermal inputs and enables the exploitation of soft excitation sources, such as visible light. Furthermore, low-energy radiation can avoid the activation of unnecessary active sites of the catalyst that could lead to undesired pathways, thereby enhancing catalytic selectivity.

In this context, photocatalytic organic transformations are of great importance for the synthesis of valuable chemicals. Photocatalysis has been predominantly focused on molecular organic transformations, where an organic molecule is used as a substrate and undergoes either reduction or oxidation through a photocatalytic process to yield the desired target product.[17,18] These transformations could be critical for several fields such as pharmaceutics, agro-chemistry, cosmetics, and other bulk or fine chemicals.[17] Moreover, photoredox reactions can be carried out in both liquid and gaseous systems, for instance when the substrate is in the gas phase, as in the case of CO_2 reduction[19,20,21] or H_2 evolution.[22,23] These transformations constitute the backbone of modern chemical industries. Another important application of light-driven catalysis is the degradation of pollutants,[24,25] where photocatalysis again represents a sustainable and effective approach for the removal of toxic compounds.

Actually, the use of visible light to drive chemical reactions is not a recent concept. Indeed, in the early 20th century, Giacomo Ciamician and Paul Silber developed photochemical reactions using visible light.[26] In 1972 Fujishima and Honda performed for the first time the photoelectrochemical water splitting using a semiconductor, TiO_2, as catalyst.[27] Again in 1984, the first photoredox catalytic reaction activated by visible light was reported by Alain Deronzier and co-workers, who used a ruthenium-based molecule as photocatalyst.[28] However, photocatalytic organic synthesis, induced by visible light, gained broad attention only in 2008, following the report by the MacMillan group on the direct asymmetric alkylation of aldehydes through the combination of photocatalysis and organocatalysis.[29]

1.2 Homogenous or heterogeneous photocatalysts?

In this regard, the synthesis of organic compounds via photocatalysis appears as a sustainable approach, where the choice of the most suitable catalyst, able to promote excited state formation upon illumination, is a key aspect. Indeed, the appropriate catalytic system can influence the success of a chemical process on multiple factors including efficiency, scalability, sustainability, and cost.

Historically, photoredox catalysis has relied mainly on homogeneous molecular photocatalysts,[30] particularly focused on transition metal complexes such as ruthenium (Ru)[31,32] and iridium (Ir).[33,34] While these catalysts have nice performances in terms of product yield and selectivity, they often suffer from significant drawbacks like lack of recyclability and high cost. These limitations have a high impact in their practical use and industrial scalability. To overcome these issues, there is a strong motivation to explore other systems, such as heterogeneous photocatalysis.[35,36] Among the possible candidates, semiconductor materials have emerged as cost-effective, recoverable and sustainable photocatalyst alternatives.[37] Notably, their activation mechanism closely mimics that of natural photosynthesis, which originally inspired the development of photocatalysis. The following paragraph will focus on semiconductors and on the properties that make them ideal heterogeneous photocatalysts.

1.3 Semiconductor materials as heterogenous photocatalysts

Semiconductors are a class of materials with electronic properties intermediate between those of conductors and insulators.[38,39,40] More precisely, their behavior arises from the presence of a band gap (E_g) that is small enough to allow the optical or electronic excitation of charge carriers at practical energies (e.g., 1.0 – 3.0 eV). At the same time, the E_g is large enough to avoid substantial thermal excitation of free charges at room temperature, which would induce a metallic behavior.

According to solid state physics and band theory, the electronic structure of a semiconductor is characterized by the energy distribution of its electrons. In isolated atoms, electrons occupy discrete energy levels called atomic orbitals (AOs). In a bulk crystal lattice, the periodic arrangement of a large number of atoms causes the overlap of AOs and the formation of quasi-continuous energy bands. The most important regions of this structure are the valence band (VB) and the conduction band (CB). The VB is the lower energy band, filled with electrons that

are normally in the ground state. The state at the very top of the VB corresponds to the Highest Occupied Molecular Orbital (HOMO). Instead, the CB is the higher energy band, situated above the valence band, and is generally empty. The state at the very bottom of the CB corresponds to the Lowest Unoccupied Molecular Orbital (LUMO). The energy difference between these two states, the bandgap (Eg), represents a "forbidden region" where no electronic states can exist. The band gap for semiconductors typically falls within a few electron volts and determines their light-absorption properties. At room temperature, an ideal bulk semiconductor has a fully occupied valence band and an empty conduction band, placing the Fermi Level approximately in the middle of the gap and resulting in a non-conductive system. This behavior can be altered by providing energy in the form of heat or light, which promotes electrons from VB to CB. As a result, the optical and electronic properties are governed by the band structure and the ways the available electronic states are populated, which can be in turn controlled via composition, crystal structure, morphology, external stimuli, etc. Such tunability makes semiconductors fundamental materials for applications in fields such as microelectronics, photonics, and catalysis.

1.3.1 Photocatalytic mechanism

In the case of photocatalysis, the fundamental prerequisite for starting a chemical transformation is the efficient energy input.[35] Indeed, the general mechanism begins when the photocatalyst, in our case a semiconductor, absorbs light with an energy (hν) that could be equal or greater than its band gap. This results in the photoexcitation of electron (e^-) from the valence band to the conduction band of the material, leaving a positive charge, named hole (h^+) in the valence band. This process is ultra-fast in a time scale of femtoseconds (~10^{-15} s).[18,41] These photogenerated charge carriers may thus take three main pathways, as depicted in Figure 1.1:

1) Recombination pathway: the electron in the conduction band and the holes in the valence band can further recombine in the bulk of the semiconductor material or on its surface, within a short time scale: from few picoseconds to nanoseconds (~10^{-12} - 10^{-9} s).
2) Side reactions pathway: the photoinduced charge carriers can also be quenched by the solvent or other reagents, meaning that electrons can reduce and the hole can oxidize other species in the medium that are not the target compounds. This process leads to the formation of unwanted products, reducing the overall efficiency of the catalytic system.

3) Desirable pathway: the photogenerated carriers get separated in the bulk and reach the surface of the catalyst without undergoing recombination or reacting with other species. This spatial charge dynamics typically are in the time scale of nanoseconds (~10^{-9} s) Finally, the charges may react with the substrate favoring the production of the target molecules.

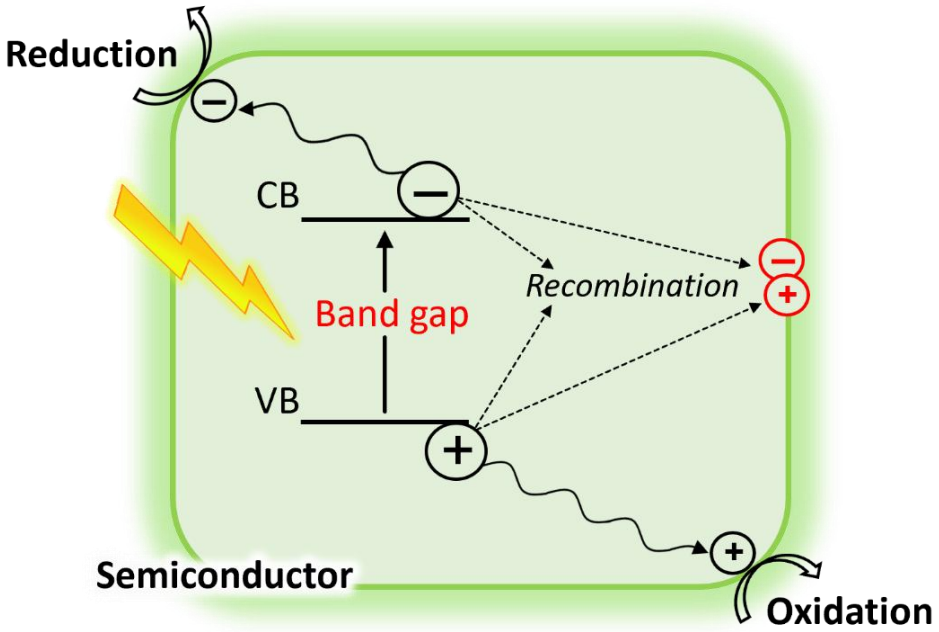

Figure 1.1. Schematic representation of semiconductor photocatalyst for organic transformation. Upon illumination the photogenerated electrons and holes can travel to the surface of the photocatalyst and perform photoreduction or oxidation reaction. Alternatively, these charges can recombine in the bulk or on the surface of the material.

The last route greatly governs the solar to chemical energy conversion efficiency of semiconductor catalyst. In particular, this path via redox processes will produce the corresponding reductive or oxidative species such as radical cation/anion substrates, or other active radical species depending on the atmosphere in which the reaction is carried out. One of the most relevant examples for this thesis is the super oxide anion ($O_2^{-\cdot}$), that is involved in most of the oxidative organic transformations.[42,43] The photogenerated charge carriers, in particular electrons, will reduce molecular oxygen (O_2) to the super oxide anion ($O_2^{-\cdot}$), which will be the main reactive species to deliver the final product. In this context, the reactivity of photogenerated charge carriers is thermodynamically governed by the band structure of the photocatalyst, in particular by the positions of the VB and CB

edges relative to the redox potentials of the involved reactants. On the other hand, the first two undesirable pathways mentioned above are detrimental for the photocatalytic efficiency since the charge carriers are not exploited to obtain the product but rather they recombine or react with other species. Hence, one must find solutions to decrease the probability of their occurrence.

With this picture in mind, when a semiconductor is employed as photocatalyst, the overall efficiency of light to chemical energy conversion is governed by three key factors: *light absorption*, *charge dynamics* and *surface photoreactions*.[35] The first factor, *light absorption*, refers to the effective use of the energy input required to activate the photocatalyst and generate the charge carriers: electrons and holes. The *charge dynamics* concerns all the possible pathways that these photogenerated carriers may follow during the photocatalytic process, as described above, including transport, reaction, and recombination phenomena. Finally, the last factor, *surface photoreactions*, controls all the processes occurring at the catalyst surface once the carriers reach it. These processes include the formation of intermediate reactive species (e.g., $O_2^{-}\cdot$) that can lead to product formation, as well as the direct interaction of electrons and holes with the target molecules. In this context, it is essential to note that the time scale of the *light absorption* and *charge dynamics* is very fast, instead the kinetics of *surface photoreactions*, that is the process responsible to deliver the desired products, is considerably slower, requiring a timescale of microseconds to milliseconds ($\sim 10^{-6}$ - 10^{-3} s).[35]

Overall, the efficiency of desirable route 3 governs the photoactivity of semiconductor materials and depends on several factors. These include material size, accessible surface area, band gap, electronic structure (redox potential of the excited state relative to the substrates redox potentials) and charge carriers dynamics (separation efficiency, diffusion length, recombination rate and carrier lifetime). Additionally, is also essential to align the photocatalyst activation with the reaction conditions required for the organic transformation.[44]

1.4 Conclusions

Overall, we presented photocatalysis as a sustainable and promising approach to exploit solar energy for driving organic transformations and producing valuable chemicals. From this brief overview, it is noteworthy to highlight that both heterogeneous photocatalysis (e.g., TiO_2) and homogeneous photocatalysis (based on metal complexes) were already subjects of investigation in the previous century. As discussed above, homogenous photocatalysts suffer from several intrinsic

drawbacks, therefore it is generally more convenient to focus on the heterogeneous ones. This naturally leads to a key question: how can the efficiency of a photocatalytic system be enhanced by improving the interaction between the heterogeneous catalyst and the target compound? Among the possible answers, one of the most effective strategies, and a central focus of research over the past decades, is the drastic reduction of the catalyst size. In this approach, bulk semiconductors are replaced by nanostructured materials, offering several advantages that will be discussed in the next chapter.

1.5 Bibliography

(1) Yan, C.; Qian, Y.; Liao, Z.; Le, Z.; Fan, Q.; Zhu, H.; Xie, Z. Recent Progress of Metal Halide Perovskite Materials in Heterogeneous Photocatalytic Organic Reactions. *Photochem. Photobiol. Sci.* **2024**, *23* (7), 1393–1415. https://doi.org/10.1007/s43630-024-00599-2.

(2) Song, H.; Luo, S.; Huang, H.; Deng, B.; Ye, J. Solar-Driven Hydrogen Production: Recent Advances, Challenges, and Future Perspectives. *ACS Energy Lett.* **2022**, *7* (3), 1043–1065. https://doi.org/10.1021/acsenergylett.1c02591.

(3) Fang, S.; Rahaman, M.; Bharti, J.; Reisner, E.; Robert, M.; Ozin, G. A.; Hu, Y. H. Photocatalytic CO_2 Reduction. *Nat. Rev. Methods Primers* **2023**, *3* (1), 61. https://doi.org/10.1038/s43586-023-00243-w.

(4) Mustafa, A.; Lougou, B. G.; Shuai, Y.; Wang, Z.; Tan, H. Current Technology Development for CO_2 Utilization into Solar Fuels and Chemicals: A Review. *J. Energy Chem.* **2020**, *49*, 96–123. https://doi.org/10.1016/j.jechem.2020.01.023.

(5) Wang, Z.; Song, H.; Liu, H.; Ye, J. Coupling of Solar Energy and Thermal Energy for Carbon Dioxide Reduction: Status and Prospects. *Angew. Chem. Int. Ed.* **2020**, *59* (21), 8016–8035. https://doi.org/10.1002/anie.201907443.

(6) Yuan, L.; Geng, Z.; Xu, J.; Guo, F.; Han, C. Metal-Semiconductor Heterostructures for Photoredox Catalysis: Where Are We Now and Where Do We Go? *Adv. Funct. Mater.* **2021**, *31* (27), 2101103. https://doi.org/10.1002/adfm.202101103.

(7) Sun, X.; Jiang, S.; Huang, H.; Li, H.; Jia, B.; Ma, T. Solar Energy Catalysis. *Angew. Chem.* **2022**, *134* (29), e202204880. https://doi.org/10.1002/ange.202204880.

(8) *Photocatalysis - Fundamentals and Perspectives*; Schneider, J., Bahnemann, D., Ye, J., Li Puma, G., Dionysiou, D. D., Eds.; RSC energy and environment series; Royal Society of Chemistry: Cambridge, 2016.

(9) Chen, K.; Dong, W.; Huang, Y.; Wang, F.; Zhou, J. L.; Li, W. Photocatalysis for Sustainable Energy and Environmental Protection in Construction: A Review on Surface Engineering and Emerging Synthesis. *J. Environ. Chem. Eng.* **2025**, *13* (5), 117529. https://doi.org/10.1016/j.jece.2025.117529.

(10) Irshad, M.; Ain, Q. T.; Zaman, M.; Aslam, M. Z.; Kousar, N.; Asim, M.; Rafique, M.; Siraj, K.; Tabish, A. N.; Usman, M.; Hassan Farooq, M. U.; Assiri,

M. A.; Imran, M. Photocatalysis and Perovskite Oxide-Based Materials: A Remedy for a Clean and Sustainable Future. *RSC Adv.* **2022**, *12* (12), 7009–7039. https://doi.org/10.1039/D1RA08185C.

(11) Nelson, N.; Ben-Shem, A. The Complex Architecture of Oxygenic Photosynthesis. *Nat. Rev. Mol. Cell Biol.* **2004**, *5* (12), 971–982. https://doi.org/10.1038/nrm1525.

(12) Blankenship, Robert E. *Molecular Mechanisms of Photosynthesis.* 3rd ed., John Wiley & Sons, 2021.

(13) Lubitz, W.; Pantazis, D. A.; Cox, N. Water Oxidation in Oxygenic Photosynthesis Studied by Magnetic Resonance Techniques. *FEBS Letters* **2023**, *597* (1), 6–29. https://doi.org/10.1002/1873-3468.14543.

(14) Yu, X.; Xu, J.; Wang, J.; Qiu, J.; An, X.; Wang, Z.; Lv, G.; Liao, L.; Ye, J. Mimicking Photosynthesis: A Natural Z-Scheme Photocatalyst Constructed from Red Mud Bauxite Waste for Overall Water Splitting. *Angew. Chem.* **2023**, *135* (19), e202302050. https://doi.org/10.1002/ange.202302050.

(15) Kathpalia, R.; Verma, A. K. Bio-Inspired Nanoparticles for Artificial Photosynthesis. *Mater. Today Proc.* **2021**, *45*, 3825–3832. https://doi.org/10.1016/j.matpr.2021.03.214.

(16) Velasco-Garcia, L.; Casadevall, C. Bioinspired Photocatalytic Systems towards Compartmentalized Artificial Photosynthesis. *Commun. Chem.* **2023**, *6* (1), 263. https://doi.org/10.1038/s42004-023-01069-z.

(17) Friend, C. M.; Xu, B. Heterogeneous Catalysis: A Central Science for a Sustainable Future. *Acc. Chem. Res.* **2017**, *50* (3), 517–521. https://doi.org/10.1021/acs.accounts.6b00510.

(18) Lin, Y.; Guo, J.; San Martin, J.; Han, C.; Martinez, R.; Yan, Y. Photoredox Organic Synthesis Employing Heterogeneous Photocatalysts with Emphasis on Halide Perovskite. *Chem.- Eur. J.* **2020**, *26* (58), 13118–13136. https://doi.org/10.1002/chem.202002145.

(19) Cheng, S.; Sun, Z.; Lim, K. H.; Gani, T. Z. H.; Zhang, T.; Wang, Y.; Yin, H.; Liu, K.; Guo, H.; Du, T.; Liu, L.; Li, G. K.; Yin, Z.; Kawi, S. Emerging Strategies for CO_2 Photoreduction to CH_4: From Experimental to Data-Driven Design. *Adv. Energy Mater.* **2022**, *12* (20), 2200389. https://doi.org/10.1002/aenm.202200389.

(20) Feng, S.; Zhao, J.; Bai, Y.; Liang, X.; Wang, T.; Wang, C. Facile Synthesis of Mo-Doped TiO_2 for Selective Photocatalytic CO_2 Reduction to

Methane: Promoted H_2O Dissociation by Mo Doping. *J. CO_2 Util.* **2020**, *38*, 1–9. https://doi.org/10.1016/j.jcou.2019.12.019.

(21) Qu, T.; Wei, S.; Xiong, Z.; Zhang, J.; Zhao, Y. Progress and Prospect of CO_2 Photocatalytic Reduction to Methanol. *Fuel Process. Technol.* **2023**, *251*, 107933. https://doi.org/10.1016/j.fuproc.2023.107933.

(22) Chen, J.-J.; Wu, J. C. S.; Wu, P. C.; Tsai, D. P. Plasmonic Photocatalyst for H_2 Evolution in Photocatalytic Water Splitting. *J. Phys. Chem. C* **2011**, *115* (1), 210–216. https://doi.org/10.1021/jp1074048.

(23) Lin, Z.; Du, C.; Yan, B.; Wang, C.; Yang, G. Two-Dimensional Amorphous NiO as a Plasmonic Photocatalyst for Solar H_2 Evolution. *Nat. Commun.* **2018**, *9* (1), 4036. https://doi.org/10.1038/s41467-018-06456-y.

(24) Zhu, D.; Zhou, Q. Action and Mechanism of Semiconductor Photocatalysis on Degradation of Organic Pollutants in Water Treatment: A Review. *Environ. Nanotechnol. Monit. Manag.* **2019**, *12*, 100255. https://doi.org/10.1016/j.enmm.2019.100255.

(25) Durodola, S. S.; Akeremale, O. K.; Ore, O. T.; Bayode, A. A.; Badamasi, H.; Olusola, J. A. A Review on Nanomaterial as Photocatalysts for Degradation of Organic Pollutants. *J. Fluoresc.* **2024**, *34* (2), 501–514. https://doi.org/10.1007/s10895-023-03332-x.

(26) Ciamician, G. The Photochemistry of the Future. *Science* **1912**, 36 (926), 385–394. https://doi.org/10.1126/science.36.926.385

(27) FUJISHIMA, A.; HONDA, K. Electrochemical Photolysis of Water at a Semiconductor Electrode. *Nature* **1972**, *238* (5358), 37–38. https://doi.org/10.1038/238037a0.

(28) Cano-Yelo, H.; Deronzier, A. Photo-Oxidation of Some Carbinols by the Ru (II) Polypyridyl Complex-Aryl Diazonium Salt System. *Tetrahedron Letters* **1984**, *25* (48), 5517–5520. https://doi.org/10.1016/S0040-4039(01)81614-2.

(29) Nicewicz, D. A.; MacMillan, D. W. C. Merging Photoredox Catalysis with Organocatalysis: The Direct Asymmetric Alkylation of Aldehydes. *Science* **2008**, *322* (5898), 77–80. https://doi.org/10.1126/science.1161976.

(30) Bobo, M. V.; Kuchta, J. J.; Vannucci, A. K. Recent Advancements in the Development of Molecular Organic Photocatalysts. *Org. Biomol. Chem.* **2021**, *19* (22), 4816–4834. https://doi.org/10.1039/D1OB00396H.

(31) Meyer, T. J. Chemical Approaches to Artificial Photosynthesis. *Acc. Chem. Res.* **1989**, 22 (5), 163–170. https://doi.org/10.1021/ar00161a001.

(32) Creutz, Carol.; Sutin, Norman. Electron-Transfer Reactions of Excited States. Reductive Quenching of the Tris(2,2'-Bipyridine)Ruthenium(II) Luminescence. *Inorg. Chem.* **1976**, *15* (2), 496–499. https://doi.org/10.1021/ic50156a062.

(33) Flamigni, L.; Barbieri, A.; Sabatini, C.; Ventura, B.; Barigelletti, F. Photochemistry and Photophysics of Coordination Compounds: Iridium. In *Photochemistry and Photophysics of Coordination Compounds II*; Balzani, V., Campagna, S., Eds.; Springer Berlin Heidelberg: Berlin, Heidelberg, 2007; pp 143–203. https://doi.org/10.1007/128_2007_131.

(34) Pitre, S. P.; McTiernan, C. D.; Scaiano, J. C. Library of Cationic Organic Dyes for Visible-Light-Driven Photoredox Transformations. *ACS Omega* **2016**, *1* (1), 66–76. https://doi.org/10.1021/acsomega.6b00058.

(35) Zhang, N.; Gong, W.; Xiong, Y. Modern Organic Transformations: Heterogeneous Thermocatalysis or Photocatalysis? *Chem. Soc. Rev.* **2025**, *54* (11), 5189–5223. https://doi.org/10.1039/D2CS00097K.

(36) Zhang, L.; Ran, J.; Qiao, S.-Z.; Jaroniec, M. Characterization of Semiconductor Photocatalysts. *Chem. Soc. Rev.* **2019**, *48* (20), 5184–5206. https://doi.org/10.1039/C9CS00172G.

(37) Mishra, B. P.; Dahiya, J.; Krishnan, V. Semiconductor Photocatalysts for Hydrogen Evolution: Critical Role of Cocatalysts in Enhancing Performance. *Chem. Commun.* **2025**, *61* (89), 17302–17329. https://doi.org/10.1039/D5CC04459F.

(38) Hoffmann, Roald. *Solids and Surfaces: A Chemist's View of Bonding in Extended Structures / Roald Hoffmann.*; VCH Publishers: New York, NY, 1988.

(39) Burdett, J. K. Electronic Structure and Properties of Solids. *J. Phys. Chem.* **1996**, *100* (31), 13263–13274. https://doi.org/10.1021/jp953650b.

(40) Pettifor, D. G. *Bonding and Structure of Molecules and Solids.* Oxford: Clarendon Press / Oxford University Press, 1995.

(41) Han, C.; Qi, M.-Y.; Tang, Z.-R.; Gong, J.; Xu, Y.-J. Gold Nanorods-Based Hybrids with Tailored Structures for Photoredox Catalysis: Fundamental

Science, Materials Design and Applications. *Nano Today* **2019**, *27*, 48–72. https://doi.org/10.1016/j.nantod.2019.05.001.

(42) Parrino, F.; Livraghi, S.; Giamello, E.; Ceccato, R.; Palmisano, L. Role of Hydroxyl, Superoxide, and Nitrate Radicals on the Fate of Bromide Ions in Photocatalytic TiO_2 Suspensions. *ACS Catal.* **2020**, *10* (14), 7922–7931. https://doi.org/10.1021/acscatal.0c02010.

(43) Yang, X.; Ding, X.; Wang, S.; Mao, J.; Cheng, L.; Li, P.; Chen, H. Superoxide Anion and Singlet Oxygen Dominated Faster Photocatalytic Elimination of Nitric Oxide over Defective Bismuth Molybdates Heterojunctions. *J. Colloid Interface Sci.* **2022**, *618*, 248–258. https://doi.org/10.1016/j.jcis.2022.03.014.

(44) Lang, X.; Chen, X.; Zhao, J. Heterogeneous Visible Light Photocatalysis for Selective Organic Transformations. *Chem. Soc. Rev.* **2014**, *43* (1), 473–486. https://doi.org/10.1039/C3CS60188A.

CHAPTER 2

Semiconductor Nanocrystals as Photocatalysts

2.1 From bulk to nano-size semiconductors

In the previous chapter we gave a simplified and brief overview on the band structure of bulk semiconductors that is adequate to describe their general behavior. However, when the size of a semiconductor decreases down to the nanoscale, its optical and electronic behavior undergoes radical transformations that cannot be explained by a simple extension of the bulk model. In this regime, it becomes essential to consider the effects of quantum confinement and the surface to volume ratio, as these factors strictly govern the physical properties of nano semiconductors.[1,2,3]

The transition from bulk materials to nanoscale materials occurs when one or more dimensions of the semiconductor become comparable with the exciton Bohr radius, leading to nanoscale-induced electronic effects.[4] The Bohr radius describes the spatial extent of an exciton, that is an electrostatically bound electron-hole pair, inside the bulk material. This value typically ranges from few nanometers to tens of nanometers (e.g., $CsPbBr_3$ ~ 7 nm,[5] PbSe ~ 40-50 nm[6]). When the semiconductor size is reduced to the nanoscale, the free carriers in the material have no choice but to fall within a strong electrostatic interaction state, thus boosting the excitonic character of the material. Moreover, while in a bulk semiconductor the valence and conduction band are quasi-continuous, in nanoparticles they can split into a discrete series of energy levels, similar to the spectrum of an atom or a molecule, as shown in Figure 2.1.

With this picture in mind, when the particle size is equal to or smaller than the exciton Bohr radius, the system is in the strong quantum confinement regime. When the particle size is comparable to the Bohr radius, the material exhibits an intermediate quantum confinement regime. Finally, when the particle size is much

larger than the Bohr radius, the material shows bulk-like behavior, closely matching that of the corresponding bulk material.[7]

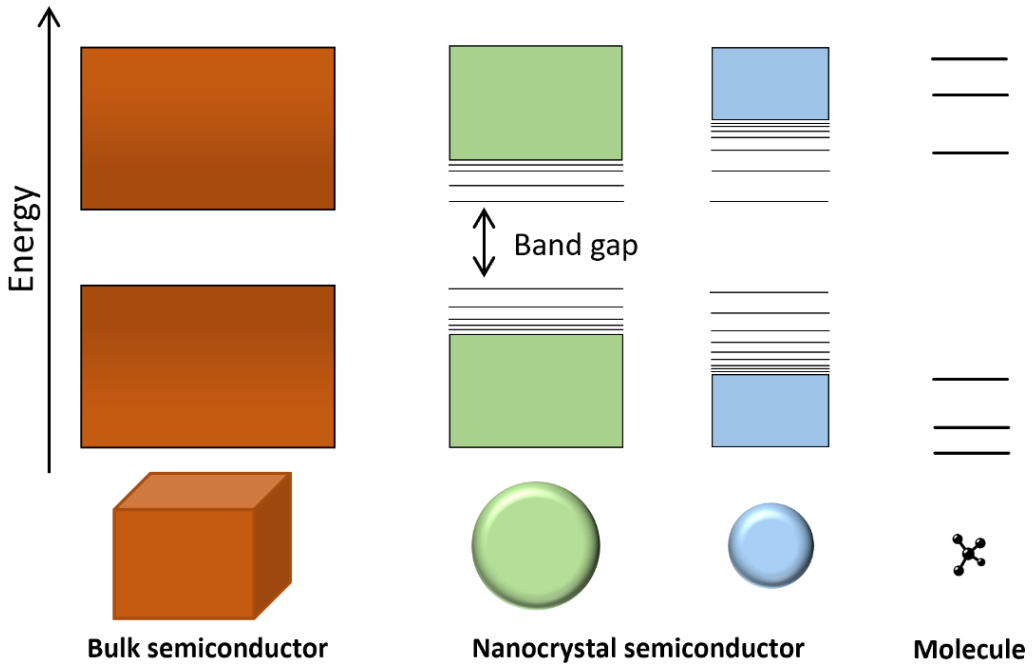

Figure 2.1. Quantum confinement effect. Comparison between bulk semiconductor, nanocrystal semiconductor and molecule to highlight the discrete energy states in the nano size.

Moreover, the dimensions of the nanoparticles play a key role in defining their physical properties. In this regard, 0D (quantum dots), 1D (nanorods, nanowires), and 2D (nanoplatelets) materials exhibit different regimes of quantum confinement and also distinct densities of states, which further modify their optical and electronic behavior. The nano-scale regime has direct consequence on the band gap which, for example, tends to increase as the particle size decreases. This property is known as "size-tunable band gap". This behavior also affects the optical properties: the absorption spectrum shifts towards higher energies (blueshift) as the size decreases, while the luminescence becomes brighter and more define.

2.2 Use of nanosemiconductors as photocatalysts

While this premise about quantum confinement is important as an overview, in this thesis we will rarely encounter particles that small to enter a significantly quantum confined regime. However, morphology control introduces another

important effect, that is the huge increase in surface/volume (S/V) ratio. This in turn comes with both positive and negative consequences, that are both extremely important when a nanoscale semiconductor is used as heterogeneous photocatalyst. Indeed, this structural shift dictates efficiency, kinetics, and stability of the photocatalytic processes.

It is important to underline that the use of bulk and nanostructured semiconductors as photocatalysts does not differ in terms of the intrinsic mechanism, since the three key factors (light absorption, charge dynamics and surface photoreactions) remain the same.[8] However, each of these factors can be strongly influenced by the nanoscale nature of the catalyst, as discussed in the next paragraph.

2.2.1 Synergistics enhancements

The first crucial aspect, derived from employing nanomaterials in heterogeneous photocatalysis, is the exponential increase in available active sites due to the enhanced S/V ratio.[9,10] In this regard, in a bulk semiconductor, the majority of the atoms are placed within the crystalline lattice, contributing to the optical and electronic bulk properties. On the contrary, as the particles size is reduced down to the nanoscale a higher fraction of atoms is located on the surfaces of the crystal. This phenomenon has direct consequences on the increased active site density. Since photocatalytic redox reactions occur only at the solid-liquid or solid-gas interface, a high S/V ensures a higher density of available active sites for the substrate molecules, consequently the reaction kinetics are faster. In this regard, the interaction between the catalyst and the substrate, prior light activation, emerges as a crucial factor for the overall efficiency of the system.[7,11]

The high S/V promotes another important consequence that is the reduced charge carrier diffusion lengths.[12,13,14] Indeed, from the previous chapter we learned that the recombination of electrons and holes is a critical drawback in photocatalysis. In nanomaterials, the distance a charge carrier has to travel to reach the surface is significantly lower than in bulk semiconductors. This phenomenon can reduce the probability of bulk recombination, ensuring that a high fraction of carriers reach the surface to react with the substrate compound.

The employment of nanoparticles can enhance the mass transfer as the dispersibility of the catalyst in the reaction medium is improved. This promotes a more effective and efficient interaction between the catalyst and the substrate.

Finally, the heterogeneous nature of the nanoparticles allows for an easy separation of the photocatalyst from the reaction medium, for example by centrifugation, thereby enabling multiple photocatalytic cycles.[15]

2.2.2 Critical drawbacks

Despite all the advantages described above, the high surface energy, associated with the increased S/V ratio, introduces significant drawbacks. The most relevant aspect is the formation of surface state defects as recombination centers. Indeed, the presence of a large fraction of atoms on the surface comes with different defect states, that are generally structural irregularities such as vacancies and interstitial defects.[16,17,18] As a result, these surface defects often create mid-gap energy states, which can act as potential recombination centers.[19,20] This means that, instead of participating to the redox reaction, the photogenerated charge carriers (e^- and h^+) can be trapped and quenched by these states, undergoing to non-radiative recombination, thus reducing the efficiency of the process.

At the same time, nanomaterials suffer from higher chemical instability in comparison with bulk systems. Indeed, due to strong van der Waals forces, nanoparticles have a natural tendency to aggregate with the aim to minimize their surface energy.[7] Consequently, these aggregates can behave like bulk materials, effectively neutralizing the advantages of the S/V ratio. Moreover, nanoparticles can be susceptible to photo-corrosion, a process in which the catalyst itself is oxidized or reduced by the photogenerated carriers or by the prolongated exposure to light.[21,22]

In this context, identifying effective strategies to mitigate the drawbacks that come with the use of nanoparticles as photocatalysts becomes a crucial aspect. The synthetic protocols employed to obtain the nanomaterials play a pivotal role since, depending on the synthesis, it is possible to obtain stable particles with low defects density. Among the various strategies available for synthesizing nanocrystals (NCs), colloidal chemistry, which is the most relevant approach for this thesis, has emerged as a highly versatile method, offering excellent control over nanocrystal surface chemistry and morphological tuning.

2.3 Colloidal synthesis of nanomaterials

Colloidal synthesis can be classified as a bottom-up approach widely employed for the preparation of nanocrystals with controlled size, shape, composition and

surface properties.[23,24] In this method, nanocrystals are formed in a liquid phase by the chemical reaction of the precursors, which can be inorganic salts (e.g., Cs_2CO_3) or organic molecules (e.g., benzoyl bromide). This leads to the formation of very small solid particles dispersed in a solvent and stabilized by the surface organic ligands. In this regard, the use of surface ligands, known also as capping agent, is a key factor of colloidal synthesis.[25] These molecules are typically long-chain organic compounds such as carboxylic acids, amines, phosphines or thiols and they are able to coordinate to the NCs surface thanks to functional groups with affinity with the inorganic core of the material.[26,27]

In this regard, the use of colloidal dispersion of nanocrystals as photocatalyst is particularly advantageous.[28] Indeed, unlike conventional solid catalysts, colloidal NCs are dispersed in a liquid medium that can be compatible with the solvent employed for the photocatalytic reaction, ensuring homogeneous distribution of the photocatalyst while preserving the colloidal stability of the nanoparticles. At the same time, NCs maintain their intrinsic solid-state nature, this allows to exploit all the benefits associated with heterogeneous nanoscale systems, as discussed above. As a consequence, it is clear that the ligands are of crucial importance as they prevent aggregation by steric or electrostatic stabilization, therefore maintaining the colloidal stability, essentially keeping the photocatalyst in the nano-size.

Several synthetic strategies have been developed for the colloidal synthesis of NCs, among them hot injection and heat-up methods are the most relevant.[29,30] In the hot injection approach,[31,32] one or more precursors are injected into a hot solution containing the solvent, the ligands and other precursors. This triggers the fast and instantaneous nucleation of the nanoparticles. The rapid increase in supersaturation promotes a narrow nucleation window, often resulting in highly monodisperse NCs, however this method can be limited in scalability and reproducibility. Instead in the heat-up syntheses,[33,34] all the precursors are initially mixed together with the solvent and the ligands; here, the nucleation event is activated by the fast increasing in temperature that promotes the reactants decomposition.

Figure 2.2 illustrates a series of nanocrystals synthetized during my PhD, characterized by different size, shape and composition. These transmission electron microscope (TEM) images clearly show that the synthetic procedure plays a key role in determining the final morphological properties of these materials. By tuning experimental parameters such as temperature, solvent, and ligands, it is possible to obtain NCs with diverse morphologies including cubes, spheres and also nanorods.

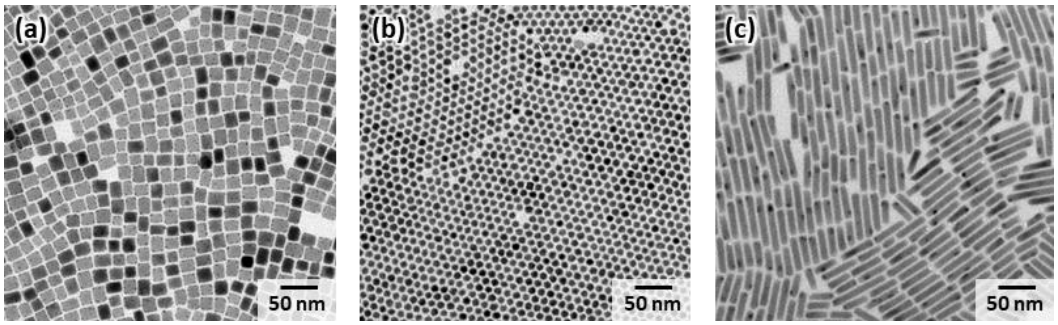

Figure 2.2. Nanocrystals of different size and shape. a) TEM image of cubic $CsPbBr_3$ NCs. b) TEM image of spherical $Pb_4S_3Br_2$ NCs. c) TEM images of $Pb_7S_2Br_{10}$ nanorods.

From this overview, heterogeneous nano-catalysts offer unique advantages stemming from their intrinsic properties and they can be summarized in three main points:

- Enhanced active sites: nanomaterials possess a high surface to volume ratio, providing an increased number of active sites for the photocatalytic process.
- Tunable properties: the ability to tune their composition and nanoscale structure allows for a fine tuning of their optoelectronic properties.
- Recovery and recyclability: their solid nature allows for an easy separation (e.g., centrifugation) and open the possibility to multiple catalytic cycles.

2.4 State-of-the-art nano-semiconductor photocatalysts

Over the past decade, as photocatalysis has gained increasing attention, a wide range of pre-existing semiconductors have been employed as photocatalysts. At the same time, significant research efforts have been focused to designing new materials and architectures capable of efficiently driving specific and complex organic transformations.[35] Figure 2.3 shows the most commonly used photocatalysts and the positions of their valence and conduction bands relative to the reference hydrogen electrode (RHE).

In this regard, it is essential to provide an overview of the photocatalysts most widely adopted in the field, to identify the key challenges and advantages associated with selecting or developing an appropriate photocatalytic material.

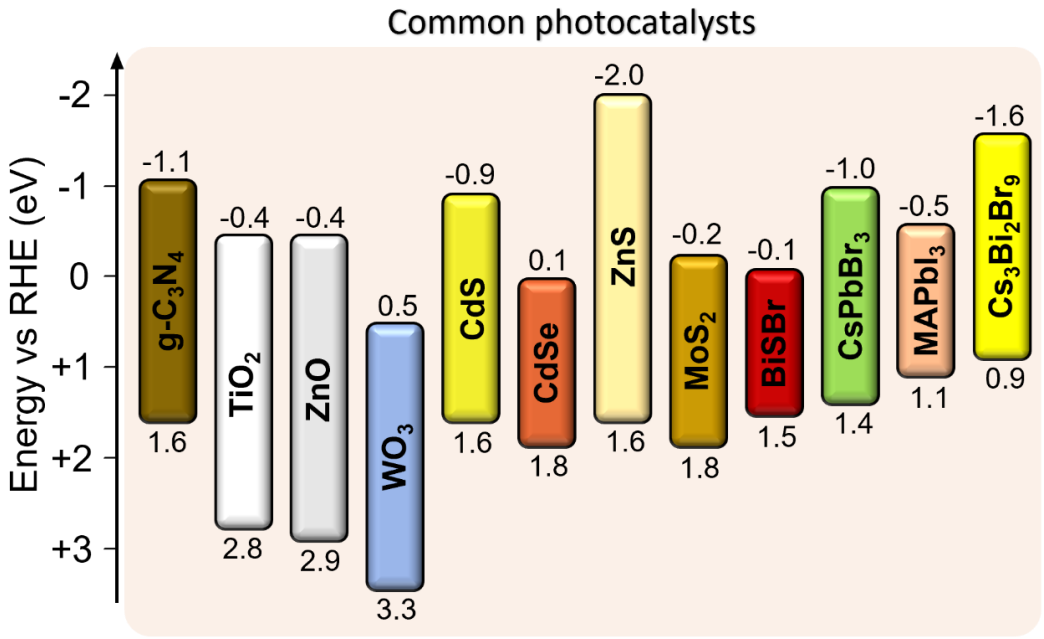

Figure 2.3. Most common photocatalysts. Band alignments of the most common photocatalysts against reference hydrogen electrode (RHE).[36,37]

Metal oxides are a rich class of materials, characterized by robustness and versatile synthetic procedures. These compounds are often exemplified by TiO_2,[38] one of the earliest and most extensively studied semiconductor photocatalysts. Indeed it has a long history of applications in environmental issue, particularly in the degradation of organic dyes.[39,40] Its excellent photocatalytic and chemical stability, along with favorable optoelectronic properties make TiO_2 a robust catalyst.[41] Among its polymorphs,[42] anatase is generally considered the most photoactive phase due to the slower recombination of charge carriers. Band gap engineering through doping has been widely explored: non-metal doping typically induces band gap narrowing, while metal doping can introduce trap states to improve charge separation.[43] However, a key limitation of TiO_2 is its relatively large band gap (~3 eV), which requires ultraviolet irradiation and consequently restricts its employment for visible-light applications.

Another important group that finds applications in photocatalysis is transition metal chalcogenides (TCM).[44] TCM are layered materials, typically described by the formula MX_2, where M is a transition metal and X is a chalcogen (S^{2-}, Se^{2-}). Among them, MoS_2 was the first to be discovered by Pauling in 1923[45] and became one of the most studied compounds. These materials crystallize in different polymorphs (1T, 2H, 3R)[46] and, notably, they can transition from an indirect to a

direct band gap when the material thickness tends to the monolayer limit.[47] These materials can be characterized by internal junctions due to the coexistence of metallic and semiconducting domains, which can enhance charge separation and suppress recombination. This property makes TMCs attractive for a broad range of photocatalytic transformations, including oxidative reactions (e.g., aerobic coupling of benzylamine).[48]

Carbon based compounds are also widely exploited in photocatalysis. This group includes graphitic carbon nitride (g-C_3N_4), carbon dots, and graphene-based derivatives. g-C_3N_4 is a metal-free semiconductor composed of a periodic arrangement of triazine or heptazine. It has a direct band gap and its surface is easily tunable through chemical modification.[49] Notably, g-C_3N_4 can be activated under visible light for various oxidation and reduction reactions.[50] Graphene consists of a single layer of sp^2-carbon atoms,[51] which can be oxidized to graphene oxide (GO) and subsequently reduced to reduced graphene oxide (rGO).[52] In photocatalysis, rGO is often coupled with semiconductors such as TiO_2 or plasmonic nanoparticles.[53] In these architectures, rGO acts as charge mediator to enhance separation and charge transport, thereby improving overall photocatalytic efficiency.

2.5 What is next? Metal halide semiconductors

Metal halides semiconductor are a class of materials that has attracted increasing attention over the past decade. These compounds show a rich landscape of structures, morphologies, and properties, providing numerous interesting case studies. Notably, the term “metal halide semiconductors” defines a broad family of materials, as it refers to a wide range of semiconductors, containing at least one metal and one halogen. This thesis will focus primarily on the lead and bismuth halide compounds. These materials are attracting a broad interest thanks to their appealing optical and electronic properties, the relative abundance and low cost of their elements and their easy processing. To date, lead and bismuth halide compounds have been investigated for their ability to photo-generate charge carriers, that can be exploited in different applications, such as photocatalysis,[54,55] photodetectors,[56] solar cells,[57,58] and LEDs.[59]

This thesis focuses on two classes of metal halide semiconductors that have been extensively studied for photocatalytic applications: all-inorganic perovskites and metal chalcohalides.

2.5.1 Perovskites nanocrystals

Metal halide perovskites are described by the general stoichiometry ABX_3, where A^+ is a monovalent cation that can be either inorganic (Cs^+, Rb^+) or organic (methylammonium MA or formamidinium FA), B^{2+} is a divalent metal cation such as Pb^{2+}, Sn^{2+} or Ge^{2+}, and X^- is a halide anion (Br^-, Cl^-, I^- or a combination of them). The crystal structure of perovskite compounds displays a 3D-connected network of corner-sharing $[PbX_6]^{4-}$ octahedra, which host A^+ monovalent cation within a cuboidal cavity.[60] The A^+ cation plays a key role in stabilizing the structure as it neutralizes the negatively charged lead-halide framework and can act as a spacer between the $[PbX_6]^{4-}$ octahedra (Figure 2.4a). As a consequence, the interplay between A^+ cations and octahedra strongly influences the stability of $APbX_3$ compounds.

In this thesis we will focus on all-inorganic lead perovskites $CsPbX_3$ (X = Br, Cl, I), that are the most widely studied in the form of colloidal nanocrystals.[61,62] In this regard, Figure 2.4b presents the typical absorbance and photoluminescence spectra of $CsPbBr_3$ NCs, which exhibit a strong excitonic absorption feature[63] and a very narrow emission band. The sharp photoluminescence peak also reflects the low trap states density[64] and the efficient radiative recombination pathways in these materials, an important feature for photocatalytic applications. Metal halide perovskites are mostly ionic in character, which enables the straightforward preparation of highly crystalline nanoparticles even at low temperatures.[60] Moreover, their band gap can be tuned within all the visible spectrum by adjusting the halide composition through anion exchange (Cl → Br → I).[60] The quantum confinement becomes significant when the size of the nanocrystal approaches the exciton Bohr radius, which is relatively small for $CsPbX_3$ NCs (~5 nm X = Cl, ~7 nm X = Br, ~12 nm X = I).[5,61,65]

The most relevant colloidal synthetic procedures to obtain perovskites NCs can be classified as bottom-up approaches and are carried out in the liquid phase. Among them, the most significant is the hot injection[61,66] that allows to obtain highly monodisperse NCs with controlled shape and size as shown in Figure 2.4c. Otherwise, another synthetic strategy is the ligand assisted reprecipitation (LARP),[67] that is a more efficient method in terms of cost and time and is performed at room temperature. Finally, other methods involve heat-up, solvothermal, microwave approaches, sometimes offering a scalable option for mass production.[68,69]

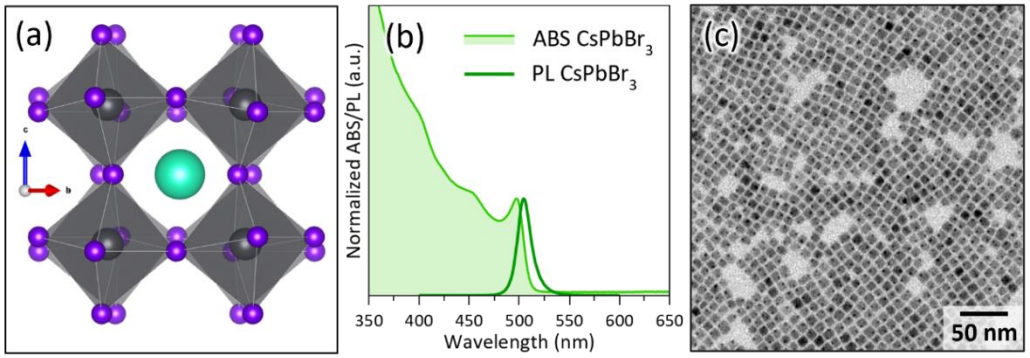

Figure 2.4. $CsPbBr_3$ perovskite nanocrystals. a) Orthorhombic distorted 3D structure of $CsPbBr_3$. b) Absorbance and photoluminescence spectra of $CsPbBr_3$ NCs. c) TEM images of $CsPbBr_3$ NCs.

Thanks to their properties, these materials find application in different filed, including photocatalysis. Perovskite-based nanocrystals have been employed for the first time as photocatalysts back in 2017, when $CsPbI_3$ NCs were used under visible light for the photocatalytic polymerization of 3,4-ethylenedioxythiophene.[70] Other works from the same year reported $CsPbBr_3$ quantum dots/ graphene oxides composites for the CO_2 photoreduction[71] and the photocatalytic hydrogen generation from hydriodic acid employing $MAPbI_3$ NCs as catalyst.[72] From that year, several efforts have been put to investigate these materials for photocatalytic applications. The reason is found on their optimal optoelectronic properties described above, which make them highly versatile in photocatalysis for mediating C-C,[73,74] C-N,[75] and C-O[76] bond formation.

2.5.2 Metal chalcohalides nanocrystals

Metal chalcohalides are a class of semiconductors characterized by the general formula "$M_aC_bH_c$" where M^{n+} is a metal cation, C^{n-} is a chalcogenide anion (S^{2-}, Se^{2-},Te^{2-}) and H^- is a halide anion (F^-, Br^-, Cl^-, I^-).[77,78] Given the high numbers of metals cations available in the periodic table, it is clear that thousands of ternary combinations with different stoichiometry are possible for this family of compounds.

In the last few years, among this large group of materials, the transition- and post transition-metal chalcohalides have attracted growing increasing interest thanks to their appealing optoelectronics properties.[79,80] Indeed, most of these compounds are semiconductors with band gaps in the visible or near infrared region. They are characterized by robustness, long-term stability, and low cost for

production due to the availability of the involved elements.[77] Furthermore, mixed-anion materials, containing two or more anionic species, are particularly attractive. The distinct formal charges, ionic radii and electronegativities of the anions provide additional degrees of freedom, allowing fine tuning of the atomic structure and, in turn, the electronic and catalytic properties of the material.[81]

So far, especially from 1960s, they have been explored in the bulk form due to their promising glass-forming abilities[82] and remarkable chemical, optical and physical properties.[83] However, one of the main issues is the use of harsh conditions required to produce this material and complex post-synthesis treatments. Moreover, the strongly directional crystal structures of many chalcohalides often lead to anisotropic grain shapes, adding further complexity.[84,85] For this reason, one possible way to overcome these problems and expand the knowledge about the metal chalcohalides family is the synthesis and development of nanocrystals.

They require lower temperatures and can be prepared in the form of solutions and inks. Chalcohalides are usually synthetized with classical colloidal synthesis like heat-up or hot-injection methods and using chemicals like those employed for metal halides (e.g., $CsPbBr_3$) but do not suffer from the intrinsic lability.[86] Figure 2.5 reports the crystal structure, absorption spectrum, and TEM image of the lead-based chalcohalide $Pb_7S_2Br_{10}$ as a representative example. Owing to the large number of possible elemental combinations, these materials can exhibit widely different features in terms of size, morphology, and optical absorption properties. However, the optoelectronic properties of metal chalcohalides and the availability of involved elements make them suitable candidates for applications in different fields such as photovoltaics,[87,77] thermoelectric[88,89] and photocatalysis[90,81] to resolve energy and environmental issues.

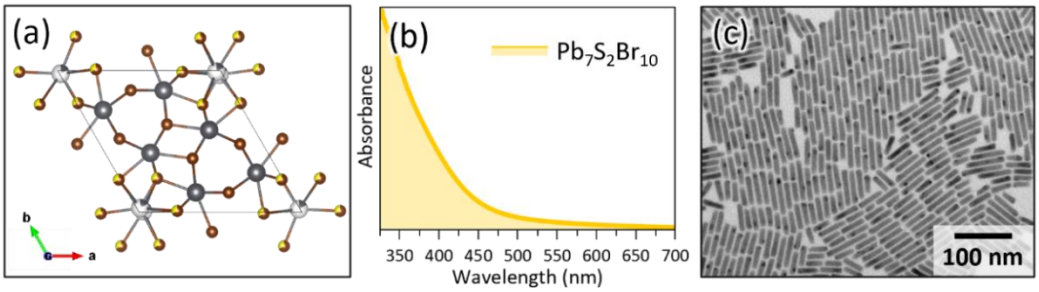

Figure 2.5. $Pb_7S_2Br_{10}$ chalcohalides nanocrystals. a) Hexagonal cell structure of $Pb_7S_2Br_{10}$. b) Absorbance spectrum of $Pb_7S_2Br_{10}$ NCs. c) TEM images of $Pb_7S_2Br_{10}$ NCs.

The literature is rich of articles reporting the use of metal chalcohalides as photocatalysts for pollutants removal, particularly for the degradation of organic dyes as well as chromium reduction.[81] The implementations of these materials benefits from their high robustness, which makes them suitable for reaction occurring in polar media such as aqueous solutions. Indeed, one of the earliest studies, dating back in 2013, reported the use of the 2D fabric-like hexagonal $Bi_{19}S_{27}Br_3$ superstructures as photocatalyst for the efficient degradation of rhodamine B (RhB) under visible-light irradiation.[91] This work opened up a solid research aimed to perform intensive studies on chalcohalide materials as photocatalysts. Indeed, in more recent years, these materials have also been exploited for energy and green applications, including CO_2 photoreduction,[92] H_2 generation[93] and N_2 fixation[94]. Overall, these are just some examples aimed to underline that metal chalcohalides represent an emerging and versatile class of materials with strong potential for a wide range of photocatalytic applications.

2.6 Conclusions

In this chapter, we have explored how nanoscale semiconductors can significantly enhance photocatalytic performance, primarily by improving charge carriers' dynamics, while simultaneously introducing new challenges. Notably, the evaluation of the factors governing the photocatalytic mechanism highlights three key aspects for the design of efficient catalytic system: visible-light activation, effective charge separation and optimized charge dynamics. The first requirement is intrinsically related to the materials band gap. Although the band gap can be tuned through doping or by controlling the NCs size, in most cases selecting materials with the suitable electronic properties turns out to be more convenient than performing multiple post-synthesis treatments. In this regard, metal halide compounds, including perovskites and chalcohalides, have emerged as promising candidates due to their favorable optoelectronic characteristics. However, achieving efficient charge separation and controlling charge-carrier dynamics remain key challenges. These aspects need to be addressed not only through materials selection but also by rational material engineering. On this basis, coupling two domains with appropriate band alignments can promote charge separation at the heterojunction, thereby increasing the charge carrier's lifetime and suppressing recombination. As a consequence, heterostructured materials appear as promising candidates to enhance photocatalytic efficiency, while simultaneously posing significant synthetic challenges and opportunities for innovation. These aspects will be discussed in the next chapter.

2.7 Bibliography

(1) Hoffmann, Roald. *Solids and Surfaces: A Chemist's View of Bonding in Extended Structures / Roald Hoffmann.*; VCH Publishers: New York, NY, 1988.

(2) Burdett, J. K. Electronic Structure and Properties of Solids. *J. Phys. Chem.* **1996**, *100* (31), 13263–13274. https://doi.org/10.1021/jp953650b.

(3) Pettifor, D. G. *Bonding and Structure of Molecules and Solids.* Oxford: Clarendon Press / Oxford University Press, 1995.

(4) Efros, A. L.; Brus, L. E. Nanocrystal Quantum Dots: From Discovery to Modern Development. *ACS Nano* **2021**, *15* (4), 6192–6210. https://doi.org/10.1021/acsnano.1c01399.

(5) Rainò, G.; Nedelcu, G.; Protesescu, L.; Bodnarchuk, M. I.; Kovalenko, M. V.; Mahrt, R. F.; Stöferle, T. Single Cesium Lead Halide Perovskite Nanocrystals at Low Temperature: Fast Single-Photon Emission, Reduced Blinking, and Exciton Fine Structure. *ACS Nano* **2016**, *10* (2), 2485–2490. https://doi.org/10.1021/acsnano.5b07328.

(6) Okuno, T.; Masumoto, Y.; Ikezawa, M.; Ogawa, T.; Lipovskii, A. A. Size-Dependent Picosecond Energy Relaxation in PbSe Quantum Dots. *Appl. Phys. Lett.* **2000**, *77* (4), 504–506. https://doi.org/10.1063/1.127025.

(7) Burda, C.; Chen, X.; Narayanan, R.; El-Sayed, M. A. Chemistry and Properties of Nanocrystals of Different Shapes. *Chem. Rev.* **2005**, *105* (4), 1025–1102. https://doi.org/10.1021/cr030063a.

(8) Zhang, N.; Gong, W.; Xiong, Y. Modern Organic Transformations: Heterogeneous Thermocatalysis or Photocatalysis? *Chem. Soc. Rev.* **2025**, *54* (11), 5189–5223. https://doi.org/10.1039/D2CS00097K.

(9) Tomar, R.; Abdala, A. A.; Chaudhary, R. G.; Singh, N. B. Photocatalytic Degradation of Dyes by Nanomaterials. *Mater. Today Proc.* **2020**, *29*, 967–973. https://doi.org/10.1016/j.matpr.2020.04.144.

(10) Sugimoto, H.; Somogyi, B.; Nakamura, T.; Zhou, H.; Ichihashi, Y.; Nishiyama, S.; Gali, A.; Fujii, M. Size-Dependent Photocatalytic Activity of Cubic Boron Phosphide Nanocrystals in the Quantum Confinement Regime. *J. Phys. Chem. C* **2019**, *123* (37), 23226–23235. https://doi.org/10.1021/acs.jpcc.9b06487.

(11) Amirjani, A.; Amlashi, N. B.; Ahmadiani, Z. S. Plasmon-Enhanced Photocatalysis Based on Plasmonic Nanoparticles for Energy and Environmental

Solutions: A Review. *ACS Appl. Nano Mater.* **2023**, *6* (11), 9085–9123. https://doi.org/10.1021/acsanm.3c01671.

(12) Guglietta, G. W.; Diroll, B. T.; Gaulding, E. A.; Fordham, J. L.; Li, S.; Murray, C. B.; Baxter, J. B. Lifetime, Mobility, and Diffusion of Photoexcited Carriers in Ligand-Exchanged Lead Selenide Nanocrystal Films Measured by Time-Resolved Terahertz Spectroscopy. *ACS Nano* **2015**, *9* (2), 1820–1828. https://doi.org/10.1021/nn506724h.

(13) Padilha, L. A.; Stewart, J. T.; Sandberg, R. L.; Bae, W. K.; Koh, W.-K.; Pietryga, J. M.; Klimov, V. I. Carrier Multiplication in Semiconductor Nanocrystals: Influence of Size, Shape, and Composition. *Acc. Chem. Res.* **2013**, *46* (6), 1261–1269. https://doi.org/10.1021/ar300228x.

(14) Kholmicheva, N.; Moroz, P.; Bastola, E.; Razgoniaeva, N.; Bocanegra, J.; Shaughnessy, M.; Porach, Z.; Khon, D.; Zamkov, M. Mapping the Exciton Diffusion in Semiconductor Nanocrystal Solids. *ACS Nano* **2015**, *9* (3), 2926–2937. https://doi.org/10.1021/nn507322y.

(15) Qu, Y.; Duan, X. Progress, Challenge and Perspective of Heterogeneous Photocatalysts. *Chem. Soc. Rev.* **2013**, *42* (7), 2568–2580. https://doi.org/10.1039/C2CS35355E.

(16) Kim, G.; Petrozza, A. Defect Tolerance and Intolerance in Metal-Halide Perovskites. *Adv. Energy Mater.* **2020**, *10* (37), 2001959. https://doi.org/10.1002/aenm.202001959.

(17) ten Brinck, S.; Zaccaria, F.; Infante, I. Defects in Lead Halide Perovskite Nanocrystals: Analogies and (Many) Differences with the Bulk. *ACS Energy Lett.* **2019**, *4* (11), 2739–2747. https://doi.org/10.1021/acsenergylett.9b01945.

(18) Mooney, J.; Krause, M. M.; Saari, J. I.; Kambhampati, P. Challenge to the Deep-Trap Model of the Surface in Semiconductor Nanocrystals. *Phys. Rev. B* **2013**, *87* (8), 081201. https://doi.org/10.1103/PhysRevB.87.081201.

(19) Layek, A.; Manna, B.; Chowdhury, A. Carrier Recombination Dynamics through Defect States of ZnO Nanocrystals: From Nanoparticles to Nanorods. *Chem. Phys. Lett.* **2012**, *539–540*, 133–138. https://doi.org/10.1016/j.cplett.2012.05.028.

(20) Peng, W.-T.; Fales, B. S.; Shu, Y.; Levine, B. G. Dynamics of Recombination *via* Conical Intersection in a Semiconductor Nanocrystal. *Chem. Sci.* **2018**, *9* (3), 681–687. https://doi.org/10.1039/C7SC04221C.

(21) Dimitropoulos, M.; Aggelopoulos, C. A.; Sygellou, L.; Tsantis, S. T.; Koutsoukos, P. G.; Yannopoulos, S. N. Unveiling the Photocorrosion Mechanism of Zinc Oxide Photocatalyst: Interplay between Surface Corrosion and Regeneration. *J. Environ. Chem. Eng.* **2024**, *12* (2), 112102. https://doi.org/10.1016/j.jece.2024.112102.

(22) Seki, K.; Higashi, T.; Kawase, Y.; Takanabe, K.; Domen, K. Exploring the Photocorrosion Mechanism of a Photocatalyst. *J. Phys. Chem. Lett.* **2022**, *13* (44), 10356–10363. https://doi.org/10.1021/acs.jpclett.2c02779.

(23) Pu, Y.; Cai, F.; Wang, D.; Wang, J.-X.; Chen, J.-F. Colloidal Synthesis of Semiconductor Quantum Dots toward Large-Scale Production: A Review. *Ind. Eng. Chem. Res.* **2018**, *57* (6), 1790–1802. https://doi.org/10.1021/acs.iecr.7b04836.

(24) Kovalenko, M. V.; Manna, L.; Cabot, A.; Hens, Z.; Talapin, D. V.; Kagan, C. R.; Klimov, V. I.; Rogach, A. L.; Reiss, P.; Milliron, D. J.; Guyot-Sionnnest, P.; Konstantatos, G.; Parak, W. J.; Hyeon, T.; Korgel, B. A.; Murray, C. B.; Heiss, W. Prospects of Nanoscience with Nanocrystals. *ACS Nano* **2015**, *9* (2), 1012–1057. https://doi.org/10.1021/nn506223h.

(25) Samanta, K.; Deswal, P.; Alam, S.; Bhati, M.; Ivanov, S. A.; Tretiak, S.; Ghosh, D. Ligand Controls Excited Charge Carrier Dynamics in Metal-Rich CdSe Quantum Dots: Computational Insights. *ACS Nano* **2024**, *18* (36), 24941–24952. https://doi.org/10.1021/acsnano.4c05638.

(26) Pan, Q.; Zhao, Q.; Wei, P.; Li, G. Surface Ligands for Perovskite Quantum Dots. *Chem. Sus. Chem*. **2025**, *18* (4), e202401875. https://doi.org/10.1002/cssc.202401875

(27) Chakraborty, I. N.; Roy, P.; Rao, A.; Devatha, G.; Roy, S.; Pillai, P. P. The Unconventional Role of Surface Ligands in Dictating the Light Harvesting Properties of Quantum Dots. *J. Mater. Chem. A* **2021**, *9* (12), 7422–7457. https://doi.org/10.1039/D0TA12623C.

(28) Chen, Y.; Yu, S.; Fan, X.-B.; Wu, L.-Z.; Zhou, Y. Mechanistic Insights into the Influence of Surface Ligands on Quantum Dots for Photocatalysis. *J. Mater. Chem. A* **2023**, *11* (16), 8497–8514. https://doi.org/10.1039/D2TA09293J.

(29) Kwon, S. G.; Hyeon, T. Formation Mechanisms of Uniform Nanocrystals via Hot-injection and Heat-up Methods. *Small* **2011**, *7* (19), 2685–2702. https://doi.org/10.1002/smll.201002022.

(30) Timonen, J. V. I.; Seppälä, E. T.; Ikkala, O.; Ras, R. H. A. From Hot-Injection Synthesis to Heating-Up Synthesis of Cobalt Nanoparticles: Observation of Kinetically Controllable Nucleation. *Angew. Chem. Int. Ed.* **2011**, *50* (9), 2080–2084. https://doi.org/10.1002/anie.201005600.

(31) de Mello Donegá, C.; Liljeroth, P.; Vanmaekelbergh, D. Physicochemical Evaluation of the Hot-injection Method, a Synthesis Route for Monodisperse Nanocrystals. *Small* **2005**, *1* (12), 1152–1162. https://doi.org/10.1002/smll.200500239

(32) Soosaimanickam, A.; Manidurai, P.; Krishna Sundaram, S.; Sridharan, M. B. Advancements and Challenges in Synthesizing Colloidal Semiconductor Nanocrystals by Hot-Injection Method. In *Nanomaterials: The Building Blocks of Modern Technology: Synthesis, Properties and Applications*; Springer, 2023; pp 143–179. https://doi.org/10.1007/978-981-99-4149-0_8

(33) Kim, B. H.; Ko, W.; Kim, J. H.; Georgiou, J. S.; Bootharaju, M. S.; Park, J.; Hyeon, T. Heat-Up Process: Road to Synthesizing Monodisperse Nanoparticles. *Israel Journal of Chemistry* **2025**, *65* (1), e202200103. https://doi.org/10.1002/ijch.202200103

(34) Lee, D.; Kim, M.; Woo, H.-Y.; Chae, J.; Lee, D.; Jeon, S.; Oh, S. J.; Paik, T. Heating-up Synthesis of Cesium Bismuth Bromide Perovskite Nanocrystals with Tailored Composition, Morphology, and Optical Properties. *RSC advances* **2020**, *10* (12), 7126–7133. https://doi.org/10.1039/C9RA10106C.

(35) Lang, X.; Chen, X.; Zhao, J. Heterogeneous Visible Light Photocatalysis for Selective Organic Transformations. *Chem. Soc. Rev.* **2014**, *43* (1), 473–486. https://doi.org/10.1039/C3CS60188A.

(36) Yan, C.; Qian, Y.; Liao, Z.; Le, Z.; Fan, Q.; Zhu, H.; Xie, Z. Recent Progress of Metal Halide Perovskite Materials in Heterogeneous Photocatalytic Organic Reactions. *Photochem. Photobiol. Sci.* **2024**, *23* (7), 1393–1415. https://doi.org/10.1007/s43630-024-00599-2.

(37) Jaiswal, K.; Mahanta, M.; De, M. Nanomaterials in Photocatalysed Organic Transformations: Development, Prospects and Challenges. *Chem. Commun.* **2023**, *59* (40), 5987–6003. https://doi.org/10.1039/D3CC00993A.

(38) Fujihira, M.; Satoh, Y.; Osa, T. Heterogeneous Photocatalytic Oxidation of Aromatic Compounds on TiO_2. *Nature* **1981**, *293* (5829), 206–208. https://doi.org/10.1038/293206a0.

(39) Pelizzetti, E.; Minero, C. Mechanism of the Photo-Oxidative Degradation of Organic Pollutants over TiO_2 Particles. *Electrochimica Acta* **1993**, *38* (1), 47–55. https://doi.org/10.1016/0013-4686(93)80009-O.

(40) Gaya, U. I.; Abdullah, A. H. Heterogeneous Photocatalytic Degradation of Organic Contaminants over Titanium Dioxide: A Review of Fundamentals, Progress and Problems. *J. Photochem. Photobiol. C: Photochem. Rev.* **2008**, *9* (1), 1–12. https://doi.org/10.1016/j.jphotochemrev.2007.12.003.

(41) Carneiro, J. T.; Savenije, T. J.; Moulijn, J. A.; Mul, G. How Phase Composition Influences Optoelectronic and Photocatalytic Properties of TiO_2. *J. of Phys. Chem. C* **2011**, *115* (5), 2211–2217. https://doi.org/10.1021/jp110190a.

(42) Eddy, D. R.; Permana, M. D.; Sakti, L. K.; Sheha, G. A. N.; Solihudin; Hidayat, S.; Takei, T.; Kumada, N.; Rahayu, I. Heterophase Polymorph of TiO_2 (Anatase, Rutile, Brookite, TiO_2 (B)) for Efficient Photocatalyst: Fabrication and Activity. *Nanomaterials* **2023**, *13* (4), 704. https://doi.org/10.3390/nano13040704.

(43) Tan, Y. N.; Wong, C. L.; Mohamed, A. R. An Overview on the Photocatalytic Activity of Nano-Doped- TiO_2 in the Degradation of Organic Pollutants. *ISRN Materials Science* **2011**, *2011*, 1–18. https://doi.org/10.5402/2011/261219.

(44) Heine, T. Transition Metal Chalcogenides: Ultrathin Inorganic Materials with Tunable Electronic Properties. *Acc. Chem. Res.* **2015**, *48* (1), 65–72. https://doi.org/10.1021/ar500277z.

(45) Dickinson, R. G.; Pauling, L. THE CRYSTAL STRUCTURE OF MOLYBDENITE. *J. Am. Chem. Soc.* **1923**, *45* (6), 1466–1471. https://doi.org/10.1021/ja01659a020.

(46) Han, J. H.; Kwak, M.; Kim, Y.; Cheon, J. Recent Advances in the Solution-Based Preparation of Two-Dimensional Layered Transition Metal Chalcogenide Nanostructures. *Chem. Rev.* **2018**, *118* (13), 6151–6188. https://doi.org/10.1021/acs.chemrev.8b00264.

(47) Chhowalla, M.; Shin, H. S.; Eda, G.; Li, L.-J.; Loh, K. P.; Zhang, H. The Chemistry of Two-Dimensional Layered Transition Metal Dichalcogenide Nanosheets. *Nat. Chem.* **2013**, *5* (4), 263–275. https://doi.org/10.1038/nchem.1589.

(48) Jaiswal, K.; Girish, Y. R.; De, M. Group-VI-Chalcogenide-Based Nanomaterials in Photo/Thermal Organic Transformations. *Acc. Mater. Res.* **2022**, *3* (10), 1033–1048. https://doi.org/10.1021/accountsmr.2c00110.

(49) Maeda, K.; Wang, X.; Nishihara, Y.; Lu, D.; Antonietti, M.; Domen, K. Photocatalytic Activities of Graphitic Carbon Nitride Powder for Water Reduction and Oxidation under Visible Light. *J. Phys. Chem. C* **2009**, *113* (12), 4940–4947. https://doi.org/10.1021/jp809119m.

(50) Qi, K.; Liu, S.; Zada, A. Graphitic Carbon Nitride, a Polymer Photocatalyst. *Journal of the Taiwan Institute of Chemical Engineers* **2020**, *109*, 111–123. https://doi.org/10.1016/j.jtice.2020.02.012.

(51) Li, X.; Yu, J.; Wageh, S.; Al-Ghamdi, A. A.; Xie, J. Graphene in Photocatalysis: A Review. *Small* **2016**, *12* (48), 6640–6696. https://doi.org/10.1002/smll.201600382.

(52) Khan, F.; Khan, M. S.; Kamal, S.; Arshad, M.; Ahmad, S. I.; Nami, S. A. A. Recent Advances in Graphene Oxide and Reduced Graphene Oxide Based Nanocomposites for the Photodegradation of Dyes. *J. Mater. Chem. C* **2020**, *8* (45), 15940–15955. https://doi.org/10.1039/D0TC03684F.

(53) Mondal, A.; Prabhakaran, A.; Gupta, S.; Subramanian, V. R. Boosting Photocatalytic Activity Using Reduced Graphene Oxide (RGO)/Semiconductor Nanocomposites: Issues and Future Scope. *ACS Omega* **2021**, *6* (13), 8734–8743. https://doi.org/10.1021/acsomega.0c06045.

(54) Zhu, X.; Lin, Y.; Sun, Y.; Beard, M. C.; Yan, Y. Lead-Halide Perovskites for Photocatalytic α-Alkylation of Aldehydes. *J. Am. Chem. Soc.* **2019**, *141* (2), 733–738. https://doi.org/10.1021/jacs.8b08720.

(55) Ran, M.-Y.; Zhou, S.-H.; Wei, W.; Song, B.-J.; Shi, Y.-F.; Wu, X.-T.; Lin, H.; Zhu, Q.-L. Quaternary Chalcohalides $CdSnSX_2$ (X = Cl or Br) with Neutral Layers: Syntheses, Structures, and Photocatalytic Properties. *Inorg. Chem.* **2021**, *60* (5), 3431–3438. https://doi.org/10.1021/acs.inorgchem.1c00010.

(56) Bao, C.; Yang, J.; Bai, S.; Xu, W.; Yan, Z.; Xu, Q.; Liu, J.; Zhang, W.; Gao, F. High Performance and Stable All-Inorganic Metal Halide Perovskite-Based Photodetectors for Optical Communication Applications. *Adv. Mater.* **2018**, *30* (38), 1803422. https://doi.org/10.1002/adma.201803422.

(57) Zhang, H.; Xia, Y.; Zhang, Y.; Ghorpade, U. V.; He, M.; Shin, S. W.; Hao, X.; Suryawanshi, M. P. The Rise of Chalcohalide Solar Cells: Comprehensive Insights from Materials to Devices. *Adv. Sci.* **2025**, *12* (19), 2413131. https://doi.org/10.1002/advs.202413131.

(58) Zhou, Y.; Game, O. S.; Pang, S.; Padture, N. P. Microstructures of Organometal Trihalide Perovskites for Solar Cells: Their Evolution from Solutions

and Characterization. *J. Phys. Chem. Lett.* **2015**, *6* (23), 4827–4839. https://doi.org/10.1021/acs.jpclett.5b01843.

(59) Fakharuddin, A.; Gangishetty, M. K.; Abdi-Jalebi, M.; Chin, S.-H.; bin Mohd Yusoff, Abd. R.; Congreve, D. N.; Tress, W.; Deschler, F.; Vasilopoulou, M.; Bolink, H. J. Perovskite Light-Emitting Diodes. *Nature Electronics* **2022**, *5* (4), 203–216. https://doi.org/10.1038/s41928-022-00745-7.

(60) Shamsi, J.; Urban, A. S.; Imran, M.; De Trizio, L.; Manna, L. Metal Halide Perovskite Nanocrystals: Synthesis, Post-Synthesis Modifications, and Their Optical Properties. *Chem. Rev.* **2019**, *119* (5), 3296–3348. https://doi.org/10.1021/acs.chemrev.8b00644.

(61) Protesescu, L.; Yakunin, S.; Bodnarchuk, M. I.; Krieg, F.; Caputo, R.; Hendon, C. H.; Yang, R. X.; Walsh, A.; Kovalenko, M. V. Nanocrystals of Cesium Lead Halide Perovskites ($CsPbX_3$, X = Cl, Br, and I): Novel Optoelectronic Materials Showing Bright Emission with Wide Color Gamut. *Nano Lett.* **2015**, *15* (6), 3692–3696. https://doi.org/10.1021/nl5048779.

(62) De Trizio, L.; Infante, I.; Manna, L. Surface Chemistry of Lead Halide Perovskite Colloidal Nanocrystals. *Acc. Chem. Res.* **2023**, *56* (13), 1815–1825. https://doi.org/10.1021/acs.accounts.3c00174.

(63) Maes, J.; Balcaen, L.; Drijvers, E.; Zhao, Q.; De Roo, J.; Vantomme, A.; Vanhaecke, F.; Geiregat, P.; Hens, Z. Light Absorption Coefficient of $CsPbBr_3$ Perovskite Nanocrystals. *J. Phys. Chem. Lett.* **2018**, *9* (11), 3093–3097. https://doi.org/10.1021/acs.jpclett.8b01065.

(64) Huang, H.; Bodnarchuk, M. I.; Kershaw, S. V.; Kovalenko, M. V.; Rogach, A. L. Lead Halide Perovskite Nanocrystals in the Research Spotlight: Stability and Defect Tolerance. *ACS Energy Lett.* **2017**, *2* (9), 2071–2083. https://doi.org/10.1021/acsenergylett.7b00547.

(65) Ha, S.-T.; Su, R.; Xing, J.; Zhang, Q.; Xiong, Q. Metal Halide Perovskite Nanomaterials: Synthesis and Applications. *Chem. Sci.* **2017**, *8* (4), 2522–2536. https://doi.org/10.1039/C6SC04474C.

(66) Imran, M.; Caligiuri, V.; Wang, M.; Goldoni, L.; Prato, M.; Krahne, R.; De Trizio, L.; Manna, L. Benzoyl Halides as Alternative Precursors for the Colloidal Synthesis of Lead-Based Halide Perovskite Nanocrystals. *J. Am. Chem. Soc.* **2018**, *140* (7), 2656–2664. https://doi.org/10.1021/jacs.7b13477.

(67) Nair, G. B.; Tamboli, S.; Kroon, R. E.; Dhoble, S. J.; Swart, H. C. Facile Room-Temperature Colloidal Synthesis of $CsPbBr_3$ Perovskite Nanocrystals by the Emulsion-Based Ligand-Assisted Reprecipitation Approach: Tuning the

Color-Emission by the Demulsification Process. *J. Alloys Compd.* **2022**, *928*, 167249. https://doi.org/10.1016/j.jallcom.2022.167249.

(68) Chen, M.; Zou, Y.; Wu, L.; Pan, Q.; Yang, D.; Hu, H.; Tan, Y.; Zhong, Q.; Xu, Y.; Liu, H.; Sun, B.; Zhang, Q. Solvothermal Synthesis of High-Quality All-Inorganic Cesium Lead Halide Perovskite Nanocrystals: From Nanocube to Ultrathin Nanowire. *Adv. Funct. Mater.* **2017**, *27* (23), 1701121. https://doi.org/10.1002/adfm.201701121.

(69) Lee, D.; Kim, M.; Woo, H.-Y.; Chae, J.; Lee, D.; Jeon, S.; Oh, S. J.; Paik, T. Heating-up Synthesis of Cesium Bismuth Bromide Perovskite Nanocrystals with Tailored Composition, Morphology, and Optical Properties. *RSC Adv.* **2020**, *10* (12), 7126–7133. https://doi.org/10.1039/C9RA10106C.

(70) Chen, K.; Deng, X.; Dodekatos, G.; Tüysüz, H. Photocatalytic Polymerization of 3,4-Ethylenedioxythiophene over Cesium Lead Iodide Perovskite Quantum Dots. *J. Am. Chem. Soc.* **2017**, *139* (35), 12267–12273. https://doi.org/10.1021/jacs.7b06413.

(71) Xu, Y.-F.; Yang, M.-Z.; Chen, B.-X.; Wang, X.-D.; Chen, H.-Y.; Kuang, D.-B.; Su, C.-Y. A $CsPbBr_3$ Perovskite Quantum Dot/Graphene Oxide Composite for Photocatalytic CO_2 Reduction. *J. Am. Chem. Soc.* **2017**, *139* (16), 5660–5663. https://doi.org/10.1021/jacs.7b00489.

(72) Park, S.; Chang, W. J.; Lee, C. W.; Park, S.; Ahn, H.-Y.; Nam, K. T. Photocatalytic Hydrogen Generation from Hydriodic Acid Using Methylammonium Lead Iodide in Dynamic Equilibrium with Aqueous Solution. *Nat. Energy* **2016**, *2* (1), 16185. https://doi.org/10.1038/nenergy.2016.185.

(73) Rosa-Pardo, I.; Zhu, D.; Cortés-Villena, A.; Prato, M.; De Trizio, L.; Manna, L.; Galian, R. E.; Pérez-Prieto, J. The Dark Side of Lead-Free Metal Halide Nanocrystals: Substituent-Modulated Photocatalytic Activity in Benzyl Bromide Reduction. *ACS Energy Lett.* **2023**, *8* (6), 2789–2798. https://doi.org/10.1021/acsenergylett.3c00771.

(74) Wang, K.; Lu, H.; Zhu, X.; Lin, Y.; Beard, M. C.; Yan, Y.; Chen, X. Ultrafast Reaction Mechanisms in Perovskite Based Photocatalytic C–C Coupling. *ACS Energy Lett.* **2020**, *5* (2), 566–571. https://doi.org/10.1021/acsenergylett.9b02714.

(75) Zhu, X.; Lin, Y.; San Martin, J.; Sun, Y.; Zhu, D.; Yan, Y. Lead Halide Perovskites for Photocatalytic Organic Synthesis. *Nat. Commun.* **2019**, *10* (1), 2843. https://doi.org/10.1038/s41467-019-10634-x.

(76) Huang, H.; Pradhan, B.; Hofkens, J.; Roeffaers, M. B. J.; Steele, J. A. Solar-Driven Metal Halide Perovskite Photocatalysis: Design, Stability, and Performance. *ACS Energy Lett.* **2020**, *5* (4), 1107–1123. https://doi.org/10.1021/acsenergylett.0c00058.

(77) Ghorpade, U. V.; Suryawanshi, M. P.; Green, M. A.; Wu, T.; Hao, X.; Ryan, K. M. Emerging Chalcohalide Materials for Energy Applications. *Chem. Rev.* **2023**, *123* (1), 327–378. https://doi.org/10.1021/acs.chemrev.2c00422.

(78) Palazon, F. Metal Chalcohalides: Next Generation Photovoltaic Materials? *Solar RRL* **2022**, *6* (2), 2100829. https://doi.org/10.1002/solr.202100829.

(79) Nielsen, R. S.; Álvarez, Á. L.; Medaille, A. G.; Caño, I.; Navarro-Güell, A.; Álvarez, C. L.; Cazorla, C.; Ferrer, D. R.; Li-Kao, Z. J.; Saucedo, E.; Dimitrievska, M. Parallel Exploration of the Optoelectronic Properties of (Sb,Bi)(S,Se)(Br,I) Chalcohalides. *J. Mater. Chem. A* **2025**, *13* (37), 31727–31739. https://doi.org/10.1039/D5TA05011A.

(80) Khan, M. S.; Binzowaimil, A. M.; Stampfl, C.; Fakhera, F.; Conquest, O. J.; Al-Hmoud, M.; Aziz, S. M. Insight into the Electronic, Optical, and Thermoelectric Properties of Novel Ternary Chalcohalides: Next-Generation Energy Applications. *RSC Adv.* **2025**, *15* (57), 49388–49398. https://doi.org/10.1039/D5RA08449K.

(81) Shyamal, S.; Pradhan, N. Nanostructured Metal Chalcohalide Photocatalysts: Crystal Structures, Synthesis, and Applications. *ACS Energy Lett.* **2023**, *8* (9), 3902–3926. https://doi.org/10.1021/acsenergylett.3c01236.

(82) Gan, F. Structure, Properties and Applications of Chalcohalide Glasses: A Review. *J. Non-Cryst. Solids* **1992**, *140*, 184–193. https://doi.org/10.1016/S0022-3093(05)80765-3.

(83) Butler, K. T.; McKechnie, S.; Azarhoosh, P.; Van Schilfgaarde, M.; Scanlon, D. O.; Walsh, A. Quasi-Particle Electronic Band Structure and Alignment of the V-VI-VII Semiconductors SbSI, SbSBr, and SbSeI for Solar Cells. *Appl. Phys. Lett.* **2016**, *108* (11), 112103. https://doi.org/10.1063/1.4943973.

(84) Quarta, D.; Toso, S.; Giannuzzi, R.; Caliandro, R.; Moliterni, A.; Saleh, G.; Capodilupo, A.; Debellis, D.; Prato, M.; Nobile, C.; Maiorano, V.; Infante, I.; Gigli, G.; Giannini, C.; Manna, L.; Giansante, C. Colloidal Bismuth Chalcohalide Nanocrystals. *Angew. Chem.* **2022**, *134* (22), e202201747. https://doi.org/10.1002/ange.202201747.

(85) Quarta, D.; Toso, S.; Saleh, G.; Caliandro, R.; Moliterni, A.; Griesi, A.; Divitini, G.; Infante, I.; Gigli, G.; Giannini, C.; Manna, L.; Giansante, C. Mixed Valence of Bismuth in Hexagonal Chalcohalide Nanocrystals. *Chem. Mater.* **2023**, *35* (3), 1029–1036. https://doi.org/10.1021/acs.chemmater.2c02941.

(86) Li, J.; Han, S.; Guo, S. Chalcohalides: A Rising Type of Second-Order Nonlinear Optical Materials. *Eur. J. Inorg. Chem.* **2022**, *2022* (33), e202200419. https://doi.org/10.1002/ejic.202200419.

(87) Kunioku, H.; Higashi, M.; Abe, R. Low-Temperature Synthesis of Bismuth Chalcohalides: Candidate Photovoltaic Materialswith Easily, Continuously Controllable Band Gap. *Sci. Rep.* **2016**, *6* (1), 32664. https://doi.org/10.1038/srep32664.

(88) Das, A.; Debnath, K.; Maria, I.; Das, S.; Dutta, P.; Swain, D.; Waghmare, U. V.; Biswas, K. Influence of Subvalent Twin-Rattler for High *n* - Type Thermoelectric Performance in $Bi_{13}S_{18}Br_2$ Chalcohalide. *J. Am. Chem. Soc.* **2024**, *146* (44), 30518–30528. https://doi.org/10.1021/jacs.4c11738.

(89) Chauhan, P.; Kumar, A. Piezoelectric, Thermoelectric, and Photocatalytic Water Splitting Properties of Janus Arsenic Chalcohalide Monolayers. *ACS Omega* **2024**, *9* (31), 33723–33734. https://doi.org/10.1021/acsomega.4c02874.

(90) Ran, M.-Y.; Zhou, S.-H.; Wei, W.; Song, B.-J.; Shi, Y.-F.; Wu, X.-T.; Lin, H.; Zhu, Q.-L. Quaternary Chalcohalides $CdSnSX_2$ (X = Cl or Br) with Neutral Layers: Syntheses, Structures, and Photocatalytic Properties. *Inorg. Chem.* **2021**, *60* (5), 3431–3438. https://doi.org/10.1021/acs.inorgchem.1c00010.

(91) Deng, C.; Guan, H.; Tian, X. Novel Bi19S27Br3 Superstructures: Facile Microwave-Assisted Aqueous Synthesis and Their Visible Light Photocatalytic Performance. *Mater. Lett.* **2013**, *108*, 17–20. https://doi.org/10.1016/j.matlet.2013.06.078.

(92) Das, R.; Patra, A.; Dutta, S. K.; Shyamal, S.; Pradhan, N. Facets-Directed Epitaxially Grown Lead Halide Perovskite-Sulfobromide Nanocrystal Heterostructures and Their Improved Photocatalytic Activity. *J. Am. Chem. Soc.* **2022**, *144* (40), 18629–18641. https://doi.org/10.1021/jacs.2c08639.

(93) Bargozideh, S.; Tasviri, M. Construction of a Novel BiSI/MoS2 Nanocomposite with Enhanced Visible-Light Driven Photocatalytic Performance. *New J. Chem.* **2018**, *42* (22), 18236–18241. https://doi.org/10.1039/C8NJ04102D.

(94) Cao, Y.; El-Shafay, A. S.; Mohammed, A. H.; Almojil, S. F.; Almohana, A. I.; Alali, A. F. Controlling the Charge Carriers Recombination

Kinetics on the G-C_3N_4-BiSI n-n Heterojunction with Efficient Photocatalytic Activity in N2 Fixation and Degradation of MB and Phenol. *Adv. Powder Technol.* **2022**, *33* (4), 103513. https://doi.org/10.1016/j.apt.2022.103513.

CHAPTER 3

Why Heterostructures?

3.1 Colloidal heterostructure nanoparticles

Colloidal heterostructures are nanoparticles composed by two different materials connected at an interface, that can show properties different from those of their individual components.[1,2,3] The idea of coupling two materials together is appealing exactly because the new architecture can share the electronic and optical properties of the two domains, giving rise to improved or new, sometimes unexpected features. A huge variety of nano-heterostructures combining many different materials and domain morphologies have been reported in the literature in the last decades.[4] Just to mention classes of materials, heterostructures can be formed between two semiconductors,[5] between a semiconductor and a metal,[6] between a semiconductor and an insulator,[7] and more. Some relevant examples include CdSe/ZnS core-shell quantum dots[8,9] and Pt-TiO_2 heterostructures.[10,11] CdSe/ZnS architectures are employed in optoelectronic applications such as light-emitting diodes (LEDs)[12] and bioimaging, as they benefit from suppressed non-radiative recombination and enhanced emission properties.[13] In the same way, Pt-TiO_2 heterostructures have played a pivotal role in catalysis, where heterojunction formation improves catalytic efficiency.[14,15]

Among all the possible heterostructures, architectures involving semiconductors can be appealing for photocatalytic applications, as they can absorb light and use this energy to produce charge carriers, which can then drive photoredox reactions. In this context, the formation of heterostructures with adequate band alignments can be beneficial, as it facilitates charge separation and reduces the probability of charge recombination. As a result, the lifetime and availability of charge carriers are increased.

Looking at it from another perspective, a semiconductor can be coupled with a metallic domain to form a heterostructure.[6,16] Metal nanocrystals (NCs) have attracted great attention due to their remarkable physical and chemical properties.

Among the various characteristics of metal NCs, one of the most relevant is the surface plasmon resonance (SPR), which refers to the collective oscillation of free charge carriers excited by incident light. This phenomenon can induce a strong localized electromagnetic field. Moreover, upon resonant excitation, plasmonic metals interact strongly with light and the coherent oscillation of free electrons rapidly dephases, leading to the generation of energetic hot electrons and hot holes.[17] Metals that exhibit a pronounced SPR include Au,[18] Ag,[19] and Cu.[20] In addition, some metals show high selectivity toward specific reactions, for instance, metallic bismuth is highly selective in CO_2 photoreduction,[21] yielding acetic acid as the main product. In this context, it is clear that coupling a semiconductor with a metal represents a promising strategy, as the metal can act as a charge sink, thereby enhancing light absorption, charge carrier generation, and charge separation during the photocatalytic process.[16]

With this picture in mind, coupling two semiconductors or a semiconductor with a metal can enhance charge dynamics, which is crucial for achieving efficient photocatalytic performance, as discussed in the previous chapter. In this regard, the following paragraph will address the different types of heterojunctions that can be formed by coupling these materials (semiconductor/metal). In particular, we will focus on the configurations most suitable for photocatalytic applications since some of these heterostructures will be employed in the next chapters for photoredox reactions.

3.2 Heterojunction types

As mentioned above, two domains (semiconductor/metal) are coupled to decrease electron and hole recombination, thereby enhancing excitons lifetime. These combinations of materials with different band alignments result in a new electronic structure after hybridization. Band bending is generated at the interface between the two components. The interface therefore induces an electric field within the space-charge region, which promotes the spatial separation of photogenerated charge carriers and is referred to as a “heterojunction”.[16]

3.2.1 Semiconductor – semiconductor heterojunctions

In this regard, coupling two semiconductors with different electronic structures gives rise to different types of heterojunctions. These configurations depend on the relative alignment of the valence and conduction bands, which governs the dynamics of photogenerated charge carriers. Based on that, four main types of

heterojunctions can be obtained: type I,[22] type II,[23] type III[24] and direct Z-scheme[25] as depicted in Figure 3.1.[26,27]

Among these configurations, the most suitable ones for photocatalytic applications are the type II (Figure 3.1b) heterojunction and the direct Z-scheme (Figure 3.1d).[28,29,30]

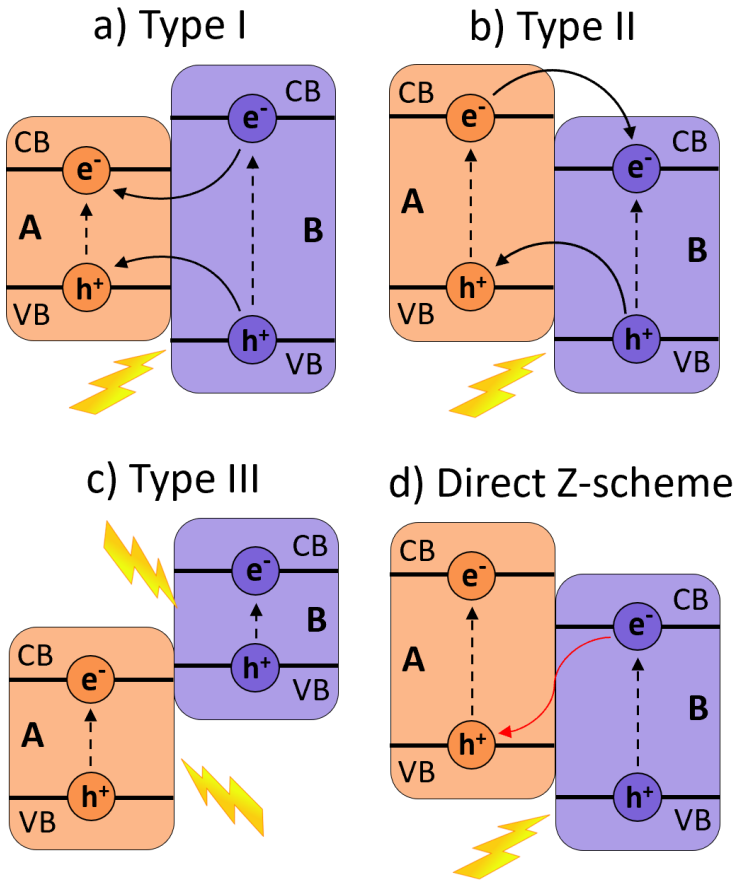

Figure 3.1. Different heterojunctions configurations. a) Type I heterojunction. b) Type II heterojunction. c) Type III heterojunction. d) Direct Z-scheme.

In type II heterojunction,[31,32] also called staggered gap, the conduction band of material B is located below that of material A, while the valence band of material A lies above the valence band of B. Upon illumination, this configuration can promote the charge separation and limit charge recombination as the electrons and holes are separated in the two different components. Even if type III (Figure 3.1c) heterojunctions are similar to type II configurations, both CB and VB in semiconductor B will be higher than semiconductor A, meaning that the band

alignment is completely staggered. Indeed, this configuration is also called "broken gap" as the CB and VB are placed far apart, thus preventing direct overlap.[33] This arrangement is not suitable for mediating the spatial separation of e^- and h^+ pairs, key factor in photocatalysis. In the same way, in type I configuration (Figure 3.1a), also known as straddling gap, the conduction and valence band of material A are both located within the band gap of material B. Under illumination, charge carriers tend to migrate to lower energy states, and as a result both electrons and holes are confined in material A. This arrangement can enhance charge recombination, therefore it is mostly utilized in optoelectronic devices, for example light emitting diodes.[34]

On the other hand, type II heterojunctions have been explored for a wide range of photocatalytic reactions.[35,36] Indeed, the band bending phenomenon can occur when this configuration is formed, establishing an internal electric filed that further drives directional charge transfer across the junction. However, it is possible that the spatial separation of charges can led to a reduction of their redox ability as electrons and holes accumulate at less energetic levels. As a consequence, type II heterojunction materials allow the accumulation of photo-generated electrons and holes on materials with weak reduction potential and weak oxidation potential. The impact of this feature strongly depends on the redox potential of the target molecule to reduce or oxidize.[32]

For what concerns the direct Z-scheme (Figure 3.1d), the band alignment of semiconductors A and B is very similar to that of the type II heterojunction; however, the direction of charge is opposite and the mechanism is actually different, as explained below.[31] In this case, the two materials are coupled in a way that, upon illumination, the photogenerated electrons in semiconductor B, with lower reduction ability, recombine with the photogenerated holes in semiconductor A, that shows lower oxidation ability. As a result, the electrons in the CB of semiconductor A, with a high reduction potential, and holes in the VB of the semiconductor B, with a high oxidation potential, are preserved for photocatalytic reactions. In addition, it is worth underlining that charge carrier migration in direct Z-scheme is physically more feasible than in type II systems. This is because the transfer of photogenerated electrons from the CB of semiconductor B to the hole-rich VB of semiconductor A is promoted by the electrostatic attraction between the charges.[37] The name "direct Z-scheme" is due to the charge carrier's migration pathways that resemble the letter "Z".

This configuration has actually a long history behind. Indeed, the concept of a photocatalytic Z-scheme was introduced by Bard in 1979.[38] The first Z-scheme generation is represented by a system in a liquid phase that combines two semiconductors linked by a redox mediator, an electron acceptor/donor pair. Upon illumination, both semiconductors generate electrons and holes. The electrons of one of the two semiconductors are transferred to the other semiconductor through the redox mediator, allowing the charge separation and optimization of the redox properties. However, this configuration has severe limitations: reverse reactions due to reversible redox mediators, reduced photocatalytic efficiency, and limited use in the liquid phase.

To overcome these issues, the second-generation Z-scheme photocatalytic system, called "all-solid-state-Z-scheme", was introduced in 2006.[39] In this new configuration, the redox mediator is replaced by noble metal nanoparticles. This approach decreases the reverse reactions, but the use of costly and rare noble metals limits the implementation of this system in large-scale applications.

Subsequently, in 2009[40] it was demonstrated that a Z-scheme mechanism can occur even without mediators when two semiconductors are in close contact. Based on this, the third-generation concept, the direct Z-scheme photocatalyst, was introduced in 2013.[41] This system combines the advantages of the previous generations, such as high charge separation and optimized redox potential, while reducing costs and light-shielding effects.

As discussed above, the structure of type II heterojunctions is very similar to the one of the direct Z-scheme. For this reason, it is important to investigate the charge carrier's migration mechanisms through various characterization methods to differentiate between the two configurations. Various techniques have been developed and proposed for this purpose. They include photocatalytic reduction testing, radical species trapping, metal loading, X ray photoelectron spectroscopy (XPS), and internal electric field simulations.[31]

In conclusion, the main difference between type II and direct-Z scheme lies in their charge dynamics: the Z-scheme provides higher redox potentials, despite the internal recombination of charge carriers, whereas the type II heterojunction extends the charge-carrier lifetime by effectively separating electrons and holes at the cost of a lower redox potential. However, beyond band alignment it is noteworthy to consider the absolute redox potential of the substrate which plays a crucial role in determining the process efficiency. Therefore, the choice between

these two architectures needs to consider several aspects, such as the redox properties of the overall system and should be guided by the specific requirements of the target photocatalytic process.

3.2.2 Semiconductor – metal heterojunctions

In the case of heterojunctions composed by a semiconductor and a metal, the different scenarios can be obtained depending on the work function (Φ) between the two materials. The work function is defined as the minimum energy requirement for releasing an electron from the Fermi level (E_{Fermi}) to the vacuum level (E_{vacuum}). As a consequence, either an Ohmic contact or a Schottky barrier is generated at the interface between the semiconductor and the metal.[32,42]

More in details, an Ohmic junction is formed when the work function of the semiconductor is higher than that of the metal. This can facilitate the flow of electrons between the two materials in both forward and reverse-biased directions, resulting in poor charge separation and photo response.[43]

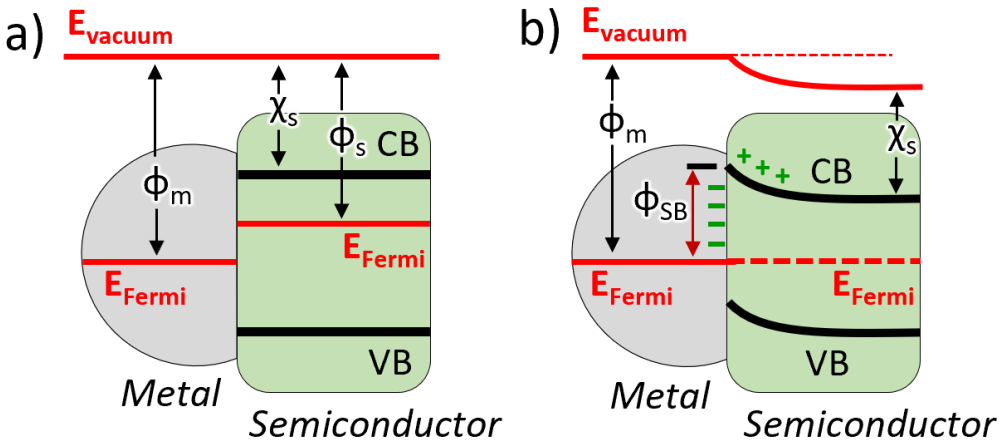

Figure 3.2. Semiconductor-Metal heterojunction. Energy band diagrams of metal and n-type semiconductor heterojunction before (a) and after reaching the equilibrium (b), where Φm is the metal work function, Φs is the semiconductor work function, χs is electron affinity of the semiconductor and $Φ_{SB}$ is the Schottky barrier.

On the contrary when the work function of the semiconductor is smaller than that of the metal, a Schottky barrier can be formed.[44] Figure 3.2 shows the most studied n-type semiconductor, whose E_{Fermi} lies closed to the CB, coupled with a metal before and after reaching the equilibrium. With this configuration, which is

the most common case in photocatalysis, the electrons will flow from the semiconductor to the metal until their Fermi levels are aligned. This process leads to an upward bending of the band edges in the semiconductor, resulting in efficient charge separation. Under equilibrium, a Helmholtz double layer will be established at the metal/semiconductor interface, where the metal is negatively charged, and the semiconductor is positively charged near its surface due to electrostatic induction. Moreover, the metal not only can act as a reservoir of electrons to enhance the charge separation of the semiconductors, but it can also provide active sites for reduction reactions.[45]

From these considerations, it is evident that the electronic structure of the junction plays a central role in the functionality of heterostructures, which is why the band alignment of matched materials is often at the center of such design problems. However, the efficacy of the heterojunction is also governed by the intimate contact between the components; in particular, the way different domains connect to each other plays an equally important role. Indeed, a poorly matched interface might introduce defect states acting as traps, which effectively capture the carriers that otherwise would be driving photoreactions. Most interfaces will be amorphous or locally disordered, implying a locally chaotic energy landscape that will likely induce the formation of defect states.

Depending on the crystallinity and structure of the two materials, an epitaxial interface may form.[46] In this case, the two matching domains share a precise structural relationship that allows the two materials to complete each other by forming a potentially defect-free interface. However, this can occur only if an epitaxial relation can be found, that is, if the interface can be described by an infinite 2D-periodic structure that is compatible with the lattices and structures of both materials. In this context, developing and exploiting tools that can actually accelerate the design of new epitaxial heterostructures becomes a fundamental step in this search.

3.3 Prediction of epitaxial interfaces

In general, the properties of heterostructure systems stem directly from the electronic structure of the junction, which is dictated by the intrinsic characteristics of the two components, as described above. Therefore, identifying suitable candidates for constructing new hetero architectures remains an open challenge. In this regard, materials selection is typically guided by the aim to achieve the optimal band alignment for a given targeted application.[47–50] While this is a valid approach

in terms of functionality, it may involve high synthetic costs, as the materials chosen for their electronic properties are not always structurally compatible, potentially resulting in defective interfaces that can be detrimental to applications governed by the electronic properties of the heterojunction such as photocatalysis.[51–53]

Structural incompatibility can also prevent the synthesis of a new nano-heterostructure. This is a serious experimental challenge, since developing a synthetic route is a demanding and time-consuming process, often driven by a trial-and-error approach.[54] Nano-heterostructures are complex systems that require balance of multiple precursors in the reaction mixture, and a poorly optimized procedure may lead to the formation of undesired phases or to the separation of the individual components of the heterostructure. This often raises the fundamental question of whether a given heterostructure is intrinsically inaccessible, or if the optimal synthetic conditions have simply not yet been identified. To address this issue, computer simulations can be employed.[55–58] Among the various strategies reported, the most used is density functional theory (DFT),[59–61] which enables predicting both the structure and properties of new heterostructures. However, DFT simulations remains largely restricted to computational experts and are often not user-friendly for experimental or synthetic scientists. Moreover, DFT calculations are computationally demanding, which greatly limits their accessibility for routine screening and high-throughput exploration of new heterojunctions.

3.4 Ogre software

In this contest, the open-source python package Ogre[62] is a powerful tool to accelerate the design and then the synthesis of new colloidal heterostructures. Ogre was initially developed by the group of Prof. Marom at Carnegie Mellon University to predict the surface of large-area epitaxial interfaces grown by thin film deposition and it was first focused on semiconductor/metal interface.[63] Then, a collaboration with members of our group extended its application to the fast screening of epitaxial interfaces between polar compounds, a direction inspired by our experimental works on metal-halide nano-heterostructures.[64] This was achieved by introducing two new features that take advantage of the ionic nature of these materials. The first is an initial screening of interface models based on charge balance, aimed at reducing the overall computational load. The second feature involves a classical potential including a Coulombic term[65] and a repulsive Born term,[62] whose parameters are automatically derived from the initial bulk structural information.

Ogre first determines all the favorable epitaxial relationships between two materials (A and B) and then tries to predict the structure of the resulting interface. The output consists of atomistic models ranked by energy, from the most stable to the least. The prediction workflow of Ogre can be resumed in three steps, as shown in Figure 3.3:

1. *Lattice Matching*
2. *Interface generation*
3. *Surface Matching and Ranking*

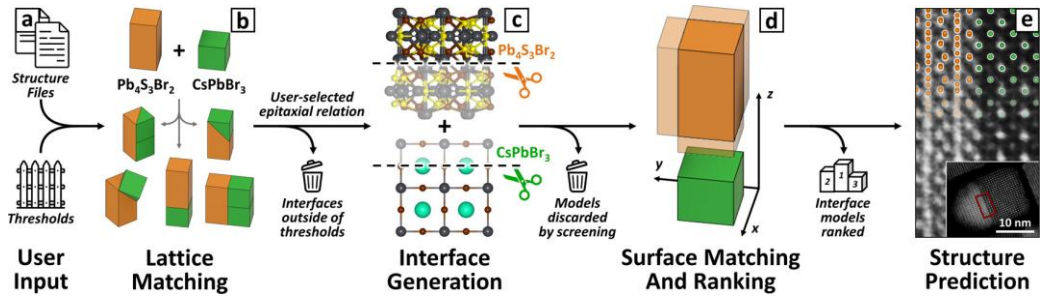

Figure 3.3. Ogre interface prediction workflow. a) Ogre takes as input the bulk structures of two materials, along with user-defined thresholds for strain, supercell area, and the Miller indices of lattice planes to consider. b) The lattice matching step identifies all the commensurate supercells that yield domain-matched interfaces within the specified thresholds. c) For selected epitaxial orientations, the interface generation step creates all possible surface terminations for both materials and combines them to construct atomistic models of the interface. d) For each model, the surface matching and ranking step identifies the optimal epitaxial registry (i.e., lateral offset) and distance between the two domains, using a fast electrostatic potential to evaluate energies. e) The output is a set of atomistic models ranked by stability. Top-ranked models can be compared with available experimental data, as demonstrated here for a $Pb_4S_3Br_2/CsPbBr_3$ heterostructure (only heavy atoms shown for clarity). Reproduced with permission from ref 62. Licensed under CC-BY 4.0. Copyright © 2025 The Authors.

3.4.1 Lattice matching

The first step in the interface modeling process is *lattice matching*. Once the user uploads the crystallographic information files (CIFs) of the two materials, Ogre employs the Zur-McGill algorithm[66] to identify suitable epitaxial relations, matching the lattice planes of the two materials. Specifically, the algorithm searches for a common 2D supercell capable of representing both materials at the interface. A match is considered valid when a supercell exists and satisfies the user-defined

requirements on strain and area. A single combination of planes may yield multiple non-equivalent supercells, differing by the relative in-plane orientation of the two materials. In these cases, the smallest supercell is chosen to reduce computational complexity and avoid ambiguities.

The user can impose specific limits on the interface strain, based on the type of interface being studied. For example, in the case of epitaxial thin film interfaces, strains above ~2% are typically considered unfavorable due to the risk of defect formation.[67] However, for nanocrystals, higher strain values, up to 10%, are often acceptable,[68,69] as the stress can be partially accommodated by local lattice deformations due to the small interface size.

Regarding the supercell area, a trade-off must be considered:

- Larger supercells reduce lattice mismatch (strain) but decrease the likelihood of atom-to-atom alignment.
- Smaller supercells increase the probability of atomic registry but may lead to higher strain.

Finally, the user may restrict the search space to specific crystallographic planes if prior knowledge is available, for instance, when the exposed facets of the nanocrystals are known. If such information is not available, it is generally reasonable to focus on low Miller index planes, as high-index surfaces are tiically less stable and less commonly exposed.[70–72]

3.4.2 Generation of interface models

The second step involves the *generation of interface models*. Since the lattice matching step relies only on crystallographic parameters, it does not account for interatomic interactions or chemical bonding at the interface. Therefore, to assess the chemical stability of the proposed epitaxial configurations, it is necessary to construct a comprehensive set of atomistic interface models and evaluate them based on their relative energies. To this end, Ogre performs the following operations:

- Cleaves both materials along planes parallel to the interface to produce surface slabs with different atomic terminations.[63,73]
- Combines these slabs in all possible ways to generate a multiple set of interface models.

The user can choose whether to distribute the strain equally between the two materials, which is common in colloidal heterostructures, or allow one material to adapt to the other fully or partially, a case more representative of thin film epitaxy on a bulk substrate.

Given the potentially large number of resulting models, Ogre implements several strategies to reduce computational cost in the subsequent ranking step, which involves the most resource-intensive calculations. These include:

- Clustering nearly coplanar atoms to ensure only reasonable surface terminations are considered from a chemical perspective.
- Removing symmetry-equivalent terminations to avoid redundant structures.

In addition, Ogre incorporates a rapid screening algorithm based on the electrostatic charge balance at the interface. For each slab, a surface charge Q is computed as:

$$\mathrm{Q} = -\frac{\sum_{\mathrm{i}} q_i \cdot d_i}{\mathrm{D}}$$

where i runs over all ions in the slabs, q_i is the charge of each ion, d_i is its distance from the interface and D is the total slab thickness. Q represents the net uncompensated surface charge of each slab, which contributes to the electrostatic compatibility at the interface. Interfaces formed by slabs with like-sign surface charges (i.e., [+/+] or [−/−]) are discarded due to electrostatic repulsion. The magnitude of Q can also be used to identify partially compensated interfaces (e.g., [+/−], [+/0], [−/0]) providing an additional criterion for screening viable interface configurations.

3.4.3 Surface matching and ranking

The final step in the workflow is *surface matching and ranking*. After generating all possible interface models, Ogre optimizes the relative positioning of the two slabs to identify the most stable bonding configuration. To perform this optimization efficiently, Ogre uses the Particle Swarm Optimization (PSO) algorithm,[74] which explores the 3D space of parameters defined by the lateral epitaxial offset (xy) and the vertical separation (z) between the slabs. The purpose is to minimize the total energy of the interface model, denoted as E_{AB}. To illustrate the results of the surface matching, Ogre provides: a 2D adhesion energy map by shifting one material on top of the other within the interface supercell at the optimal

z distance, a 1D plot of energy vs interfacial distance at the optimal xy-offset, and a 3D atomistic model of the most stable configuration, which can be visualized using programs such as VESTA.[75]

The adhesion energy is defined as:[76]

$$E_{adh} = E_{AB} - (E_A + E_B)$$

where E_A and E_B are the energies of the isolated slabs. The sign of E_{adh} indicates if the interface model is more stable than the two separate surfaces slabs. The global minimum of E_{adh} corresponds to the most stable interface configuration, while local minima indicate metastable states. All the generated interfaces are then ranked based on their interface energy (E_{int}). This value (E_{int}) reflects how energetically favorable it is to interrupt the growth of one material and switch to another, providing a quantitative basis for interface stability. Since the evaluation of all energy terms is the most computationally demanding part of the workflow, Ogre incorporates a classical interatomic potential to significantly reduce computational cost compared to density functional theory (DFT). This classical potential includes two components: a Coulombic electrostatic term, computed using the damped-shifted force method,[65,77] and a Born repulsion term,[63] which accounts for short-range interatomic repulsion.

A cutoff radius of 18 Å is used, which is sufficient for ionic materials, where long-range dispersion interactions (e.g., Van der Waals forces) are generally minimal. Each ion pair is described by a free parameter in the Born term, which is optimized so that the energy minimum coincides with the equilibrium bond length observed in the bulk structures. For bonds that are exclusive to the interface, the equilibrium distance is estimated as the sum of the ionic radii of the constituent ions. Although the accuracy of the method improves when the same bonds exist in both the bulk and the interface, it still produces reasonable and consistent results for most cases.

Finally, The Ogre workflow was applied to the $CsPbBr_3/Pb_4S_3Br_2$ epitaxial heterostructure previously reported by some members of the group in 2021.[64] The predicted most stable interface was in excellent agreement with experimental observations and DFT calculations. These results demonstrate that Ogre reliably reproduces the energy and structure of epitaxial interfaces at a substantially lower computational cost.

3.5 Heterostructures geometry

Ogre can be a useful tool also to assess the feasibility of epitaxial heterostructures with different geometries. In this regard, two main architectures can be distinguished when coupling two materials at the nanoscale: core@shell (CS) structures[78] and heterodimers[79] (HD), as illustrated in Figure 3.4. Both systems are hybrid nanoscale heterostructures composed of two (or more) different materials, in which the individual domains can interact leading to combined optical and electronical properties.

The core@shell heterostructures are the most studied and reported in literature to date.[80,81] They consist of a centrale "core" material that is uniformly coated by a second material forming a "shell". Heterodimers are instead anisotropic structures in which the two domains are adjacent, sharing only a localized interfacial facet, while a large part of the surface volume of each material remains directly exposed.[82,64] In both architectures, the two components can differ in composition, structure and electronic properties, allowing an effective tuning of their combined functionalities.

From a crystallographic perspective, the key difference between these two heterostructures lies in how the two crystalline phases are spatially arranged and how their lattices interact at the interface. For the successful growth of an epitaxial shell several key requirements must be met. First, the two materials should establish energetically favorable epitaxial interfaces along several lattice directions, to allow the seed material to be fully developed. Second, these interfaces need to preserve a consistent relative orientation between the two atomic lattices, so that the shell can grow as a single-crystalline domain. Indeed, in a core@shell architecture, the shell phase grows epitaxially and continuously around the core domain. This requires a high lattice compatibility with small lattice mismatch, similar crystal symmetry and favorable interfacial energy. All these features enable the formation of coherent or semi-coherent epitaxial interfaces over the core domain. For a core@shell architecture uniform nucleation of the shell on all crystallographic facets is required.[83]

In contrast, heterodimers form when the nucleation of the second phase is selective form a crystallographic perspective. This nucleation event will occur only on specific facets of the two phases due to anisotropic surface energies, larger lattice mismatch, or symmetry incompatibilities that prevent uniform epitaxial overgrowth.[5]

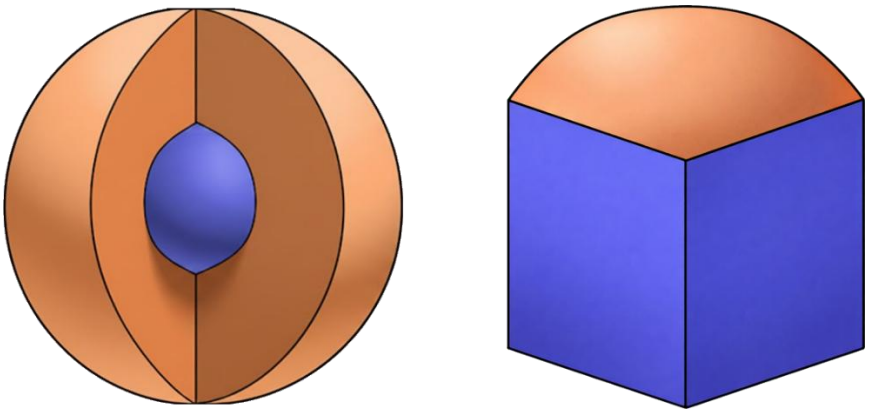

Figure 3.4. Different heterostructure geometries. Comparison between core-shell and heterodimer architectures.

These configurations offer several advantages, including high chemical and thermal stability, improved solubility, and enhanced catalytic activity. Among the most relevant features for photocatalytic applications, interfacial charge transfer and long-term stability stand out to be the critical ones.[84] Indeed, efficient separation of photogenerated charge carriers (e^- and h^+) across the interface can strongly enhance the photocatalytic performance of the system, improving both product yield and selectivity when appropriate band alignments are established.[85]

However, the core-shell and heterodimer architectures differ significantly in terms of accessibility to reactive sites. In the core-shell structure, the shell can protect the core from photocorrosion and chemical degradation, increasing stability, but a thick or insulating shell can limit charge transfer.[86] On the contrary, in the heterodimers, the surfaces of both domains remain essentially exposed to the reaction environment, allowing the adsorption of the reactants potentially in both components and making the active sites more available. This arrangement often facilitates charge separation. On the other hand, this increased reactivity can affect the stability as both domains directly participate in the photoreaction, being fully exposed to light. As a result, heterodimers may undergo faster surface degradation and photocorrosion in comparison with core-shell structures.

Therefore, the choice between these two architectures needs to consider several aspects, balancing reactivity, charge-transfer efficiency, and structural robustness, depending on the requirements of the targeted photocatalytic process.[87]

3.6 Conclusions

In this chapter, we introduced epitaxial heterostructure, which are the core of this thesis, as engineered materials designed to overcome limitations related to charge dynamics in photocatalytic mechanism. In this context, Type II and Z-scheme heterojunctions at semiconductor-semiconductor interfaces, as well as Schottky junctions formed at metal-semiconductor interfaces have emerged as effective candidates. These configurations possess favorable band alignments that promote efficient charge separation while suppressing charge recombination. As a result, the lifetime of the photogenerated electrons and holes can be enhanced, enabling their participation in photochemical transformations. This underscores the central role of electronic structure at the junction in heterostructures functionality. At the same time, these heteroarchitectures pose significant challenges from a design perspective. In particular, the way different domains are connected is equally crucial to the overall performances. As mentioned, poorly matched interfaces can introduce defect states that act as charge traps, capturing carriers that would otherwise drive photocatalytic reactions. To minimize these detrimental effects, it is essential to employ tools that enable efficient and reliable screening of heterostructures design. On this basis, we introduced the Ogre software as a powerful computational framework to predict the feasibility of novel epitaxial heterostructures. The software is able to evaluate not only crystallographic matching but also chemical terminations and the electrostatic interactions at the interface, which play a key role in guiding the formation of stable and functional hetero-compounds. Building on the fundamental principles governing photocatalysis and heterostructure design discussed in these chapters, the following chapters will be purely experimental and will focus on the results obtained during my three years of PhD research.

3.7 Copyright

Some elements of this chapter were adapted from external sources:

- **Figure 3.3.** Reprinted with permission from ACS Nano **2025**, 19 (5), 5326–5341. Licensed under CC-BY 4.0. Copyright © 2025 The Authors. https://doi.org/10.1021/acsnano.4c12713.

3.8 Bibliography

(1) Carbone, L.; Cozzoli, P. D. Colloidal Heterostructured Nanocrystals: Synthesis and Growth Mechanisms. *Nano Today* **2010**, *5* (5), 449–493. https://doi.org/10.1016/j.nantod.2010.08.006.

(2) Bera, S.; Pradhan, N. Perovskite Nanocrystal Heterostructures: Synthesis, Optical Properties, and Applications. *ACS Energy Lett.* **2020**, *5* (9), 2858–2872. https://doi.org/10.1021/acsenergylett.0c01449.

(3) Ha, M.; Kim, J.-H.; You, M.; Li, Q.; Fan, C.; Nam, J.-M. Multicomponent Plasmonic Nanoparticles: From Heterostructured Nanoparticles to Colloidal Composite Nanostructures. *Chem. Rev.* **2019**, *119* (24), 12208–12278. https://doi.org/10.1021/acs.chemrev.9b00234.

(4) Li, Y.; Zhang, J.; Chen, Q.; Xia, X.; Chen, M. Emerging of Heterostructure Materials in Energy Storage: A Review. *Adv. Mater.* **2021**, *33* (27), 2100855. https://doi.org/10.1002/adma.202100855.

(5) Livakas, N.; Zito, J.; Ivanov, Y. P.; Otero-Martínez, C.; Divitini, G.; Infante, I.; Manna, L. Nanocrystal Heterostructures Based on Halide Perovskites and Metal Sulfides. *J. Am. Chem. Soc.* **2024**, *146* (40), 27571–27582. https://doi.org/10.1021/jacs.4c08565.

(6) Dutta, S. K.; Mehetor, S. K.; Pradhan, N. Metal Semiconductor Heterostructures for Photocatalytic Conversion of Light Energy. *J. Phys. Chem. Lett.* **2015**, *6* (6), 936–944. https://doi.org/10.1021/acs.jpclett.5b00113.

(7) Jeong, H.; Bang, S.; Oh, H. M.; Jeong, H. J.; An, S.-J.; Han, G. H.; Kim, H.; Kim, K. K.; Park, J. C.; Lee, Y. H.; Lerondel, G.; Jeong, M. S. Semiconductor–Insulator–Semiconductor Diode Consisting of Monolayer MoS_2, h-BN, and GaN Heterostructure. *ACS Nano* **2015**, *9* (10), 10032–10038. https://doi.org/10.1021/acsnano.5b04233.

(8) Dabbousi, B. O.; Rodriguez-Viejo, J.; Mikulec, F. V.; Heine, J. R.; Mattoussi, H.; Ober, R.; Jensen, K. F.; Bawendi, M. G. (CdSe)ZnS Core−Shell Quantum Dots: Synthesis and Characterization of a Size Series of Highly Luminescent Nanocrystallites. *J. Phys. Chem. B* **1997**, *101* (46), 9463–9475. https://doi.org/10.1021/jp971091y.

(9) Mathew, S.; Bhardwaj, B. S.; Saran, A. D.; Radhakrishnan, P.; Nampoori, V. P. N.; Vallabhan, C. P. G.; Bellare, J. R. Effect of ZnS Shell on Optical Properties of CdSe–ZnS Core–Shell Quantum Dots. *Opt. Mater.* **2015**, *39*, 46–51. https://doi.org/10.1016/j.optmat.2014.10.061.

(10) Siemon, U.; Bahnemann, D.; Testa, J. J.; Rodríguez, D.; Litter, M. I.; Bruno, N. Heterogeneous Photocatalytic Reactions Comparing TiO_2 and Pt/TiO_2. *J. Photochem. Photobiol. A: Chem.* **2002**, *148* (1), 247–255. https://doi.org/10.1016/S1010-6030(02)00050-3.

(11) Sola, A. C.; Piscina, P. R. de la; Homs, N. Behaviour of Pt/TiO_2 Catalysts with Different Morphological and Structural Characteristics in the Photocatalytic Conversion of Ethanol Aqueous Solutions. *Catalysis Today* **2020**, *341*, 13–20. https://doi.org/10.1016/j.cattod.2018.06.017.

(12) Shen, H.; Wang, S.; Wang, H.; Niu, J.; Qian, L.; Yang, Y.; Titov, A.; Hyvonen, J.; Zheng, Y.; Li, L. S. Highly Efficient Blue–Green Quantum Dot Light-Emitting Diodes Using Stable Low-Cadmium Quaternary-Alloy ZnCdSSe/ZnS Core/Shell Nanocrystals. *ACS Appl. Mater. Interfaces* **2013**, *5* (10), 4260–4265. https://doi.org/10.1021/am400433y.

(13) Wang, X.; Li, W.; Sun, K. Stable Efficient CdSe/CdS/ZnS Core/Multi-Shell Nanophosphors Fabricated through a Phosphine-Free Route for White Light-Emitting-Diodes with High Color Rendering Properties. *J. Mater. Chem.* **2011**, *21* (24), 8558–8565. https://doi.org/10.1039/C1JM00061F.

(14) Qin, L.; Wang, G.; Tan, Y. Plasmonic Pt Nanoparticles—TiO_2 Hierarchical Nano-Architecture as a Visible Light Photocatalyst for Water Splitting. *Scientific Reports* **2018**, *8* (1), 16198. https://doi.org/10.1038/s41598-018-33795-z.

(15) Li, D.; Li, Y.; Liao, D.; Cao, M.; Zhang, L.; Zhang, S.; Chen, L.; Chen, Y.; Wang, H.; Qi, J.; You, F. Enhanced Light Harvesting Ability in Hollow Pt/TiO_2 Nanoreactor for Boosting Tetracycline Photodegradation. *Prog. Nat. Sci.: Mater. Int.* **2024**, *34* (4), 767–775. https://doi.org/10.1016/j.pnsc.2024.07.005.

(16) Balapure, A.; Ray Dutta, J.; Ganesan, R. Recent Advances in Semiconductor Heterojunctions: A Detailed Review of the Fundamentals of Photocatalysis, Charge Transfer Mechanism and Materials. *RSC Appl. Interfaces* **2024**, *1* (1), 43–69. https://doi.org/10.1039/D3LF00126A.

(17) Ma, L.; Chen, S.; Shao, Y.; Chen, Y.-L.; Liu, M.-X.; Li, H.-X.; Mao, Y.-L.; Ding, S.-J. Recent Progress in Constructing Plasmonic Metal/Semiconductor Hetero-Nanostructures for Improved Photocatalysis. *Catalysts* **2018**, *8* (12). https://doi.org/10.3390/catal8120634.

(18) Nie, J.; Schneider, J.; Sieland, F.; Zhou, L.; Xia, S.; Bahnemann, D. W. New Insights into the Surface Plasmon Resonance (SPR) Driven Photocatalytic H_2 Production of Au–TiO_2. *RSC Adv.* **2018**, *8* (46), 25881–25887. https://doi.org/10.1039/C8RA05450A.

(19) Leong, K. H.; Gan, B. L.; Ibrahim, S.; Saravanan, P. Synthesis of Surface Plasmon Resonance (SPR) Triggered Ag/TiO_2 Photocatalyst for Degradation of Endocrine Disturbing Compounds. *Appl. Surf. Sci.* **2014**, *319*, 128–135. https://doi.org/10.1016/j.apsusc.2014.06.153.

(20) Cheng, Y.; Lin, Y.; Xu, J.; He, J.; Wang, T.; Yu, G.; Shao, D.; Wang, W.-H.; Lu, F.; Li, L.; Du, X.; Wang, W.; Liu, H.; Zheng, R. Surface Plasmon Resonance Enhanced Visible-Light-Driven Photocatalytic Activity in Cu Nanoparticles Covered Cu_2O Microspheres for Degrading Organic Pollutants. *Appl. Surf. Sci.* **2016**, *366*, 120–128. https://doi.org/10.1016/j.apsusc.2015.12.238.

(21) Kumar, A.; Singh, P.; Khan, A. A. P.; Le, Q. V.; Nguyen, V.-H.; Thakur, S.; Raizada, P. CO_2 Photoreduction into Solar Fuels via Vacancy Engineered Bismuth-Based Photocatalysts: Selectivity and Mechanistic Insights. *Chem. Eng. J.* **2022**, *439*, 135563. https://doi.org/10.1016/j.cej.2022.135563.

(22) Liu, H.; Tan, Y.; Cao, M.; Hu, H.; Wu, L.; Yu, X.; Wang, L.; Sun, B.; Zhang, Q. Fabricating $CsPbX_3$ -Based Type I and Type II Heterostructures by Tuning the Halide Composition of Janus $CsPbX_3$ /ZrO_2 Nanocrystals. *ACS Nano* **2019**, *13* (5), 5366–5374. https://doi.org/10.1021/acsnano.9b00001.

(23) Li, Y.; Zeng, Y.; Ou, Z.; Dai, W.; Wang, C.; Li, Z.; Li, W.; Yan, J.; Yu, S.; Yu, Y.; Wang, T.; Xu, H. Tunability of the Energy Transfer Process in Type-II Heterostructures. *ACS Photonics* **2024**, *11* (9), 3722–3729. https://doi.org/10.1021/acsphotonics.4c00903.

(24) Lei, C.; Ma, Y.; Xu, X.; Zhang, T.; Huang, B.; Dai, Y. Broken-Gap Type-III Band Alignment in WTe_2 /HfS_2 van Der Waals Heterostructure. *J. Phys. Chem. C* **2019**, *123* (37), 23089–23095. https://doi.org/10.1021/acs.jpcc.9b07862.

(25) Malefane, M. E.; Mafa, P. J.; Managa, M.; Nkambule, T. T. I.; Kuvarega, A. T. Understanding the Principles and Applications of Dual Z-Scheme Heterojunctions: How Far Can We Go? *J. Phys. Chem. Lett.* **2023**, *14* (4), 1029–1045. https://doi.org/10.1021/acs.jpclett.2c03387.

(26) Yang, H. A Short Review on Heterojunction Photocatalysts: Carrier Transfer Behavior and Photocatalytic Mechanisms. *Mater. Res. Bull.* **2021**, *142*, 111406. https://doi.org/10.1016/j.materresbull.2021.111406.

(27) Sharma, B. L.; Purohit, R. K. *Semiconductor Heterojunctions*, 1st ed.; International series of monographs in the science of the solid state; Pergamon Press: Oxford New York, 1974.

(28) Bilal, M.; Alfaifi, M. Q.; Ben Ahmed, S.; Abduljawad, M. M.; Alrashed, Y. I.; Aldurahim, E. S.; Alassmy, Y. A. A Review of Strategies to Switch

Heterojunction System from Type-II to S-Scheme for Photocatalytic Applications. *Mater. Sci. Semicond. Process.* **2025**, *186*, 109051. https://doi.org/10.1016/j.mssp.2024.109051.

(29) Song, W.; Chong, K. C.; Qi, G.; Xiao, Y.; Chen, G.; Li, B.; Tang, Y.; Zhang, X.; Yao, Y.; Lin, Z.; Zou, Z.; Liu, B. Unraveling the Transformation from Type-II to Z-Scheme in Perovskite-Based Heterostructures for Enhanced Photocatalytic CO_2 Reduction. *J. Am. Chem. Soc.* **2024**, *146* (5), 3303–3314. https://doi.org/10.1021/jacs.3c12073.

(30) Shabbir, A.; Sardar, S.; Mumtaz, A. Mechanistic Investigations of Emerging Type-II, Z-Scheme and S-Scheme Heterojunctions for Photocatalytic Applications – A Review. *J. Alloys Compd.* **2024**, *1003*, 175683. https://doi.org/10.1016/j.jallcom.2024.175683.

(31) Low, J.; Jiang, C.; Cheng, B.; Wageh, S.; Al-Ghamdi, A. A.; Yu, J. A Review of Direct Z-Scheme Photocatalysts. *Small Methods* **2017**, *1* (5), 1700080. https://doi.org/10.1002/smtd.201700080.

(32) Kumari, P.; Bahadur, N.; Kong, L.; O'Dell, L. A.; Merenda, A.; Dumée, L. F. Engineering Schottky-like and Heterojunction Materials for Enhanced Photocatalysis Performance – a Review. *Mater. Adv.* **2022**, *3* (5), 2309–2323. https://doi.org/10.1039/D1MA01062J.

(33) Lei, C.; Ma, Y.; Xu, X.; Zhang, T.; Huang, B.; Dai, Y. Broken-Gap Type-III Band Alignment in WTe_2/HfS_2 van Der Waals Heterostructure. *J. Phys. Chem. C* **2019**, *123* (37), 23089–23095. https://doi.org/10.1021/acs.jpcc.9b07862.

(34) Kistner-Morris, J.; Shi, A.; Liu, E.; Arp, T.; Farahmand, F.; Taniguchi, T.; Watanabe, K.; Aji, V.; Lui, C. H.; Gabor, N. Electric-Field Tunable Type-I to Type-II Band Alignment Transition in MoSe2/WS2 Heterobilayers. *Nat. Commun.* **2024**, *15* (1), 4075. https://doi.org/10.1038/s41467-024-48321-1.

(35) Meng, X.; Wang, S.; Zhang, C.; Dong, C.; Li, R.; Li, B.; Wang, Q.; Ding, Y. Boosting Hydrogen Evolution Performance of a CdS-Based Photocatalyst: In Situ Transition from Type I to Type II Heterojunction during Photocatalysis. *ACS Catal.* **2022**, *12* (16), 10115–10126. https://doi.org/10.1021/acscatal.2c01877.

(36) Ren, X.; Wu, K.; Qin, Z.; Zhao, X.; Yang, H. The Construction of Type II Heterojunction of Bi_2WO_6/BiOBr Photocatalyst with Improved Photocatalytic Performance. *J. Alloys Compd.* **2019**, *788*, 102–109. https://doi.org/10.1016/j.jallcom.2019.02.211.

(37) Li, H.; Tu, W.; Zhou, Y.; Zou, Z. Z-Scheme Photocatalytic Systems for Promoting Photocatalytic Performance: Recent Progress and Future Challenges. *Adv. Sci.* **2016**, *3* (11), 1500389. https://doi.org/10.1002/advs.201500389.

(38) Bard, A. J. Photoelectrochemistry and Heterogeneous Photo-Catalysis at Semiconductors. *J. Photochem.* **1979**, *10* (1), 59–75. https://doi.org/10.1016/0047-2670(79)80037-4.

(39) Tada, H.; Mitsui, T.; Kiyonaga, T.; Akita, T.; Tanaka, K. All-Solid-State Z-Scheme in CdS–Au–TiO2 Three-Component Nanojunction System. *Nat. Mater.* **2006**, *5* (10), 782–786. https://doi.org/10.1038/nmat1734.

(40) Wang, X.; Liu, G.; Chen, Z.-G.; Li, F.; Wang, L.; Lu, G. Q.; Cheng, H.-M. Enhanced Photocatalytic Hydrogen Evolution by Prolonging the Lifetime of Carriers in ZnO/CdS Heterostructures. *Chem. Commun.* **2009**, No. 23, 3452–3454. https://doi.org/10.1039/B904668B.

(41) Yu, J.; Wang, S.; Low, J.; Xiao, W. Enhanced Photocatalytic Performance of Direct Z-Scheme g-C_3N_4–TiO_2 Photocatalysts for the Decomposition of Formaldehyde in Air. *Phys. Chem. Chem. Phys.* **2013**, *15* (39), 16883–16890. https://doi.org/10.1039/C3CP53131G.

(42) Fu, Y.; Li, J.; Li, J. Metal/Semiconductor Nanocomposites for Photocatalysis: Fundamentals, Structures, Applications and Properties. *Nanomaterials* **2019**, *9* (3), 359. https://doi.org/10.3390/nano9030359.

(43) Yuan, L.; Geng, Z.; Xu, J.; Guo, F.; Han, C. Metal-Semiconductor Heterostructures for Photoredox Catalysis: Where Are We Now and Where Do We Go? *Adv. Funct. Mater.* **2021**, *31* (27), 2101103. https://doi.org/10.1002/adfm.202101103.

(44) Zhang, Z.; Yates, J. T. Band Bending in Semiconductors: Chemical and Physical Consequences at Surfaces and Interfaces. *Chem. Rev.* **2012**, *112* (10), 5520–5551. https://doi.org/10.1021/cr3000626.

(45) Amirjani, A.; Amlashi, N. B.; Ahmadiani, Z. S. Plasmon-Enhanced Photocatalysis Based on Plasmonic Nanoparticles for Energy and Environmental Solutions: A Review. *ACS Appl. Nano Mater.* **2023**, *6* (11), 9085–9123. https://doi.org/10.1021/acsanm.3c01671.

(46) Dutta, S. K.; Bera, S.; Pradhan, N. Why Is Making Epitaxially Grown All Inorganic Perovskite–Chalcogenide Nanocrystal Heterostructures Challenging? Some Facts and Some Strategies. *Chem. Mater.* **2021**, *33* (11), 3868–3877. https://doi.org/10.1021/acs.chemmater.1c01000.

(47) Drake, G. A.; Keating, L. P.; Shim, M. Design Principles of Colloidal Nanorod Heterostructures. *Chem. Rev.* **2023**, *123* (7), 3761–3789. https://doi.org/10.1021/acs.chemrev.2c00410.

(48) Fiorito, S.; Soni, N.; Silvestri, N.; Brescia, R.; Gavilán, H.; Conteh, J. S.; Mai, B. T.; Pellegrino, T. Fe_3O_4@Au@$Cu_{2-x}S$ Heterostructures Designed for Tri-Modal Therapy: Photo- Magnetic Hyperthermia and ^{64}Cu Radio-Insertion. *Small* **2022**, *18* (18). https://doi.org/10.1002/smll.202200174.

(49) Ha, M.; Kim, J.-H.; You, M.; Li, Q.; Fan, C.; Nam, J.-M. Multicomponent Plasmonic Nanoparticles: From Heterostructured Nanoparticles to Colloidal Composite Nanostructures. *Chem. Rev.* **2019**, *119* (24), 12208–12278. https://doi.org/10.1021/acs.chemrev.9b00234.

(50) Nasir, J. A.; Rehman, Z. U.; Shah, S. N. A.; Khan, A.; Butler, I. S.; Catlow, C. R. A. Recent Developments and Perspectives in CdS-Based Photocatalysts for Water Splitting. *J. Mater. Chem. A* **2020**, *8* (40), 20752–20780. https://doi.org/10.1039/d0ta05834c.

(51) Yuan, C.; He, M.; Liao, X.; Liu, M.; Zhang, Q.; Wan, Q.; Qu, Z.; Kong, L.; Li, L. Interface Defects Repair of Core/Shell Quantum Dots through Halide Ion Penetration. *Chem. Sci.* **2023**, *14* (45), 13119–13125. https://doi.org/10.1039/d3sc04136k.

(52) Stein, J. L.; Holden, W. M.; Venkatesh, A.; Mundy, M. E.; Rossini, A. J.; Seidler, G. T.; Cossairt, B. M. Probing Surface Defects of InP Quantum Dots Using Phosphorus Kα and Kβ X-Ray Emission Spectroscopy. *Chem. Mater.* **2018**, *30* (18), 6377–6388. https://doi.org/10.1021/acs.chemmater.8b02590.

(53) Tessier, M. D.; Baquero, E. A.; Dupont, D.; Grigel, V.; Bladt, E.; Bals, S.; Coppel, Y.; Hens, Z.; Nayral, C.; Delpech, F. Interfacial Oxidation and Photoluminescence of InP-Based Core/Shell Quantum Dots. *Chem. Mater.* **2018**, *30* (19), 6877–6883. https://doi.org/10.1021/acs.chemmater.8b03117.

(54) Dutta, S. K.; Bera, S.; Pradhan, N. Why Is Making Epitaxially Grown All Inorganic Perovskite–Chalcogenide Nanocrystal Heterostructures Challenging? Some Facts and Some Strategies. *Chem. Mater.* **2021**, *33* (11), 3868–3877. https://doi.org/10.1021/acs.chemmater.1c01000.

(55) Mathew, K.; Singh, A. K.; Gabriel, J. J.; Choudhary, K.; Sinnott, S. B.; Davydov, A. V.; Tavazza, F.; Hennig, R. G. MPInterfaces: A Materials Project Based Python Tool for High-Throughput Computational Screening of Interfacial Systems. *Comput. Mater. Sci.* **2016**, *122*, 183–190. https://doi.org/10.1016/j.commatsci.2016.05.020.

(56) Taylor, N. T.; Davies, F. H.; Rudkin, I. E. M.; Price, C. J.; Chan, T. H.; Hepplestone, S. P. ARTEMIS: Ab Initio Restructuring Tool Enabling the Modelling of Interface Structures. *Comput. Phys. Commun.* **2020**, *257*, 107515. https://doi.org/10.1016/j.cpc.2020.107515.

(57) Grundmann, M. Formation of Epitaxial Domains: Unified Theory and Survey of Experimental Results. *Phys. Status Solidi (b)* **2011**, *248* (4), 805–824. https://doi.org/10.1002/pssb.201046530.

(58) Raclariu, A.-M.; Deshpande, S.; Bruggemann, J.; Zhuge, W.; Yu, T. H.; Ratsch, C.; Shankar, S. A Fast Method for Predicting the Formation of Crystal Interfaces and Heterocrystals. *Comput. Mater. Sci.* **2015**, *108*, 88–93. https://doi.org/10.1016/j.commatsci.2015.05.023.

(59) Choudhary, K.; Garrity, K. F. InterMat: Accelerating Band Offset Prediction in Semiconductor Interfaces with DFT and Deep Learning. *Digit. Discov.* **2024**, *3* (7), 1365–1377. https://doi.org/10.1039/d4dd00031e.

(60) Choudhary, K.; Garrity, K. F.; Hartman, S. T.; Pilania, G.; Tavazza, F. Efficient Computational Design of Two-Dimensional van Der Waals Heterostructures: Band Alignment, Lattice Mismatch, and Machine Learning. *Phys. Rev. Mater.* **2023**, *7* (1). https://doi.org/10.1103/physrevmaterials.7.014009.

(61) Gao, B.; Gao, P.; Lu, S.; Lv, J.; Wang, Y.; Ma, Y. Interface Structure Prediction via CALYPSO Method. *Science Bulletin* **2019**, *64* (5), 301–309. https://doi.org/10.1016/j.scib.2019.02.009.

(62) Toso, S.; Dardzinski, D.; Manna, L.; Marom, N. Structure Prediction of Ionic Epitaxial Interfaces with Ogre Demonstrated for Colloidal Heterostructures of Lead Halide Perovskites. *ACS Nano* **2025**, *19* (5), 5326–5341. https://doi.org/10.1021/acsnano.4c12713.

(63) Moayedpour, S.; Dardzinski, D.; Yang, S.; Hwang, A.; Marom, N. Structure Prediction of Epitaxial Inorganic Interfaces by Lattice and Surface Matching with Ogre. *J. Chem. Phys.* **2021**, *155* (3), 034111. https://doi.org/10.1063/5.0051343.

(64) Imran, M.; Peng, L.; Pianetti, A.; Pinchetti, V.; Ramade, J.; Zito, J.; Di Stasio, F.; Buha, J.; Toso, S.; Song, J.; Infante, I.; Bals, S.; Brovelli, S.; Manna, L. Halide Perovskite–Lead Chalcohalide Nanocrystal Heterostructures. *J. Am. Chem. Soc.* **2021**, *143* (3), 1435–1446. https://doi.org/10.1021/jacs.0c10916.

(65) Fennell, C. J.; Gezelter, J. D. Is the Ewald Summation Still Necessary? Pairwise Alternatives to the Accepted Standard for Long-Range

Electrostatics. *J. Chem. Phys.* **2006**, *124* (23), 234104. https://doi.org/10.1063/1.2206581.

(66) Zur, A.; McGill, T. C. Lattice Match: An Application to Heteroepitaxy. *J. Appl. Phys.* **1984**, *55* (2), 378–386. https://doi.org/10.1063/1.333084.

(67) Li, Y.; Wan, J.; Smilgies, D.-M.; Bouffard, N.; Sun, R.; Headrick, R. L. Nucleation and Strain-Stabilization during Organic Semiconductor Thin Film Deposition. *Sci. Rep.* **2016**, *6* (1). https://doi.org/10.1038/srep32620.

(68) Kim, D.; Shcherbakov-Wu, W.; Ha, S. K.; Lee, W. S.; Tisdale, W. A. Uniaxial Strain Engineering *via* Core Position Control in CdSe/CdS Core/Shell Nanorods and Their Optical Response. *ACS Nano* **2022**, *16* (9), 14713–14722. https://doi.org/10.1021/acsnano.2c05427.

(69) Cao; Banin, U. Growth and Properties of Semiconductor Core/Shell Nanocrystals with InAs Cores. *J. Am. Chem. Soc.* **2000**, *122* (40), 9692–9702. https://doi.org/10.1021/ja001386g.

(70) Pradhan, N. Why Do Perovskite Nanocrystals Form Nanocubes and How Can Their Facets Be Tuned? A Perspective from Synthetic Prospects. *ACS Energy Lett.* **2021**, *6* (1), 92–99. https://doi.org/10.1021/acsenergylett.0c02099.

(71) Xia, Y.; Xiong, Y.; Lim, B.; Skrabalak, S. E. Shape-Controlled Synthesis of Metal Nanocrystals: Simple Chemistry Meets Complex Physics? *Angew. Chem. Int. Ed* **2009**, *48* (1), 60–103. https://doi.org/10.1002/anie.200802248.

(72) Huang, M. H.; Lin, P. Shape-Controlled Synthesis of Polyhedral Nanocrystals and Their Facet-Dependent Properties. *Adv Funct Materials* **2012**, *22* (1), 14–24. https://doi.org/10.1002/adfm.201101784.

(73) Sun, W.; Ceder, G. Efficient Creation and Convergence of Surface Slabs. *Surf. Sci.* **2013**, *617*, 53–59. https://doi.org/10.1016/j.susc.2013.05.016.

(74) Wang, D.; Tan, D.; Liu, L. Particle Swarm Optimization Algorithm: An Overview. *Soft. Comput.* **2018**, *22* (2), 387–408. https://doi.org/10.1007/s00500-016-2474-6.

(75) Momma, K.; Izumi, F. It VESTA: A Three-Dimensional Visualization System for Electronic and Structural Analysis. *J. Appl. Crystallogr.* **2008**, *41* (3), 653–658. https://doi.org/10.1107/S0021889808012016.

(76) Dardzinski, D.; Yu, M.; Moayedpour, S.; Marom, N. Best Practices for First-Principles Simulations of Epitaxial Inorganic Interfaces. *J. Phys.: Condens. Matter.* **2022**, *34* (23), 233002. https://doi.org/10.1088/1361-648x/ac577b.

(77) Zimmermann, N. E. R.; Jain, A. Local Structure Order Parameters and Site Fingerprints for Quantification of Coordination Environment and Crystal Structure Similarity. *RSC Adv.* **2020**, *10* (10), 6063–6081. https://doi.org/10.1039/c9ra07755c.

(78) Shafiee, A.; Rabiee, N.; Ahmadi, S.; Baneshi, M.; Khatami, M.; Iravani, S.; Varma, R. S. Core–Shell Nanophotocatalysts: Review of Materials and Applications. *ACS Appl. Nano Mater.* **2022**, *5* (1), 55–86. https://doi.org/10.1021/acsanm.1c03714.

(79) Drake, G. A.; Keating, L. P.; Shim, M. Design Principles of Colloidal Nanorod Heterostructures. *Chem. Rev.* **2023**, *123* (7), 3761–3789. https://doi.org/10.1021/acs.chemrev.2c00410.

(80) Mondal, K.; Sharma, A. Recent Advances in the Synthesis and Application of Photocatalytic Metal–Metal Oxide Core–Shell Nanoparticles for Environmental Remediation and Their Recycling Process. *RSC Adv.* **2016**, *6* (87), 83589–83612. https://doi.org/10.1039/C6RA18102C.

(81) Liu, Z.; Llusar, J.; Karakkal, H. H.; Zhu, D.; Ivanov, Y. P.; Prato, M.; Divitini, G.; Brovelli, S.; Infante, I.; De Trizio, L.; Manna, L. Amino-Arsine and Amino-Phosphine Based Synthesis of InAs@InP@ZnSe Core@shell@shell Quantum Dots. *Adv. Energy Mater.* **2024**, *14* (47), 2402246. https://doi.org/10.1002/aenm.202402246.

(82) Rusch, P.; Toso, S.; Ivanov, Y. P.; Marras, S.; Divitini, G.; Manna, L. Nanocrystal Heterostructures Based On Halide Perovskites and Lead–Bismuth Chalcogenides. *Chem. Mater.* **2023**, *35* (24), 10684–10693. https://doi.org/10.1021/acs.chemmater.3c02503.

(83) Lauhon, L. J.; Gudiksen, M. S.; Wang, D.; Lieber, C. M. Epitaxial Core–Shell and Core–Multishell Nanowire Heterostructures. *Nature* **2002**, *420* (6911), 57–61. https://doi.org/10.1038/nature01141.

(84) Emeline, A. V.; Rudakova, A. V.; Mikhaylov, R. V.; Bulanin, K. M.; Bahnemann, D. W. Photoactive Heterostructures: How They Are Made and Explored. *Catalysts* **2021**, *11* (2). https://doi.org/10.3390/catal11020294.

(85) Teranishi, T.; Sakamoto, M. Charge Separation in Type-II Semiconductor Heterodimers. *J. Phys. Chem. Lett.* **2013**, *4* (17), 2867–2873. https://doi.org/10.1021/jz4013504.

(86) Wei, H.; Wang, L.; Li, Z.; Ni, S.; Zhao, Q. Synthesis and Photocatalytic Activity of One-Dimensional CdS@TiO_2 Core-Shell Heterostructures. *Nano-Micro Letters* **2011**, *3* (1), 6–11. https://doi.org/10.1007/BF03353645.

(87) Yang, T.; Lu, B.; Zuo, Y.; Huang, J. Configuration Engineering of Plasmonic-Metal/Semiconductor Nanohybrids for Solar Fuel Production. *Chem. Mater.* **2025**, *37* (5), 1685–1715. https://doi.org/10.1021/acs.chemmater.4c03170.

CHAPTER 4

AgBr@$CsPbBr_3$ Core@Shell Heterostructure

4.1 Testing the predictive power of Ogre

In the previous chapter, we highlighted the advantages of epitaxial heterostructures composed of two distinct domains for targeted applications, such as photocatalysis. At the same time, we underlined the synthetic challenges associated with coupling two different materials, as crystallographic incompatibility often limits the formation of coherent heterointerfaces. In this context, we introduced the Ogre software[1] as a powerful computational tool to accelerate the screening process and assess the feasibility of potentially new heterostructures. The algorithm has shown remarkable capabilities in confirming experimental results of previously reported and existing heteroarchitectures (e.g., $CsPbBr_3/Pb_4S_3Br_2$).[2] However, any robust theoretical framework should not only validate what has already been achieved, but also provide reliable guidance for predicting and designing new systems. In this regard, this chapter focuses on the prediction and synthesis of a novel heteroarchitecture, presented as a case study, synthesized for the first time by our group.

Given our objective of validating the predictive power of Ogre through the synthesis of a novel heterostructure, we selected a relatively straightforward case study from the wide range of possible material combinations. In this context, "straightforward" refers to the choice of two compounds that are already of interest to our group, whose colloidal chemistry is well-known and established, and which, crucially, satisfy all the structural requirements for the formation of a coherent epitaxial interface.

Based on these considerations, we selected the all-inorganic perovskite $CsPbBr_3$ as first material, owing to its well-established wet chemistry, the extensive expertise of our group[3,4,5] in synthesizing this compound and its remarkable

optoelectronic properties,[6,7,4] as discussed in Chapter 2. In this context, one of the key strengths of perovskites lies in the straightforward preparation of highly crystalline nanoparticles even at low temperatures,[4] enabled by the predominantly ionic nature of metal halides perovskites. However, this advantage comes at the cost of an intrinsic lability toward ambient humidity and light exposure, which also compromises their stability in polar solvents such as water and alcohols.[8,9] This feature represents a high limitation, which significantly prevent the broader application of perovskite materials.

Given these considerations, an effective strategy to mitigate the well-known instability of $CsPbBr_3$ NCs in polar solvent is to couple them with a more robust material, preferably in a core@shell heterostructure.[10] In this architecture, the perovskite ideally constitutes the core, that is surrounded and "protected" by the shell of the secondary domain. In this context, several key requirements must be met for the successful growth of an epitaxial shell, as discussed in Chapter 3.[11] First, the two materials should form favorable epitaxial interfaces along multiple directions of their lattice, to ensure that the seed material can be fully developed. Second, these interfaces should be formed while retaining the same relative orientations of the two atomic lattices, to ensure that the outer shell can grow as a single-crystalline domain.

To satisfy these requirements, it is advantageous to focus on compounds with a cubic crystallographic lattice and lattice parameters comparable to those of perovskites. Indeed, in a cubic system, the principal lattice planes, (100), (110), (111), are equivalent along all major crystallographic directions. This symmetry allows the shell to grow homogeneously on all faces of the core. Moreover, the cubic geometry minimizes anisotropic strain because stress is distributed uniformly across the cube's faces.[1] Finally, epitaxial growth on cubic surfaces tends to produce fewer dislocations than growth on less symmetric structures (e.g., triclinic and monoclinic), as the principal directions are equivalent and the lattice is regular. In contrast, more complex lattices not only complicate interfaces formation but would also increase Ogre's computational demand. Overall, materials with cubic lattice facilitate the overgrowth in a core@shell architecture and promote the formation of a coherent epitaxial interface.

These considerations guide the choice of the second material. Indeed, among the potential candidates, we focused on silver halides[12] as they satisfy the requirements both from a purely crystallographic perspective and in terms of stability and chemical compatibility. More specifically, silver halides are

characterized by very low solubility products in water (Kps)[13] and therefore exhibit remarkable stability even in highly polar environments. Within this family, AgBr emerged as the most promising choice for our system for several reasons. AgBr crystallizes in a cubic lattice, which is likely compatible with perovskites and should facilitate the formation of a core@shell structure, as mentioned above. Additionally, silver halide wet chemistry is well established,[14,15,16] with decades of research and several colloidal synthesis strategies available,[17,18] making them highly compatible with perovskite synthetic protocols and facilitating synergy between the two systems. Finally, the presence of bromine in AgBr further enhances its suitability for forming a coherent interface with $CsPbBr_3$. First, the shared halide reduces lattice mismatch, favoring an interface with minimal strain. Second, from a synthetic perspective, the same bromine precursor can be used for both domains, simplifying the reaction design. Third, given the ionic nature of both materials, using the same halide prevents undesirable anion exchange reactions that could occur if the silver halide were chlorine- or iodine-based.

4.2 Simulation of $CsPbBr_3$@AgBr core@shell heterostructure

In this regard, the likelihood of a successful growth of $CsPbBr_3$@AgBr core@shell architecture was evaluated by simulating the possible AgBr/$CsPbBr_3$ epitaxial relations, following the workflow discussed in Chapter 3 and using the Ogre library.[1]

In the simulations, we initially considered using the Pm-3m cubic perovskite prototype[19] due to the negligible deviations with the actual orthorhombic Pnma $CsPbBr_3$ structure, as this choice allows for a more intuitive interpretation of results.

4.2.1 Lattice matching of $CsPbBr_3$/AgBr interfaces

Following the first step of the Ogre's workflow, the crystallographic information files (CIFs) of AgBr and $CsPbBr_3$ were uploaded, resulting in the matching table reported in Figure 4.1. More specifically, at this stage the software searches for common 2D-supercell surfaces that can describe both materials at the interface by matching the lattice planes identified by their Miller indices. Each circle in the table summarizes the geometric properties of the corresponding $(hkl)_{CsPbBr3}/(hkl)_{AgBr}$ interface. The circle area represents the interface supercell surface: a smaller circle corresponds to a smaller supercell area, indicating a higher probability for the interface to form. At the same time, the circle color indicates the

interface strain. According to this color-code, the blue and light blue dots identify interfaces with low strain values (< 4%) that are suitable to support the formation of an heterostructure when matching nanoparticles, as discussed in Chapter 3.

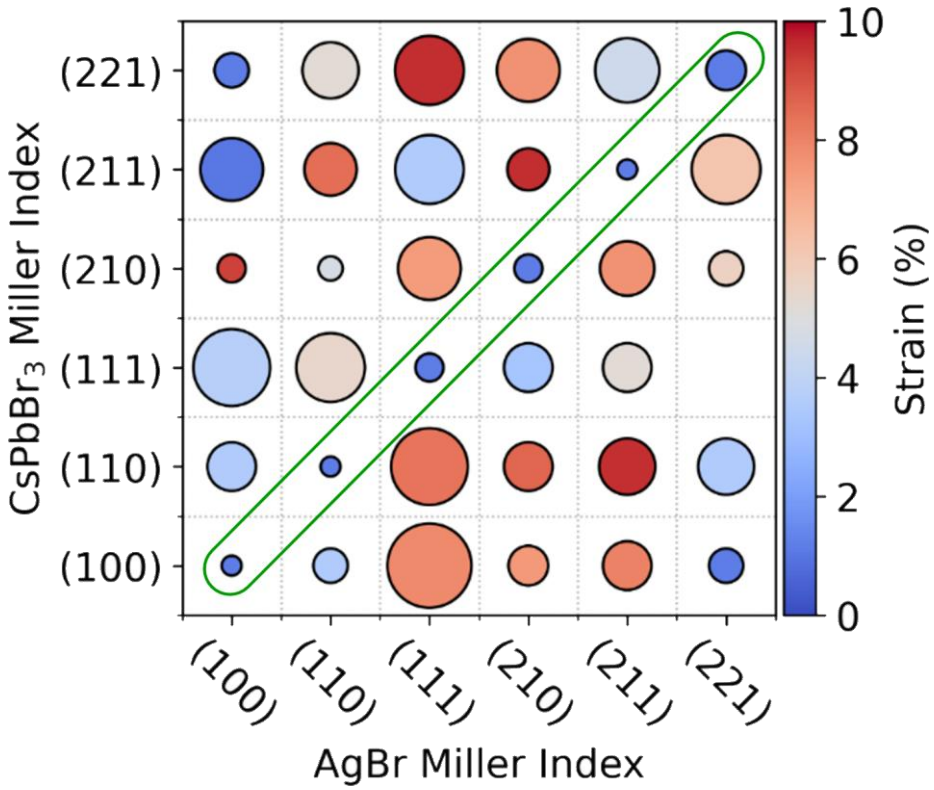

Figure 4.1. Lattice matching table for the AgBr/cubic-$CsPbBr_3$ pair. Each circle summarizes the geometric properties of the corresponding $(hkl)_{AgBr}/(hkl)_{CsPbBr3}$ interface. The circle area indicates the interface supercell surface (smaller = better), while the circle color indicates the interface strain (blue = better). Adapted with permission from ref 34. Licensed under CC-BY 4.0. Copyright © 2025 The Authors.

As mentioned above, the key requirements for epitaxial shell growth are: (1) the formation of stable interfaces along multiple lattice directions in order to fully enclose the seed, and (2) the preservation of the relative lattice orientation to enable single-crystalline shell growth. In this context, the lattice matching table clearly indicates that these conditions can be met for AgBr/$CsPbBr_3$. This is facilitated by the cubic structures of both materials, as discussed in the previous paragraph. In addition, the cubic symmetry of AgBr and $CsPbBr_3$ enables a more intuitive visualization of the favorable conditions for forming a core@shell structure. Specifically, all interfaces where $(hkl)_{AgBr} = (hkl)_{CsPbBr3}$ display suitable geometric matching, characterized by small interface supercells and low strain. This is

highlighted along the diagonal of the table, indicated with a green circle. But this can be seen also in other circle of the table, not just at the diagonal, attesting and confirming the excellent structural compatibility between the two domains. Indeed, simulations of the possible interface structures, performed by considering $(hkl)_{CsPbBr3} = (hkl)_{AgBr}$ up to h,k,l = 2, indicate that all main crystallographic directions can give rise to stable interfaces between AgBr and $CsPbBr_3$ (Table 4.1).

Table 4.1. Predicted geometric parameters and interface energies for AgBr/$CsPbBr_3$ interfaces of the $(hkl)_{AgBr} = (hkl)_{CsPbBr3}$ type. Reproduced with permission from ref 34. Licensed under CC-BY 4.0. Copyright © 2025 The Authors.

(hkl) AgBr	**(hkl) $CsPbBr_3$**	**Strain (%)**	**Area /Å^2**	**Interface energy mev/Å^2**
(100)	(100)	1.16	33.7	5.1
(110)	(110)	1.16	47.7	42.0
(110)	(110)	1.16	58.4	47.6
(210)	(210)	1.16	150.7	22.1
(211)	(211)	1.16	82.6	49.8
(221)	(221)	1.16	199.9	17.7

Matching planes with hkl > 1 is informative, as these matches further confirm the high structural compatibility between the two materials. Nevertheless, from a more realistic perspective, these planes are less likely to be present at the interface, since both AgBr and $CsPbBr_3$ typically expose other facets upon synthesis.

4.2.2 Surfaces matching and models of $CsPbBr_3$/AgBr interfaces

Following the other two steps of Ogre's workflow,[1] all the relevant information associated with the matching of the AgBr and $CsPbBr_3$ surface slabs can be obtained, including the surface energies and, finally, the atomistic models. In this

context, Figure 4.2 shows the 2D supercells, the potential energy surfaces and the atomistic models predicted by Ogre for AgBr and $CsPbBr_3$ along the principal directions.

Figure 4.2a-d-g depict the relative orientation of the AgBr and $CsPbBr_3$ lattice vectors at the interface within the surface supercell for $(100)_{AgBr}/(100)_{CsPbBr3}$, $(110)_{AgBr}/(110)_{CsPbBr3}$ and $(111)_{AgBr}/(111)_{CsPbBr3}$, respectively. The surface areas are very small in all cases, with the smallest belonging to the 100/100 interface (33.7 $Å^2$). These results indicate that it is possible to define and describe coherent interfaces between the two materials, along the principal directions, in which the lattice mismatch is minimized. In particular, individual lattices of AgBr and $CsPbBr_3$ are shown in green and orange, while the black square outlines the surface area where the two structures periodically repeat together.

Figure 4.2b-e-h show the potential energy surface (PES) as a function of the lateral displacement, namely the shifts along the x and y directions, between the two surface slabs for the three principal directions. The energy landscape is defined by a color-code: the blue regions correspond to energy minima, representing the most stable configurations, while the red regions indicate less stable arrangements. The most stable configuration corresponds to the specific lateral alignment in which the atoms of one material occupy the most energetically favorable positions relative to those of the other. In this configuration, favorable electrostatic and bonding interactions between the two materials are maximized, while atomic repulsion is minimized. In addition, the periodicity of the PES reflects the symmetry of the supercell identified in panel (a), (d) and (g), respectively.

Finally, Figure 4.2c-f-i illustrate the atomic model of the most stable AgBr/$CsPbBr_3$ interface, corresponding to the minimum-energy configuration identified in panel (b), (e) and (h), respectively. The red dashed box highlights the interface region. Here, the stability of the interface is governed by the degree of alignment between Br^- anions and metal cations (Ag^+, Pb^{2+}, Cs^+) across the junction. The minimum-energy lateral shift preferentially aligns Ag atoms above Br-rich sites of $CsPbBr_3$, thereby optimizing interfacial bonding. As a result, the bromide ions form a continuous lattice across the interface, that could be seen in all the principal directions under investigation. This “halide-sharing” framework enables the formation of a low-defect and epitaxial interface.

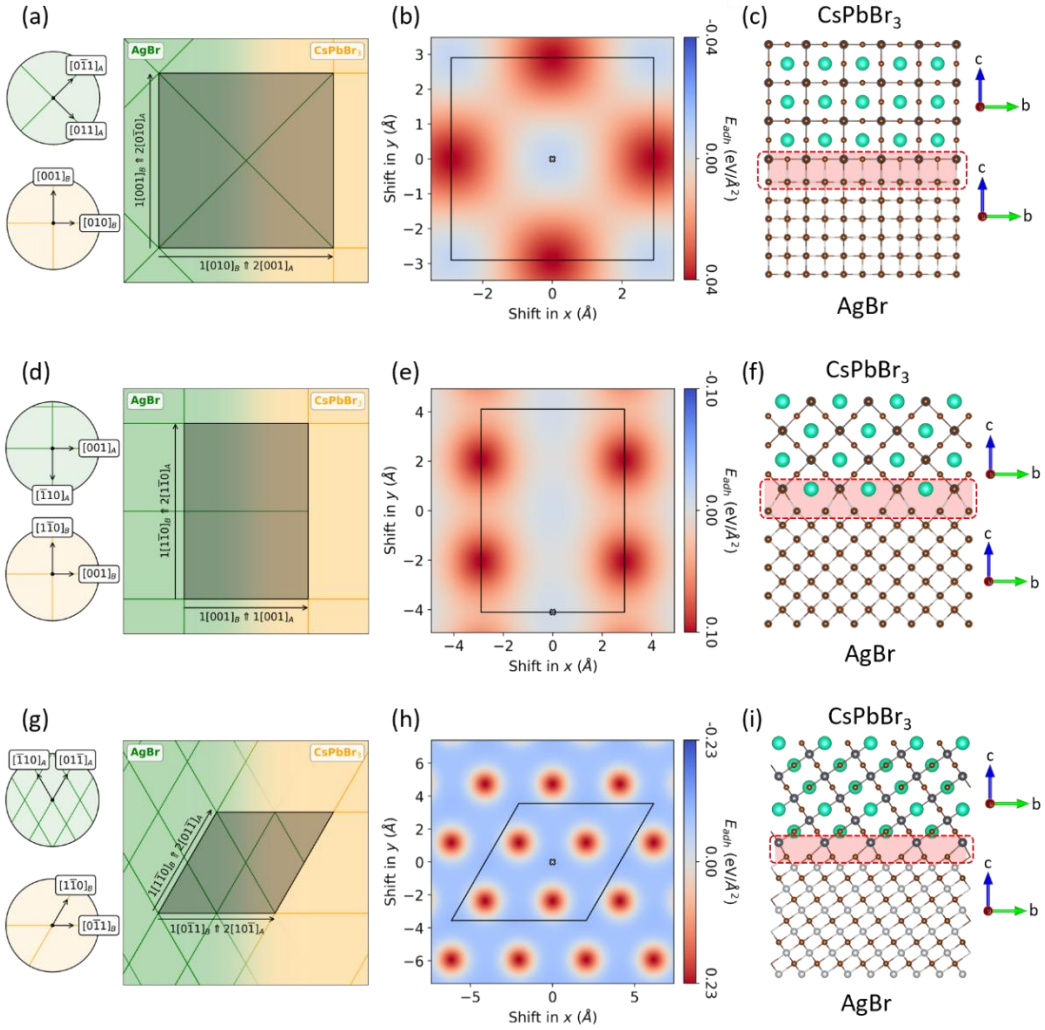

Figure 4.2. Most stable AgBr/CsPbBr$_3$ interfaces. (a,b,c) identify the $100_{AgBr}/100_{CsPbBr3}$ interface. (d,e,f) identify $110_{AgBr}/110_{CsPbBr3}$ interface. (g,h,i) identify the $111_{AgBr}/111_{CsPbBr3}$ interface. a,d,g) Supercell scheme, showing the relative orientation of the AgBr and CsPbBr$_3$ lattice vectors at the interface. b,e,h) Potential energy surface describing the relative in-plane shift of the two materials which leads to the most stable interface configuration. c,f,i) Atomic model of the interface as produced by Ogre. Adapted with permission from ref 34. Licensed under CC-BY 4.0. Copyright © 2025 The Authors.

Additionally, for the three models, it is noteworthy to note that the atoms near the interface undergo slight displacements from their ideal bulk positions to accommodate the residual lattice mismatch, leading to a coherent interface without dangling bonds. This characteristic is seen most clearly in the first model (Figure 4.2c, $(100)_{AgBr}/(100)_{CsPbBr3}$ interface), where the growth of one material on top of the other does not appear to displace atoms from the different crystal lattices at all.

The very small interfacial strain (1.16 %) is achieved through the choice of the appropriate supercell and lateral shift, in which the most favorable $CsPbBr_3$ surface termination, namely the $PbBr_2$ plane, promotes the formation of Pb-Br and Ag-Br bonds at the interface.

From a thermodynamic perspective, the formation of a core@shell architecture between two cubic materials can be described in terms of the Wulff construction applied to interfacial energies.[20,21] The Wulff's construction is a principle for minimizing surface free energy.[22,23] It states that the equilibrium shape of a crystal is the one that minimizes the total surface energy at constant volume. In the case of a core@shell structure, a domain is surrounded by another phase. In this context, the Wulff construction is particularly useful to explain the interface energy, the shape of the internal domain and the crystallographic coherence. More specifically, the equilibrium shape of the core domain is determined by the minimization of the total interfacial energy. In our system, the most stable configuration corresponds to the $100_{CsPbBr3}/100_{AgBr}$ interface, enabling the facets belonging to the {100} family to dominate the equilibrium morphology of the domain. As a result, the core material is expected to adopt a Wulff-like polyhedral shape rather than a spherical geometry, with faces aligned along the principal cubic directions shared by both lattices.

Finally, the fact that, among the three models discussed, the most stable configuration corresponds to the $100_{CsPbBr3}/100_{AgBr}$ interface is also highly favorable from a practical and synthetic perspective. Indeed, perovskites NCs preferentially expose the (100) facet rather than the (110) or the (111), unless specific synthetic conditions are employed. Consequently, if the heteroarchitecture forms, it is expected to follow the intrinsically stable surface termination of the perovskite.

Control simulations performed considering the orthorhombic Pnma structure for $CsPbBr_3$ instead of the simplified Pm-3m confirmed the same results (Table 4.2), with minimal stability differences between the (100)/(010) AgBr/Pnma-$CsPbBr_3$ interface (9.5 meV/Å^2) and the (100)/(101) AgBr/Pnma-$CsPbBr_3$ interface (9.3 meV/Å^2). In the interest of structural accuracy, an interface model displaying the orthorhombic structure for $CsPbBr_3$ is shown in Figure 4.3.

Table 4.2. Predicted geometric parameters and energies for the (100)/(100) – AgBr/Pm-3m $CsPbBr_3$ interface compared the two equivalent interfaces (100)/(101) – AgBr/Pnma $CsPbBr_3$ and (100)/(010) – AgBr/Pnma $CsPbBr_3$. Reproduced with permission from ref 34. Licensed under CC-BY 4.0. Copyright © 2025 The Authors

(hkl) AgBr	(hkl) $CsPbBr_3$	Strain (%)	Area /Å^2	Interface Energy meV/Å^2
(100)	(100) Pm-3m	1.16	33.7	5.1
(100)	(101) Pnma	1.42	135.0	9.35
(100)	(010) Pnma	0.88	67.2	9.41

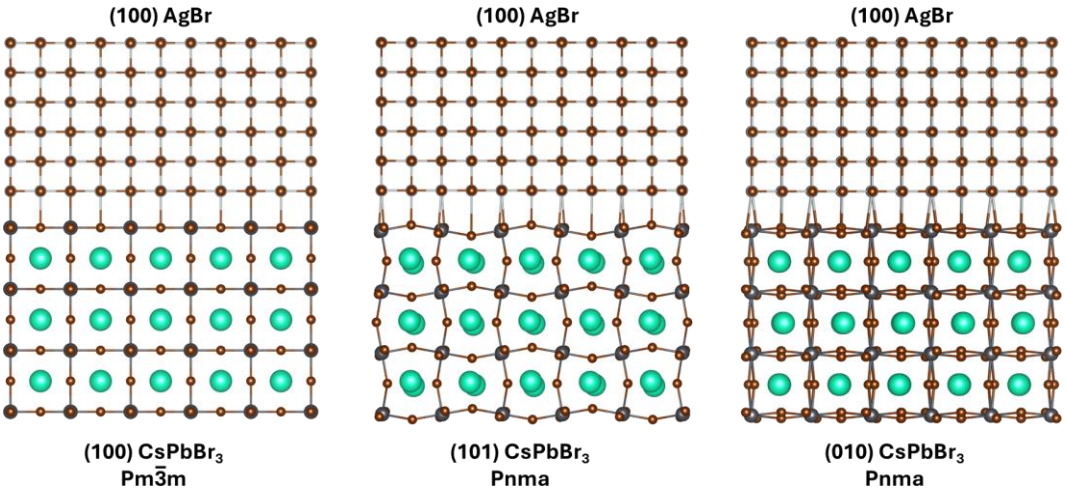

Figure 4.3. Interface models with $CsPbBr_3$ in the cubic vs orthorhombic setting. From left to right: (100)/(100) – AgBr/Pm-3m $CsPbBr_3$ interface; (100)/(101) – AgBr/Pnma $CsPbBr_3$ and (100)/(010) – AgBr/Pnma $CsPbBr_3$.

As shown in Figure 4.3, AgBr and $CsPbBr_3$ exhibit a very high structural affinity along multiple crystallographic directions. Indeed, further inspections at the different interfaces confirm what was found for the cubic analogue: (1) the presence of the shared bromide layer, (2) the atoms at the interface are arranged at bond distances favoring electrostatic interactions between the two domains, (3) the absence of dangling bonds and (4) an extremely low interfacial strain. As a result, atoms near the interface are only slightly displaced from their bulk positions.

In conclusion, the simulation results, both in the cubic and orthorhombic cases, indicate that the formation of a core@shell structure is highly favorable, as the principal lattice directions produce interfacial configurations while preserving the same relative crystallographic orientation between the two domains.

4.3 Synthesis in attempt to promote $CsPbBr_3$@AgBr core@shell heterostructure

After the simulations confirmed that the formation of a core@shell heterostructure between $CsPbBr_3$ and AgBr is likely, we proceeded to develop a synthetic strategy to obtain the desired architecture. Our initial approach was based on the use of preformed $CsPbBr_3$ nanocrystals, followed by the addition of different silver sources like silver oleate and silver-TOP (trioctylphosphine)[24] to grow a AgBr shell around the perovskite core.

Multiple synthetic strategies, such as hot injection[25] and ligand assisted reprecipitation,[26] are available for the preparation of perovskite NCs. Among these approaches, we adopted the hot injection method, as it allows for excellent separation between nucleation and growth, resulting in monodisperse nanocrystals with controlled shape and size. For this reason, the $CsPbBr_3$ nanocrystals were synthesized by the hot injection of benzoyl bromide into a mixture of cesium and lead oleates at 80 °C under a nitrogen atmosphere, following a synthetic protocol reported previously by some members of our group.[27] We decided to avoid amines and used instead oleic acid as the sole surfactant to prevent the reduction of Ag^+ to metallic silver, which could otherwise occur due to the amine's reducing properties.[28,29] Figure 4.4a shows the typical absorbance and photoluminescence spectra of the resulting NCs. These synthetic conditions tend to deliver relatively large nanocrystals (Figure 4.4b), with a size around 15-18 nm.

After purification of the nanocrystals, the silver source solution was introduced in an attempt to promote the formation of a silver bromide shell on the surface of the $CsPbBr_3$ domains. As shown in Figure 4.4c, after the treatment with the silver-oleate solution, spectroscopic analysis revealed a blue shift in both absorption and photoluminescence spectra. Transmission electron microscopy (TEM), as depicted in Figure 4.4d, revealed a morphological evolution of the nanocrystals toward a more spherical shape with a reduced size, likely induced by the relatively high concentration of oleic acid present in the Ag-oleate solution. Indeed, a plausible size-reduction mechanism, induced by the oleic acid (OA), can be described by considering the surface chemistry dynamics of $CsPbBr_3$ NCs in relation with the

excess ligands in the system. After the treatment with the Ag-oleate solution, the relatively high excess of OA is introduced in the reaction environment. This excess can protonate surface bromide ions or weakly coordinate surface metal cations, thereby promoting partial dissolution of the outer atomic layers. This ligand-assisted etching process preferentially removes high-energy surface sites, such as edges and corners, leading to a gradual reduction in NCs, eventually acquiring a more spherical geometry. At the same time, this process can enhance surface passivation and increase ligand coverage. These observations agree with the spectroscopical evidence: the blue shift and the more intense PL.

Additionally, a distinct dark spherical domain was observed on the surface of the $CsPbBr_3$ nanocrystals. This feature is most likely due to the beam-induced reduction of silver during the exposition under the electron beam (Figure 4.4d). This interpretation is further supported by the absence of any plasmonic absorption peak associated with metallic Ag in the absorbance spectra. In addition, the color of the colloidal solution was the characteristic of $CsPbBr_3$ NCs, exhibiting a green-yellow color without brownish shades that could be associated with silver nanoparticles. As a note, it is well-known that silver halides are photosensitive materials that are quickly degraded under light/electron beam irradiation.[30,31] These observations suggest that a thin AgBr shell might have initially formed, but quickly reduced in situ under electron beam illumination.

Similar features were observed for the silver-TOP solution as the absorbance spectrum revealed a blue shift (Figure 4.4e). These findings are consistent with the smaller size of the nanocrystals observed in the TEM images (Figure 4.4f), as well as with the presence of reduced silver on the surface of the perovskite NCs. A clear and pronounced increase in photoluminescence (PL) intensity was detected. To better evaluate the temporal evolution of this enhancement, we performed ex situ time-resolved PL measurements using a custom-built experimental setup. This system enables both ex situ absorbance and photoluminescence measurements (see Figure 4.8 and Photograph 1, Appendix).

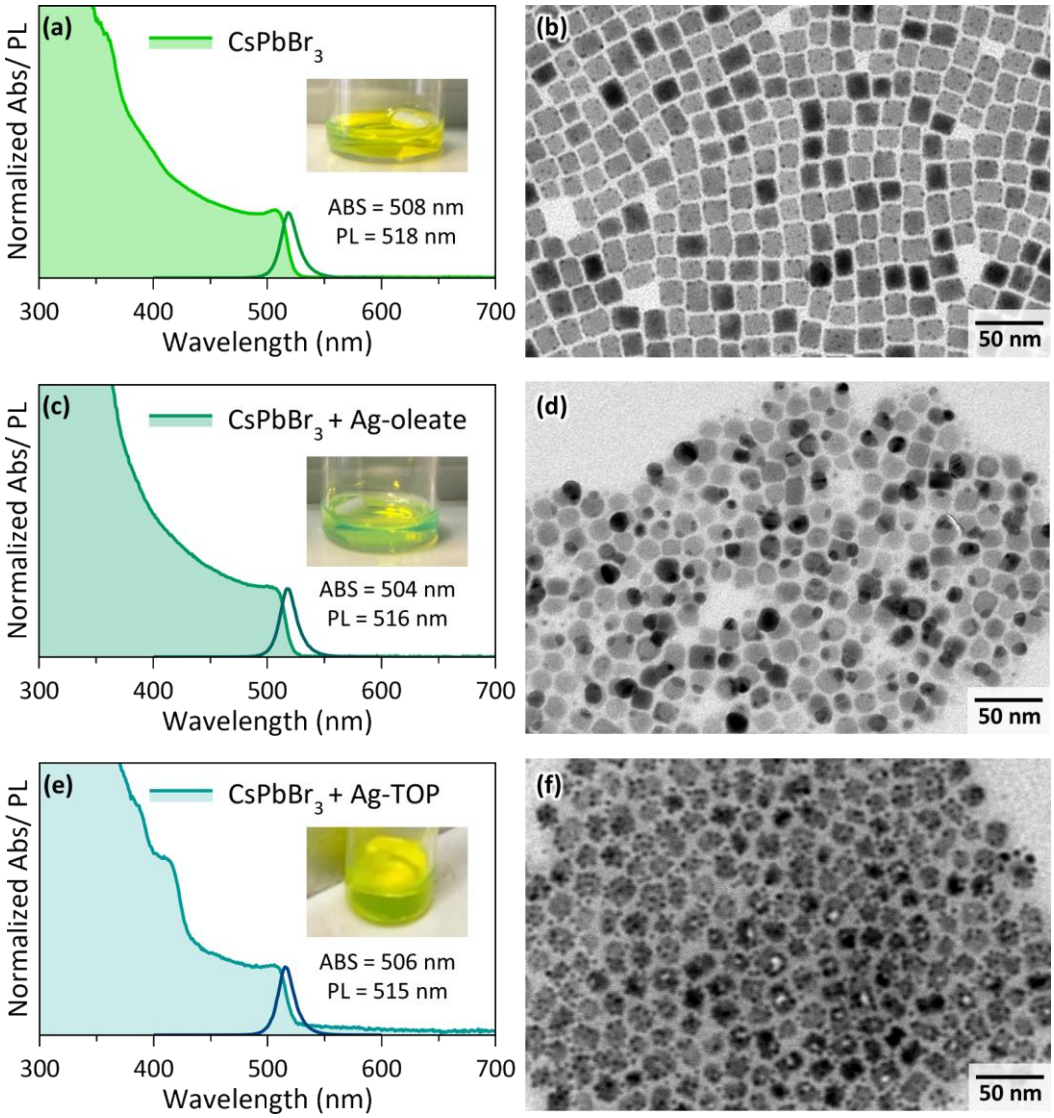

Figure 4.4. Absorbance, photoluminescence spectra and TEM images. a) Absorbance and photoluminescence spectra of $CsPbBr_3$ NCs as synthetized and relative (b) TEM image. c) Absorbance and photoluminescence spectra of $CsPbBr_3$ NCs after the addition of silver oleate solution and relative (d) TEM image. The images clearly show that following the addition of the silver oleate solution, there is a reduction in particle size, attributed to the action of the oleate ligand. Additionally, the formation of the silver domain is observed, appearing as a dark spherical contrast on the perovskite structure. e) Absorbance and photoluminescence spectra of $CsPbBr_3$ NCs after the addition of silver-TOP solution and relative (f) TEM image. In this case as well, the nanocrystals exhibit a morphological transition towards a more spherical geometry, accompanied by the presence of reduced metallic silver on their surfaces.

The white light source for absorbance measurements (200-800 nm) is connected via an optical fiber to a custom-fabricated sample holder, while a second optical fiber links the holder to the detector. For PL measurements, a dedicated hole in the sample holder allows integration of a UV excitation source. The detector is directly connected to a computer equipped with Avasoft4 software, which facilitates real-time data acquisition and analysis during measurements. As shown in Figure 4.5, the PL intensity increases rapidly during the initial minutes of the reaction, eventually reaching a plateau. Additionally, a blue shift in the emission peak was observed, consistent with the smaller size of the NCs after the Ag-TOP treatment and in agreement with what observed for the silver oleate system.

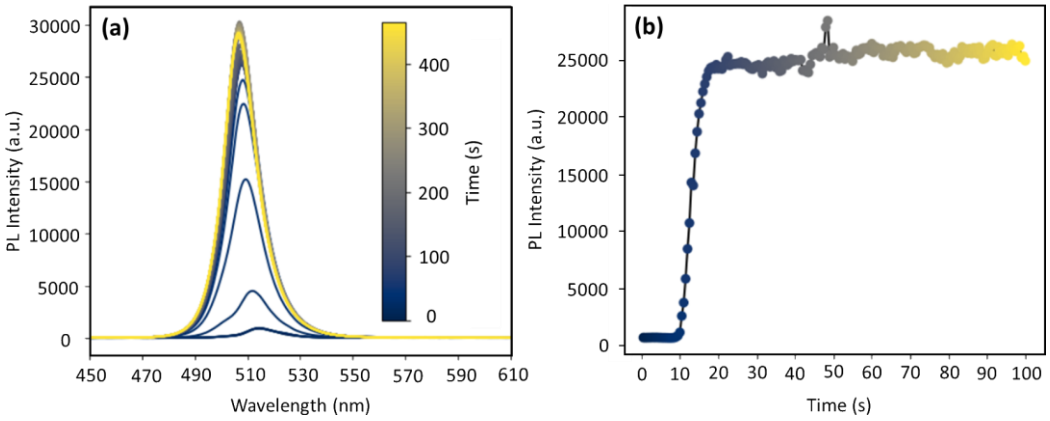

Figure 4.5. Photoluminescence measurements by time. a) Photoluminescence spectra of $CsPbBr_3$ NCs recorded during the addition of the Ag-TOP solution. The spectra were acquired for a total time of 5 minutes with a time step between two acquisitions of 500 ms. b) Time-dependent PL intensity profile following the introduction of the Ag-TOP solution, which was added 10 seconds after the start of the measurement. A rapid increase in PL intensity is observed between 10 and 20 seconds, followed by a plateau, indicating the stabilization of the signal.

When comparing the performance of the two silver precursors, silver oleate appears to be more promising than Ag-TOP, as it better preserves the nanoparticle morphology, despite inducing a slight reduction in crystal size. Based on these observations, further characterizations were carried out on $CsPbBr_3$ nanocrystals treated with Ag-oleate. To check the formation of the possible silver bromide layer, X-ray powder diffraction (XRD) was employed. However, due to the overlapping diffraction peaks of AgBr and $CsPbBr_3$ in the XRD patterns (Figure 4.9, Appendix), the structural distinction of the two materials remained inconclusive.

To further investigate this, high-resolution transmission electron microscopy (HR-TEM) coupled with EDX (Energy-Dispersive X-ray) mapping were employed (Figure 4.6). HR-TEM-EDX analysis revealed a uniform distribution of Cs, Pb, and Br across the surface of the nanocrystals, confirming the preservation of the perovskite domain after the treatment with the silver oleate solution. Consistent with TEM findings, the dark spherical features correspond to silver domains. In a few nanocrystals (highlighted with red arrows in Figure 4.6), a thin and uniform silver bromide shell was observed surrounding the entire $CsPbBr_3$ nanocrystal, rather than forming discrete silver domains.

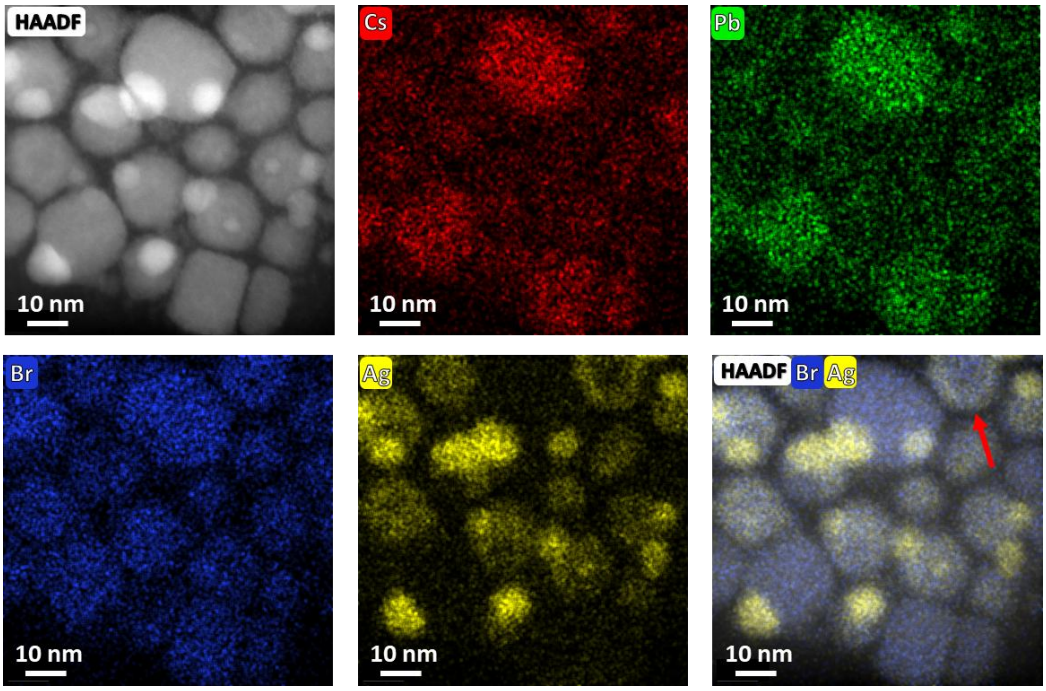

Figure 4.6. High-Angle Annular Dark-Field (HAADF) images and elemental composition. HAADF images of $CsPbBr_3$ NCs following the addition of the silver oleate solution reveal a uniform distribution of Cs, Pb, and Br, indicating the preservation of the perovskite domain. Moreover, silver is predominantly present as a shell surrounding most of the nanocrystals, with partial reduction under the electron beam resulting in the appearance of dark spherical domains. The red arrow highlights a nanoparticle in which the core is primarily composed of Cs, Pb, and Br, while the shell consists of Ag and Br. However, such core@shell architectures are relatively rare within the sample.

Overall, the limited and poorly reproducible formation of a well-defined $CsPbBr_3$@AgBr core@shell heterostructure using the post-synthetic treatment can be rationalized by considering several thermodynamic and kinetic factors governing the system. First, the surface chemistry of $CsPbBr_3$ NCs is highly

dynamic; consequently, the introduction of the Ag precursors in a ligand-rich environment, particularly in the presence of excess oleic acid, can alter the equilibrium at the NCs surface. Rather than promoting a controlled growth of AgBr, the system favors ligand-assisted etching and surface reconstruction, as evidenced by the size reduction and morphological evolution toward more spherical particles. This indicates that dissolution-reprecipitation processes compete with shell growth, preventing the formation of a continuous AgBr layer.

Second, from a nucleation perspective, the addition of Ag^+ to preformed $CsPbBr_3$ NCs does not guarantee selective heterogeneous nucleation on the perovskite surface. In colloidal systems, homogeneous nucleation of a secondary phase in solution often competes with interfacial growth. Although $CsPbBr_3$ and AgBr share bromide as a common anion, small differences in crystal structure and surface terminations may hinder coherent epitaxial overgrowth. As a result, silver species may preferentially form small, separate domains or undergo partial reduction to metallic Ag rather than assembling into a uniform shell. The occasional observation of thin AgBr layers in HR-TEM suggests that shell formation is kinetically accessible but not thermodynamically favored under the adopted conditions.

Taken together, these considerations indicate that this two-step, post-synthetic approach does not provide sufficient control over interfacial energetics and reaction kinetics to successfully synthetize the desired core@shell architectures. The competing processes of surface etching, homogeneous nucleation and partial reduction prevent the effective formation of AgBr shell. These limitations motivated the development of a one-pot synthetic strategy, in which nucleation and interfacial growth can be more effectively coupled and kinetically controlled from the early stages of nanocrystal formation, thereby increasing the likelihood of obtaining a well-defined and reproducible heterostructure.

4.4 Synthesis of AgBr@$CsPbBr_3$ core@shell heterostructure

The revised synthetic strategy, focused on obtaining the desired $CsPbBr_3$@AgBr heterostructures, relied on the incorporation of the silver precursor from the early stages of the synthesis, aiming to promote a more controlled and homogeneous formation of the core@shell structure. Therefore, we implemented substantial modifications to a synthetic protocol that was previously developed by

members of our group.[32] The optimization of this synthetic protocol was performed in collaboration with my colleague Zhanzhao Li.

The synthetic approach relied on the hot injection, at 100 °C, of a benzoyl bromide solution into a mixture containing all the metal oleate complexes (Cs, Pb, Zn, and Ag oleate), using hexadecane as the solvent and without the employment of amine as surfactants, always to prevent the reduction of Ag by this ligand. In addition, this one-pot approach uses the same bromine precursor (benzoyl bromide) for synthetizing both materials, exploiting the advantage of choosing AgBr as the secondary domain to couple with $CsPbBr_3$, as anticipated in the introduction. The synthesis is let to proceed for 1 min, after which the reaction is quenched by immersing the flask in an ice-water bath. By adopting this strategy, we were finally able to obtain a distinct core@shell morphology of the NCs.

As shown by the TEM image (inset of Figure 4.7a), the products of this synthetic protocol are cubic nanocrystals with a lateral size of 45 ± 7 nm. The cubes exhibit a core region at the center of the NCs, which in most cases consists of a cubic cavity approximately 12 ± 1.8 nm in size, carrying inside a higher-contrast domain of 9.9 ± 1.7 nm (see Figure 4.10 for estimates of sizes of NCs and related core regions). The presence of Zn^{2+} together with Ag^{+} led to a narrower size distribution of the final NCs than those prepared in the sole presence of Ag^{+}. According to previous works, Zn^{2+} ions are not incorporated in the $CsPbBr_3$ NCs, although they can influence their growth.[32,33]

Using this strategy, the first domain to form is AgBr, as its formation energy is lower than that of $CsPbBr_3$. As a consequence, contrary to our initial idea, $CsPbBr_3$ constitutes the shell of the heterostructure. Control experiment, in which the reaction was quenched only a few seconds after the injection of benzoyl bromide, revealed the presence of the sole AgBr domain, further confirming that is served as the core of the final architecture. Considering the relative size of the two domains, the overall volume fraction occupied by the AgBr core is only around 2% of the whole NC volume.

The optical absorption and PL spectra of colloidal suspensions of the core@shell sample are consistent with those expected for large $CsPbBr_3$ NCs. In particular, the absorption spectrum shows a tail at low energy, which can be attributed to the strong light scattering due to partial aggregation of these large NCs in solution (Figure 4.7a). The XRD analysis revealed the presence of the orthorhombic $CsPbBr_3$ phase, as all reflections could be matched to the reference

pattern. (Figure 4.7b). Apparently, no additional phases, such as AgBr or metallic Ag, were detected. However, as discussed before, the detection of AgBr by XRD would be particularly challenging due to the exact overlap with $CsPbBr_3$ peaks and to the small volume ratio of AgBr in the sample.

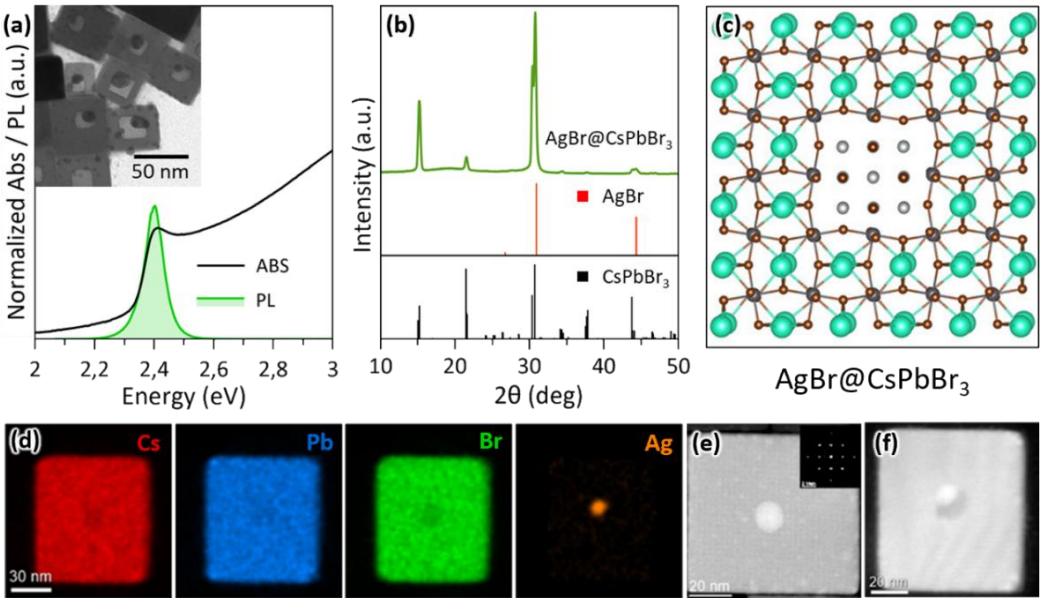

Figure 4.7. Characterization of AgBr@$CsPbBr_3$ cubes. a) Absorption and PL spectra, inset: TEM image of the core@shell heterostructures. b) XRD pattern of the core@shell sample in green (reference pattern: black - $CsPbBr_3$ (ICSD number 97851), red - AgBr (ICSD number 56546)). c) Interface layer visualized along the z-direction. d) STEM-EDX elemental maps of a single nanoparticle, that is actually the one in panel (f). (e, f) STEM-HAADF images of two different nanoparticles (inset: FFT). Adapted with permission from ref 34. Licensed under CC-BY 4.0. Copyright © 2025 The Authors.

In Figure 4.7c is reported the atomistic model at the interface along the z direction. In this context, even though the experimentally obtained heterostructure is the reverse of our initial intent, in which $CsPbBr_3$ was supposed to constitute the core of the architecture, the simulations remain fully valid. From a predictive perspective, the identity of the core and shell materials does not affect the interfacial analysis. As a result, the experimentally observed core@shell heterostructure confirms the simulation results: the interface is coherent and epitaxial, characterized by a shared bromide framework that connects the two domains and favors interfacial bond formation. Additionally, the geometry of the core region is consistent with that predicted by the Wulff construction, as the AgBr domain exhibits a cubic morphology.

Elemental mapping by EDX of a single NC revealed the presence of a small Ag-rich domain in the core region (Figure 4.7d). The detection of metallic silver instead of AgBr is probably a consequence of the fast reduction of silver bromide induced by the electron beam. This finding agrees with observations from other experiments previously discussed. To further investigate the structural composition of the NCs, a high-angle annular dark-field high-resolution scanning TEM (STEM-HAADF) analysis was carried out. Figure 4.7e is a STEM- HAADF image of a core@shell NC in which the core appears as a bright central region in the image due to the higher mass density of AgBr (or Ag). Fast Fourier transform (FFT) analysis (inset of Figure 4.7e) confirmed that the NC is essentially monocrystalline $CsPbBr_3$. As confirmed by the simulations, AgBr has an excellent lattice match with $CsPbBr_3$ (with a mismatch of 1.2%), making it challenging to distinguish the AgBr lattice reflections overlapping with those from the thick $CsPbBr_3$ shell. Figure 4.7f is a high-resolution STEM image of the much more common case of a NC with a cubic shaped cavity and a Ag-rich domain inside. This is the same NC on which EDX mapping is reported in Figure 4.7d.

The cubic geometry of the cavity is likely dictated by the original morphology of the AgBr domain. According to the simulations, this domain would adopt a cubic shape to minimize the interfacial energy with $CsPbBr_3$ through the preferential formation of (100)/(100) interfaces. However, we cannot entirely exclude that the initial shape of the AgBr core deviates from a perfect cube and the cubic shape of the cavity results from a partial rearrangement of the $CsPbBr_3$ lattice following the degradation of the core induced by light or electron beam irradiation.

A series of anion-exchange experiments involving chloride and iodide were carried out by my colleague Zhanzhao Li. Notably, he found that, depending on the halide introduced during the exchange, the resulting architecture exhibited an internal cavity and no longer contained AgBr (or metallic Ag). This finding opened an interesting research direction toward hollow nanostructures, systems that remain relatively underexplored within the otherwise extensive literature on $CsPbX_3$ perovskites. The results are presented and discussed in the publication.[34]

4.5 Conclusions

In conclusion, we successfully developed a synthetic protocol to obtain core@shell heterostructure composed of AgBr and $CsPbBr_3$, by employing a hot injection strategy. This architecture was characterized by different techniques, which allowed us to confirm that the core is composed of silver bromide and the

shell of perovskite. This synthetic result is in excellent agreement with the simulations performed using Ogre, thereby demonstrating the strong predictive capability of the software as an effective tool for designing novel heterostructures with complex architectures. In particular, the software can support synthetic chemists by significantly reducing the time required for experimental trial-and-error during materials development.

Notably, although our initial design strategy aimed at obtaining a core@shell architecture with perovskites domain as the core, the experimental results instead revealed the formation of AgBr surrounded by a $CsPbBr_3$ shell. Importantly, this deviation from the starting target structure does not undermine the validity of this computational approach, rather, it highlights that, in addition to structural compatibility, thermodynamic factors play a crucial role in determining the final architecture of the system. This effect is particularly relevant when all precursors are mixed together from the early stage of the reaction, as in the present case. Overall, this work paves the way for future studies on the rational design and synthesis of advanced heterostructures guided by computational tools.

4.6 Methods

Chemicals

Hexadecane (99%), oleic acid (OA, technical grad, 90%), cesium(I) carbonate (Cs_2CO_3, 98%), lead (II) acetate trihydrate ($Pb(OAc)_2 \cdot 3H_2O$, 99.99%), silver acetate (AgOAc, 99.9%), zinc (II) acetate ($Zn(OAc)_2$, 99%), toluene (anhydrous, 99.8%) and toluene-d_8 (anhydrous, 99.6%), dimethyl sulfoxide-d_6 (DMSO, 99.8%), trifluoro acetic acid (TFA, 98%), oleylamine (OLAm, 98%), Silver nitrate ($AgNO_3$ 99.9%), didodecyldimethylammonium bromide (DDAB, 98%) were purchased from Sigma-Aldrich. Benzoyl bromide (98%), didodecylmethyl amine (DDMA, >85%) were purchased from Tokyo Chemical Industry (TCI). All reagents were used as received without any further experimental purification.

Synthesis of core@shell AgBr@$CsPbBr_3$ cubes

Synthesis of core@shell AgBr@$CsPbBr_3$ cubes: 0.05 mmol of $Cs_2(CO_3)$, 0.1 mmol of $Pb(OAc)_2 \cdot 3H_2O$, 0.2 mmol of Ag(OAc), and 0.025 mmol of $Zn(OAc)_2$ were dissolved in a mixture of 1.5 ml (4.73 mmol) of oleic acid and 6 ml of hexadecane in a flask. The resulting mixture was pumped to vacuum at room temperature for 30 min and at 100 °C for 50 min. The mixture was subsequently placed under a nitrogen atmosphere, and the temperature was raised to 125 °C for 10 minutes to achieve a transparent solution. The solution was then cooled down to 100 ºC and a benzoyl bromide solution (obtained by mixing 50 μL of benzoyl bromide (0.42 mmol) in 500 μL of hexadecane) was swiftly injected, triggering the growth of the $CsPbBr_3$ cubes. After 1 min of reaction, a tertiary amine solution (obtained by mixing 100 μL DDMA (0.2 mmol) dispersed in 900 μL hexadecane) was swiftly injected, and the reaction was quenched within 10 sec by rapidly cooling it down to room temperature using an ice-water bath. The crude solution was precipitated with centrifugation at 6000 rpm for 10 min. The precipitate was kept and redispersed in 4 ml anhydrous toluene. Then the resulting dispersion was centrifugated at 2000 rpm for 5 min. The supernatant was discarded, and the precipitate was redispersed in 4 ml anhydrous toluene. The final solution was stored in a nitrogen filled glovebox under the dark condition for further characterizations.

Reaction condition optimizations: different reaction temperature (90 ºC, 100 ºC and 110 ºC), different amount of Ag(OAc) addition (0.15mmol, 0.2mmol and 0.25mmol) and different amount of $Zn(OAc)_2$ addition (0.025mmol, 0.05mmol and 0.1mmol) were conducted in the same reaction protocol of core@shell AgBr@$CsPbBr_3$ cubes as above.

X-ray Diffraction (XRD)

XRD analysis was performed on a PANanalytical Empyrean X-ray diffractometer, equipped with a 1.8 kW Cu Kα ceramic X-ray tube (λ = 1.5406 Å) and a PIXcel3D 2 × 2 area detector, operating at 45 kV and 40 mA. Cubes solutions were concentrated in the vial through a flow of nitrogen, then they were drop-cast on a zero-diffraction single crystal silicon substrate. The XRD patterns were collected under ambient conditions.

Transmission Electron Microscopy (TEM) and Scanning TEM (STEM)

Bright-field TEM (BF-TEM) images with a large field of view were acquired on a JEOL JEM-1400Plus microscope with a thermionic gun (LaB_6 crystal) with an acceleration voltage of 120 kV. Cubes solutions were diluted ten times in anhydrous toluene and then drop-cast on the copper TEM grids with an ultrathin carbon film. High-resolution scanning transmission electron microscopy (HRSTEM) images were acquired on a probe-corrected Thermo Fisher Spectra 30-300 STEM operated at 300 kV. Images were acquired on a High-Angle annular Dark Field (HAADF) detector with a current of 30 pA. Compositional maps were acquired using Velox, with a probe current of ~150 pA and rapid rastered scanning by Energy-Dispersive X-ray (EDX) on a Dual-X system comprising two detectors, on either side of the sample, for a total acquisition angle of 1.76 Sr. STEM-HAADF tilt series were acquired by tilting a single tilt tomography sample holder from -70° at 65° with a step of 5° to minimize sample damage. The 3D volume was reconstructed using commercial software (Inspect3D) using the SIRT algorithm.

Optical Measurements

The PL spectra of NCs were measured on a Varian Cary Eclipse spectrophotometer (λex = 350 nm). The photoluminescence (PL) quantum yield (QY) was measured using a FLS920 Edinburgh Instruments spectrofluorimeter equipped with an integrating sphere. The NC samples were dispersed in anhydrous toluene with an optical density of 0.12 at 400 nm, which was the excitation wavelength employed for PLQY measurements, to minimize self-absorption. PL measurements at vanishingly low excitation fluencewere performed with a Horiba Triax 190 spectrometer, exciting the samples with a laser (λex = 360 nm, 405 nm) and collecting the emitted light with a CCD. Time-resolved PL were carried out using a femtosecond amplified laser operated at 20 kHz (see description below), tuned at

360 nm or 405 nm. The emitted light was collected with a phototube coupled to a Cornerstone 260 1/4 m VIS-NIR

4.7 Appendix

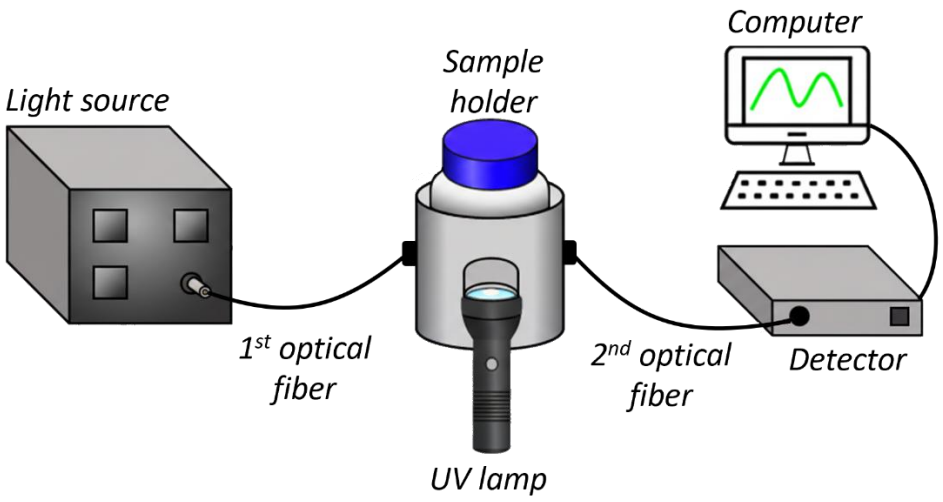

Figure 4.8. Scheme of the ex-situ set-up for abs and PL measurements. The sample holder is connected through two different optical fibers to the light source (first one) and to the detector (second one). When the light source is off, PL measurements can be performed using the UV lamp (405 nm), this lamp is integrated in the holder with a costumed entrance. The detector is linked to the computer to analyse and collect the optical spectra.

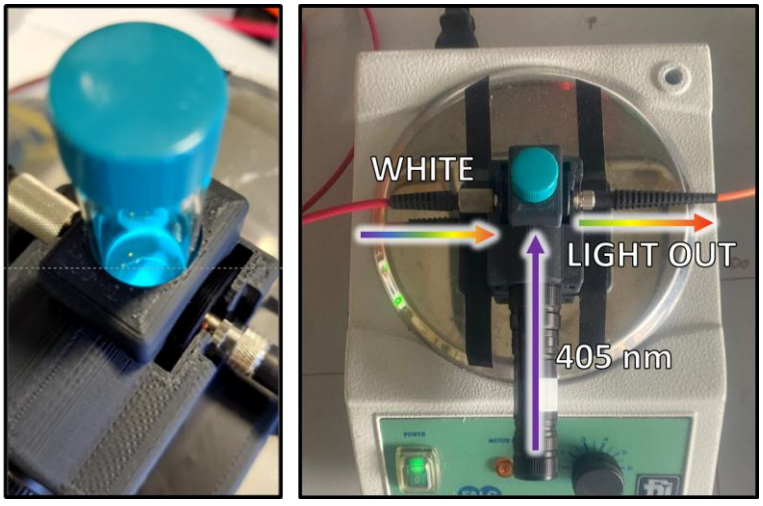

Photograph 1. Picture of the sample holder highlighting the in and out optical fibers.

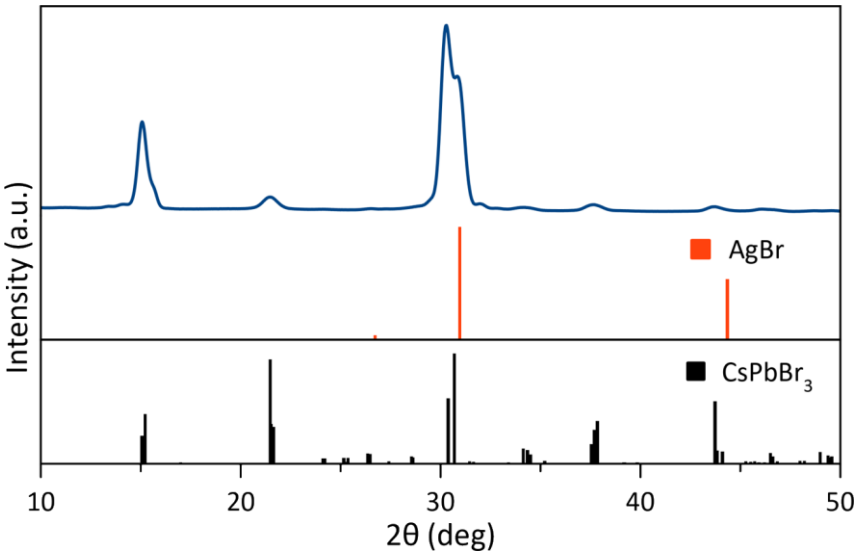

Figure 4.9. XRD pattern. XRD pattern of $CsPbBr_3$ NCs after treatment with the Ag-oleate solution (blue line), reference pattern of AgBr (red line) and reference pattern of $CsPbBr_3$ (black line). Perovskite and silver bromide peaks occupied barely the same position, making the distinction of these two phases particularly challenging.

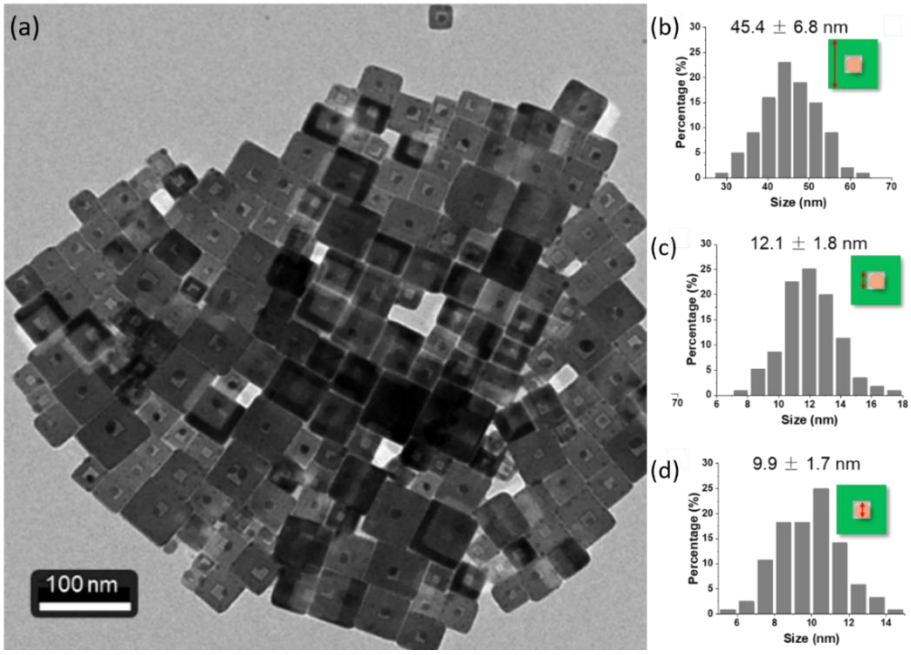

Figure 4.10. Tem images and size distribution. a) TEM image of AgBr@$CsPbBr_3$ nanocubes synthesized with Zn^{2+} addition (molar ratio Cs:Pb:Ag:Zn = 1:1:2:0.25). b, c, d)

Size distributions of the nanocube, cavity, and core. The core has an irregular shape, smaller than the cubic cavity in AgBr@$CsPbBr_3$ nanocubes. To investigate the initial morphology of isolated AgBr, we stopped the reaction early on (10 sec). The resulting AgBr nanocrystals present an inhomogeneous spherical shape, often with some darker dots, a potential indication of photodegradation. This is attributed to the high photosensitivity of AgBr, which leads to the partial or complete photodegradation to metallic Ag. Thus, in the AgBr@$CsPbBr_3$ nanocubes, AgBr cores degradation is often inevitable, and therefore capturing the pristine morphology of AgBr is challenging. We hypothesize that the reduction of Ag^+ to metallic Ag goes hand in hand with the reorganization of the cavity walls in the $CsPbBr_3$ cube, such that the cavity ends up exposing (100) facets. Adapted with permission from ref 34.

4.8 Source Publications and Contributions

Part of this chapter is based on the following publication:

Li, Z.; Ivanov, Y. P.; Cabona, A.; Fratelli, A.; Toso, S.; Chakraborty, S.; Divitini, G.; Kriegel, I.; Brovelli, S.; Manna, L. Core@Shell AgBr@$CsPbBr_3$ Nanocrystals as Precursors to Hollow Lead Halide Perovskite Nanocubes. *J. Am. Chem. Soc.* **2025**, *147* (26), 23192–23201. https://doi.org/10.1021/jacs.5c07200.

This article stemmed from the idea of synthesizing a new heterostructure to test predictive power of Ogre. In this context, Stefano Toso supported the simulations, guiding me in the use of the software. The optimized synthetic protocol was developed through a collaboration with Zhanzhao Li. This work was also made possible thanks to the constructive discussion with Stefano Toso, Zhanzhao Li and Liberato Manna, whom I thank for their insightful perspective, guidance, and assistance in preparing the manuscript.

4.8.1 Copyright

Some elements of this chapter were adapted from external source:

Figures:

- **Figure 4.1., Figure 4.2., Figure 4.7., Figure 4.10.** Adapted with permission from J. Am. Chem. Soc. **2025**, 147 (26), 23192–23201. Licensed under CC-BY 4.0. Copyright © 2025 The Authors.

Text (parts):

- Adapted with permission from J. Am. Chem. Soc. **2025**, 147 (26), 23192–23201. Licensed under CC-BY 4.0. Copyright © 2025 The Authors.

4.9 Bibliography

(1) Toso, S.; Dardzinski, D.; Manna, L.; Marom, N. Structure Prediction of Ionic Epitaxial Interfaces with Ogre Demonstrated for Colloidal Heterostructures of Lead Halide Perovskites. *ACS Nano* **2025**, *19* (5), 5326–5341. https://doi.org/10.1021/acsnano.4c12713.

(2) Imran, M.; Peng, L.; Pianetti, A.; Pinchetti, V.; Ramade, J.; Zito, J.; Di Stasio, F.; Buha, J.; Toso, S.; Song, J.; Infante, I.; Bals, S.; Brovelli, S.; Manna, L. Halide Perovskite–Lead Chalcohalide Nanocrystal Heterostructures. *J. Am. Chem. Soc.* **2021**, *143* (3), 1435–1446. https://doi.org/10.1021/jacs.0c10916.

(3) De Trizio, L.; Infante, I.; Manna, L. Surface Chemistry of Lead Halide Perovskite Colloidal Nanocrystals. *Acc. Chem. Res.* **2023**, *56* (13), 1815–1825. https://doi.org/10.1021/acs.accounts.3c00174.

(4) Shamsi, J.; Urban, A. S.; Imran, M.; De Trizio, L.; Manna, L. Metal Halide Perovskite Nanocrystals: Synthesis, Post-Synthesis Modifications, and Their Optical Properties. *Chem. Rev.* **2019**, *119* (5), 3296–3348. https://doi.org/10.1021/acs.chemrev.8b00644.

(5) Imran, M.; Caligiuri, V.; Wang, M.; Goldoni, L.; Prato, M.; Krahne, R.; De Trizio, L.; Manna, L. Benzoyl Halides as Alternative Precursors for the Colloidal Synthesis of Lead-Based Halide Perovskite Nanocrystals. *J. Am. Chem. Soc.* **2018**, *140* (7), 2656–2664. https://doi.org/10.1021/jacs.7b13477.

(6) Pradhan, N. Tips and Twists in Making High Photoluminescence Quantum Yield Perovskite Nanocrystals. *ACS Energy Lett.* **2019**, *4* (7), 1634–1638. https://doi.org/10.1021/acsenergylett.9b00946.

(7) Maes, J.; Balcaen, L.; Drijvers, E.; Zhao, Q.; De Roo, J.; Vantomme, A.; Vanhaecke, F.; Geiregat, P.; Hens, Z. Light Absorption Coefficient of $CsPbBr_3$ Perovskite Nanocrystals. *J. Phys. Chem. Lett.* **2018**, *9* (11), 3093–3097. https://doi.org/10.1021/acs.jpclett.8b01065.

(8) García-Fernández, A.; Moradi, Z.; Bermúdez-García, J. M.; Sánchez-Andújar, M.; Gimeno, V. A.; Castro-García, S.; Señarís-Rodríguez, M. A.; Mas-Marzá, E.; Garcia-Belmonte, G.; Fabregat-Santiago, F. Effect of Environmental Humidity on the Electrical Properties of Lead Halide Perovskites. *J. Phys. Chem. C* **2019**, *123* (4), 2011–2018. https://doi.org/10.1021/acs.jpcc.8b03915.

(9) Singh, A. N.; Kajal, S.; Kim, J.; Jana, A.; Kim, J. Y.; Kim, K. S. Interface Engineering Driven Stabilization of Halide Perovskites against Moisture,

Heat, and Light for Optoelectronic Applications. *Adv. Energy Mater.* **2020**, *10* (30), 2000768. https://doi.org/10.1002/aenm.202000768.

(10) R, S.; Nayak, V.; Jyothi, M. S.; Balakrishna, R. G. Review on Recent Advances of Core-Shell Structured Lead Halide Perovskites Quantum Dots. *J. Alloys Compd.* **2020**, *834*, 155246. https://doi.org/10.1016/j.jallcom.2020.155246.

(11) Ghosh Chaudhuri, R.; Paria, S. Core/Shell Nanoparticles: Classes, Properties, Synthesis Mechanisms, Characterization, and Applications. *Chem. Rev.* **2012**, *112* (4), 2373–2433. https://doi.org/10.1021/cr100449n.

(12) Glaus, S.; Calzaferri, G. The Band Structures of the Silver Halides AgF, AgCl, and AgBr: A Comparative Study. *Photochem. Photobiol. Sci.* **2003**, *2* (4), 398–401. https://doi.org/10.1039/b211678b.

(13) Shiao, D. D. F.; Fortmiller, L. J.; Herz, A. H. Dissolution Rates of Aqueous Silver Halide Dispersions. *J. Phys. Chem.* **1975**, *79* (8), 816–821. https://doi.org/10.1021/j100575a009.

(14) Urakaev, F. Kh.; Khan, N. V.; Shalabaev, Zh. S.; Tatykaev, B. B.; Nadirov, R. K.; Burkitbaev, M. M. Synthesis and Photocatalytic Properties of Silver Chloride/Silver Composite Colloidal Particles. *Colloid J.* **2020**, *82* (1), 76–80. https://doi.org/10.1134/S1061933X20010160.

(15) Monnoyer, P.; Fonseca, A.; Nagy, J. B. Preparation of Colloidal AgBr Particles from Microemulsions. *Colloids Surf. A: Physicochem. Eng. Asp.* **1995**, *100*, 233–243. https://doi.org/10.1016/0927-7757(95)03187-I.

(16) Koh, J. H.; Seo, J. A.; Park, J. T.; Kim, J. H. Synthesis and Characterization of AgBr Nanocomposites by Templated Amphiphilic Comb Polymer. *J. Colloid Interface Sci.* **2009**, *338* (2), 486–490. https://doi.org/10.1016/j.jcis.2009.07.010.

(17) Abeyweera, S. C.; Rasamani, K. D.; Sun, Y. Ternary Silver Halide Nanocrystals. *Acc. Chem. Res.* **2017**, *50* (7), 1754–1761. https://doi.org/10.1021/acs.accounts.7b00194.

(18) Li, Z.; Sun, Y. Silver Chlorobromide Nanoparticles with Highly Pure Phases: Synthesis and Characterization. *J. Mater. Chem. A* **2013**, *1* (23), 6786–6793. https://doi.org/10.1039/C3TA00020F.

(19) Liu, C.; Chen, H.; Lin, P.; Hu, H.; Meng, Q.; Xu, L.; Wang, P.; Wu, X.; Cui, C. Growth, Characterization and Photoelectrical Properties of Orthorhombic and Cubic CsPbBr3 Single Crystals. *J. Mater. Sci: Mater. Electron.* **2022**, *33* (32), 24895–24905. https://doi.org/10.1007/s10854-022-09199-1.

(20) Herring, C. Some Theorems on the Free Energies of Crystal Surfaces. *Phys. Rev.* **1951**, *82* (1), 87–93. https://doi.org/10.1103/PhysRev.82.87.

(21) Srolovitz, D. J. On the Stability of Surfaces of Stressed Solids. *Acta Metall.* **1989**, *37* (2), 621–625. https://doi.org/10.1016/0001-6160(89)90246-0.

(22) Lai, F.; Chen, Y.; Guo, H. Surface Energies of Non-Centrosymmetric Nanocrystals by the Inverse Wulff Construction Method. *Phys. Chem. Chem. Phys.* **2019**, *21* (30), 16486–16496. https://doi.org/10.1039/C9CP01975H.

(23) Roosen, A. R.; McCormack, R. P.; Carter, W. C. Wulffman: A Tool for the Calculation and Display of Crystal Shapes. *Comput. Mater. Sci.* **1998**, *11* (1), 16–26. https://doi.org/10.1016/S0927-0256(97)00167-5.

(24) Huang, X.; Li, H.; Zhang, C.; Tan, S.; Chen, Z.; Chen, L.; Lu, Z.; Wang, X.; Xiao, M. Efficient Plasmon-Hot Electron Conversion in Ag–$CsPbBr_3$ Hybrid Nanocrystals. *Nat. Commun.* **2019**, *10* (1). https://doi.org/10.1038/s41467-019-09112-1.

(25) Protesescu, L.; Yakunin, S.; Bodnarchuk, M. I.; Krieg, F.; Caputo, R.; Hendon, C. H.; Yang, R. X.; Walsh, A.; Kovalenko, M. V. Nanocrystals of Cesium Lead Halide Perovskites ($CsPbX_3$, X = Cl, Br, and I): Novel Optoelectronic Materials Showing Bright Emission with Wide Color Gamut. *Nano Lett.* **2015**, *15* (6), 3692–3696. https://doi.org/10.1021/nl5048779.

(26) Nair, G. B.; Tamboli, S.; Kroon, R. E.; Dhoble, S. J.; Swart, H. C. Facile Room-Temperature Colloidal Synthesis of $CsPbBr_3$ Perovskite Nanocrystals by the Emulsion-Based Ligand-Assisted Reprecipitation Approach: Tuning the Color-Emission by the Demulsification Process. *J. Alloys Compd.* **2022**, *928*, 167249. https://doi.org/10.1016/j.jallcom.2022.167249.

(27) Imran, M.; Ijaz, P.; Baranov, D.; Goldoni, L.; Petralanda, U.; Akkerman, Q.; Abdelhady, A. L.; Prato, M.; Bianchini, P.; Infante, I.; Manna, L. Shape-Pure, Nearly Monodispersed $CsPbBr_3$ Nanocubes Prepared Using Secondary Aliphatic Amines. *Nano Lett.* **2018**, *18* (12), 7822–7831. https://doi.org/10.1021/acs.nanolett.8b03598.

(28) De Trizio, L.; Figuerola, A.; Manna, L.; Genovese, A.; George, C.; Brescia, R.; Saghi, Z.; Simonutti, R.; Van Huis, M.; Falqui, A. Size-Tunable, Hexagonal Plate-like Cu_3P and Janus-like Cu–Cu_3P Nanocrystals. *ACS Nano* **2012**, *6* (1), 32–41. https://doi.org/10.1021/nn203702r.

(29) Cabona, A.; Toso, S.; Griesi, A.; Rizzo, M.; Ferri, M.; Rusch, P.; Divitini, G.; Pérez-Prieto, J.; Galian, R. E.; Kriegel, I.; Manna, L. Synthesis,

Growth Mechanism, and Photocatalytic Properties of Metallic-Bi/$Bi_{13}S_{18}Br_2$ Nano-Bell Heterostructures. *ACS Mater. Lett.* **2025**, *7* (5), 1707–1716. https://doi.org/10.1021/acsmaterialslett.5c00043.

(30) Huang, K.; Li, C.; Zheng, Y.; Wang, L.; Wang, W.; Meng, X. Recent Advances on Silver-Based Photocatalysis: Photocorrosion Inhibition, Visible-Light Responsivity Enhancement, and Charges Separation Acceleration. *Sep. Purif. Technol.* **2022**, *283*, 120194. https://doi.org/10.1016/j.seppur.2021.120194.

(31) Hamilton, J. F. The Silver Halide Photographic Process. *Adv. Phys.* **1988**, *37* (4), 359–441. https://doi.org/10.1080/00018738800101399.

(32) Li, Z.; Goldoni, L.; Wu, Y.; Imran, M.; Ivanov, Y. P.; Divitini, G.; Zito, J.; Panneerselvam, I. R.; Baranov, D.; Infante, I.; De Trizio, L.; Manna, L. Exogenous Metal Cations in the Synthesis of $CsPbBr_3$ Nanocrystals and Their Interplay with Tertiary Amines. *J. Am. Chem. Soc.* **2024**, *146* (30), 20636–20648. https://doi.org/10.1021/jacs.4c03084.

(33) Dong, Y.; Qiao, T.; Kim, D.; Parobek, D.; Rossi, D.; Son, D. H. Precise Control of Quantum Confinement in Cesium Lead Halide Perovskite Quantum Dots via Thermodynamic Equilibrium. *Nano Lett.* **2018**, *18* (6), 3716–3722. https://doi.org/10.1021/acs.nanolett.8b00861.

(34) Li, Z.; Ivanov, Y. P.; Cabona, A.; Fratelli, A.; Toso, S.; Chakraborty, S.; Divitini, G.; Kriegel, I.; Brovelli, S.; Manna, L. Core@Shell AgBr@$CsPbBr_3$ Nanocrystals as Precursors to Hollow Lead Halide Perovskite Nanocubes. *J. Am. Chem. Soc.* **2025**, *147* (26), 23192–23201. https://doi.org/10.1021/jacs.5c07200.

CHAPTER 5

Exploiting $CsPbX_3/Pb_4S_3Y_2$ Heterostructure as Photocatalyst for the Photo-Induced Coupling of Thiophenol

5.1 Lead based chalcohalides

Among all the possible metal chalcohalides described in Chapter 2, the lead-based ones have attracted growing interest thanks to the extensive knowledge developed on lead chalcogenide (PbE)[1] and cesium lead halide ($CsPbBr_3$) nanocrystals (NCs).[2] In this context, PbE nanomaterials have been widely investigated for near-infrared optoelectronics,[3] while perovskite nanocrystals have found numerous applications in the visible range thanks to their remarkable optoelectronic properties.[4] This provides a solid background in synthetic strategies that can also be applied to lead chalcohalides. Another important aspect is that PbE and $CsPbX_3$ NCs are obtained under similar conditions: they typically use octadecene as the solvent, oleic acid and oleylamine as ligands, and reaction temperatures in the range of 150-200 °C.[2] Despite these similarities, and although the binary systems PbE and PbX_2 have been studied for decades, their ternary derivatives remained largely unexplored for a long time. Until only few years ago, just four stable bulk compositions ($PbTeF_6$, $Pb_7S_2Br_{10}$, $Pb_5S_2I_6$, Pb_4SeBr_6)[5,6] and few metastable phases ($Pb_4S_3I_2$, $Pb_3Se_2Br_2$),[7,8] accessible only under high pressure, were known.

The recent rediscovery of interest in lead chalcohalides derives primarily from advances in colloidal chemistry, which enabled to synthetize, for the first time, nanocrystals of new metastable phases such as $Pb_4S_3Br_2$, $Pb_4S_3I_2$ and $Pb_3S_2Cl_2$, reported by some members of the group in 2020.[9] These phases cannot be obtained under normal equilibrium conditions. In this regard, lead-based chalcohalides stand

out for their remarkable size tunability, long-term stability, and photoconductivity. $Pb_4S_3X_2$ (X = Br, I) nanocrystals can be synthesized using either hot-injection or heat-up methods. In the hot-injection approach, a sulfur-octadecene solution is injected at around 150 °C (depending on the target nanocrystals size) into a $PbBr_2$ solution in octadecene, with oleic acid and oleylamine serving as ligands. In contrast, in the heat-up method all the precursors of Pb, Br, and S are added directly to the flask in the form of lead bromide ($PbBr_2$) and lead thiocyanate ($Pb(SCN)_2$), with octadecene as the solvent. The reaction proceeds at 150 °C and relies on the thermal decomposition of SCN^- ions as a source of S^{2-}, in the presence of Pb^{2+} and Br^- ions.

The $Pb_4S_3X_2$ NCs exhibit an indirect band gap of about 2 eV and display strong absorption in the visible range, beginning in an intermediate region between that of white, wide-bandgap lead bromide and black, small-bandgap lead sulfide. The absorption gradually decreases at lower energies and becomes negligible beyond ~650 nm, which causes the material to appear red when in concentrated solution. This semiconductor material also shows promising photoconductive and photoharvesting capabilities, as demonstrated in preliminary tests on photodetectors and solar cells.[9] Moreover, just one year later, in 2021, the first epitaxial colloidal heterostructure between $Pb_4S_3Br_2$ and $CsPbBr_3$ was successfully synthetized by some of my colleagues.[10] Based on the optoelectronic properties of this lead chalcohalide phase, together with its ability to create a quasi–type II heterojunctions with perovskites (supported by DFT calculations),[10] we decided to further investigate this system. In this chapter we will study deeply these heterostructures and exploit them as a platform for photocatalytic applications.

5.1.1 Metal halide perovskite/lead chalcohalides heterostructure for photocatalysis

In Chapter 3 we already discussed the advantages of using a semiconductor-semiconductor heterostructure (HS) for light-harvesting applications.[11,12] These benefits primarily derive from the capability of both domains to absorb light and generate electron-hole pairs. The other key aspect is to choose the appropriate band alignment at the heterojunction that can promote charge separation to improve accessibility and reduce carrier recombination.[13,14] In this regard, our $CsPbX_3/Pb_4S_3Y_2$ (X, Y = Cl, Br, I) perovskite-chalcohalide epitaxial HSs appeared to be promising for photocatalytic applications since the intimate coupling of these two semiconductors and the quasi-type II band alignment promote efficient charge separation upon illumination.[10]

It is noteworthy to highlight that the HSs based on lead halide perovskites have recently emerged as promising photocatalysts,[15,16,17] as they combine tunable band gaps[18,19] and the intrinsic defect tolerance[20] of $CsPbX_3$ with the additional electronic tunability of the heterojunctions. Indeed, significant progress has been reported in the use of $CsPbBr_3$ nanocrystals as photocatalysts for organic transformations.[21–25] However, to further enhance their performance, especially considering their intrinsic instability under heat and humidity,[26] several key aspects must be taken into account, including charge-carrier dynamics and the surface reaction kinetics occurring at the nanocrystals interface. A highly effective strategy consists in coupling perovskite photocatalysts with a secondary semiconductor, enabling improved surface reaction rate through advanced configurations such as Type II[27] or Z-scheme.[28] In this picture, also the perovskite-chalcohalide HSs were recently employed for CO_2 photoreduction by Pradhan at al.[29] They demonstrated that $CsPbBr_3/Pb_4S_3Br_2$ HSs outperform simple $CsPbBr_3$ nanocrystals due to suppressed radiative recombination and efficient charge transfer across the heterojunction.[29]

However, the use of these HSs in organic transformations occurring in non-polar media remains largely unexplored. To address this gap, we systematically investigate the band alignment of three different $CsPbX_3/Pb_4S_3Y_2$ (X, Y = Cl, Br, I) HSs, as interfacial energy level matching is crucial to design an effective photocatalyst for specific target reactions. Based on this knowledge, the oxidative coupling of thiophenols into disulfides was selected as a *proof-of-concept* reaction to directly assess how the use of a semiconductor-semiconductor heterostructure catalyst enhances the photocatalytic performance. This model transformation was chosen not only for the growing interest in disulfides synthesis[30,31] in organic chemistry[32,33], biochemistry[34,35], and industry,[36,37] but, crucially, because the explanation of its reaction mechanism provides a platform to demonstrate the higher performances of engineered heterojunctions over single-phase nanocrystals. Compared to conventional methods, this photocatalytic approach offers a milder and more sustainable alternative,[38] avoiding over-oxidation and simplifying purification.[39]

To assess the photocatalytic activity of the $CsPbX_3/Pb_4S_3Y_2$ HSs in the oxidation of *p*-thiophenols we compared their reactivity against their individual components ($CsPbX_3$ and $Pb_4S_3X_2$ NCs). Among all HSs we tested, the $CsPbBr_3/Pb_4S_3Br_2$ HSs revealed the highest yield (81%) and selectivity (87%), outperforming stand-alone nanocrystals and suggesting efficient charge separation at the interface. These results were obtained in only 90 minutes upon 450 nm

illumination, a significantly shorter time than previous studies with perovskite-based photocatalyst.[38] These results underscore the pivotal role of heterojunction configuration in promoting charge separation and boosting photocatalytic efficiency. Moreover, the interactions between the substrate and the HSs surface were investigated. In addition, the reactive species involved in the formation of intermediates were analyzed using various trapping agents (electron and hole scavengers) in order to elucidate the plausible photocatalytic mechanism.

5.2 Synthesis of $CsPbX_3/Pb_4S_3Y_2$ heterostructures

The first protocol developed for the synthesis of $CsPbBr_3/Pb_4S_3Br_3$ HSs relied on perovskite nanoclusters[40] as precursors. These clusters are sub nanometer size and have an exciton absorption peak at 402 nm, they are non-emissive at room temperature. They have been used as convenient "monomer" for perovskite nanocrystals as it is possible to achieve better control over size and shape. For the heterostructures synthesis, the nanoclusters were reacted with a sulfur in octadecene (S-ODE) and a 1-dodecanthiol (DDT) solution at 200 °C, the reaction took place for 3 minutes to obtain the product.[10] Such protocol, while producing heterostructures with well-controlled morphology, has a low reaction yield, thus preventing extensive testing, that is needed for photocatalysis.

Therefore, we optimized an alternative published protocol,[29] based on the reaction of pre-formed $CsPbBr_3$ nanocrystals with lead oleate, 1-dodecanthiol, and sulfur dissolved in 1-octadecene. This approach significantly increases the yield (130 mg/batch), albeit at the cost of a less controlled morphology and a higher fraction of stand-alone $CsPbBr_3$ nanocrystals (≈ 20-25 %, quantified by analyzing more than 500 NCs from TEM images). Figure 5.1a shows the synthetic workflow followed to obtain the HSs. This could be divided in two steps, the first one involving the synthesis of $CsPbX_3$ nanocrystals and the second one the synthesis of the heterostructures. $CsPbX_3$ nanocrystals are synthetized *via* hot-injection method; briefly, PbX_2 salts are reacted with surfactants such as oleic acid and oleylamine using 1-octadecene as a solvent. Once the salt is solubilized, the Cs-oleate solution is injected at high temperature to trigger the nanocrystals nucleation. Then, the system is let under stirring at room temperature for 5 minutes to let it stabilize. After that, without performing any kind of purification, the crude solution is heated up until 220 °C and the precursors of the chalcohalides are injected.

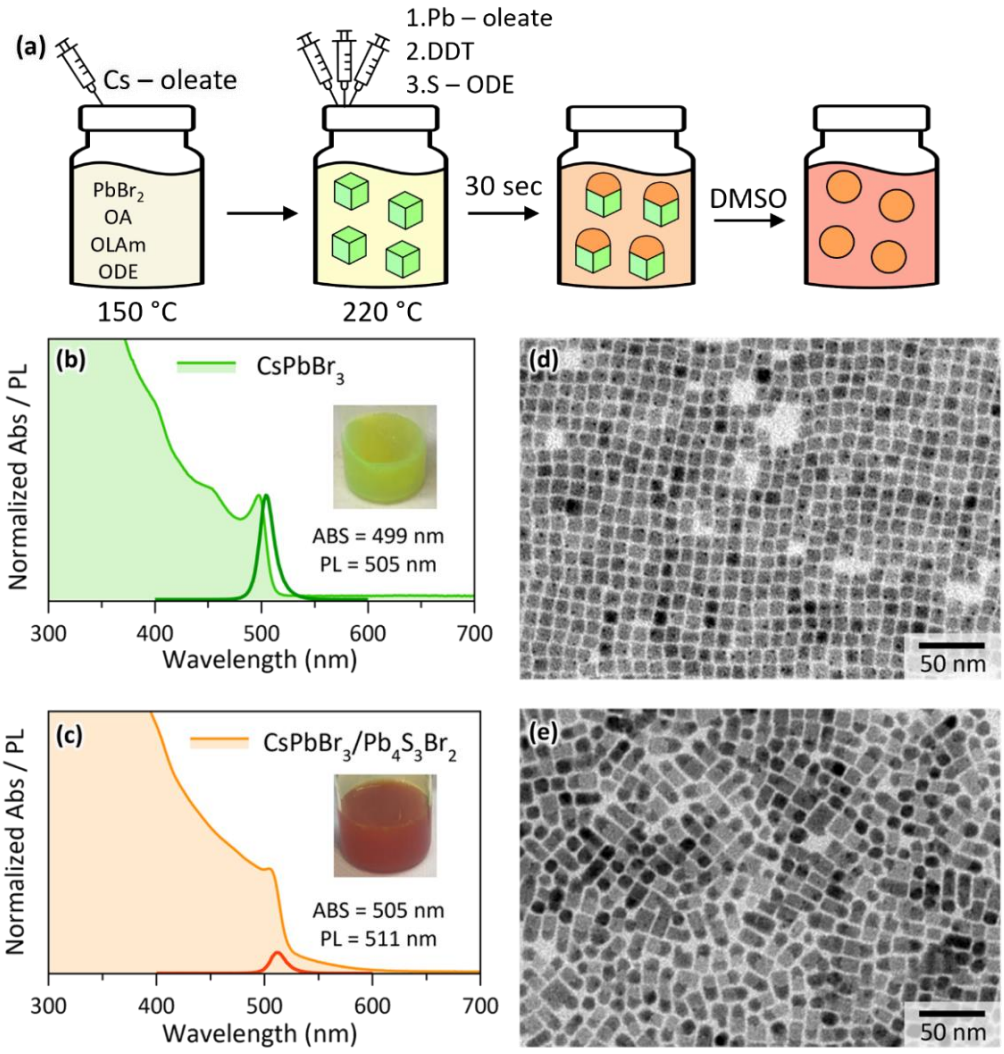

Figure 5.1. Reaction scheme, optical characterization, and TEM images of $CsPbBr_3$ NCs and $CsPbBr_3/Pb_4S_3Br_2$ HSs. a) Scheme of the synthetic route used to obtain $CsPbBr_3$ NCs and $CsPbBr_3/Pb_4S_3Br_2$ HSs, followed by the selective etching of the perovskite domain to isolate free-standing $Pb_4S_3Br_2$ NCs. b) Absorption and PL spectra of $CsPbBr_3$ NCs synthetized at 150 °C prior to the growth of the chalcohalide domains. c) Absorption and PL spectra of $CsPbBr_3/Pb_4S_3Br_2$ HSs after the growth of the chalcohalide domains. The PL was acquired with the same dilution factor and conditions of panel (b) and shows a marked reduction in intensity compatible with the formation of the HSs, which are known to suppress the PL of the $CsPbBr_3$ domain. d) TEM images of the same $CsPbBr_3$ NCs. e) TEM images of $CsPbBr_3/Pb_4S_3Br_2$ HSs. Adapted with permission from ref 58. Licensed under CC-BY 4.0. Copyright © 2025 The Authors.

After 30 seconds the reaction is quenched by immersing the flask in an ice water bath. The heterostructures are purified via centrifugation and collected in

toluene. "Free standing" $CsPbX_3$ nanocrystals, used later as reference, were obtained by interrupting the synthesis after the first step, while $Pb_4S_3Y_2$ nanocrystals were recovered by selective etching of the perovskite domain in the corresponding heterostructures using dimethyl sulfoxide (DMSO), as discussed later in the chapter.[41]

Figure 5.1b-c show the typical optical absorption spectra of the isolated NCs and HSs for the X=Y=Br case, with characteristic absorption features of the perovskite highlighted in green. As expected, the HSs absorption spectrum combines both features of the free-standing nanocrystals. In this picture, compared to the $CsPbBr_3$ NCs, the heterostructures exhibited an additional absorption tail at long wavelengths, which became more prominent for wavelengths shorter than 550 nm. This feature can be attributed to the presence of the chalcohalides domain. The $CsPbBr_3$ NCs evidenced the typical narrow PL peak at 505 nm, as depicted in Figure 5.1b. The formation of the heterostructures led to a remarkable suppression of the perovskite's emission, as discussed in detail later. The much weaker emission from the HSs can be ascribed to the presence of free standing $CsPbBr_3$ NCs in the sample. Representative TEM images of the samples are displayed in Figure 5.1d-e (see Figures 5.8-9 for additional characterization). By comparing the positions of the absorption features and TEM images before and after the growth of the chalcohalide, one can note an enlargement of the $CsPbBr_3$ domains, whose average size increases from 9.1 nm to 11.7 nm. This is likely due to the reaction of some of the additional Pb-oleate with unreacted Cs^+ present in the reaction environment.

The presence of two independent semiconductor domains allows some tuning of the band gap to a specific target reaction, in principle expanding the scope of HSs as photocatalysts. For instance, $CsPbCl_3/Pb_4S_3Cl_2$ heterostructures (Figure 5.2a-b) were successfully synthesized by replacing $PbBr_2$ with $PbCl_2$ and increasing the injection temperature for the $CsPbCl_3$ nanocrystals to 185 °C. At lower injection temperatures, only platelet-like nanoparticles were obtained (Figure 5.10, Appendix), under which conditions the nucleation and growth of the secondary $Pb_4S_3Cl_2$ domain did not occur. Notably, the system exhibits multiple analogies to the bromide-based heterostructures. First, as shown in Figure 5.11 (Appendix), the $CsPbCl_3/Pb_4S_3Cl_2$ HSs also display a red shift of the perovskite absorption band edge upon heterostructure formation. This effect can again be attributed to the presence of excess Pb-oleate in the reaction mixture, which may react with Cs^+ and promote an increase in the size of the perovskite domain. From a spectroscopic perspective, a pronounced quenching of the photoluminescence (PL) signal is also

observed. Figure 5.12 (Appendix) reports the representative X-ray diffraction (XRD) patterns of the three samples: $CsPbCl_3$ NCs, $Pb_4S_3Cl_2$ NCs and $CsPbCl_3/Pb_4S_3Cl_2$ HSs, where the contribution of $Pb_4S_3Cl_2$ to the HSs pattern remains minor due to its significantly lower volume fraction relative to $CsPbCl_3$, as well as the broader distribution of diffracted intensities over a larger number of reflections arising from its lower structural symmetry.

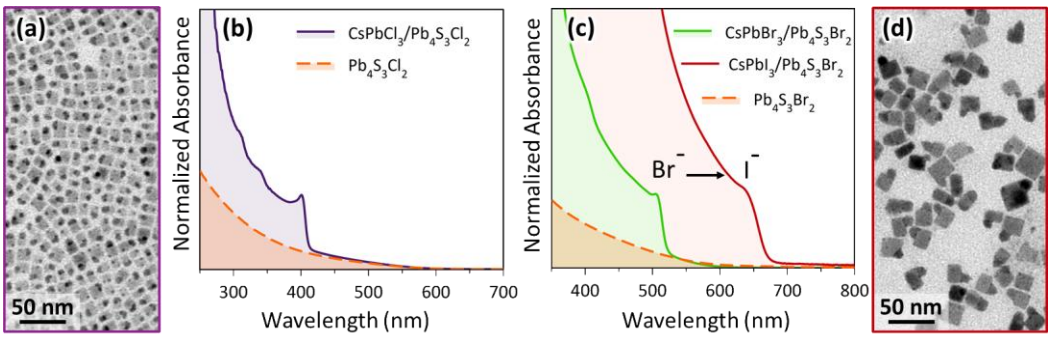

Figure 5.2. Synthesis of Cl-/I-based HSs. a) TEM images of $CsPbCl_3/Pb_4S_3Cl_2$ HSs. b) Absorption spectra of $CsPbCl_3/Pb_4S_3Cl_2$ HSs (purple line) and $Pb_4S_3Cl_2$ chalcohalides NCs (orange line). c) Absorption spectra of $CsPbBr_3/Pb_4S_3Br_2$ HSs (green line), $CsPbI_3/Pb_4S_3Br_2$ HSs after anion exchange (red line) and $Pb_4S_3Br_2$ chalcohalides NCs (orange line). d) TEM images of $CsPbI_3/Pb_4S_3Br_2$ HSs after anion exchange. Adapted with permission from ref 58. Licensed under CC-BY 4.0. Copyright © 2025 The Authors.

Conversely, the direct synthesis of $CsPbI_3/Pb_4S_3I_2$ HSs was unsuccessful, probably due to the increased lattice mismatch of $CsPbI_3/Pb_4S_3I_2$ compared to the Br- and Cl-analogues. However, $CsPbI_3$-based HSs can still be obtained via halide exchange from $CsPbBr_3/Pb_4S_3Br_2$ HSs, as shown by some members of the group in a previous work.[10] Due to the low ionic mobility in the chalcohalide domain, such reaction primarily affects the perovskite domain,[10] resulting in $CsPbI_3/Pb_4S_3Br_2$ HSs (Figure 5.2c-d, Figure 5.13). The exchange was tracked by the redshift of the perovskite absorption onset, while the contribution from the chalcohalides domain remained essentially unchanged (Figure 5.2c).

5.2.1 Etching the perovskite domain

Chalcohalide nanocrystals were later used as reference materials. For this reason, the heterostructures were employed as templates to first promote the nucleation of the desired chalcohalide phase and the perovskite domain was subsequently etched, exploiting the solubility of $CsPbX_3$ nanocrystals in polar solvents such as dimethyl sulfoxide (DMSO). This approach is particularly

important for the chloride-based heterostructures, as the direct synthesis of the chalcohalide phase leads to the formation of the monoclinic $Pb_3S_2Cl_2$ phase instead of the desired orthorhombic $Pb_4S_3Cl_2$.[9] Furthermore, the $Pb_3S_2Cl_2$ crystal structure differs significantly from that of the other $Pb_4S_3X_2$ compounds, to the extent that epitaxial compatibility with the $CsPbX_3$ perovskite would be lost. Therefore, the lead sulfochloride ($Pb_4S_3Cl_2$) phase can only be obtained through etching of the corresponding $CsPbCl_3$-based heterostructure.[41]

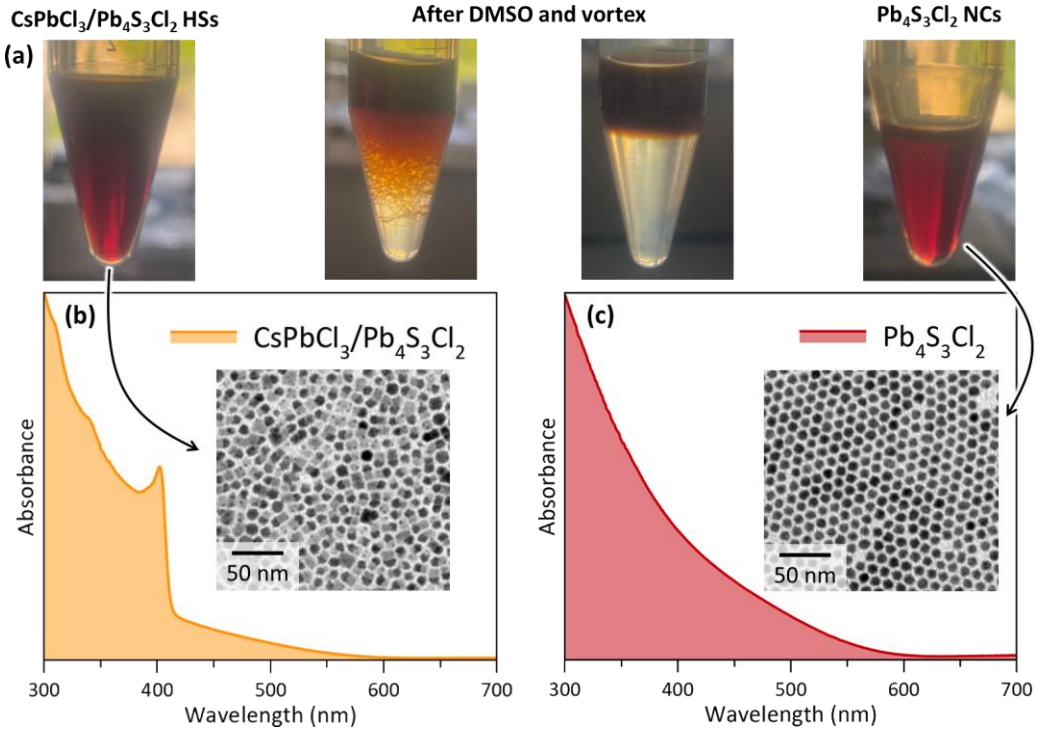

Figure 5.3. Pictures of selective perovskites etching, absorbance and TEM images of $CsPbCl_3/Pb_4S_3Cl_2$ HSs before and after etching. a) Pictures of heterostructures sample before and after the addition of DMSO to etch the perovskites domain. b) Absorbance spectrum of $CsPbCl_3/Pb_4S_3Cl_2$ HSs before addition of DMSO, inset: TEM images of HSs. c) Absorbance of the resulting $Pb_4S_3Cl_2$ NCs, inset: TEM images of the NCs. Reprinted with permission from ref 58. Licensed under CC-BY 4.0. Copyright © 2025 The Authors.

As shown in Figure 5.3a, to etch the perovskite domain, a solution of heterostructures in hexane is first centrifuged at low rpm to remove aggregates and obtain a clear and homogeneous solution, ensuring uniform and effective etching. Subsequently, the hexane dispersion of heterostructures is mixed with DMSO and 60 µL of oleylamine to maintain the colloidal stability of the nanocrystals. The mixture is vortexed for approximately 60 seconds, and after a few minutes, phase

separation occurs due to the mutual insolubility and density difference between hexane and DMSO. The upper hexane layer, which appears red due to the presence of chalcohalide nanoparticles, is collected, while the lower DMSO layer is discharged. Finally, the hexane fraction is washed with ethyl acetate to precipitate the nanoparticles, which are then collected by centrifugation and redispersed in hexane.

The absorbance spectrum (Figure 5.3.b-c) after the DMSO treatment no longer shows the feature related to $CsPbX_3$, attesting to the complete etching of the perovskite phase. Moreover, after the etching, the chalcohalide phase appears as spherical particles, even if only half of the sphere is visible in the TEM images of the heterostructures (insets of Figure 5.3.b-c). This phenomenon can be ascribed to the fact that, during the process, the more faceted (squared) portion of the chalcohalide phase tends to rearrange, evolving toward a more spherical geometry. In addition, this phase intrinsically tends to nucleate in the form of spherical particles. The reshaping is likely driven by material diffusion and mass transport during the procedure, which favor configurations with lower surface energy. As a result, high-energy facets are minimized, leading to the observed spherical morphology. Furthermore, the colloidal stability was preserved thanks to the addition of surfactants like oleylamine and oleic acid.

5.3 Band Alignments of $CsPbX_3/Pb_4S_3X_2$ Heterostructures Families

The combination of these synthetic strategies enables to cover the whole visible spectrum with the family of $CsPbX_3/Pb_4S_3X_2$ HSs. The band alignments and redox properties of the "free standing" nanocrystals ($CsPbX_3$ and $Pb_4S_3X_2$) were characterized by combining optical absorption spectroscopy, to determine the optical band gap, with ultraviolet photoelectron spectroscopy (UPS) and ambient pressure photoemission spectroscopy (APS) to establish the position of the valence band (VB) edge with respect to the vacuum level.

In the case of $CsPbBr_3$ the valence band is found at -5.80 eV, and the optical band gap estimation (2.38 eV) through the Tauc plot (Figure 5.4a-b) allows to derive the position of the conduction band at -3.40 eV. The same measurements were performed for the chloride based perovskite ($CsPbCl_3$) (Figure 5.4c-d), in both cases the results agree with the rich literature reports on the band positions of $CsPbX_3$ nanocrystals.[42] Instead, for the chalcohalides nanocrystals, very limited experimental data are available in literature.[41,9]

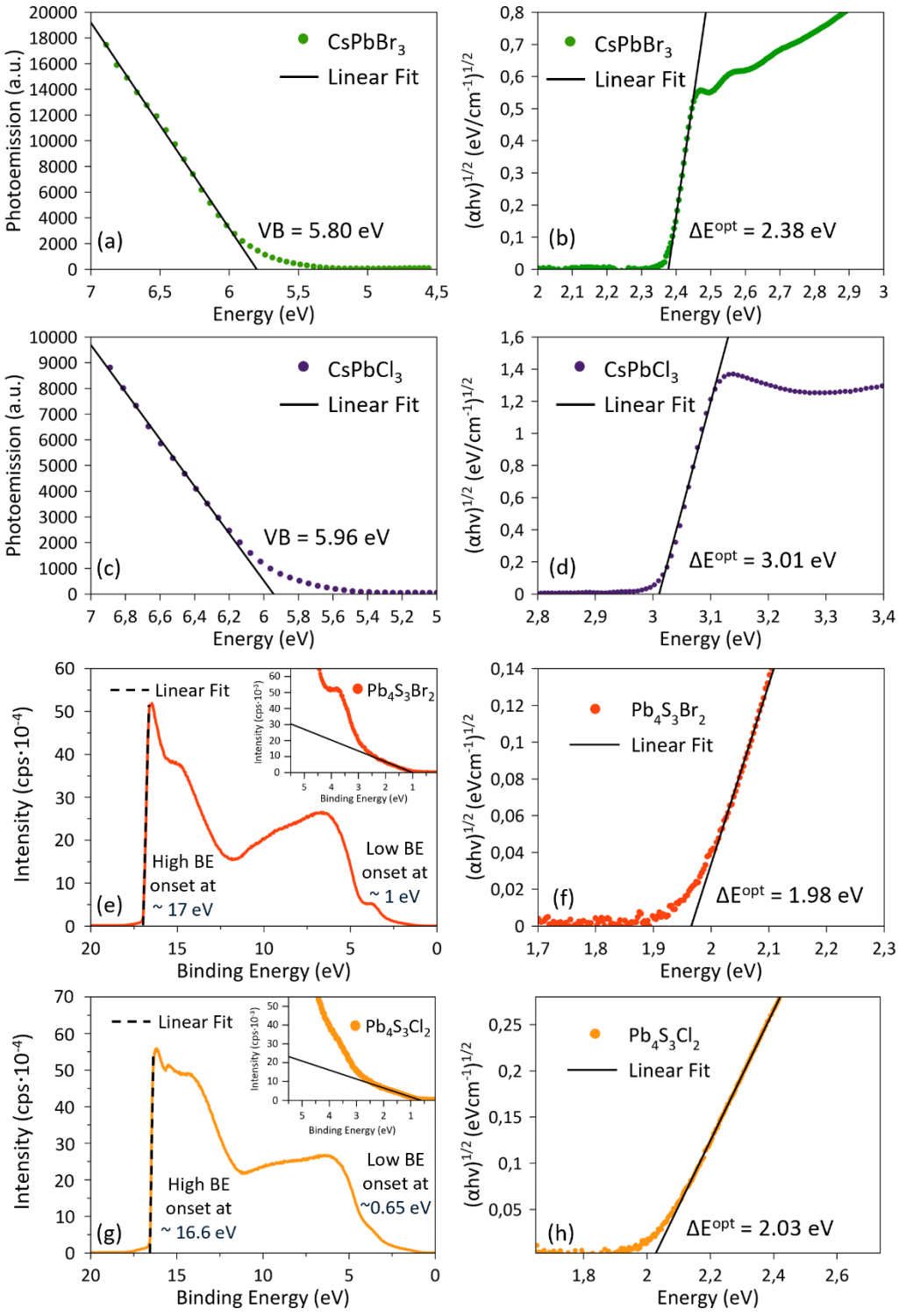

Figure 5.4. Ambient Pressure Photoemission Spectroscopy (APS), Ultraviolet Photoelectron Spectroscopy (UPS) and Tauc plot for $CsPbX_3$ and $Pb_4S_3X_2$ (X = Br, Cl) NCs. a) Photoemission of $CsPbBr_3$ NCs, used to determine the valence band of the

material. b) Tauc plot from the absorbance spectrum of $CsPbBr_3$ NCs, used to determine the optical band gap of the material. c) Photoemission of $CsPbCl_3$ NCs, used to determine the valence band of the material. d) Tauc plot from the absorbance spectrum of $CsPbCl_3$ NCs, used to determine the optical band gap of the material. e) UPS data used to determine the valence band of $Pb_4S_3Br_2$ NCs. f) Tauc plot from the absorbance spectrum of $Pb_4S_3Br_2$ NCs, used to determine the optical band gap of the material. g) UPS data used to determine the valence band of $Pb_4S_3Cl_2$ NCs. h) Tauc plot from the absorbance spectrum of $Pb_4S_3Cl_2$ NCs, used to determine the optical band gap of the material. Adapted with permission from ref 58. Licensed under CC-BY 4.0. Copyright © 2025 The Authors.

Our results confirm the current computational predictions,[9,10] for which the band gap is around 2 eV. For both chalcohalides phase was performed an X-ray photoelectron spectroscopy (XPS) analysis to further confirm the stoichiometry and elemental percentage of each compound (Figure 5.14a-b, Appendix). From the ultraviolet photoelectron spectroscopy (UPS) measurements, we found the valence band of $Pb_4S_3Br_2$ at 1.0 eV ± 0.1 eV eV vs Fermi Level, since the work function is 4.3 eV, the valence band vs vacuum level is at 5.23 eV (Figure 5.4e). At the same time, the Tauc Plot of $Pb_4S_3Br_2$ NCs, shown in Figure 5.4f, reveals an optical band gap of 1.98 eV, in agreement with DFT data. Concerning the $Pb_4S_3Cl_2$ UPS data, the valence band is found at 0.65 eV vs Fermi Level, since the work function is 4.67 eV, the valence band vs vacuum level is at 5.32 eV (Figure 5.4g). Also in this case the Tauc Plot (Figure 5.4h) allows to obtain the position of the conduction band. This result highlights that the band gap of lead chalcohalides (both $Pb_4S_3Br_2$ and $Pb_4S_3Cl_2$) is only minimally affected by the halide composition, likely due to the band edge states being predominantly derived from Pb^{2+} (conduction band) and S^{2-} (valence band) orbitals.[9]

From these measurements, it was possible to depict the overall band alignments picture for this family of compounds, as shown in Figure 5.5. Moreover, we confirmed the type-I and type-II band alignments predicted respectively for $CsPbCl_3/Pb_4S_3Cl_2$ and $CsPbBr_3/Pb_4S_3Br_2$ HSs, which explains the photoluminescence quenching observed in both systems. Notably, for the $CsPbBr_3/Pb_4S_3Br_2$ HSs the conduction band edges of the two materials are closely aligned in energy (–3.4 eV for $CsPbBr_3$ and –3.3 eV for $Pb_4S_3Br_2$), which facilitates electron delocalization across the whole HS.

According to the energy levels estimated for the $CsPbX_3/Pb_4S_3X_2$ HSs and the highest occupied molecular orbital HOMO value for thiophenol (–4.2 eV, calculated from cyclic voltammetry, Figure 5.15), the $CsPbBr_3/Pb_4S_3Br_2$ HSs present the optimal conditions to perform the photocatalytic reaction. These data

indicate that the electron transfer process from the HOMO of thiophenol to the hole of the $CsPbBr_3/Pb_4S_3Br_2$ HSs should be thermodynamically favorable.

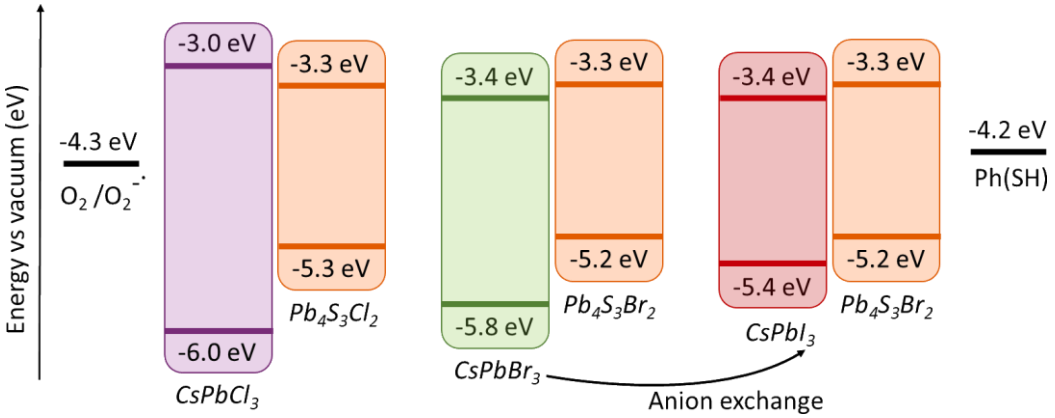

Figure 5.5. Band alignments of the different HSs families. Band alignments of the Valence Band (VB) and Conduction Band (CB) of different HSs with the highest-occupied molecular orbital (HOMO) of thiophenol (PhSH) and the reduction potential of O_2. Adapted with permission from ref 58. Licensed under CC-BY 4.0. Copyright © 2025 The Authors.

In the case of $CsPbCl_3/Pb_4S_3Cl_2$ HSs, the type-I alignment would lead to a competitive non-radiative recombination in the chalcohalide domain, limiting charge separation, while $CsPbI_3/Pb_4S_3Br_2$ HSs require an additional halide exchange step in the synthesis without offering sensible advantage over the $CsPbBr_3/Pb_4S_3Br_2$ HSs band alignment for this reaction. The redox properties of the systems, together with additional factors such as substrate-surface interactions, the nature of the photocatalyst, and colloidal stability collectively contribute to defining the photocatalytic behavior of the $CsPbX_3/Pb_4S_3X_2$ HSs. Each of these variables will be discussed in detail in the next paragraphs.

5.4 Photocatalytic Activity of $CsPbX_3/Pb_4S_3X_2$ HSs for thiophenol coupling

Based on these considerations, we selected as a benchmark the photooxidation of PhSH (1a) catalyzed by $CsPbBr_3/Pb_4S_3Br_2$ HSs under 450 nm LED excitation. Reactions were carried out in a custom-designed high-throughput screening photoreactor (see methods and Photograph 1), in aerobic conditions and without the use of an external sacrificial electron donor, as discussed in detail later. The product

yield of diphenyl disulfide (1b) was determined by gas chromatography coupled with mass spectrometry (GC-MS).

5.4.1 Role of the solvent

The polarity of the solvent can affect the conformation of the ligands bound to the nanocrystals, thereby either facilitating or limiting selective photo transformations by modulating the degree of available space close to the particles surface. The kinetics of the catalytic process may be controlled by the diffusion coefficient of the substrate through the NC-ligand interface and by the solvation free energy, the latter arising from both ligand-substrate and solvent-substrate interactions.

Indeed, preliminary solvent screening led to determine that the highest product yield was obtained using cyclohexane as a solvent (81%, Table 5.1, see also Scheme 5.1, Table 5.6 and Figure 5.16). Cyclohexane outperformed hexane, likely due to structural features that enhance solvation of both nanoparticles and substrate, improving photocatalyst-substrate interactions.[43,44] A mixture of CH_2Cl_2 with cyclohexane (1:1) resulted in high chemical yield (76%) but lower selectivity, which is unfavorable for further photocatalytic investigations. In contrast, the photoreaction carried out in CH_2Cl_2 yielded even lower yield (33%, Table 1). This was attributed to the partial anion exchange between Br^- in the perovskite domain and Cl^- ions from CH_2Cl_2 as a result of the C-Cl bound cleavage promoted by the perovskites, as previously reported by Wu et al. (Figure 5.17).[38]

These results highlight that the kinetics of the reaction depends also on substrate diffusion through the NC-ligand interface and solvation free energy, the latter governed by ligand-substrate and solvent–substrate interactions.[45] The solvent has a significant role in the photoreaction by likely modulating the substrate adsorption onto the NCs surface and consequently the S-S bond formation. Here, solvent effects emerged as a critical determinant of catalytic efficiency.

Scheme 5.1. Standard conditions for the oxidative coupling of *p*-substituted thiophenols.

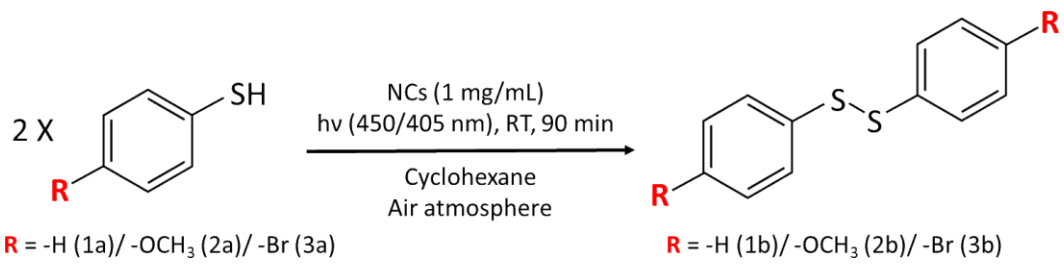

Table 5.1. Standard conditions using different solvents for the coupling of the thiophenol.

Entry[a]	Solvent	Conversion (%)	Yield of 1b (%)	Selectivity (%)
1	Cyclohexane	93.0	81	87
2	Cyclohexane: CH_2Cl_2 (1:1)	98.0	76	76
3	Hexane	88.0	57	65
4	CH_2Cl_2	100.0	33	33

[a] Conditions: thiophenol (0.034 mmol), $CsPbBr_3/Pb_4S_3Br_2$ HSs (1 mg) in 1 mL of solvent after 90 min of irradiation (λ_{max} = 450 nm) at 20 °C under air atmosphere. Yields are determined by GC-MS using biphenyl as internal standard.

5.4.2 Photocatalytic properties of $CsPbBr_3/Pb_4S_3Br_2$ HSs

The photocatalytic activity of the HSs was compared with single-component $CsPbBr_3$ and $Pb_4S_3Br_2$ nanocrystals, using 1 mg of photoactive material in all the photoreactions (calculated by TGA analysis Figure 5.18). Although both HSs and single-component NCs can photocatalyze the reaction (Table 5.2), given their band alignment and the oxidation potential of thiophenol, both product yield and selectivity were significantly improved for $CsPbBr_3/Pb_4S_3Br_2$ HSs. This can be ascribed to the effective charge separation induced by the electronic junction in the HSs. Control experiments conducted in the absence of the photocatalyst, or light resulted in only 2% or 10% of **1b**, respectively, further confirming the photocatalytic activity of the HSs under visible-light in aerobic conditions. The turnover number (TON) and turnover frequency (TOF) were determined according to the method previously reported by Rosa-Pardo *et al.*[46] The HSs exhibited the highest photocatalytic performance, with a TON of 14300 and a TOF of 9560; while significantly lower values were obtained for the $CsPbBr_3$ (TON = 3680; TOF = 2460) and $Pb_4S_3Br_2$ nanocrystals (TON = 2070; TOF = 1380).

Table 5.2. Standard conditions using different photocatalysts (bromide based) for the coupling of the thiophenol and *p*-substituted thiophenols.

Entry	Variance	-R	Photocat.	Conversion (%)	Product 1b (%)	Selectivity (%)
1	None	-H	$CsPbBr_3$ /$Pb_4S_3Br_2$	93.0	81 ± 1*	87
2	None	-H	$CsPbBr_3$	73.4	50 ± 4*	72
3	None	-H	$Pb_4S_3Br_2$	71.6	59 ± 4*	86
4	Without photocatalyst	-H	-	19	2	-
5	Without light	-H	$CsPbBr_3$ /$Pb_4S_3Br_2$	51	10	-
6	Without light	-H	$CsPbBr_3$	45	4	-
7	Without light	-H	$Pb_4S_3Br_2$	40	7	-
8	In nitrogen	-H	$CsPbBr_3$ /$Pb_4S_3Br_2$	61	22	-
9	In nitrogen	-H	$CsPbBr_3$	40	2	-
10	In nitrogen	-H	$Pb_4S_3Br_2$	40	5	-
11	None	-OCH_3	$CsPbBr_3$ /$Pb_4S_3Br_2$	100	94	94
12	None	-OCH_3	$CsPbBr_3$	100	86	86
13	None	-OCH_3	$Pb_4S_3Br_2$	100	93	93
14	None	-Br	$CsPbBr_3$ /$Pb_4S_3Br_2$	92	61	66
15	None	-Br	$CsPbBr_3$	99	53	53
16	None	-Br	$Pb_4S_3Br_2$	93	44	47

*Obtained by triplicate measurements.

Collectively, these results demonstrate that the heterostructures outperform their single-component counterparts in the photocatalytic oxidative coupling of

thiophenol, owing to enhanced charge separation and improved charge availability enabled by the heterojunction.

To investigate the influence of the electronic properties of para-substituents on thiophenol reactivity, we selected two representative substrates: 4-bromothiophenol and 4-methoxythiophenol, bearing either an electron-withdrawing (-Br) or electron-donor (-OCH_3) groups, respectively. As shown in Table 5.2, the product yields for both substrates were again higher when using the HSs than when using the single-component $CsPbBr_3$ and $Pb_4S_3Br_2$ NCs. Notably, with 4-methoxythiophenol the yield of **2b** was ca. 94 % (Figure 5.19, Table 5.2, entry 11).

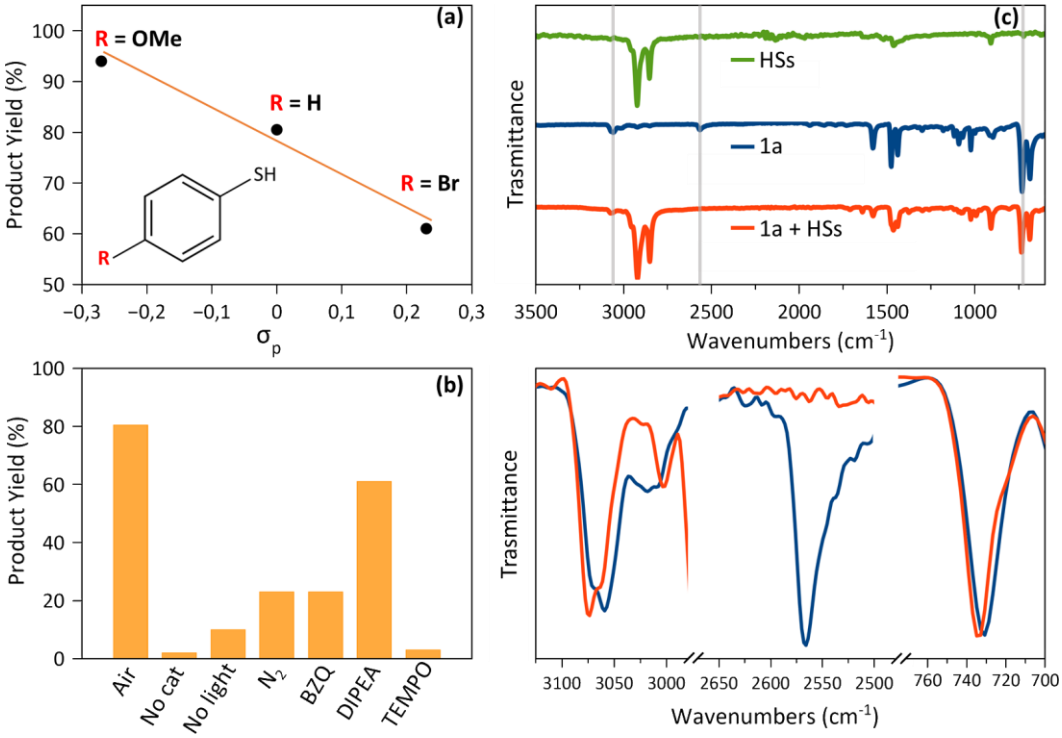

Figure 5.6. Evaluation of different *p*-substituted thiophenols, different reaction conditions tested and interaction photocatalyst/substrate. a) Correlation between the electronegativity of the -R substituent on thiophenol and the disulfide yield. b) Product yield obtained from photocatalytic reactions tested under different conditions and in the presence of radical anion, holes, and radical scavengers. c) Top: FTIR spectra of $CsPbBr_3/Pb_4S_3Br_2$ HSs (green trace), 1a-thiophenol (blue trace), and the mixture between $CsPbBr_3/Pb_4S_3Br_2$ HSs with 1a-thiophenol (red trace). Bottom: Zoom of selected FTIR stretching regions highlighting differences between thiophenol (blue trace) and the HSs-

thiophenol mixture (red trace). Reprinted with permission from ref 58. Licensed under CC-BY 4.0. Copyright © 2025 The Authors.

This result is consistent with the electron-donating nature of the -OCH_3 group, which increases the electron density of the aromatic ring, thereby enhancing its reactivity. Conversely, the -Br substituent, being more electron-withdrawing, makes the aromatic ring more electron-deficient, resulting in lower reactivity (Figure 5.20, Table 5.2, entry 14). The substituent effect on product yield aligns with theoretical correlations between the electronic properties of *p*-substituted thiophenols, thiyl radical stability, and S-H bond dissociation energy.[47] Electron-donating groups stabilize the thiyl radical by reducing the spin density at the sulfur atom, explaining the highest yield with *p*-OCH_3-thiophenol (Table 5.2). Figure 5.6a shows a clear correlation between the substituent's sigma value (σ_p)[48] and product yield for $CsPbBr_3/Pb_4S_3Br_2$ HSs, consistent with expected electronic effects.

5.4.3 Photocatalytic mechanism

To elucidate the photocatalytic mechanism, several experiments with active trapping species were performed, employing 1,4 benzoquinone (BZQ)[49,50], *N,N*-diisopropylethylamine (DIPEA),[51] and 2,2′,6,6′-tetramethylpiperidine-1-oxyl (TEMPO), as shown in Figure 5.6b and summarized in Table 5.3. BZQ, a well-known scavenger of superoxide anion ($O_2^{\cdot-}$), afforded **1b** in 23% yield, which closely matches the yield observed under anaerobic conditions (N_2 atmosphere). Conversely, DIPEA, which is a hole (h^+) scavenger, led to a moderate reduction in yield (61%), suggesting that photogenerated holes also contribute, albeit to a lesser extent, to the oxidation of thiophenol.

Table 5.3. Standard conditions using different scavengers and $CsPbBr_3/Pb_4S_3Br_2$ HS as photocatalyst for the coupling of the thiophenol.

Entry	Scavenger	Variance	Conversion (%)	Product 1b (%)
1	BZQ	None	97	23
2	DIPEA	None	99	61
3	TEMPO	None	100	3
4	TEMPO	N_2	100	3

Although these findings show that the superoxide anion is one of the main active species in the aerobic oxidation of thiophenols, the participation of photogenerated holes should also be highlighted (as discussed below). When the reaction was performed in the presence of TEMPO[54,55] as radical scavenger, under both aerobic and anaerobic conditions, only negligible amounts of product were obtained (Figure 5.6b), indicating that a free radical process was involved in the reaction. To further identify the radical intermediate, GC-MS analyses were performed after the reaction in both atmospheres and the TEMPO-PhS adduct was identified (Figure 5.21), confirming the production of thiyl radical as intermediate to deliver the disulfide products.

The surface chemistry of the photocatalyst also plays an important role in the photocatalytic activity of the system. The possible thiophenol adsorption onto the nanocrystals' surface was analyzed by Fourier-transform infrared spectroscopy (FTIR): the $CsPbBr_3/Pb_4S_3Br_2$-PhSH mixture spectrum was compared with those of the individual components, that is, the heterostructures and thiophenol alone (Figure 5.6c top). The $CsPbBr_3/Pb_4S_3Br_2$-PhSH mixture displays the typical Pb-S stretching at 800 cm^{-1},[38] while the S-H band at 2565 cm^{-1} is absent, indicating the interaction between thiophenol and the HSs. The C-S stretching, in the fingerprint zone, shifts from 730 to 735 cm^{-1}, and the C-H stretching at 3050 cm^{-1} shifts to higher energy ($\Delta\nu$ =14 cm^{-1}), reflecting changes in the chemical environment (Figure 5.6c down). Similar shifts were observed for mixtures of PhSH and "free standing" NCs ($CsPbBr_3$ and $Pb_4S_3Br_2$) and in the case of the *p*-Br thiophenol and *p*-OCH_3 thiophenol (Figure 5.22). Comparable shifts toward higher energy have been previously observed for the interaction of anchoring groups from functional organic molecules in proximity to the surface of perovskite nanocrystals, such as the C=O group in terephthalic acid[52] or the N−H moiety in benzylamine.[53] Collectively, these data support the adsorption of the different substrates onto the surface of the photocatalyst, suggesting that this interaction may facilitate the organic transformation.

The proposed mechanism for the photooxidation of *p*-substituted thiophenols under both aerobic and anaerobic conditions is represented in Figure 5.7. Once the contact between the photocatalyst and the substrate is established, upon visible-light illumination, the photogenerated holes migrate toward the $Pb_4S_3Br_2$ domain, while electrons are delocalized across the conduction band of the HS, thanks to quasi-type II band alignment. This partial charge separation, as discussed in Chapter 3, can reduce charge recombination, and thus enhance photocatalytic activity compared to the individual components (perovskite and chalcohalide).

Under aerobic conditions, two parallel pathways can occur to produce thiyl radicals: i) photogenerated electrons from the conduction band of the HS reduce O_2 to form the superoxide anion ($O_2^{\cdot -}$), which reacts with thiophenol molecule producing a thiyl radical (PhS·) and HO_2^-; and ii) photogenerated holes react directly with thiophenol: direct electron transfer from PhSH to the valence band of the HSs, forming also a thiyl radical (PhS·) and a proton (H^+). Subsequently, two thiyl radicals can couple to form the target disulfide product. As the intermediate HO_2^- is unstable, it can react with H^+ to produce H_2O_2. These findings confirm the cooperative activity of both photogenerated charge carriers (electrons and holes) under aerobic conditions to produce thiyl radicals, thus improving the photocatalytic activity in the heterostructures.

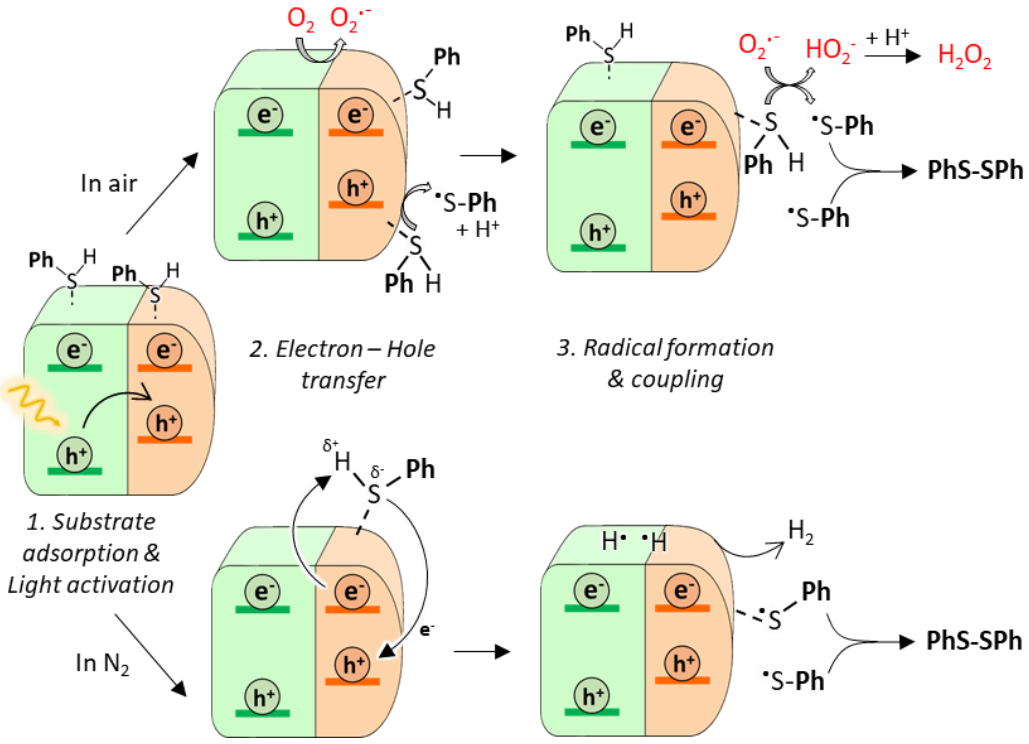

Figure 5.7. Possible reaction mechanism. Proposed photocatalytic mechanisms for the oxidative coupling of thiophenol under aerobic and anaerobic conditions. Adapted with permission from ref 58. Licensed under CC-BY 4.0. Copyright © 2025 The Authors.

However, under nitrogen atmosphere, there is only one pathway to produce thiyl radicals: the photogenerated electrons and holes interact with the thiophenol leading to the thiyl and hydrogen radicals, which after coupling produce the disulfide compound and molecular hydrogen (H_2), respectively. It is noteworthy

that the latter has been identified by gas chromatography (Figure 5.23). The plausible mechanism proposed under anaerobic conditions is consistent with previous observations of thiol photooxidation by $CsPbBr_3$ nanocrystals. [38]

The performance of the photocatalyst was evaluated after one photocatalytic cycle. XRD patterns recorded before and after the the reaction confirmed the preservation of crystallinity of the HSs (Figure 5.24a). The absorption spectrum of the $CsPbBr_3/Pb_4S_3Br_2$ HSs retained the characteristic band edge of the perovskite, with a sight red shift, although an increased scattering was observed (Figure 5.24b). This behavior could be attributed to the partial removal of surface ligands during the photocatalytic reaction, leading to some nanocrystal aggregation, as previously observed for the C-C coupling reactions using $CsPbBr_3$ nanocrystals as photocatalysts.[54] Although TEM images of the crude solution post-photoreaction (Figure 5.25) revealed significant aggregation in part of the sample, the composition of the heterostrucures was preserved. This aggregation is consistent with the observed changes in optical spectra and the absence of a sacrificial electron donor in the system.

5.4.4 Other $CsPbX_3/Pb_4S_3X_2$ heterodimers as photocatalysts

To further validate our initial selection criteria for the bromide based HS in the preparation of disulfide compounds, the photoreactions were performed also using mixed I/Br-HSs (Table 5.4) and Cl-HSs (Table 5.5). As shown in Table 5.4, the $CsPbI_3/Pb_4S_3Br_2$ HSs, obtained via anion exchange, delivered the coupling product in 80% yield for 2a, a value comparable to that obtained with the bromide-based system, consistent with a band alignment. Nonetheless, in all cases, a reduction in the selectivity was observed.

Table 5.4. Standard condition using different photocatalysts (I-based) for the coupling of the thiophenol and its derivates.

Entry	R substituent	Photocatalyst	Conversion (%)	Product (%)	Selectivity (%)
1	-H	$CsPbI_3/Pb_4S_3Br_2$	100	80	80
2	-H	$CsPbI_3$	86	52	61
3	$-OCH_3$	$CsPbI_3/Pb_4S_3Br_2$	100	83	83
4	$-OCH_3$	$CsPbI_3$	100	82	82

5	-Br	$CsPbI_3/Pb_4S_3Br_2$	100	64	64
6	-Br	$CsPbI_3$	100	60	60

In the case of $CsPbCl_3/Pb_4S_3Cl_2$ HSs the observed trend is consistent with the one found for the bromide analogue: the HSs outperform both pristine $CsPbCl_3$ and $Pb_4S_3Cl_2$, in terms of yield and selectivity. Using the $CsPbCl_3/Pb_4S_3Cl_2$ HSs a 70% recovery of the product was achieved for 2a, which is slightly lower than the 81% value obtained with the $CsPbBr_3/Pb_4S_3Br_2$ HSs. As anticipated, the Cl-HSs exhibited lower photocatalytic performances. We attribute this difference to the type I band alignment, where the non-radiavite recombination is promoted and the charge separation is limited.

Table 5.5. Standard conditions using different photocatalysts (Cl-based) for the coupling of the thiophenol and its derivates.

Entry	R substituent	Photocatalyst	Conversion (%)	Product (%)	Selectivity (%)
1	-H	$CsPbCl_3$ /$Pb_4S_3Cl_2$	99	70	70
2	-H	$CsPbCl_3$	99	47	47
3	-H	$Pb_4S_3Cl_2$	73	44	60
4	-OCH_3	$CsPbCl_3$ /$Pb_4S_3Cl_2$	99	86	86
5	-OCH_3	$CsPbCl_3$	76	54	71
6	-OCH_3	$Pb_4S_3Cl_2$	80	52	65
7	-Br	$CsPbCl_3$ /$Pb_4S_3Cl_2$	95	77	81
8	-Br	$CsPbCl_3$	87	62	71
9	-Br	$Pb_4S_3Cl_2$	71	27	38

All the results are presented and discussed in the publication.[58]

5.5 Conclusions

In conclusion, we developed an optimized direct synthesis for semiconductor/semiconductor HSs ($CsPbBr_3/Pb_4S_3Br_2$, $CsPbCl_3/Pb_4S_3Cl_2$) and $CsPbI_3/Pb_4S_3Br_2$ via post-synthetic anion exchange, achieving tens-of-milligrams yields, above typical literature reports, and enabling broader photocatalytic applications. Their chemical tunability allowed modulation of the band alignment, which was systematically studied through optical and spectroscopic methods. Using *p*-substituted thiophenol coupling to disulfide as a model, the HSs outperformed the corresponding "free-standing" nanocrystals. Under aerobic conditions, the combined action of photogenerated electrons and holes producing thiyl radicals enhanced the photocatalytic efficiency of the HSs compared to individual components, which was further improved by charge carrier separation at the heterojunction. This work establishes a versatile strategy for constructing semiconductor-semiconductor heterostructures. It demonstrates that heterojunction engineering, specifically, type II band alignment, controlled surface chemistry, and the cooperative participation of photogenerated charge carriers to produce intermediate radicals, is an effective approach for enhancing photocatalytic performances.

5.6 Methods

Chemicals

1-Octadecene (ODE, tech, 90%), oleic acid (OA, tech, 90%), oleylamine (OLA, tech, 70%), lead(II) bromide ($PbBr_2$, 98%), lead(II) chloride ($PbCl_2$, 98%), lead(II) iodide (PbI_2, 98%), cesium carbonate (Cs_2CO_3, 99%), 1-dodecanethiol (DDT, 99.9%), sulfur powder (S, 99.99%), lead acetate trihydrate ($Pb(OAc)_2 \cdot 3H_2O$, 99.99%), dimethyl sulfoxide (DMSO, 99.5%), were purchased from Sigma-Aldrich. All reagents were used as received without any further experimental purification.

Preparation of Cs-oleate Stock Solution

In a typical synthesis, 120 mg (0,37 mmol) of Cs_2CO_3 were mixed with 1.75 mL of OA and 15 mL ODE in 50 mL three-neck flask, dried for 1h at 110°C and then heated under N_2 to 150°C until the solution turned clear. Thereafter, the solution was transferred into N_2-filled glass vials. The solution is solid at room temperature and needs to be pre-heated before using it.

Preparation of $Pb(OA)_2$ Stock Solution

$Pb(OAc)_2 \cdot 3H_2O$ powder (0.38 g, 1 mmol) and OA (950 uL) were mixed with ODE (9.35 mL) in a 50 mL three-neck round-bottom flask. The reaction mixture was degassed under vacuum for 1 h at 110°C and then heated under N_2 to 150°C until all $Pb(OAc)_2 \cdot 3H_2O$ reacted with OA. Thereafter, the solution was cooled to room temperature (25 °C) and transferred into N_2-filled glass vials.

Preparation of S-ODE Stock Solution

1 mmol of S powder was mixed with 10 mL ODE (predegassed at 120°C for an hour) in a 20 mL glass. Then, the resulting mixture was sonicated until the complete dissolution of S (ca. 20 min).

Synthesis of $CsPbBr_3/Pb_4S_3Br_2$ HSs

A typical HS synthesis involves two steps, performed consecutively: synthesis of $CsPbBr_3$ nanocrystals and growth of $CsPbBr_3/Pb_4S_3Br_3$ HSs. In the first step, 72 mg of $PbBr_2$ are mixed with 5 ml of octadecene, 50 μL of oleic acid, and 500 μL of oleylamine inside a 20 mL glass vial, under nitrogen atmosphere. The mixture is

heated to 170°C to achieve the full solubilization of the powder, followed by the injection at 150°C of 500 µL of a Cs-oleate solution is injected to initiate the growth of perovskite nanocrystals (NCs). After 5 seconds, the reaction is quenched by immersion in a water bath. The reaction batch is then stirred for 5 minutes at room temperature without performing any purification. Subsequently, the vial is reheated to 220°C, and the precursors needed for the growth of the chalcohalide are injected: 800 µL of lead oleate, 32 µL of 1-dodecanethiol and 480 µL of sulfur-ODE. The reaction is allowed to proceed for 30 seconds before being quenched in an ice water bath. The crude solution is then centrifuged at 6000 rpm for 5 minutes to isolate the NCs. The precipitate is collected in hexane, followed by a second centrifugation at a 2000 rpm for 2 minutes to remove larger perovskite NCs that may have formed during the re-heating step. The precipitate is discarded, and the supernatant is kept for further use.

Synthesis of $CsPbCl_3/Pb_4S_3Cl_2$ HSs

The synthesis of Cl-based HSs follows the same protocol adopted for Br-based HSs, with the following adaptations: 1) 53 mg of $PbCl_2$ were used instead of $PbBr_2$ and the amount of oleic acid was increased to 500 µL to facilitate the dissolution of $PbCl_2$, 2) the first injection temperature was raised to 185°C, as lower temperature (150°C) resulted in a high number of platelets instead of nanoparticles. The procedure to obtain and purify the HSs is the same of the bromide-based sample.

Isolation of $Pb_4S_3X_2$ nanocrystals

Pure $Pb_4S_3X_2$ nanocrystals can be obtained by etching the perovskite domains of the corresponding $CsPbX_3/Pb_4S_3X_2$ HSs. First, a solution of HSs in hexane is centrifuged at 2000 rpm for 2 minutes to remove aggregates, which ensures uniform and effective etching. Subsequently, 1 mL of the HS solution in hexane is mixed with 1 mL of dimethyl sulfoxide and 60 µL of oleylamine. The mixture is vortexed for approximately 60 seconds. After a few minutes, phase separation occurs due to the mutual insolubility and density difference between hexane and dimethyl sulfoxide. The upper hexane layer, which appears red due to the presence of chalcohalide nanoparticles, is collected. After that, 4 mL of ethyl acetate and 60 µL of oleic acid are added to the hexane fraction to precipitate the particles, which are collected by centrifugation (6000 rpm for 5 minutes) and then redispersed in hexane or toluene for further use.

Anion exchange

The anion exchange reactions were performed under ambient conditions following previously reported methods.[10] First, a PbI_2 stock solution was prepared: 2 mmol of PbI2, 5 mL of OA and 5 mL of OLAm were mixed with 30 mL of ODE in a 100 mL three-neck flask. The reaction mixture was dried/degassed under vacuum for 30 min at 110°C. Then, the flask was filled with N_2, and the temperature was raised to 150°C. After complete dissolution of PbI_2 salt, the solution turned yellow and then cooled down to room temperature (25°C) and transferred into a N_2-filled glass vial. Then, 4 mL of the $CsPbBr_3$–$Pb_4S_3Br_2$ HSs in toluene was added into a 10 mL glass vial, and different amounts of PbI_2 stock solution (ranging from 300 uL to 900 μL) were added under vigorous stirring at RT for at least 30 min. Thereafter, the HSs were collected by centrifugation at 6000 rpm for 5 min and redispersed in toluene for further use.

Optical Properties

Absorbance spectra were measured with a Cary300 UV–Vis absorption spectrophotometer, while PL spectra were recorded by a Varian Cary Eclipse spectrophotometer using an excitation wavelength at 350 nm for the bromide-based samples and 300 for the chloride-based ones. The NC solutions were diluted in hexane in quartz cuvettes (path length = 1 cm) to a maximum optical density below 1.0.

Transmission Electron Microscopy

Bright Field Transmission Electron Microscopy (BF-TEM) measurements of the NCs were performed using a JEOL JEM-1011 with a W thermionic source at an acceleration voltage of 100 kV. The highly diluted NC solution was drop-cast onto copper grids (200 mesh) with carbon film and the solvent was then allowed to evaporate in a vapor-controlled environment. The longitudinal and lateral dimensions were assessed through statistical analysis of TEM images of several hundred NCs using the ImageJ software.

X-ray Powder Diffraction

Characterization by X-ray Powder Diffraction (XRD) was performed by employing a PANalytical Empyrean X-ray diffractometer using a 1.8 kV Cu Kα ceramic X-ray tube operating at 45 kV and 40 mA and detected by a PIXcel3D 2 × 2 area detector.

Samples were prepared by drop-casting highly concentrated solutions on zero-diffraction silicon substrates. All diffraction patterns were acquired at room temperature under ambient conditions. Data analysis was performed using the HighScore 4.9 software from PANalytical.

X-ray Photoelectron Spectroscopy

XPS specimens were prepared by drop casting a few microliters of the sample dispersions onto freshly cleaved highly oriented pyrolytic graphite (HOPG, ZYB grade) substrates. XPS data were acquired using a Kratos Axis UltraDLD spectrometer, equipped with a monochromatic Al Kα source operated at 20 mA and 15 kV. Wide scans were acquired at a pass energy of 160 eV, energy step of 1 eV, over an analysis area of 300 x 700 μm2. Spectra have been charged corrected, the lowest binding-energy component of the carbon 1s spectrum was set at 284.8 eV. The collected data were then analyzed with CasaXPS software (version 2.3.24).[55]

Ultraviolet Photoelectron Spectroscopy

UPS was carried out on the same spectrometer, using a He I (21.22 eV) discharge lamp, on an area of 55 μm in diameter, at a pass energy of 10 eV and with a dwell time of 100 ms. The work function (that is, the position of the Fermi level with respect to the vacuum level) was measured from the threshold energy for the emission of secondary electrons during He I excitation. A −9.0 V bias was applied to the sample to precisely determine the low-kinetic-energy cutoff, as discussed in ref [56]. The position of the cutoff was then estimated with CasaXPS software, using the "Edge Up" background function for the energy interval around the cutoff. Then, the position of the VBM versus the vacuum level was estimated by measuring its distance from the Fermi level, focusing on the high-kinetic energy (i.e., low-binding energy) cutoff region and using the "Edge Down" background function in CasaXPS software.

Ambient Pressure Photoemission Spectroscopy

The ionization (I) energy or valence band (VB) energy of the studied materials was determined using an Ambient Pressure Photoemission Spectroscopy (APS) system (model APS02, KP Technology Ltd, Highlands and Islands, United Kingdom). The APS02 system was operated with an incident photon energy range from 4.56 to 6.89 eV, generated using a tunable UV light source of Deuterium. The samples for APS measurements were prepared by drop-casting thin films of the materials onto ITO-

coated glass substrates, which provide a conductive and transparent support compatible with photoemission studies. The APS chamber was continuously purged with nitrogen gas during operation to effectively suppress ozone formation throughout the measurement. The onset of the photoemission signal with the background was used to determine the VB energy.

Electrochemistry

Electrochemical characterization was performed on an Autolab 128N potentiostat/galvanostat using a three-electrode system in a glass beaker. Cyclic voltammetry (CV) experiments were carried out in 0.1 M tetrabutylammonium tetrafluoroborate ($TBABF_4$) solution in a mixture of anhydrous ACN:toluene (1:3 v/v) with a thiophenol concentration of 0.12 M. A glassy carbon, Pt wire and Ag/AgCl were used as working, counter and reference electrodes, respectively. The measurements were performed at room temperature (298 ± 1 K) and under aerated conditions, with a scan rate of 100 mV/s. To determine the energy of the highest-occupied molecular orbital (HOMO) level, the anodic peak potential (in volts) was referred to the Fc/Fc+ redox couple using 0.5 mM solutions of ferrocene in 0.1 M $TBABF_4$ in the same electrolyte.

Thermogravimetric analysis

Thermogravimetric analysis (TGA) of the NCs was carried out with a Mettler Toledo TGA/SDTA851e/SF/1100 apparatus in the 25-800°C temperature range under a 10°C min' scan rate under nitrogen atmosphere.

Attenuated total reflectance-Fourier transform infrared spectroscopy

To ascertain the substrate approach to the photocatalysts NCs surface, the NCs and the substrates were mixed at the same concentration used in the photocatalytic reactions and the mixture was stirred to ensure the interaction between them. Then, the ATR-FTIR analyses were performed in a Bruker alpha II spectrometer by drop-casting the colloidal mixtures.

Photocatalytic Experiments

For the photocatalytic experiments, 1 mg of the photocatalyst was mixed with the stock solution of the substrate (thiophenol/ 1,4-bromothiophenol/ 1,4-

methoxythiophenol) in 1 mL of solvent (cyclohexane) to reach the final concentration of 34 mM. Subsequently, the photoreactions were performed in a 10 mL gastight crimped vials under stirring (160 rpm) using an orbital shaker in a photoreactor with blue LEDs (450/405 nm) for 90 min at 20°C. After the reaction time, the crude solution was centrifuged at 12500 rpm for 15 minutes, the precipitate was collected in 1 mL of hexane for further use while the supernatant was analyzed by GC-MS to determine the conversion of the substrate and the yield of product. For the GC analysis the biphenyl (internal standard) stock solution was added to the supernatant to have a final concentration of 150 mM. Biphenyl was solubilized in ethyl acetate.

Control experiments of the photocatalytic coupling of thiophenol. All the reactions have been performed in the same conditions reported for the photocatalytic reactions but in the presence of the scavengers. Regarding the control experiments, 10 equivalent of 1,4-benzoquinone, *N,N*-Diisopropylethylamine (DIPEA) and 2,2′,6,6′-tetramethylpiperidine-1-oxyl (TEMPO) were added as scavengers.

Photocatalytic Setup. Light source: the reactions were performed using (1= 450‡10 m or 1= 405‡10 m) LUXEON LED, mounted on a 10mm Square Saber - 1030 mW@700mA as a light source. Temperature Control: reaction temperature was controlled by a high-precision thermoregulation Hubber K6 cryostat. Likewise, to guarantee stable irradiation the temperature of the LEDs was set up at 20°C. The reactions have been carried out in an in-house parallel High Throughput Screening (HTS) photoreactor with capacity to set up to 25 reactions with different excitation wavelengths, respectively, under high-intensity irradiation. These unique HTS platforms allow for tight control of the light intensity and the temperature of the reactions. The 25-positions photoreactor is operable at 1-15 mL reaction volumes for each reaction.

Gas chromatography – mass spectroscopy

The work-up of the reaction was performed by adding biphenyl (IS) to the crude. Then, 0.1 mL of the mixture was diluted with 0.9 mL of cyclohexane. The solution was injected into the GC-MS (Agilent 7890B - 5977A) and the products were identified according to the retention time and mass. A calibration curve was established using different concentrations of analytes (C_{AN}) relative to a fixed concentration of the internal standard (C_{IS} = 150 mM). The GC signals were then analyzed by comparing the peak areas of the analytes with that of the internal standard. The ratio between the product area and the internal standard allowed us

to quantify the product concentrations in the reactions. This calibration plot was subsequently used to quantify the obtained products. (Figure 5.26)

The following equations were used to calculate the product yield (1), substrate conversion (2) and the selectivity (3):

$$\boldsymbol{Product\ Yield}\ (\%) = [\boldsymbol{Produc}(\boldsymbol{AN})]/\ [\boldsymbol{Initial\ substrate}]\ \boldsymbol{x100}\% \quad (1)$$

$$\boldsymbol{Conversion}\ (\%) = \boldsymbol{100} - [\boldsymbol{Final\ substrate}]/\ [\boldsymbol{Initial\ substrate}]\ \boldsymbol{x100}\% \quad (2)$$

$$\boldsymbol{Selectivity}\ (\%) = [\boldsymbol{Product\ Yield}]/[\boldsymbol{Conversion}]\boldsymbol{x100}\% \quad (3)$$

5.7 Appendix

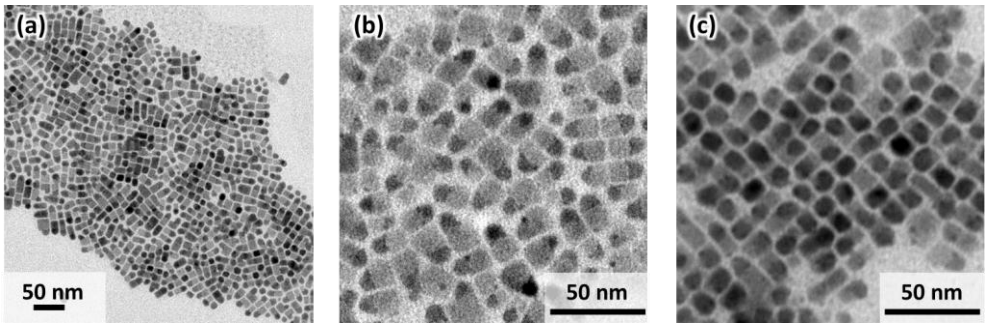

Figure 5.8. TEM images of $CsPbBr_3/Pb_4S_3Br_2$ heterostructures at different magnifications. The different projections visible in panel (a) allow to see some heterostructures lying flat on the TEM grid (b) (rectangular cross-section) as well as some standing upright (c) (squared cross-section). Reprinted with permission from ref 58. Licensed under CC-BY 4.0. Copyright © 2025 The Authors.

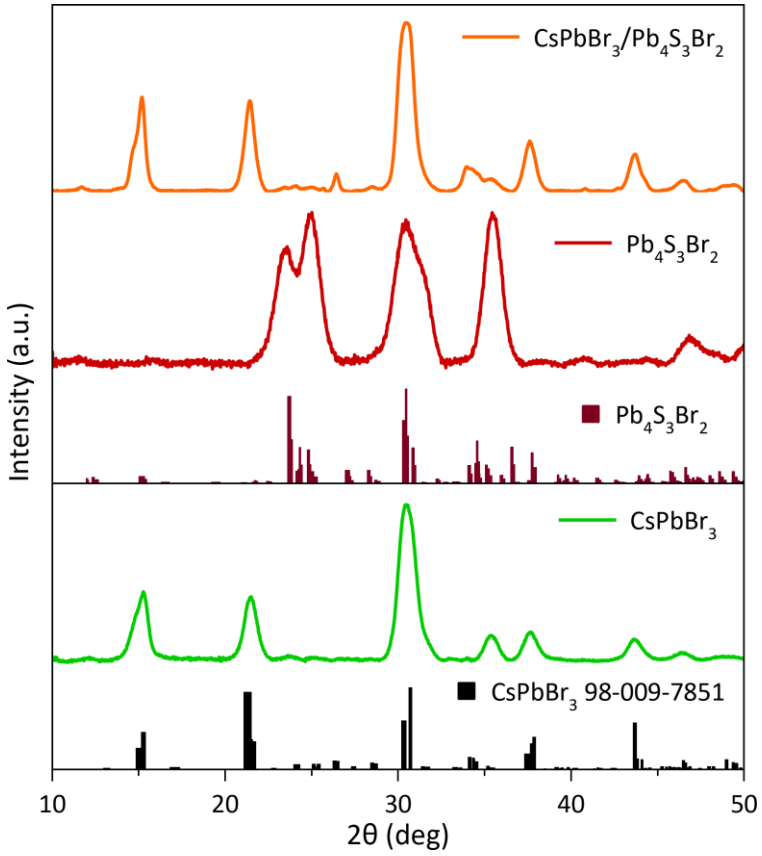

Figure 5.9. XRD patterns of $CsPbBr_3$ and $Pb_4S_3Br_2$ free-standing NCs and HSs. XRD patterns of $CsPbBr_3/Pb_4S_3Br_2$ HSs (orange line), $Pb_4S_3Br_2$ NCs (red line) and reference

pattern (bordeaux line), $CsPbBr_3$ NCs (green line) and $CsPbBr_3$ reference (black line). The contribution of $Pb_4S_3Br_2$ to the heterostructures pattern is minor due to the much lower volume fraction compared to $CsPbBr_3$ and to the spread of diffracted intensities over more peaks due to the lower symmetry (although both materials crystallize in the Pnma space group, the pseudocubic symmetry of $CsPbBr_3$ causes many broad reflections to stack onto each other). Reprinted with permission from ref 58. Licensed under CC-BY 4.0. Copyright © 2025 The Authors.

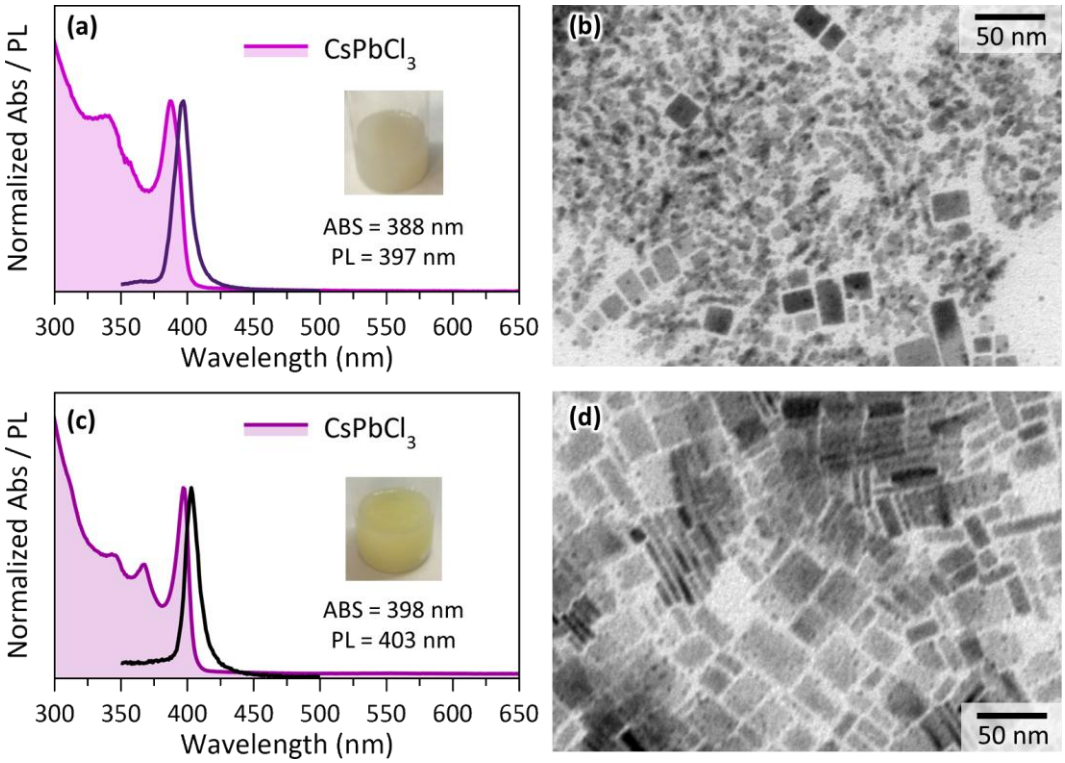

Figure 5.10. Optimization of the $CsPbCl_3$ NCs seeds for HSs growth. a) Absorption and photoluminescence spectra of $CsPbCl_3$ NCs synthetized at 150 °C and with the use of TOP (trioctylphosphine). b) TEM image of the same $CsPbCl_3$ NCs. c) Absorption and photoluminescence spectra of HSs growth tests performed on the $CsPbCl_3$ NCs (panel b). d) TEM image of the same test, no HSs are found with these conditions. Reprinted with permission from ref 58. Licensed under CC-BY 4.0. Copyright © 2025 The Authors.

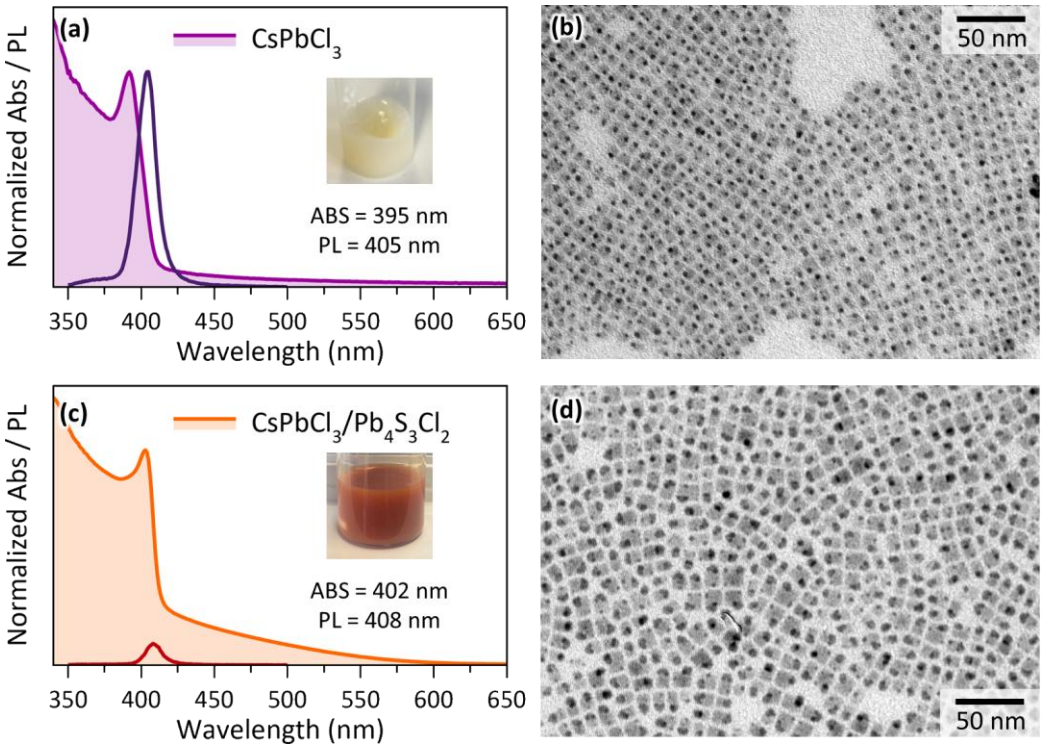

Figure 5.11. Optical characterization and TEM images of $CsPbCl_3$ NCs and $CsPbCl_3/Pb_4S_3Cl_2$ HSs. a) Absorption and photoluminescence spectra of $CsPbCl_3$ NCs synthetized at 185 °C. b) TEM images of the same $CsPbCl_3$ NCs. c) Absorption and photoluminescence spectra of $CsPbCl_3/Pb_4S_3Cl_2$ HSs. d) TEM images of the same $CsPbBr_3/Pb_4S_3Cl_2$ HSs. Reprinted with permission from ref 58. Licensed under CC-BY 4.0. Copyright © 2025 The Authors.

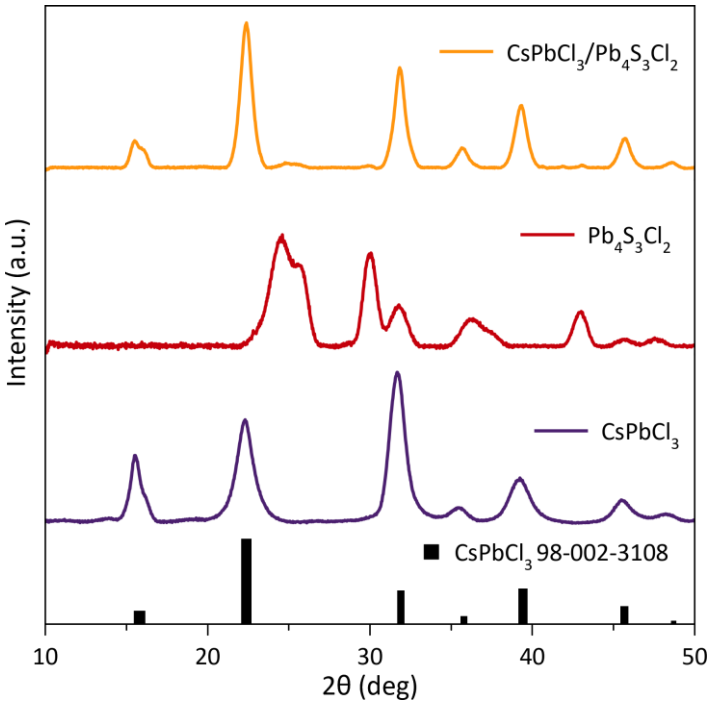

Figure 5.12. XRD patterns of $CsPbCl_3$ and $Pb_4S_3Cl_2$ free-standing NCs and HSs. XRD pattern of $CsPbCl_3/Pb_4S_3Cl_2$ HSs (orange line), $Pb_4S_3Cl_2$ NCs (red line) and $CsPbCl_3$ (purple line) $CsPbCl_3$ reference (black line). The contribution of $Pb_4S_3Cl_2$ to the HSs pattern is minor due to the much lower volume fraction compared to $CsPbCl_3$ and to the spread of diffracted intensities over more peaks due to the lower symmetry. Reprinted with permission from ref 58. Licensed under CC-BY 4.0. Copyright © 2025 The Authors.

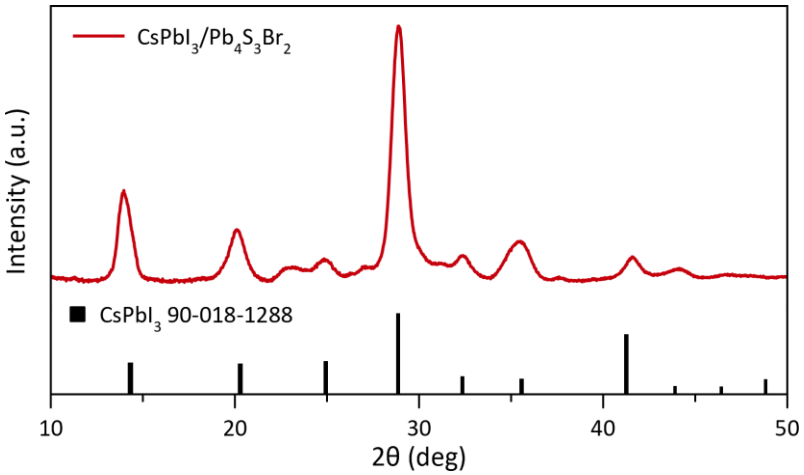

Figure 5.13. XRD patterns of $CsPbI_3/Pb_4S_3Br_2$ HSs. XRD pattern of $CsPbI_3/Pb_4S_3Br_2$ HSs (red) after anion exchange, $CsPbI_3$ reference (black line). The contribution of $Pb_4S_3Br_2$ to the heterostructures pattern is minor due to the much lower volume fraction compared

to $CsPbI_3$ and to the spread of diffracted intensities over more peaks due to the lower symmetry. Reprinted with permission from ref 58. Licensed under CC-BY 4.0. Copyright © 2025 The Authors.

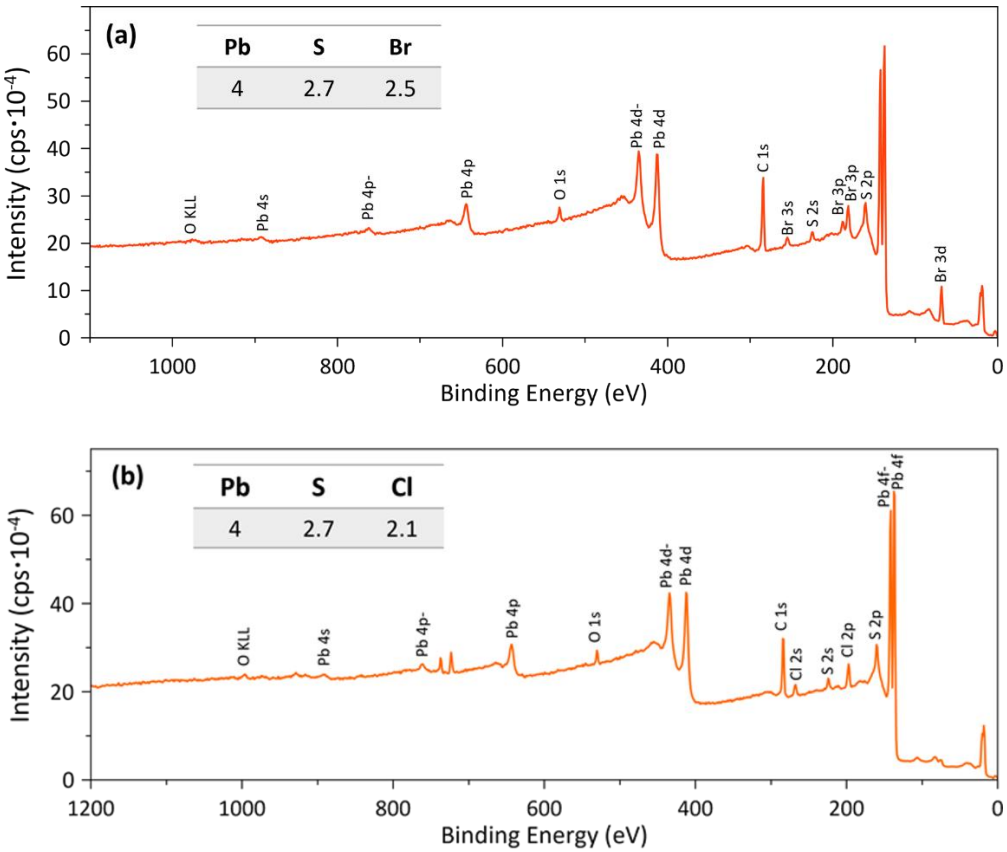

Figure 5.14. X-ray Photoelectron Spectroscopy (XPS) of $Pb_4S_3X_2$ NCs (X = Br, Cl). a) XPS data for $Pb_4S_3Br_2$. Inset: composition of element by XPS analysis, in agreement with the stoichiometry of the material. b) XPS data for $Pb_4S_3Cl_2$. Inset: composition of element by XPS analysis, in agreement with the stoichiometry of the material. Adapted with permission from ref 58. Licensed under CC-BY 4.0. Copyright © 2025 The Authors.

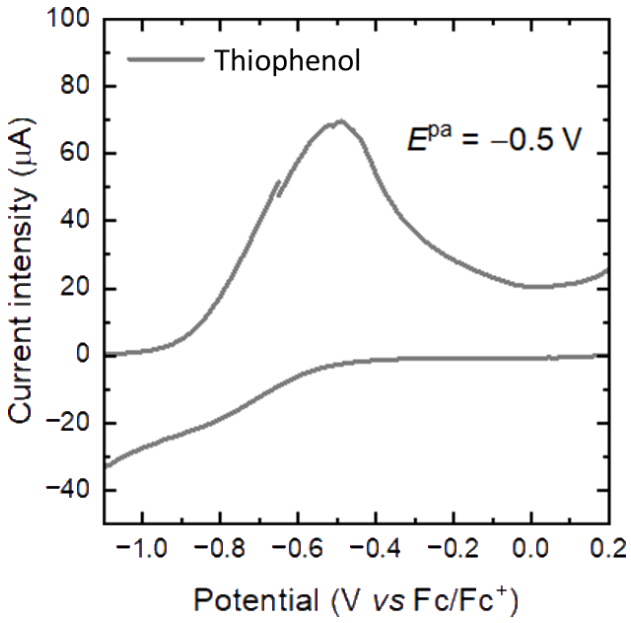

Figure 5.15. Electrochemical measurements. CV curve of thiophenol, used to determine the highest occupied molecular orbital (HOMO) of the molecule (-4.2 eV) at the anodic peak maximum. Reprinted with permission from ref 58. Licensed under CC-BY 4.0. Copyright © 2025 The Authors.

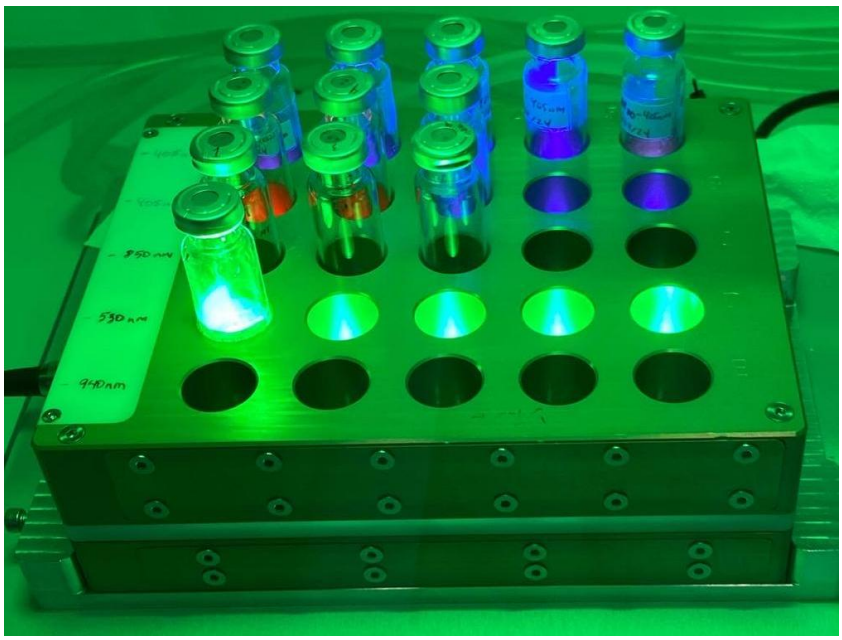

Picture 1. The photoreactor used for the photoreactions is equipped with five LED lines, with different wavelength emissions. Reprinted with permission from ref 58. Licensed under CC-BY 4.0. Copyright © 2025 The Authors.

Table 5.6. GC retention time of the different compounds.

Retention time (min)	Compound
15.122 – 15.128	Biphenyl (internal standard)
7.627	Thiophenol
20.510	Disulfide diphenyl
26.045	Bis(4-bromophenyl) disulfide
25.454	Bis(4-methoxyphenyl) disulfide
14.015-14.021	Cyclohexanone
19.880-19.887	1-octadecene

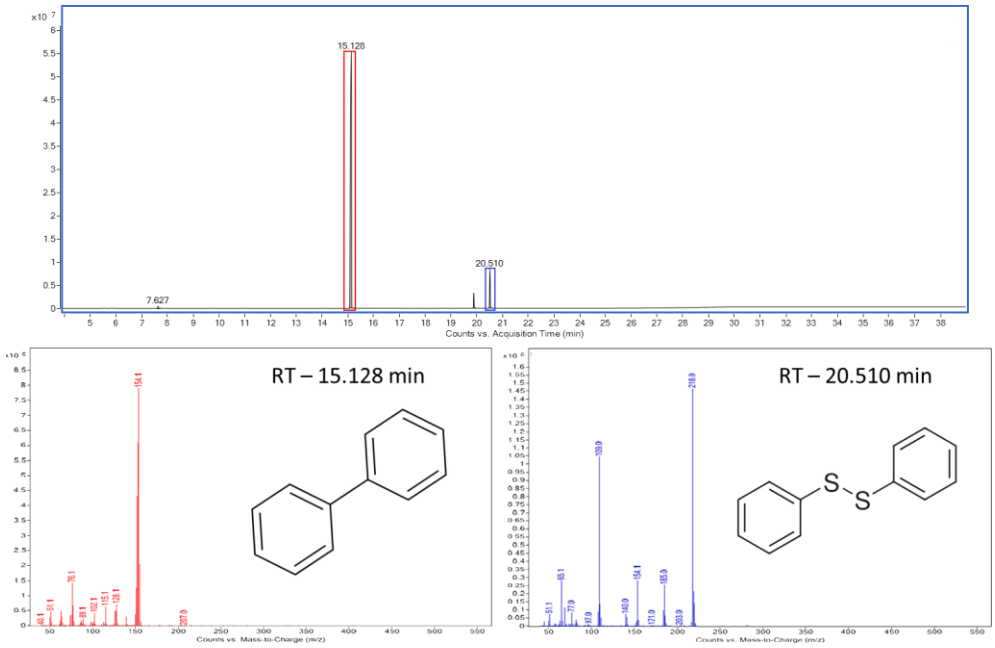

Figure 5.16. Gas Chromatography – Mass Spectrometry of thiophenol. Gas chromatography of the thiophenol reaction in cyclohexane and mass spectra of the internal standard (bottom left) and the product (bottom right). Reprinted with permission from ref 58. Licensed under CC-BY 4.0. Copyright © 2025 The Authors.

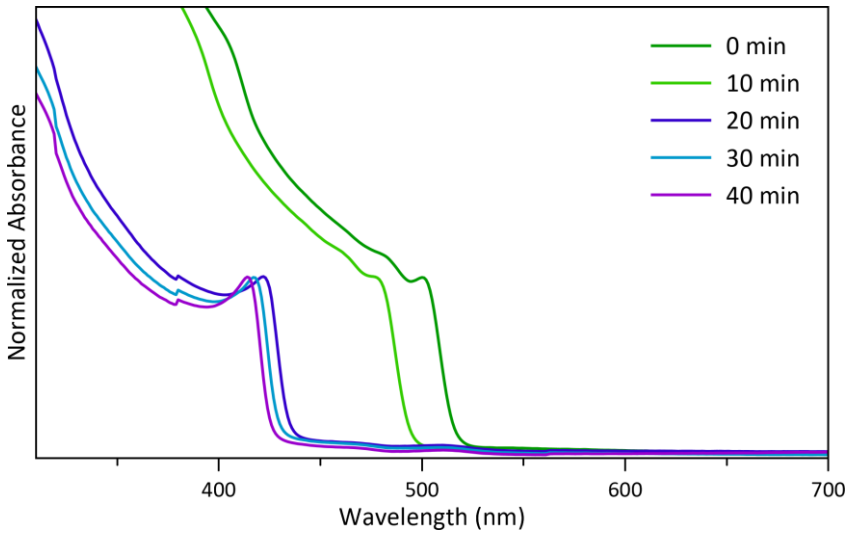

Figure 5.17. Absorbance spectra of $CsPbBr_3$ in CH_2Cl_2 under light. Time evolution of the absorption spectrum of $CsPbBr_3$ in CH_2Cl_2 under illumination at 450 nm. Reprinted with permission from ref 58. Licensed under CC-BY 4.0. Copyright © 2025 The Authors.

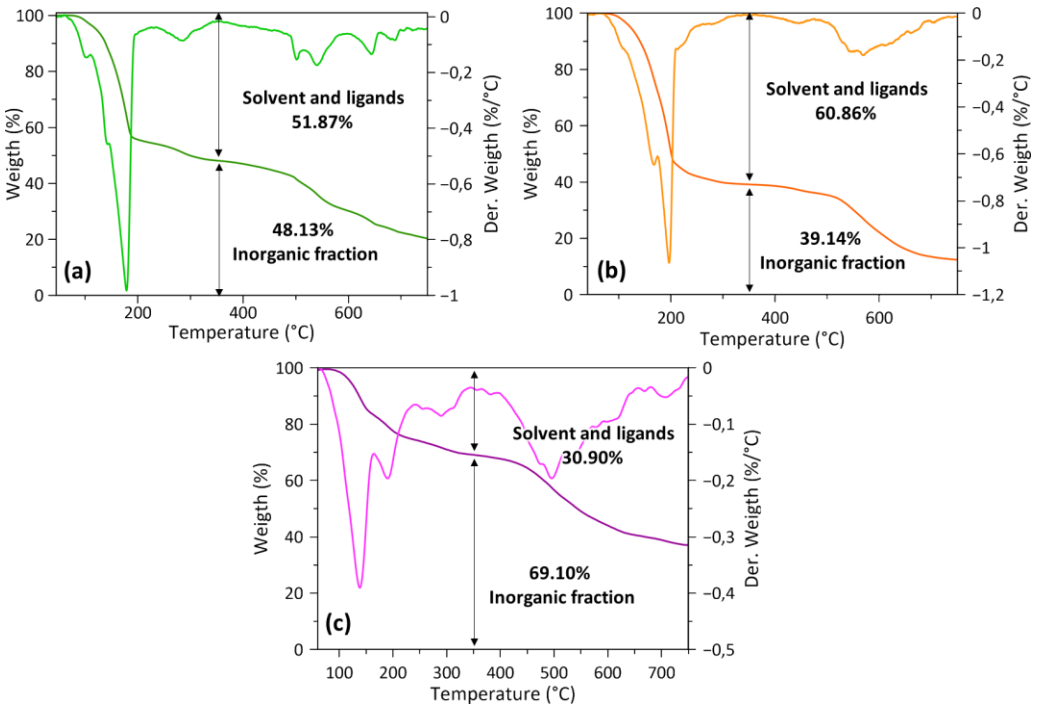

Figure 5.18. Thermogravimetric analysis. a) TGA analysis of $CsPbBr_3$ NCs (green line) and first derivative (light green line). b) TGA analysis of $CsPbBr_3/Pb_4S_3Br_2$ HSs (orange line) and first derivative (light orange line). c) TGA analysis of $Pb_4S_3Br_2$ NCs (purple line) and first derivative (light purple line). Thermogravimetry analyses (TGA) indicated that the first weight loss is due to two different contributions: hexane adsorbed on the NCs surface, as reported previously,[57] and organic ligands (both bound and free ligands). Therefore, the inorganic NC cores accounted for the remaining 39.1% of weight in the case of the heterostructures, 48.1 % in the case of perovskites, and 69.1 % for the chalcohalides. Reprinted with permission from ref 58. Licensed under CC-BY 4.0. Copyright © 2025 The Authors.

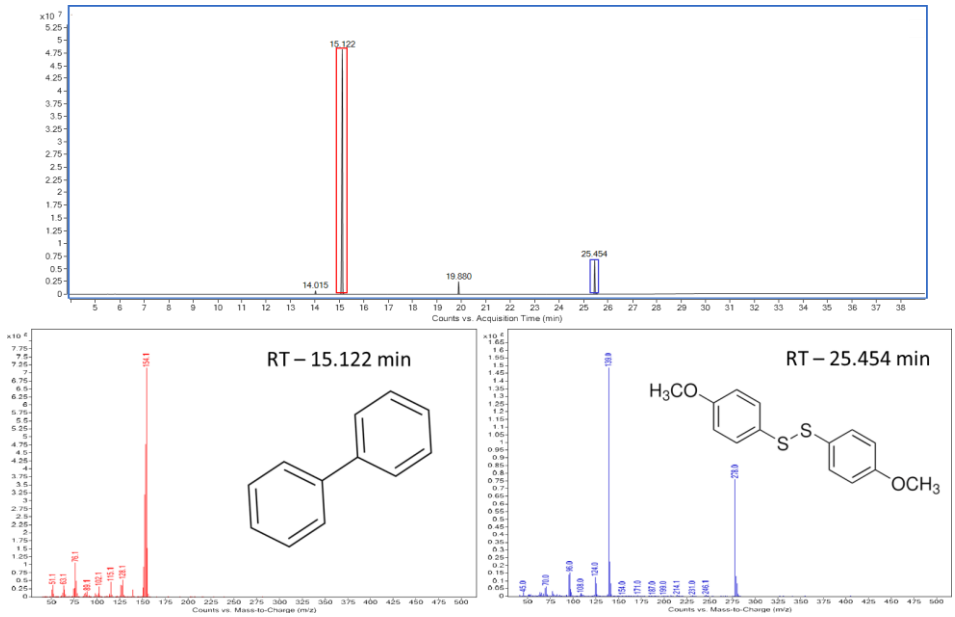

Figure 5.19. Gas Chromatography – Mass Spectrometry of OCH_3-thiophenol. Gas chromatography of the 4-methoxythiophenol reaction in cyclohexane and mass spectra of the internal standard (bottom left) and the product (bottom right). Reprinted with permission from ref 58. Licensed under CC-BY 4.0. Copyright © 2025 The Authors.

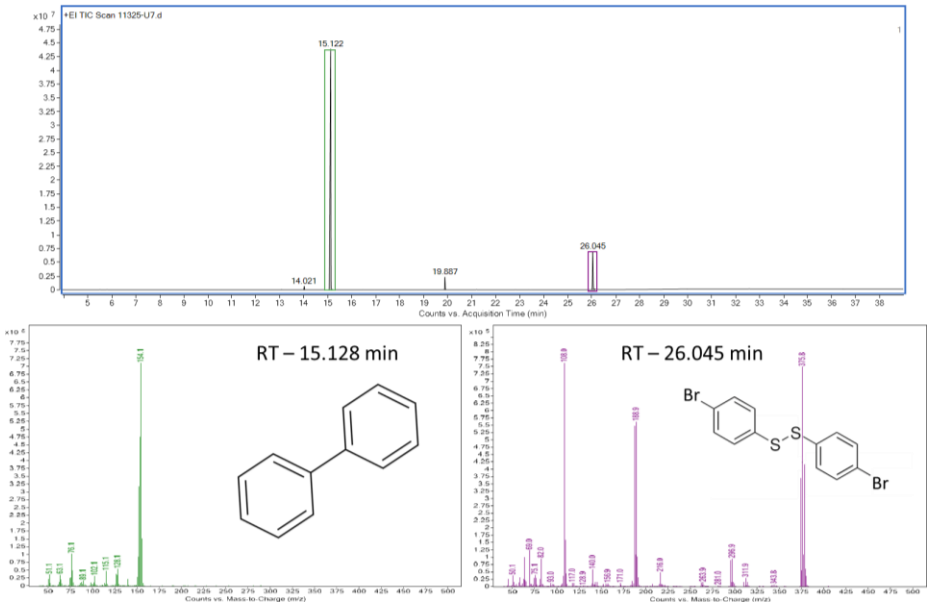

Figure 5.20. Gas Chromatography – Mass Spectrometry of Br-thiophenol. Gas chromatography of the 4-bromothiophenol reaction in cyclohexane and mass spectra of the internal standard (bottom left) and the product (bottom right). Reprinted with permission from ref 58. Licensed under CC-BY 4.0. Copyright © 2025 The Authors.

Figure 5.21. Gas Chromatography – Mass Spectrometry of TEMPO-PhS adduct. Mass spectrum of the adduct (TEMPO-PhS) between TEMPO and thiyl radical, showing the typical fragments of both units. Reprinted with permission from ref 58. Licensed under CC-BY 4.0. Copyright © 2025 The Authors.

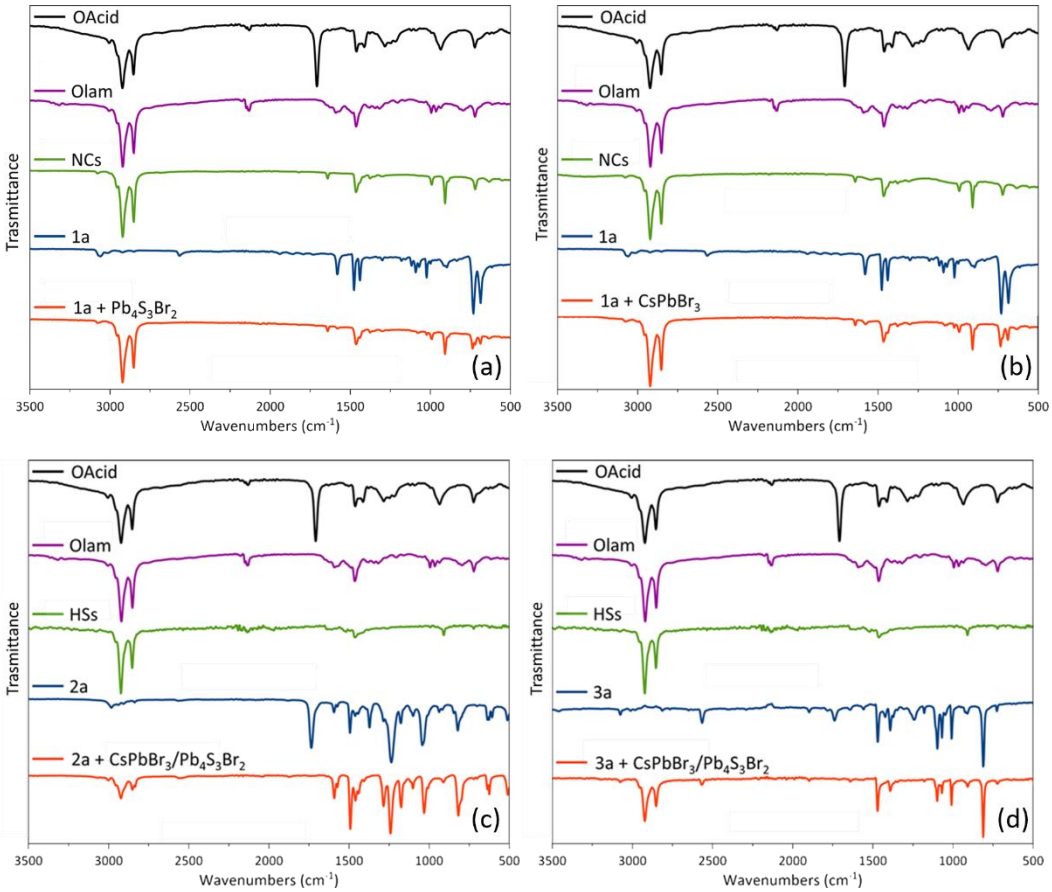

Figure 5.22. Fourier transform infrared spectroscopy. a) FTIR spectra of OAcid (black line), Olam (purple line), $Pb_4S_3Br_2$ NCs (green line), 1a-thiophenol (blue line) and a mixture of $Pb_4S_3Br_2$ NCs and 1a (red line). b) FTIR spectra of OAcid (black line), Olam (purple line), $CsPbBr_3$ NCs (green line), 1a-thiophenol (blue line) and a mixture of $CsPbBr_3$ NCs and 1a (red line). c) FTIR spectra of OAcid (black line), Olam (purple line), $CsPbBr_3/Pb_4S_3Br_2$ HSs (green line), 2a (4-methoxythiophenol, blue line) and a mixture of $CsPbBr_3/Pb_4S_3Br_2$ HSs and 2a (red line). d) FTIR spectra of OAcid (black line), Olam (purple line), $CsPbBr_3/Pb_4S_3Br_2$ HSs (green line), 3a (4-Bromothiophenol, blue line) and a mixture of $CsPbBr_3/Pb_4S_3Br_2$ HSs and 3a (red line). Adapted with permission from ref 58.

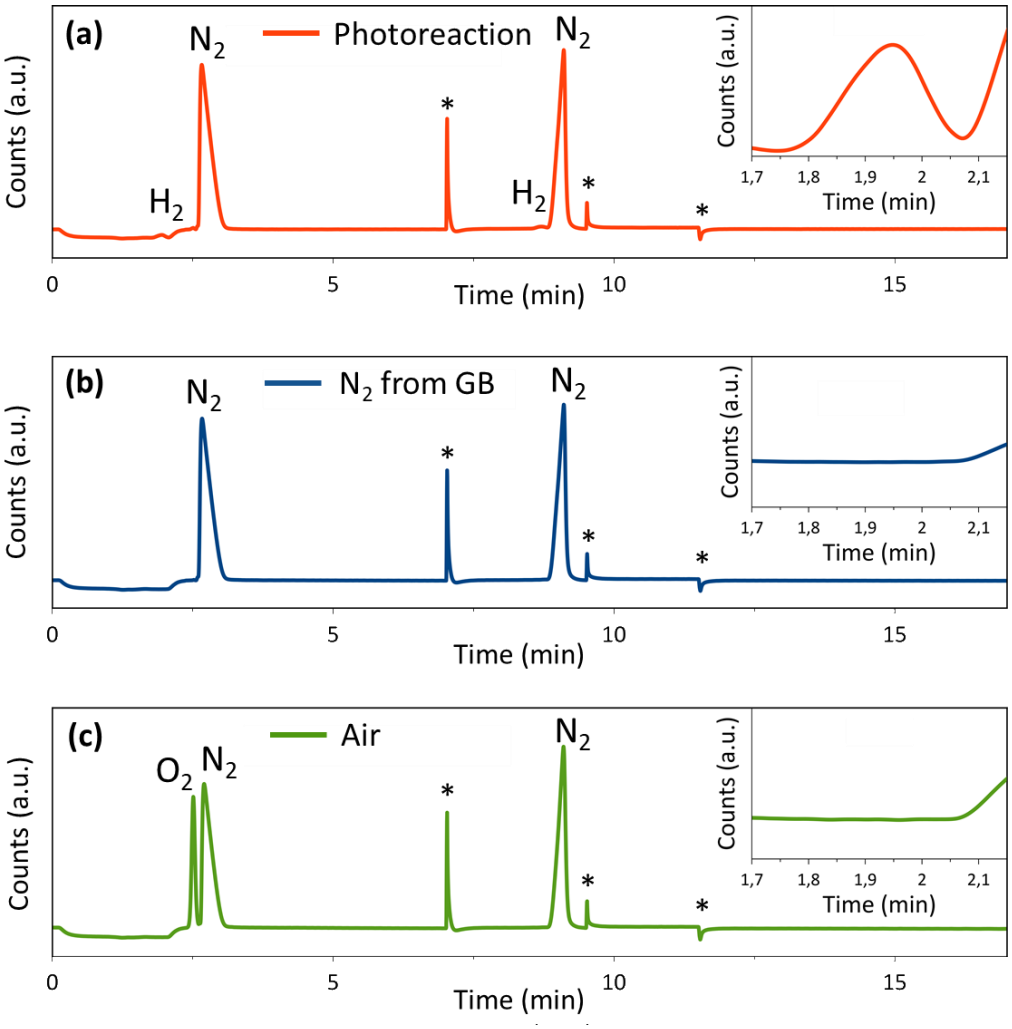

Figure 5.23. Typical chromatographs (Thermal Conductivity Detector, TCD) obtained upon the injection of controls and photoreaction samples. a) TCD trace of the headspace gas from the photoreaction performed under inert atmosphere (N_2). Inset: magnification of the region corresponding to the first H_2 peak. b) TCD trace of a gas sample collected from the glovebox, showing only N_2. Inset: magnification of the H_2 region, confirming the absence of hydrogen. c) TCD trace of a gas sample taken from air, showing the presence of N_2 and O_2. Inset: magnified view of the H_2 region, again showing no hydrogen signal. Asterisks (*) identify valve events. Reprinted with permission from ref 58. Licensed under CC-BY 4.0. Copyright © 2025 The Authors.

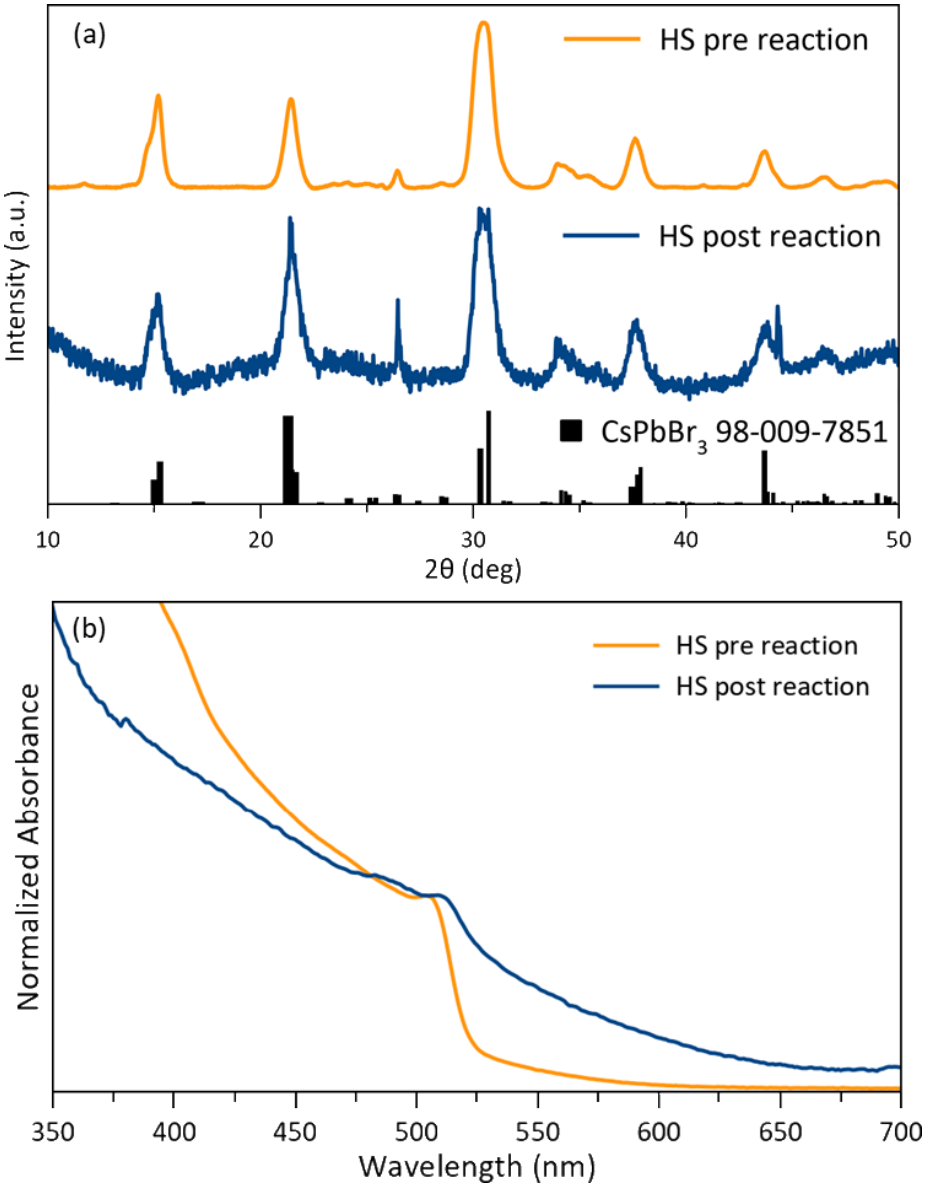

Figure 5.24. XRD patterns and absorbance spectra after photoreaction. a) XRD patterns of $CsPbBr_3/Pb_4S_3Br_2$ HSs before (orange line) and after (blue line) photoreaction and $CsPbBr_3$ (black line) as reference. b) Absorbance spectra of $CsPbBr_3/Pb_4S_3Br_2$ HSs before (orange trace) and after (blue trace) photoreaction. Adapted with permission from ref 58. Licensed under CC-BY 4.0. Copyright © 2025 The Authors.

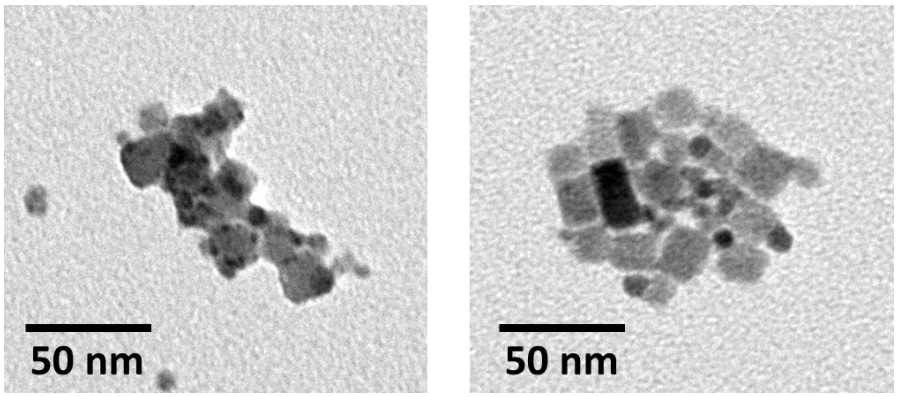

Figure 5.25. TEM images after photoreaction. TEM images of $CsPbBr_3/Pb_4S_3Br_2$ HSs after photoreaction. Reprinted with permission from ref 58. Licensed under CC-BY 4.0. Copyright © 2025 The Authors.

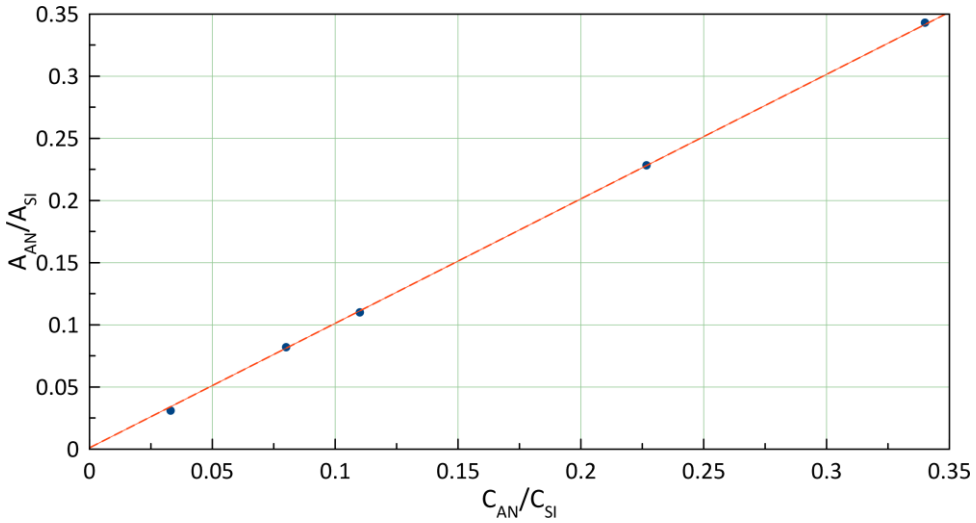

Figure 5.26. Calibration curve. Correlation between concentration and peak area ratio (analyte/IS). Reprinted with permission from ref 58. Licensed under CC-BY 4.0. Copyright © 2025 The Authors.

5.8 Source Publications and Contributions

This chapter is based on the following publication:

Cabona, A.; Toso, S.; Cortés-Villena, A.; Rosa-Pardo, I.; Prato, M.; Ferri, M.; Pérez-Prieto, J.; Kriegel, I.; Manna, L.; Galian, R. E. Metal Halide Perovskite/Chalcohalide Heterojunctions for the Photoinduced Oxidative Coupling of p-Substituted Thiophenols. *ACS Applied Nano Materials* **2025**. https://doi.org/10.1021/acsanm.5c05834

This article stemmed from the idea of optimizing the synthesis of functional semiconductor-semiconductor heterostructure as photocatalysts for organic transformations. This work was made possible through collaboration with many colleagues. Stefano Toso collaborated with me in the initial stage of the optimization of the heterostructures synthesis. Ignacio Rosa-Pardo helped me with the initial photocatalytic testing. Michele Ferri helped me with the identification of the hydrogen in the photocatalytic reactions. Raquel Galian guided me in the photocatalysis experiments. Finally, I would like to thank Liberato Manna, Ilka Kriegel and Raquel Galian for their guidance and assistance in preparing the manuscript.

5.8.1 Copyright

Some elements of this chapter were adapted from external source:

Figures:

Text (parts):

5.9 Bibliography

(1) Balazs, D. M.; Loi, M. A. Lead-Chalcogenide Colloidal-Quantum-Dot Solids: Novel Assembly Methods, Electronic Structure Control, and Application Prospects. *Adv. Mater.* **2018**, *30* (33), 1800082. https://doi.org/10.1002/adma.201800082.

(2) Shamsi, J.; Urban, A. S.; Imran, M.; De Trizio, L.; Manna, L. Metal Halide Perovskite Nanocrystals: Synthesis, Post-Synthesis Modifications, and Their Optical Properties. *Chem. Rev.* **2019**, *119* (5), 3296–3348. https://doi.org/10.1021/acs.chemrev.8b00644.

(3) Priyadarshini, P.; Das, S.; Naik, R. A Review on Metal-Doped Chalcogenide Films and Their Effect on Various Optoelectronic Properties for Different Applications. *RSC Adv.* **2022**, *12* (16), 9599–9620. https://doi.org/10.1039/D2RA00771A.

(4) Kovalenko, M. V.; Protesescu, L.; Bodnarchuk, M. I. Properties and Potential Optoelectronic Applications of Lead Halide Perovskite Nanocrystals. *Science* **2017**, *358* (6364), 745–750. https://doi.org/10.1126/science.aam7093.

(5) Ider, A.; Laval, J. P.; Frit, B.; Carré, J.; Bastide, J. P. Crystal Structure of $PbTeF_6$. *J. Fluorine Chem.* **1996**, *78* (1), 15–20. https://doi.org/10.1016/0022-1139(96)03411-2.

(6) Krebs, B. Die Kristallstrukturen von Pb_4SeBr_6, $Pb_5S_2J_6$ und $Pb_7S_2Br_{10}$. *Z. Anorg. Allg. Chem.* **1973**, *396* (2), 137–151. https://doi.org/10.1002/zaac.19733960203.

(7) Ni, D.; Guo, S.; Yang, Z. S.; Powderly, K. M.; Cava, R. J. Pb4S3I2–A High-Pressure Phase in the PbS-PbI_2 System. *Solid State Sci.* **2019**, *91*, 49–53. https://doi.org/10.1016/j.solidstatesciences.2019.03.012.

(8) Ni, D.; Guo, S.; Powderly, K. M.; Zhong, R.; Cava, R. J. A High-Pressure Phase with a Non-Centrosymmetric Crystal Structure in the PbSe–$PbBr_2$ System. *J. Solid State Chem.* **2019**, *280*, 120982. https://doi.org/10.1016/j.jssc.2019.120982.

(9) Toso, S.; Akkerman, Q. A.; Martín-García, B.; Prato, M.; Zito, J.; Infante, I.; Dang, Z.; Moliterni, A.; Giannini, C.; Bladt, E.; Lobato, I.; Ramade, J.; Bals, S.; Buha, J.; Spirito, D.; Mugnaioli, E.; Gemmi, M.; Manna, L. Nanocrystals of Lead Chalcohalides: A Series of Kinetically Trapped Metastable Nanostructures. *J. Am. Chem. Soc.* **2020**, *142* (22), 10198–10211. https://doi.org/10.1021/jacs.0c03577.

(10) Imran, M.; Peng, L.; Pianetti, A.; Pinchetti, V.; Ramade, J.; Zito, J.; Di Stasio, F.; Buha, J.; Toso, S.; Song, J.; Infante, I.; Bals, S.; Brovelli, S.; Manna, L. Halide Perovskite–Lead Chalcohalide Nanocrystal Heterostructures. *J. Am. Chem. Soc.* **2021**, *143* (3), 1435–1446. https://doi.org/10.1021/jacs.0c10916.

(11) Razgoniaeva, N.; Moroz, P.; Lambright, S.; Zamkov, M. Photocatalytic Applications of Colloidal Heterostructured Nanocrystals: What's Next? *J. Phys. Chem. Lett.* **2015**, 6 (21), 4352–4359. https://doi.org/10.1021/acs.jpclett.5b01883.

(12) Shim, M. Colloidal Nanorod Heterostructures for Photovoltaics and Optoelectronics. *J. Phys. D: Appl. Phys.* **2017**, *50* (17), 173002. https://doi.org/10.1088/1361-6463/aa65a5.

(13) Low, J.; Yu, J.; Jaroniec, M.; Wageh, S.; Al-Ghamdi, A. A. Heterojunction Photocatalysts. *Adv. Mater.* **2017**, *29* (20), 1601694. https://doi.org/10.1002/adma.201601694.

(14) Li, F.; Zhu, G.; Jiang, J.; Yang, L.; Deng, F.; Arramel; Li, X. A Review of Updated S-Scheme Heterojunction Photocatalysts. *J. Mater. Sci. Technol.* **2024**, *177*, 142–180. https://doi.org/10.1016/j.jmst.2023.08.038.

(15) Bera, S.; Pradhan, N. Perovskite Nanocrystal Heterostructures: Synthesis, Optical Properties, and Applications. *ACS Energy Lett.* **2020**, *5* (9), 2858–2872. https://doi.org/10.1021/acsenergylett.0c01449.

(16) Wang, X.; Wang, Z.; Li, Y.; Wang, J.; Zhang, G. Efficient Photocatalytic CO_2 Conversion over 2D/2D Ni-Doped $CsPbBr_3/Bi_3O_4Br$ Z-Scheme Heterojunction: Critical Role of Ni Doping, Boosted Charge Separation and Mechanism Study. *Appl. Catal., B* **2022**, *319*, 121895. https://doi.org/10.1016/j.apcatb.2022.121895.

(17) Martin, J. S.; Zeng, X.; Chen, X.; Miller, C.; Han, C.; Lin, Y.; Yamamoto, N.; Wang, X.; Yazdi, S.; Yan, Y.; Beard, M. C.; Yan, Y. A Nanocrystal Catalyst Incorporating a Surface Bound Transition Metal to Induce Photocatalytic Sequential Electron Transfer Events. *J. Am. Chem. Soc.* **2021**, *143* (30), 11361–11369. https://doi.org/10.1021/jacs.1c00503.

(18) Kovalenko, M. V.; Protesescu, L.; Bodnarchuk, M. I. Properties and Potential Optoelectronic Applications of Lead Halide Perovskite Nanocrystals. *Science* **2017**, *358* (6364), 745–750. https://doi.org/10.1126/science.aam7093.

(19) Ghosh, S.; Manna, L. The Many "Facets" of Halide Ions in the Chemistry of Colloidal Inorganic Nanocrystals. *Chem. Rev.* **2018**, *118* (16), 7804–7864. https://doi.org/10.1021/acs.chemrev.8b00158.

(20) Huang, H.; Bodnarchuk, M. I.; Kershaw, S. V.; Kovalenko, M. V.; Rogach, A. L. Lead Halide Perovskite Nanocrystals in the Research Spotlight: Stability and Defect Tolerance. *ACS Energy Lett.* **2017**, *2* (9), 2071–2083. https://doi.org/10.1021/acsenergylett.7b00547.

(21) Jagadeeswararao, M.; Galian, R. E.; Pérez-Prieto, J. Photocatalysis Based on Metal Halide Perovskites for Organic Chemical Transformations. *Nanomaterials* **2023**, *14* (1), 94. https://doi.org/10.3390/nano14010094.

(22) Thanetchaiyakup, A.; Sadek, M.; Bati, G.; Xiao, Y.; Wang, X.; Yang, J.; Liu, Z.; Wang, S.; Soo, H. S. Metal Halide Perovskites for Photocatalysis: Performance and Mechanistic Studies. *Chem. – Asian J.* **2024**, *19* (24), e202400787. https://doi.org/10.1002/asia.202400787.

(23) Huang, Y.; Yu, J.; Wu, Z.; Li, B.; Li, M. All-Inorganic Lead Halide Perovskites for Photocatalysis: A Review. *RSC Adv.* **2024**, *14* (7), 4946–4965. https://doi.org/10.1039/D3RA07998H.

(24) Zhu, X.; Lin, Y.; San Martin, J.; Sun, Y.; Zhu, D.; Yan, Y. Lead Halide Perovskites for Photocatalytic Organic Synthesis. *Nat. Commun.* **2019**, *10* (1), 2843. https://doi.org/10.1038/s41467-019-10634-x.

(25) Lee, J.; Molina, J. C. B.; Rosso, L.; Tüysüz, H. Halide Perovskite Photocatalysts for Solar Energy Harvesting: Concept, Major Advances, and Challenges. *ChemCatChem* **2025**, *17* (14), e00410. https://doi.org/10.1002/cctc.202500410.

(26) Zhou, Y.; Zhao, Y. Chemical Stability and Instability of Inorganic Halide Perovskites. *Energy Environ. Sci.* **2019**, *12* (5), 1495–1511. https://doi.org/10.1039/C8EE03559H.

(27) Wang, J.; Wang, J.; Li, N.; Du, X.; Ma, J.; He, C.; Li, Z. Direct Z-Scheme 0D/2D Heterojunction of $CsPbBr_3$ Quantum Dots/Bi_2WO_6 Nanosheets for Efficient Photocatalytic CO_2 Reduction. *ACS Appl. Mater. Interfaces* **2020**, *12* (28), 31477–31485. https://doi.org/10.1021/acsami.0c08152.

(28) Lv, K.; Li, Z.; Huang, X.; Cheng, Z.; Wang, Z.; Zhao, H. $CsPbBr_3$ Perovskite-Based Heterostructures in Photocatalysis: Mechanisms, Stability, and Multifunctional Performance. *Adv. Sci.* **2025**, *12* (34), e07747. https://doi.org/10.1002/advs.202507747.

(29) Das, R.; Patra, A.; Dutta, S. K.; Shyamal, S.; Pradhan, N. Facets-Directed Epitaxially Grown Lead Halide Perovskite-Sulfobromide Nanocrystal Heterostructures and Their Improved Photocatalytic Activity. *J. Am. Chem. Soc.* **2022**, *144* (40), 18629–18641. https://doi.org/10.1021/jacs.2c08639.

(30) Talla, A.; Driessen, B.; Straathof, N. J. W.; Milroy, L.; Brunsveld, L.; Hessel, V.; Noël, T. Metal-Free Photocatalytic Aerobic Oxidation of Thiols to Disulfides in Batch and Continuous-Flow. *Adv. Synth. Catal.***2015**, *357* (10), 2180–2186. https://doi.org/10.1002/adsc.201401010.

(31) Xu, L.; Deng, X.; Li, Z. Photocatalytic Splitting of Thiols to Produce Disulfides and Hydrogen over PtS/ZnIn2S4 Nanocomposites under Visible Light. *Appl. Catal., B* **2018**, *234*, 50–55. https://doi.org/10.1016/j.apcatb.2018.04.030.

(32) Kim, H. J.; Yoon, J. H.; Yoon, S. Photooxidative Coupling of Thiophenol Derivatives to Disulfides. *J. Phys. Chem. A* **2010**, *114* (45), 12010–12015. https://doi.org/10.1021/jp1077483.

(33) Xu, X.; Yan, L.; Huang, W.; Wang, Y.; Wang, M.; Feng, L.; Wang, P.; Wang, S. Facile and Efficient Transformation of Thiols to Disulfides *via* a Radical Pathway with *N*-Anomeric Amide. *RSC Adv.* **2024**, *14* (25), 17780–17784. https://doi.org/10.1039/d4ra03545c.

(34) Heras, B.; Kurz, M.; Shouldice, S. R.; Martin, J. L. The Name's Bond……disulfide Bond. *Curr. Opin. Struct. Biol.* **2007**, *17* (6), 691–698. https://doi.org/10.1016/j.sbi.2007.08.009.

(35) Dombkowski, A. A.; Sultana, K. Z.; Craig, D. B. Protein Disulfide Engineering. *FEBS Letters* **2014**, *588* (2), 206–212. https://doi.org/10.1016/j.febslet.2013.11.024.

(36) Park, K. W.; Leitao, E. M. The Link to Polysulfides and Their Applications. *Chem. Commun.* **2021**, *57* (26), 3190–3202. https://doi.org/10.1039/d1cc00505g.

(37) McKeen, L. W. 12 - Elastomers and Rubbers. In *The Effect of UV Light and Weather on Plastics and Elastomers (Third Edition)*; McKeen, L. W., Ed.; Plastics Design Library; William Andrew Publishing: Boston, 2013; pp 299–370. https://doi.org/10.1016/B978-1-4557-2851-0.00012-8.

(38) Wu, W.-B.; Wong, Y.-C.; Tan, Z.-K.; Wu, J. Photo-Induced Thiol Coupling and C–H Activation Using Nanocrystalline Lead-Halide Perovskite Catalysts. *Catal. Sci. Technol.* **2018**, *8* (16), 4257–4263. https://doi.org/10.1039/C8CY01240G.

(39) Misra, A. K.; Agnihotri, G. Nitric Acid Mediated Oxidative Transformation of Thiols to Disulfides. *Synth. Commun.* **2004**, *34* (6), 1079–1085. https://doi.org/10.1081/scc-120028640.

(40) Zhang, B.; Altamura, D.; Caliandro, R.; Giannini, C.; Peng, L.; De Trizio, L.; Manna, L. Stable $CsPbBr_3$ Nanoclusters Feature a Disk-like Shape and a Distorted Orthorhombic Structure. *J. Am. Chem. Soc.* **2022**, *144* (11), 5059–5066. https://doi.org/10.1021/jacs.1c13544.

(41) Toso, S.; Imran, M.; Mugnaioli, E.; Moliterni, A.; Caliandro, R.; Schrenker, N. J.; Pianetti, A.; Zito, J.; Zaccaria, F.; Wu, Y.; Gemmi, M.; Giannini, C.; Brovelli, S.; Infante, I.; Bals, S.; Manna, L. Halide Perovskites as Disposable Epitaxial Templates for the Phase-Selective Synthesis of Lead Sulfochloride Nanocrystals. *Nat. Commun.* **2022**, *13* (1), 3976. https://doi.org/10.1038/s41467-022-31699-1.

(42) Ravi, V. K.; Markad, G. B.; Nag, A. Band Edge Energies and Excitonic Transition Probabilities of Colloidal $CsPbX_3$ (X = Cl, Br, I) Perovskite Nanocrystals. *ACS Energy Lett.* **2016**, *1* (4), 665–671. https://doi.org/10.1021/acsenergylett.6b00337.

(43) Doblas, D.; Kister, T.; Cano-Bonilla, M.; González-García, L.; Kraus, T. Colloidal Solubility and Agglomeration of Apolar Nanoparticles in Different Solvents. *Nano Lett.* **2019**.

(44) Hasan, M. R.; Niebuur, B.-J.; Siebrecht, M.; Kuttich, B.; Schweins, R.; Widmer-Cooper, A.; Kraus, T. The Colloidal Stability of Apolar Nanoparticles in Solvent Mixtures. *ACS Nano* **2023**, *17* (10), 9302–9312. https://doi.org/10.1021/acsnano.3c00812.

(45) Wu, X. The Overlooked Solvent Effects: A Reconsideration of the Paradigm in Semiconductor Photocatalysis. *Energy. Environ. Sci.* 2025, 18, 1191–1204. https://doi.org/10.1039/D4EE04157G

(46) Rosa-Pardo, I.; Zhu, D.; Cortés-Villena, A.; Prato, M.; De Trizio, L.; Manna, L.; Galian, R. E.; Pérez-Prieto, J. The Dark Side of Lead-Free Metal Halide Nanocrystals: Substituent-Modulated Photocatalytic Activity in Benzyl Bromide Reduction. *ACS Energy Lett.* **2023**, *8* (6), 2789–2798. https://doi.org/10.1021/acsenergylett.3c00771.

(47) Fu, Y.; Lin, B.-L.; Song, K.-S.; Liu, L.; Guo, Q.-X. Substituent Effects on the S–H Bond Dissociation Energies of thiophenolsElectronic Supplementary Information (ESI) Available: Detailed Results of the Bond Lengths, Charge and Spin Distributions, and Vibration Frequencies. See Http://Www.Rsc.Org/Suppdata/P2/B2/B201003h/. *J. Chem. Soc., Perkin Trans. 2* **2002**, No. 7, 1223–1230. https://doi.org/10.1039/b201003h.

(48) Taft, R. W. SIGMA VALUES FROM REACTIVITIES[1]. *J. Phys. Chem.* **1960**, *64* (12), 1805–1815. https://doi.org/10.1021/j100841a003.

(49) Fónagy, O.; Szabó-Bárdos, E.; Horváth, O. 1,4-Benzoquinone and 1,4-Hydroquinone Based Determination of Electron and Superoxide Radical Formed in Heterogeneous Photocatalytic Systems. *J. Photochem. Photobiol. A: Chem.* **2021**, *407*, 113057. https://doi.org/10.1016/j.jphotochem.2020.113057.

(50) Zhu, M.; Lu, J.; Hu, Y.; Liu, Y.; Hu, S.; Zhu, C. Photochemical Reactions between 1,4-Benzoquinone and $O_2^{\bullet-}$. *Environ. Sci. Pollut. Res.* **2020**, *27* (25), 31289–31299. https://doi.org/10.1007/s11356-020-09422-8.

(51) Hao, J.; Liu, H.; Wang, K.; Sun, X. W.; Delville, J.-P.; Delville, M.-H. Hole Scavenging and Electron–Hole Pair Photoproduction Rate: Two Mandatory Key Factors to Control Single-Tip Au–CdSe/CdS Nanoheterodimers. *ACS Nano* **2021**, *15* (9), 15328–15341. https://doi.org/10.1021/acsnano.1c06383.

(52) Hou, X.; Huang, S.; Ou-Yang, W.; Pan, L.; Sun, Z.; Chen, X. Constructing Efficient and Stable Perovskite Solar Cells via Interconnecting Perovskite Grains. *ACS Appl. Mater. Interfaces* **2017**, *9* (40), 35200–35208. https://doi.org/10.1021/acsami.7b08488.

(53) Vickers, E. T.; Graham, T. A.; Chowdhury, A. H.; Bahrami, B.; Dreskin, B. W.; Lindley, S.; Naghadeh, S. B.; Qiao, Q.; Zhang, J. Z. Improving Charge Carrier Delocalization in Perovskite Quantum Dots by Surface Passivation with Conductive Aromatic Ligands. *ACS Energy Lett.* **2018**, *3* (12), 2931–2939. https://doi.org/10.1021/acsenergylett.8b01754.

(54) Rosa-Pardo, I.; Casadevall, C.; Schmidt, L.; Claros, M.; Galian, R. E.; Lloret-Fillol, J.; Pérez-Prieto, J. The Synergy between the $CsPbBr_3$ Nanoparticle Surface and the Organic Ligand Becomes Manifest in a Demanding Carbon–Carbon Coupling Reaction. *Chem. Commun.* **2020**, *56* (37), 5026–5029. https://doi.org/10.1039/D0CC01339K.

(55) Fairley, N.; Fernandez, V.; Richard-Plouet, M.; Guillot-Deudon, C.; Walton, J.; Smith, E.; Flahaut, D.; Greiner, M.; Biesinger, M.; Tougaard, S.; Morgan, D.; Baltrusaitis, J. Systematic and Collaborative Approach to Problem Solving Using X-Ray Photoelectron Spectroscopy. *Appl. Surf. Sci. Adv.* **2021**, *5*, 100112. https://doi.org/10.1016/j.apsadv.2021.100112.

(56) Helander, M. G.; Greiner, M. T.; Wang, Z. B.; Lu, Z. H. Pitfalls in Measuring Work Function Using Photoelectron Spectroscopy. *Appl. Surf. Sci.* **2010**, *256* (8), 2602–2605. https://doi.org/10.1016/j.apsusc.2009.11.002.

(57) Ramanath, G.; D'Arcy-Gall, J.; Maddanimath, T.; Ellis, A. V.; Ganesan, P. G.; Goswami, R.; Kumar, A.; Vijayamohanan, K. Templateless Room-Temperature Assembly of Nanowire Networks from Nanoparticles. *Langmuir* **2004**, *20* (13), 5583–5587. https://doi.org/10.1021/la0497649.

(58) Cabona, A.; Toso, S.; Cortés-Villena, A.; Rosa-Pardo, I.; Prato, M.; Ferri, M.; Pérez-Prieto, J.; Kriegel, I.; Manna, L.; Galian, R. E. Metal Halide Perovskite/Chalcohalide Heterojunctions for the Photoinduced Oxidative Coupling of *p*-Substituted Thiophenols. *ACS Applied Nano Materials* **2025.** https://doi.org/10.1021/acsanm.5c05834

CHAPTER 6

Bi/$Bi_{13}S_{18}Br_2$ Nano-Bell Heterostructures: Synthesis and Photo-electrocatalytic Properties

6.1 Heavy pnictogen chalcohalides

In Chapter 2, we introduced the class of metal chalcohalides and we focused in the previous chapter on the lead-based compounds. Another important subclass of materials is represented by the heavy pnictogen chalcohalides, in which the metal belongs to group 15 of the periodic table.[1] These compounds are described by the general formula $M_aE_bX_c$, where M is Bi^{3+}, Sb^{3+}, or As^{3+}; E is a chalcogen anion (S^{2-}, Se^{2-}, or Te^{2-}); and X is a halogen (Br^-, Cl^-, I^- or F^{2-}).[2]

The synthesis of the first heavy pnictogen chalcohalides dates back to the early 19th century, with the preparation of antimony sulfoiodide (SbSI) in 1824. Despite this early discovery, systematic scientific investigation did not emerge until the second half of the 20th century. Indeed, the discovery of photoconductivity in 1960, followed by the identification of ferroelectric behavior in 1962,[3] highlighted the technological relevance of these compounds and motivated extensive research.[4,5] Since then, heavy pnictogen chalcohalides have attracted growing interest as multifunctional semiconductors for optoelectronics and nonlinear optics applications. Among their appealing properties, we can recognize tunable band structures, high absorption coefficients, and potential for defect-tolerant behavior, analogous to that observed in other semiconductors such as halide perovskites.[6]

Generally, heavy pnictogen chalcohalides crystallize in orthorhombic structures, especially in the Pnma and Pnam space groups. They are characterized by rod- or needle-like morphologies, which derive from their intrinsic structural anisotropy, as these ternary compounds preferentially grow along the c-direction.[7] This anisotropy arises from the lone-pair electrons on the heavy pnictogen metal

cations (Bi^{3+}, Sb^{3+}, As^{3+}), which induce asymmetric coordination environments and promote low-dimensional structural motifs such as chains or layered frameworks.[6] Indeed, their crystal structures are typically characterized by the presence of M-E polyhedra, which share edges and corners. This shared network generates long 1D fragments stabilized by the secondary M-X interactions. Considering the bonding nature of these compounds, the M-E-X network results in mixed ionic and covalent interactions. The trivalent metal cations (Bi, Sb) do not provide sufficient charge for the chalcogen anions to satisfy a purely ionic bond. As a consequence, after partial electron transfer to the halogen (X) anions, the metal (M) and chalcogen (E) form covalent bonds. This leads the M-E bond to exhibit a more pronounced covalent behavior in comparison with the more ionic M-X bond. This characteristic bonding landscape, combined with the presence of non-bonding lone-pair electrons, gives rise to significant structural anisotropy, which strongly influences the physical properties of these materials, including their low lattice thermal conductivity, pronounced optical anisotropy, photoconductive behavior and notable dielectric responses.[7]

In addition to that, heavy pnictogen chalcohalides often exhibit a strong dependance of their electronic structure on the specific chalcogen and halogen species involved in the compound. In particular, heavier chalcogens like tellurium and halogen such as iodine exhibit lower band gaps in comparison with the ones of chalcohalides composed by lighter chalcogens (S and Se) and halogens (Br, Cl).[8] This reflects the progressive increase in orbital energy within the lattice. Regarding the optical properties, these materials can exhibit both direct and indirect band alignments, and they may display either n-type or p-type conductivity depending on their synthesis route and the resulting bonding environment within the crystal lattice.

From a synthetic perspective, the different preparation method can influence the anisotropic growth of the chalcohalides phase. In this context, low-temperature solvothermal and ion-exchange routes often promote nanoscale one-dimensional morphologies, whereas melt-growth or Bridgman techniques yield larger, well-faceted crystals with well-defined orientation along the chain direction. The strong correlation between synthetic procedure, morphological and electronic properties makes heavy pnictogen chalcohalides interesting to study for different applications.

6.1.1 Bismuth based chalcohalides NCs

Among these metal chalcohalides, the bismuth-based compounds[9–11] have attracted significant attention in recent years owing to their low cost, low toxicity, promising photovoltaic,[12] thermoelectric properties[13–15] and well-established solid-state chemistry.[16,17] Indeed, as mentioned above, these materials are primarily known in their bulk form; however, different synthetic strategies have been developed for nanocrystals as well.

For what concerns the colloidal synthesis, which is focus of this thesis, two routes have been developed for two distinct bismuth chalcohalide phases: the orthorhombic BiSX (X = Cl, Br, I)[18] and the hexagonal $Bi_{13}S_{18}X_2$ (X = Br, I) one.[19] These two compounds were synthetized for the first time by Carlo Giansante's group in collaboration with some members of our group back in 2022. BiSX (X = Cl, Br, I) and $Bi_{13}S_{18}X_2$ (X = Br, I) are obtained *via* hot injection of sulfur (trimethylsilyl sulfide) and bromine (benzoyl bromide or trimethylsilyl bromide) precursors at 180 °C in a bismuth-oleate solution, using 1-octadecene as solvent. The reaction runs for 15 minutes and then the material is purified *via* centrifugation (6000 rpm for 5 minutes). The formation of the hexagonal phase rather than the orthorhombic one is determined by the ratio between the bromine and sulfur precursors.

Both chalcohalide phases exhibit very similar morphological characteristics, as they form rod-shaped nanocrystals due to their anisotropic crystal structures, characterized by tubular Bi-S networks, with lengths reaching hundreds of nanometers. A comparable trend is observed in their optical properties: all phases possess an indirect band gap. The orthorhombic phase begins to absorb at around 650 nm for BiSCl and BiSBr, and at approximately 850 nm for BiSI. In contrast, the hexagonal phase exhibits an absorption onset in the near-infrared region. Both phases exhibit strong long-term stability under air conditions. Indeed, the XRD patterns of the samples as synthetized and after few weeks do not show significant modifications.[19] The remarkable light-absorption properties and promising stability of the orthorhombic phase has enabled the evaluation of the material in photo-electrocatalysis for the reduction of the iodine/iodide redox couple.[18] Furthermore, the BiSBr nanocrystals showed no appreciable signs of degradation under intense irradiation in an electrolytic solution containing the iodine/iodide redox couple. Such robustness is particularly noteworthy since photoelectrochemical measurements under similar conditions are often not suitable for Pb-chalcogenide and halide perovskite nanocrystals due to their rapid degradation. Concerning the

catalytic properties, also the hexagonal phase ($Bi_{13}S_{18}X_2$) showed activity for the photoreduction of CO_2 and Cr (VI), highlighting the potential of these materials in catalytic applications.[17]

Based on this knowledge, our initial objective was to synthesize a novel colloidal heterostructure composed of a bismuth-based chalcohalide and metallic bismuth, considering that elemental bismuth is already present in the system. This approach was motivated by the potential of colloidal nano-heterostructures[20–23] to integrate the properties of distinct materials within a single functional nanocomposite, potentially giving rise to emergent properties resulting from their interfacial interactions, as explained in Chapter 3. On these bases, in the previous chapter we discussed the benefits of using a semiconductor-semiconductor heterojunction in photocatalysis. Here, we will explore another heterostructure's architecture composed of a metal and a semiconductor. This system stands out as promising candidate for light harvesting applications,[24–26] as the semiconductor domain can convert light into electron-hole pairs and the metal domain makes them easy to access. Relevant examples include Au-CdSe,[27] Pt-CdS[28] and M-$CsPbBr_3$ (M = Pd,Pt) heterostructures,[29] which exhibit promising performance as light-harvesters,[30–32] photodetectors,[33] and photocatalysts.[34]

6.2 Synthesis of Bi/$Bi_{13}S_{18}Br_2$ nano-bell heterostructures

Given the purpose to synthetize a new heterostructure that could couple a metallic domain with a semiconductor, in this chapter we demonstrate the growth of metallic-Bi/$Bi_{13}S_{18}Br_2$-chalcohalide architecture exhibiting a bell-shape (Figure 6.1a-e). This was made possible by introducing substantial modifications in the synthesis procedure for bismuth chalcohalide nanocrystals, initially developed by Quarta *et al.* in collaboration with our research group.[18] Notably, the original protocol relied on bis(trimethylsilyl)sulfide (TMS) and benzoyl bromide (BzBr) as highly reactive sulfur and bromine precursors. Additionally, this synthetic route avoided the use of amines as surfactants to prevent the reduction of Bi^{3+} to metallic Bi (Figure 6.8, Appendix). Indeed, it is known that amines can act as reducing agents due to the presence of unpaired electrons.

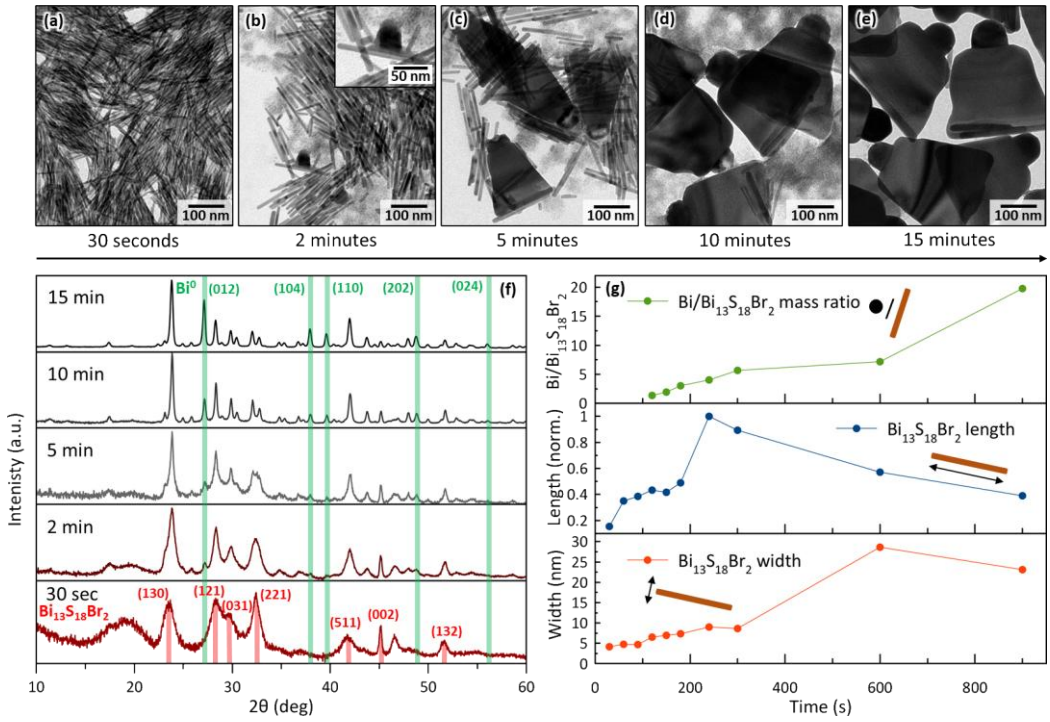

Figure 6.1. Synthesis of $Bi/Bi_{13}S_{18}Br_2$ nano-bells. a-e) TEM images of aliquots collected at 0.5, 2, 5, 10, and 15 mins from the start of the reaction. The inset in panel (b) highlights an early-stage $Bi/Bi_{13}S_{18}Br_2$ heterostructure, where the chalcohalide domain is still rod-shaped. f) XRD patterns of the aliquots, showing a progressive enlargement of the chalcohalide domains (peaks becoming sharper) and the growth of metallic-Bi domains (additional peaks appearing, marked in green). g) Compositional and morphological descriptors extracted from the Rietveld fit of XRD profiles. From top to bottom: $Bi/Bi_{13}S_{18}Br_2$ mass ratio (metallic Bi is not detectable in the first three patterns, top); average $Bi_{13}S_{18}Br_2$ crystallites length along the *c* lattice direction (rod length, middle); average $Bi_{13}S_{18}Br_2$ crystallites thickness perpendicular to the *c* lattice direction (bottom). Reproduced with permission from ref 60. Licensed under CC-BY 4.0. Copyright © 2025 The Authors.

Here, we hypothesized that the formation of functional metal-semiconductor heteroarchitectures could be facilitated by regulating this reduction process. On this basis, the synthetic procedure for orthorhombic BiSBr nanocrystals was modified by introducing oleylamine immediately before the addition of the sulfur and bromine precursors. Unexpectedly, these preliminary experiments resulted in the formation of $Bi_{13}S_{18}Br_2$ rather than BiSBr. Notably, peculiar heterostructures were detected, in which a triangular sheet of $Bi_{13}S_{18}Br_2$ was attached to a metallic bismuth cap (Figure 6.9, Appendix), giving rise to a bell-shaped morphology in projection.

The nucleation of $Bi_{13}S_{18}Br_2$ rather than BiSBr suggests the presence of a more reducing reaction environment, in agreement with the incorporation of subvalent $[Bi\text{-}Bi]^{4+}$ dimers within the $Bi_{13}S_{18}Br_2$ structure.[19,35,36] Nevertheless, the reduction of metallic bismuth was not effectively promoted by the addition of a primary amine, contrary to initial expectations. To overcome this, we employed a tertiary amine (*N,N* - didodecylmethylamine) instead of oleylamine, based on the hypothesis that the inductive effect of the alkyl substituents, together with significant steric hindrance, would make it a stronger nucleophile and more effective reducing agent, thereby promoting the heterogeneous nucleation of bismuth on the surface of $Bi_{13}S_{18}Br_2$ nanorods.

Figure 6.1a-e depict the temporal evolution of particle morphology, monitored by collecting several aliquots at selected time steps. During the initial stages of the synthesis (30 sec - 1.5 min, see Figure 6.10a-c, Appendix), transmission electron microscopy (TEM) images revealed the presence of just $Bi_{13}S_{18}Br_2$ nanorods. These rods nucleated immediately after the injection of the bromine and sulfur precursors and exhibited a gradual increase in length during the early stages of the reaction. However, after 2 minutes, metallic-Bi domains started to form at the center of some nanorods, appearing as large and dark hemispheres (Figure 6.1b). As the reaction proceeded, the population of free nanorods steadily decreased, while the metal-rod heterostructures increased in lateral size and progressively developed their characteristic bell-shaped morphology. After 15 minutes, no free nanorods were observed in the sample (Figure 6.1d-e, see also Figure 6.10 d-h, Appendix).

The trend observed via electron microscopy was confirmed by Rietveld refinements of X-ray diffraction (XRD)[37] patterns collected from the same reaction aliquots (Figure 6.1f, see also Figure 6.11, Appendix). Although metallic bismuth was initially absent, it became detectable after approximately 2 min, with its relative fraction increasing linearly as the reaction proceeded (Figure 6.1g, top). In parallel, the average lateral dimension of the $Bi_{13}S_{18}Br_2$ phase, determined using an anisotropic spherical harmonics model of the crystallite shape,[18,38–40] grew from an initial value of about 4 nm to ~ 25 nm. The nanorod length also increased at early stages of the reaction (up to ~ 4 min), indicating continued growth of $Bi_{13}S_{18}Br_2$ nanorods. After 5 minutes, however, the length of these isolated rods decreased rapidly, consistent with their progressive consumption during the formation of nano-bell structures, likely driven by an Ostwald ripening mechanism. It should be noted that absolute rod length values from XRD are not strictly quantitative, as modeling strongly anisotropic and flexible particles along their longest dimension

remains challenging. Nevertheless, relative length trends are meaningful, and agree with TEM observations, albeit with lower statistics (See Figure 6.12, Appendix).

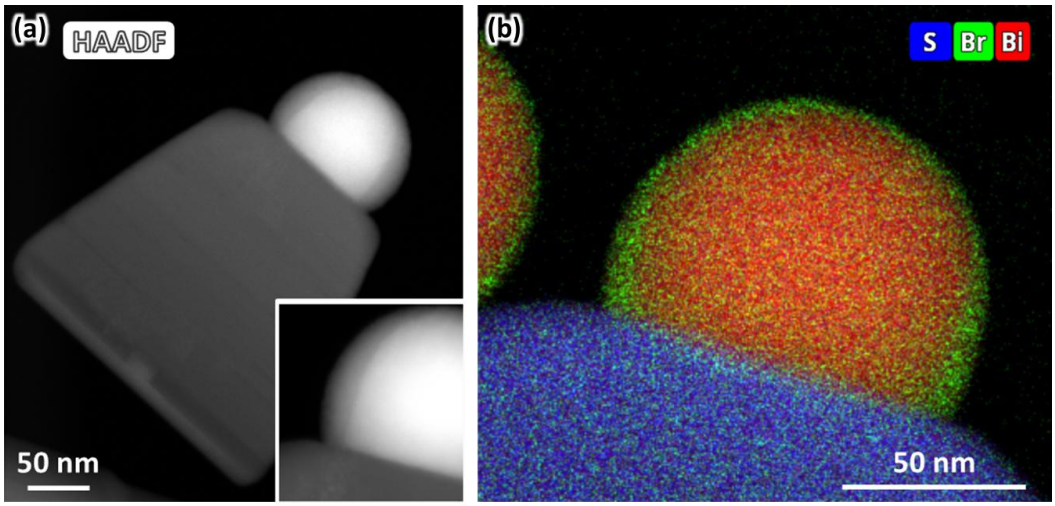

Figure 6.2. Composition and structure of Bi/$Bi_{13}S_{18}Br_2$ nano-bells. a) HAADF image of one heterostructure. b) STEM-EDX compositional map of the Bi/chalcohalide contact region, showing the presence of a Br-rich shell surrounding the metal hemisphere. Adapted with permission from ref 60. Licensed under CC-BY 4.0. Copyright © 2025 The Authors.

Scanning-transmission electron microscopy (STEM, Figure 6.2a) and energy-dispersive X-ray spectroscopy (EDX, Figure 6.2b) analyses provided further insight into the structural and compositional features of the heterostructures. The obtained images and corresponding EDX elemental maps evidenced that Bi, S, and Br atoms are uniformly distributed within the chalcohalide domain (Figure 6.13, Appendix), confirming the high compositional homogeneity of this region. Moreover, the presence of a thin Br-rich interfacial layer, approximately 1.3 nm in thickness, was detected on the surface of the metallic Bi hemisphere (Figure 6.14, Appendix). This layer becomes significantly thicker (~7–8 nm) at the neck region connecting the metallic and chalcohalide domains, suggesting a local accumulation of bromine species. The morphology and composition of this interfacial region indicate that it is likely polycrystalline in nature and originates from residual, unreacted bromine precursor remaining in the solution during the synthesis. This hypothesis is supported by the compositional gradients observed across the interface and by the correspondence between the atomic ratios determined by EDX and those expected from the $Bi_{13}S_{18}Br_2$ stoichiometry (Figure 6.15, Appendix). These results collectively confirm the well-defined chemical separation between the metallic Bi

and chalcohalide domains while also highlighting the presence of a distinct, Br-rich interfacial zone on the metallic hemisphere.

6.3 Epitaxial interface resolution

The interface was further investigated by high-resolution (HR)-STEM and 4D-STEM. The results are consistent with the presence of an epitaxial relationship between the two domains, evidenced by the matching lattice-fringe periodicity across the interface and the near alignment of the corresponding atomic planes. Based on this evidence, we sought to identify the most likely epitaxial interfaces using the Ogre software.[41] As described in Chapter 3, Ogre enables the prediction of plausible epitaxial relationships between two crystalline phases by systematically comparing their lattice parameters and crystallographic symmetries. In our case, the crystallographic information for both the bismuth chalcohalide phase ($Bi_{13}S_{18}Br_2$) and the metallic bismuth domain was available, allowing us to perform a targeted analysis of potential lattice matching and orientation relationships.

Indeed, a plausible epitaxial relation is the (001)//(1-10) - Bi/$Bi_{13}S_{18}Br_2$, which was identified by feeding the probable lattice orientations inferred by 4D-STEM into the lattice matching module of the Ogre library. In particular, the morphology of early stage heterostructures suggests that metallic Bi attaches to the sides of the chalcohalide rods. These nanocrystals grow preferentially along the [001] direction, (Figure 6.3a), indeed the resulting particles nucleate in the shape of nanorod which is strongly anisotropic. This implies that $Bi_{13}S_{18}Br_2$ exposes a (hk0) plane at the interface. Fourier transforms of HAADF images (Figure 6.3b) support this hypothesis, as indicated by the three parallel stripes of reflections corresponding to the [hk-1], [hk0], and [hk1] planes in reciprocal space (Figure 6.3 c-d). The Bi orientation, however, could not be fully reconstructed from FFT due to the visibility of only a single reflection, identified as [012] based on its real-space periodicity (d = 3.28 Å).

To resolve this, the Ogre library's lattice matching algorithm was used to screen potential (hkl)//(1-10) Bi/$Bi_{13}S_{18}Br_2$ interfaces (with Bi-h, k, l < 2). The epitaxial relation was evaluated by its ability to reproduce the observed relative orientation of the lattice vectors [001]-$Bi_{13}S_{18}Br_2$ and [012]-Bi. The analysis identified the (001)//(1-10) Bi/$Bi_{13}S_{18}Br_2$ relation as the most suitable one, characterized by a 2D supercell with an area of 248 Å² and 2.4% strain. The software was able to find a plausible surface supercell, which can describe both domains (Bi and $Bi_{13}S_{18}Br_2$) at

the interface, as illustrated in Figure 6.3e. The yellow dashed lines in panel (c) mark the orientations of the Bismuth lattice vectors as predicted by Ogre. The plausible epitaxial model of the interface (001)//(1-10) – Bi/$Bi_{13}S_{18}Br_2$ is shown in figure 6.3f with the two domains oriented in accordance with panel (b). Only bismuth atoms are shown for clarity, and the relative positions of the two domains are estimated (i.e., no model optimization performed).

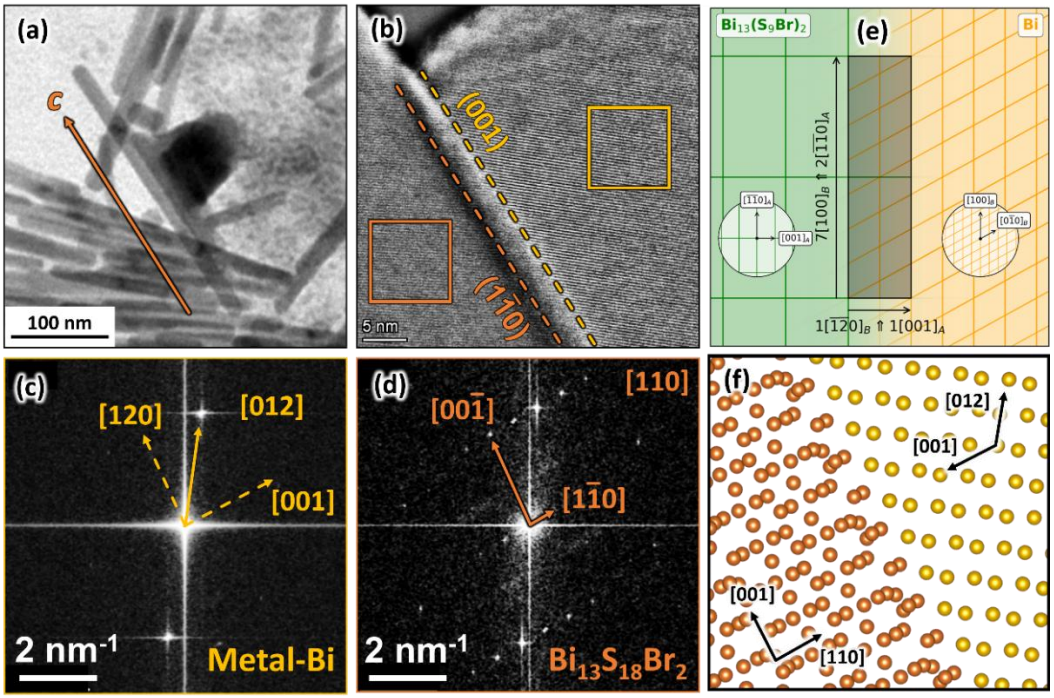

Figure 6.3. Identification of the 001//1-10 – Bi/$Bi_{13}S_{18}Br_2$ epitaxial relation. a) TEM image of the early stage heterostructure. b) HAADF image of the Bi/$Bi_{13}S_{18}Br_2$ interface region, with lattice fringes enhanced by a high-pass filter. c-d) Fourier transforms of the yellow (metallic bismuth) and orange areas ($Bi_{13}S_{18}Br_2$), respectively of panel (b). e) Supercell scheme, showing the relative orientation of the metallic Bi and $Bi_{13}S_{18}Br_2$ lattice vectors at the interface. f) Proposed Bi/$Bi_{13}S_{18}Br_2$ epitaxial model of the interface as produced by Ogre. Adapted with permission from ref 60. Licensed under CC-BY 4.0. Copyright © 2025 The Authors.

6.4 Growth mechanism of Bi/$Bi_{13}S_{18}Br_2$ nano-bell HSs

Once all these data were combined, we were able to outline a possible growth mechanism for the Bi/$Bi_{13}S_{18}Br_2$ nano-bells (Figure 6.4a). The process begins with the injection of bis(trimethylsilyl)sulfide and benzoyl bromide, which triggers the nucleation of $Bi_{13}S_{18}Br_2$ nanorods, driven by the precursors' reactivity and the ionic

character of the chalcohalides. During the first 2 minutes of the synthesis, only nanorods are present in the reaction environment. Soon after, the tertiary amine begins to reduce Bi^{3+} to metallic bismuth, a process facilitated by the nanorods acting as heterogeneous nucleation templates. This reduction process proceeds gradually, reflecting both the moderate reducing power of the tertiary amine and its progressive consumption during the reaction.

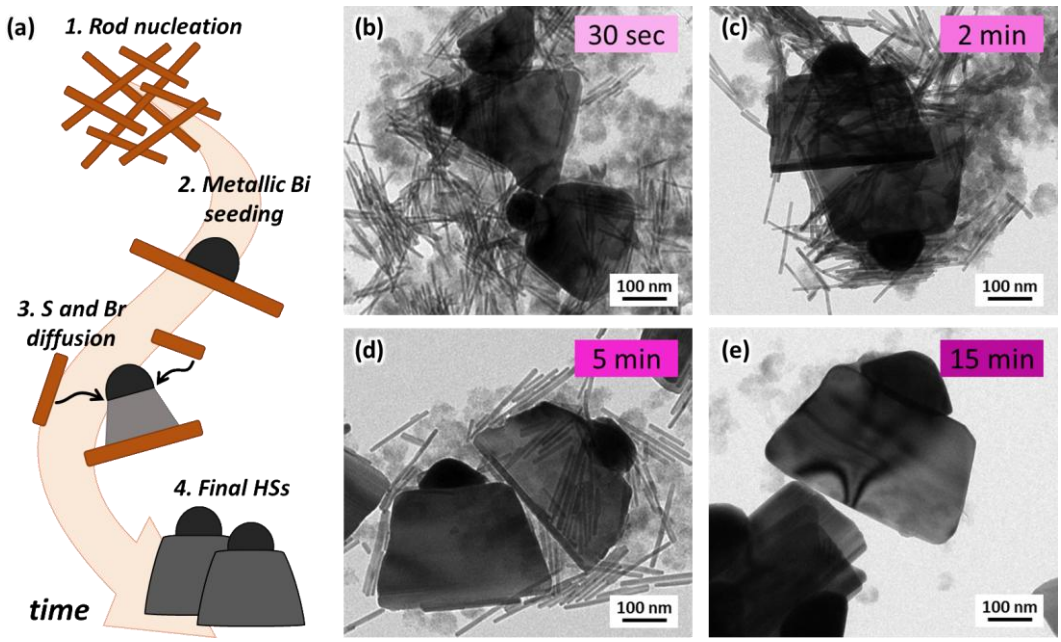

Figure 6.4. Possible reaction mechanism and Ostwald ripening growth test. a) Proposed reaction mechanism. b,c,d,e) TEM images of Bi/$Bi_{13}S_{18}Br_2$ solution aliquots taken at (b) 30 sec, (c) 2 min, (d) 5 min and (e) 15 min after the two crude reaction solutions (one of nanorods and one of bells) have been put to react together at 180°C. Adapted with permission from ref 60. Licensed under CC-BY 4.0. Copyright © 2025 The Authors.

Once the Bi/$Bi_{13}S_{18}Br_2$ interface forms, it serves as a sink for excess anion precursors from the reaction medium. Bromine is already found at the surface of the metallic hemisphere, while sulfur adsorption promotes additional $Bi_{13}S_{18}Br_2$ growth at the interface. As a result, the chalcohalide sheet expands, gradually displacing the original nanorod, which now forms the lower edge of the bell structure. Similar growth mechanisms are well established in nanofabrication via molecular beam epitaxy, for example, Au nanoparticles driving the growth of GaAs nanopillars,[42–44] but remain rare in colloidal heterostructures.[45] The mechanism continues until the solution is depleted of precursors (~5 min). At this stage, Ostwald ripening drives a further material transfer from the nanorods to the

heterostructures. Consequently, the remaining metal-free nanorods shrink and eventually disappear, leaving only the fully formed Bi/$Bi_{13}S_{18}Br_2$ nano-bells at the conclusion of the reaction.

To further validate this mechanism, two separate reaction batches were combined: one in which the nano-bells were allowed to fully develop, and another that had been quenched at the nanorod stage after 1.5 minutes of reaction. The resulting mixture of nano-bell heterostructures and nanorods was reheated to 180 °C to resume the reaction for an additional 15 minutes. Aliquots at different reaction times were taken and analyzed by TEM to understand how the system behaves. As expected, the nanorods from the second batch did not develop into new, small heterostructures; rather, they were gradually consumed to further enlarge the pre-existing nano-bells (see Figure 6.4b-e). Indeed after 2 and 5 min of reaction, the nucleation of metallic bismuth on the nanorods was not observed, but the NCs serve as reservoir for the already exiting heterostructures. The morphology evolution highlights the transfer of material from the nanorods to the nano-bells, which confirms the hypothesis of an Ostwald ripening-mediated growth mechanism. Interestingly, it is also evident how the bismuth domain becomes progressively faceted, and how, at some point, the chalcohalide resumes expanding along the *c*-preferred orientation growth, tipical of the $Bi_{13}S_{18}Br_2$ phase. (Figure 6.16, Appendix)

6.4.1 Strain analysis on Bi/$Bi_{13}S_{18}Br_2$ nano-bell HSs

The epitaxial relationship proposed in Figure 6.3f should induce expansion of the chalcohalide along the plane of the interface. To investigate this, we performed a 4D-STEM analysis, scanning across individual heterostructures while recording local electron diffraction patterns. This analysis revealed a strain field originating from the Bi/$Bi_{13}S_{18}Br_2$ interface.

Reconstruction of the linear strain components (ϵ_{xx} and ϵ_{yy}), along with the shear strain and local lattice rotation (ϵ_{xy} and θ) (Figure 6.5a-d) using py4DSTEM[46] demonstrates that the $Bi_{13}S_{18}Br_2$ lattice expands along ϵ_{yy} parallel to the interface, while a corresponding compression along ϵ_{xx} maintains the unit cell volume, in agreement with the predictions. Figure 6.5e illustrates a virtual bright field image reconstructed from the diffraction patterns of the two domains (Bi and $Bi_{13}S_{18}Br_2$) collected at each pixel, attesting their high crystallinity.

Interestingly, HAADF tilt series revealed that the darker domain often observed at the base of the bells in TEM images does not correspond to a local thickening. Instead, it arises from a curling of the chalcohalide sheet at its lower edge (Figure 6.5f). This behavior is likely a response to accommodate some interfacial strain and is facilitated by the hexagonal crystal structure of $Bi_{13}S_{18}Br_2$, which allows the domain to expose the same surface at the interface after a 60° rotation.

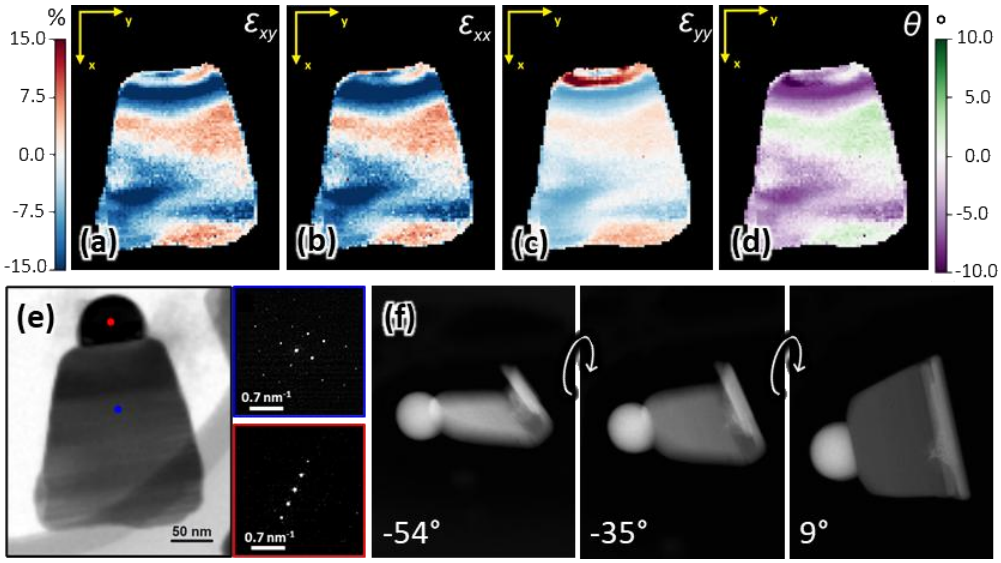

Figure 6.5. 4D-STEM and tomography analysis of Bi/$Bi_{13}S_{18}Br_2$ nano-bells. a-b) Map of the shear strain and rotation of the lattice. c-d) $Bi_{13}S_{18}Br_2$ strain field components along the x- and y-directions. The x and y axes in panels (c-d) indicate the images reference system and are not related to crystallographic directions. e) Virtual bright field image reconstructed from the diffraction patterns of Bi and $Bi_{13}S_{18}Br_2$ collected at each pixel. f) Frames from a HAADF tilt series, showing curling of the lower section of a bell. Adapted with permission from ref 60. Licensed under CC-BY 4.0. Copyright © 2025 The Authors.

6.5 Photo(electro)catalytic properties of Bi/$Bi_{13}S_{18}Br_2$ HSs

Once the growth mechanism of the Bi/$Bi_{13}S_{18}Br_2$ heterostructure and the epitaxial relationship between the two domains had been elucidated, the resulting nanobell architectures were evaluated for their photo(electro)catalytic properties. This investigation was motivated by the fact that the intimate junction between a metallic and a semiconductor domain can promote efficient charge carrier separation and transfer, limiting the recombination phenomenon, thereby enhancing the catalytic activity of the system, as explained in Chapter 3. Given the band gap of $Bi_{13}S_{18}Br_2$ (1.65 eV),[47] its high optical absorption coefficient,[19] and the intimate

structural connection with the metallic Bi domain, this system provides an effective platform for visible-light-driven processes. The coherent epitaxial interface ensures efficient electronic coupling and favorable band alignment, promoting electron transfer from the semiconductor to the metal while retaining holes in the semiconductor. These synergistic effects make the $Bi/Bi_{13}S_{18}Br_2$ nanobell heterostructures promising candidates for applications such as photocatalysis and photoelectrochemical energy conversion.

6.5.1 Photodegradation of organic dyes

In order to test the photocatalytic properties of these new architectures, the photodegradation of Rhodamine B (RhB) was selected as a model reaction, given that other bismuth-based semiconductors have demonstrated activity in this process.[48,49] Experiments were carried out in isopropanol under irradiation at 420 nm (see Methods), leading to complete RhB degradation within 1 hour. (Figure 6.6a). The photodegradation process was monitored every 15 minutes by recording absorbance spectra. Due to the relatively large size of the nano-bells, which promotes their aggregation in suspension, a centrifugation step before spectral acquisition was required to minimize light scattering effects.

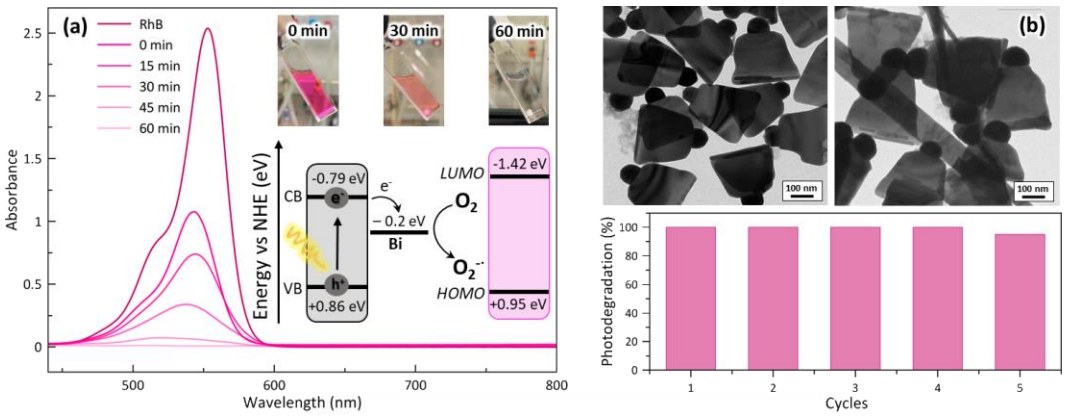

Figure 6.6. Photo- and photoelectro-catalytic activity of $Bi/Bi_{13}S_{18}Br_2$ nano-bells. a) Absorption spectra and pictures (insets) of the RhB solution taken at various stages of the photodegradation reaction (top) and scheme of the proposed photodegradation mechanism (down). b) TEM images of HSs before (left) and after (right) 5 cycles of RhB photodegradation (top); photodegradation activity for the five cycles (down). Adapted with permission from ref 60. Licensed under CC-BY 4.0. Copyright © 2025 The Authors.

Control experiments carried out without the photocatalyst (nano-bells) showed that the intrinsic photodegradation of the dye was negligible under these conditions

(4.5 %, Figure 6.17a, Appendix). Similarly, dark experiments, where the adsorption-desorption equilibrium between the catalyst and RhB was established before particle removal, led to only a minor decrease in absorbance (< 1 % RhB adsorption on the HSs, Figure 6.17b, Appendix). Together, these results confirm that the observed dye degradation arises from a photocatalytic process mediated by the Bi/$Bi_{13}S_{18}Br_2$ heterostructures, serving as active catalyst.

The RhB degradation was further investigated in the presence of benzoquinone, a known scavenger of superoxide anions ($O_2{\cdot}^-$),[50] to validate the photocatalytic mechanism. Under these conditions, only 5.4 % of the dye was degraded (Figure 6.18a Appendix), indicating that $O_2{\cdot}^-$ plays a crucial role in the process. Consistently, carrying out the reaction under an oxygen-free (N_2) atmosphere, which suppresses superoxide formation, resulted in almost complete inhibition of RhB photodegradation. The involvement of hydroxyl radicals (·OH) was excluded, as isopropanol efficiently scavenges ·OH.[51,52] A summary of control experiments, including reactions conducted under N_2, in the presence of benzoquinone, without photocatalyst, and in the dark condition, is provided in Figure 6.18b (Appendix).

Based on these findings, the reaction mechanism illustrated in Figure 6.6a (inset) is proposed. Upon light absorption, photogenerated electrons transfer from the $Bi_{13}S_{18}Br_2$ domain to the metallic Bi regions, which serve as co-catalytic sites. As a result, this charge separation reduces the likelihood of electron-hole recombination, as the hole remains localized on the chalcohalide domain. The electrons can then reduce O_2 to superoxide anions ($O_2{\cdot}^-$), which subsequently oxidizes the RhB molecules.[53,54] The exact fate of the photogenerated holes remains uncertain, they may either participate in the oxidation of isopropanol or further activate $O_2{\cdot}^-$, generating singlet oxygen ($^1O_2$), a highly reactive oxidizing species. The marked decrease in RhB degradation observed in the presence of benzoquinone confirms that $O_2{\cdot}^-$ is the primary reactive oxygen species (ROS) responsible for the photocatalytic process. The photodegradation process mediated by this reactive oxygen species (ROS) is likely to proceed through N-de-ethylation, chromophore cleavage, and eventual complete mineralization. The hypsochromic shift observed in the absorption spectra during irradiation ($\Delta\lambda$ = 16 nm at 45 min) suggests N-de-ethylation of RhB, forming of a series of N-de-ethylated intermediates. This is likely followed by the cleavage of the chromophore, indicating a stepwise breakdown of the dye molecule, consistent with previous studies.[55] Moreover, the use of isopropanol as the solvent excludes the involvement of hydroxyl radicals ($OH^{\cdot}$) and photogenerated holes (h^+), since IPA is known to efficiently scavenge both species.[56]

Further photocatalytic tests performed using methylene blue (MB) evidenced similar behavior to that observed for Rhodamine B (RhB), with approximately 93% degradation achieved after 2 hours of visible-light irradiation (Figures 6.19-6.20, Appendix). In contrast, no significant degradation was detected when methyl orange (MO) was used under the same experimental conditions (Figure 6.21, Appendix). This marked difference in photocatalytic performance can be attributed to the distinct molecular structures and charge characteristics of the dyes. This difference is due to the poor surface affinity between Methyl Orange, an anionic dye, with the photocatalyst, limiting the adsorption of MO molecules on the active sites of the heterostructures, thereby hindering their subsequent photodegradation. On the other hand, Methylene blue and Rhodamine B are cationic dyes, which exhibit strong electrostatic interactions with the Bi/$Bi_{13}S_{18}Br_2$ nano-bells. All these findings agree with the strongly negative Zeta potential value of the heterostructures (–58.3 mV, Table 6.1, Appendix). These outcomes emphasize the importance of interfacial charge interactions and right adsorption-desorption equilibrium between the dye and the photocatalyst in determining the photocatalytic selectivity of Bi/ $Bi_{13}S_{18}Br_2$.

Notably, the nano-bells maintained almost complete photocatalytic activity, achieving approximately 95% degradation of the selected dyes even after five photodegradation cycles. (Figure 6.6b). Minimal catalyst degradation and only slight aggregation were observed, despite extended exposure to a polar medium. Although the large size of the nanocrystals limits their colloidal stability, post-reaction TEM analysis revealed no significant morphological changes, attesting the robustness of the heterostructures. These results highlight the potential of these heterostructures for practical applications that demand both durability and reliable performance.

6.5.2 Photo-electrocatalysis of CO_2 reduction reaction

Motivated by this remarkable stability, a preliminary evaluation of Bi/$Bi_{13}S_{18}Br_2$ heterostructures for the CO_2 reduction reaction (CO_2RR) was attempted. In this context, metallic-Bi is a well-established catalyst for CO_2RR, and the heterostructures' resilience toward a polar solvent such as IPA suggested they could also withstand water. Furthermore, the valence and conduction band positions of $Bi_{13}S_{18}Br_2$ are suitably aligned to enable CO_2 reduction from a thermodynamic standpoint.

The CO_2RR tests were performed employing the electrochemical setup previously reported by members of the group.[57] In brief, photoelectrodes were prepared by spin-coating the $Bi/Bi_{13}S_{18}Br_2$ nano-bells onto fluorine-doped tin-oxide (FTO) glass substrates, which were then assembled in a three-electrode, single-compartment quartz cell (see Figure 6.7a and Methods). Preliminary Open Circuit Voltage (OCP, Figure 6.22, Appendix) measurements under intermittent 415 nm illumination revealed a photo-response, in the form of a reversible shift toward more cathodic potentials when the light was on. Figure 6.22 in the Appendix gathers the OCP traces collected on control (a) and Bi HSs (b) samples.

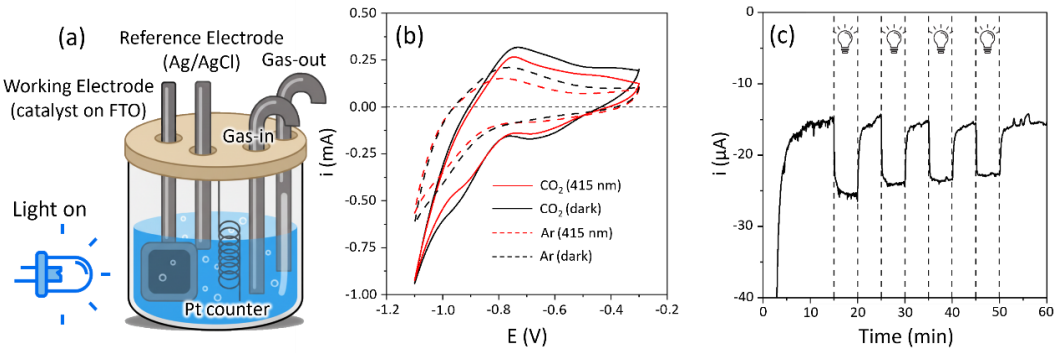

Figure 6.7. Photoelectro-catalytic activity of $Bi/Bi_{13}S_{18}Br_2$ nano-bells. a) Scheme of the cell used for the photo-electrochemical testing of heterostructure-based electrodes. b) Cyclic voltammetry traces collected on the heterostructures (v = 100 mV s^{-1}). The dashed curves have been collected under Ar bubbling (blank tests, only hydrogen evolution reaction is possible), while the full traces are related to CO_2 reduction reaction tests. Black: dark conditions. Red: 415 nm LED illumination. c) Chronoamperometric scan, performed at -1 V vs the reference electrode under intermittent illumination. Adapted with permission from ref 60. Licensed under CC-BY 4.0. Copyright © 2025 The Authors.

Upon illumination, the open circuit voltage of control sample and heterostructures show a decrease in absolute value (i.e., the potential shifts towards more cathodic values). In both cases, this behavior is transient and reversible. Noteworthy, Bi HSs exhibit the noisier and more complex trend (Figure 6.22b), with several spikes in the OCP value during the illumination. Nonetheless, a clear decrease/increase when the illumination is switched on/off is evident throughout the whole graph, thus confirming the interaction between Bi HSs and the light source. Conversely, Cyclic Voltammetry (CV)[58] displayed limited sensitivity to light in terms of current/voltage relationship (black versus red traces in Figure 6.7b). For reference, a comparable signal was measured from the bare FTO control electrode, (Figure 6.23a in the Appendix) CVs do not show a significant variation

upon illumination. This might be due to the limited contribution of the photogenerated currents with respect with the currents generated by the direct voltage application.

As for Bi HSs electrodes, CVs of bare FTO show additional voltammetric features when CO_2 is fed to the system, indicating a possible interaction of the material with CO_2. However, it must be noticed that the potentials screened in the bare FTO testing are much more cathodic than those investigated for Bi-based samples (Figure 6.23b). This indicates a general inertness of FTO towards both HER and CO_2RR.

However, clear changes in the CV profiles were observed after introducing CO_2 into the system, indicating catalytic activity. Under argon atmosphere (dashed lines in Figure 6.7b) the voltammogram exhibits a smooth response with a clear onset potential (E_{Onset}) around -0.8 V vs RE, corresponding to the Hydrogen Evolution Reaction (HER). In contrast, in the presence of CO_2 (full lines in Figure 6.7b), additional features appear in the voltammogram, with peaks or wave at *ca*. -0.6 and -1 V vs RE, consistent with the CO_2 pre-adsorption and reduction onset. This hypothesis is further supported by the increase in current density at more cathodic potentials, suggesting that CO_2RR contributes to the current attributed to HER under Ar.

To investigate the distribution of CO_2RR and parasitic HER products as well as the Faradaic efficiency, a 1-hour chronoamperometric (CA) measurement was carried out at -1 V vs RE under CO_2RR conditions. Intermittent illumination (5-minute on/off cycles, Figure 6.7c) clearly enhanced the current density, confirming the photoelectrochemical activity of the heterostructures for CO_2RR, as no such photoresponse was observed in control experiments (Figure 6.23b, Appendix). Despite these indications of CO_2RR activity, particularly on electrodes based on HSs, accurate detection, and quantification of reaction products, including parasitic H_2 from HER, were limited by the low currents recorded, which correspond to low production rates.

Overall, the inability to reliably quantify the CO_2RR products does not appear to stem from a lack of catalytic activity, but rather from intrinsic limitations of the experimental setup employed. Indeed, the adaptation of our electrochemical CO_2RR setups, originally optimized for flow-operation, was not specifically designed for product collection and quantitative analysis. In particular, operation under continuous flow conditions prevents the accumulation of gaseous products in

the cell headspace, resulting in concentrations below the instrumental detection limits (Figure 6.24a Appendix). On the other hand, the relatively large electrolyte volume combined with the low current densities recorded leads to significant dilution of liquid-phase products, hindering their reliable identification by HPLC. (Figure 6.24b Appendix). Therefore, future investigations should implement an experimental configuration specifically tailored for product quantification, such as compartmentalized cells, static or gas-tight systems, in order to establish a quantitative correlation between the observed photoelectrocatalytic activity and the actual reaction yields and selectivity.

6.6 Conclusions

In conclusion, this chapter reports a synthetic protocol to obtain Bi/$Bi_{13}S_{18}Br_2$ metal/semiconductor heterostructure through the controlled introduction of a reducing agent. The resulting architectures exhibit a distinctive bell-shaped morphology, which derives from a complex and multi-step growth mechanism. This process involves the initial formation of $Bi_{13}S_{18}Br_2$ nanorods, followed by the nucleation of metallic bismuth on their surface, and a final interfacial growth stage driven by Ostwald ripening. The nano-bell heterostructures exhibit excellent photocatalytic performance under visible-light irradiation for the degradation of Rhodamine B and Methylene Blue. Preliminary activity toward CO_2 reduction was also demonstrated. Notably, these heterostructures show outstanding structural and chemical stability under operando conditions, even in the presence of polar solvents such as water and isopropanol. This remarkable robustness enables to employ the nano-bells for multiple photocatalytic cycles. The potential of these new architecture was also highlighted by Pradhan *et al.* in a recent report, where they synthetized similar metal-semiconductor heterostructures based on bismuth chalcohalides and exploit them for photocatalytic applications.[59] Overall, this work establishes a versatile synthetic approach to obtain a metal-semiconductor heterostructure, characterized by the use of non-toxic and earth-abundant elements. It demonstrates that functional heteroarchitectures could enhance the photo(electro)catalytic performances, highlighting the potential of these nano-bells for future applications, both within and beyond the field of photocatalysis.

All the results presented in this chapter are also reported in the publication.[60]

6.7 Methods

Chemicals

All chemicals were of the highest purity available unless otherwise noted and were used as received. Bismuth (III) acetate ($Bi(Ac)_3$; 99.99 %), oleic acid (technical grade, 90 %), 1-octadecene (technical grade, 90 %), bis(trimethylsilyl)sulfide ($(Me_3Si)_2S$; synthesis grade) and trimethylsilyl bromide ($(Me_3Si)Br$; 97 %) were purchased from Sigma-Aldrich. *N,N* - Didodecylmethylamine (85%) was purchased from TCI. Hexane and toluene were purchased from Sigma-Aldrich. All solvents were purchased anhydrous and were used as received.

Synthesis of $Bi/Bi_{13}S_{18}Br_2$ nano-bells

The synthesis is a modification of the already reported method by Giansante et al.[18] In short: all colloidal nanocrystals (NCs) were synthesized in three-necked flasks attached to a standard Schlenk line, ensuring oxygen- and moisture-free conditions. In a typical procedure to obtain Bi / $Bi_{13}S_{18}Br_2$ NCs, 0.3 mmol (120 mg) of $Bi(Ac)_3$ and 6.3 mmol (2 mL) of oleic acid were combined in 3 mL of 1-octadecene. The mixture was stirred vigorously and deoxygenated through several cycles of vacuum and nitrogen purging at around 80 °C. Subsequently, the mixture was heated to 110 °C to fully dissolve $Bi(Ac)_3$, which caused the solution to turn colorless and optically clear, indicating the complete formation of bismuth(III)-oleate complex(es). The solution was maintained under vacuum at 110 °C for 30 minutes to eliminate any acetic acid formed during the complexation process. Afterward, the solution was reheated under nitrogen flow, with the temperature stabilized at 180°C. At this stage, 300 µL of didodecylmethylamine was injected, followed immediately by the co-injection of a half equivalent of $(Me_3Si)_2S$ (0.15 mmol; 32 µL) and one equivalent of $(Me_3Si)Br$ (0.3 mmol; 39.5 µL) dissolved in 2 mL of octadecene. The reaction was allowed to proceed for 15 minutes before the heating source was removed. The colloidal dispersion was quickly cooled to room temperature by placing the reaction flask in an ice bath. After the reaction, the mixture was centrifuged at 6000 rpm for 5 minutes. The clear supernatant was discarded, and the resulting black precipitate was collected in 1 mL of toluene or hexane. No additional purification steps were carried out on the NC heterostructures.

Electron microscopy

Bright Field Transmission Electron Microscopy (BF-TEM) measurements of the NCs were performed using either a JEOL JEM-1011 with a W thermionic source at an acceleration voltage of 100 kV or a JEOL JEM-1400Plus TEM, with LaB_6 thermionic source and maximum acceleration voltage 120 kV. The highly diluted NC solution was first put in ultrasound for 1 minute and then drop-cast onto copper grids (200 mesh) with carbon film and the solvent was then allowed to evaporate in a vapor-controlled environment. The longitudinal and lateral dimensions were assessed through statistical analysis of TEM images of several hundred NCs using the ImageJ software. Selected area electron diffraction measurements were performed on the same microscope and evaluated using the CrysTBox software package.

High-resolution scanning transmission electron microscopy (HRSTEM) images were acquired on a probe-corrected Thermo Fisher Spectra 300 STEM operated at 300 kV. Images were acquired on a high-angle annular dark-field (HAADF) detector with a current of ~100 pA. Compositional maps were acquired and analyzed using Velox, with a probe current of ~150 pA and rapid rastered scanning, on a Dual-X detector setup. 4DSTEM data were collected on a Gatan Continuum using STEM-X, with a current of ~5 pA and a dwell time of 1 ms. The analysis of the 4DSTEM datasets was carried out using the open-source Python code py4DSTEM.[46]

X-ray Powder Diffraction

Characterization by X-ray Powder Diffraction (XRD) was performed by employing a PANalytical Empyrean X-ray diffractometer using a 1.8 kV Cu Kα ceramic X-ray tube operating at 45 kV and 40 mA and detected by a PIXcel3D 2 × 2 area detector. Samples were prepared by dropcasting highly concentrated solutions on zero-diffraction silicon substrates. All diffraction patterns were acquired at room temperature under ambient conditions. Data analysis was performed using the HighScore 4.9 software from PANalytical. The Rietveld fits of XRD patterns were performed with the FullProf suite[38] and were specifically oriented to the extraction of morphological information and mass ratios. To this end, additional effort was devoted to the appropriate modelling of the peak intensities and profiles. The instrumental broadening was quantified by measuring and fitting a LaB_6 diffraction pattern (not shown) to construct the instrumental response function. Then, the pattern was fitted by refining for both phases (metallic Bismuth and $Bi_{13}S_{18}Br_2$) the

following parameters: scale factor, lattice parameters (*a,b,c*, whereas angles were fixed by symmetry), polynomial background, instrumental zero, and spherical harmonics size parameters (1 parameter for metallic Bismuth = spherical crystallite, up to 3 parameters for $Bi_{13}S_{18}Br_2$ = Y00, Y20, Y40). March-Dollase modelling for the preferred orientation of $Bi_{13}S_{18}Br_2$ was included to account for the possible orientation of the large and flat nano-bells upon deposition on the substrate, to correctly account for the observed intensity of reflections. Instead, the position of atoms was not refined to avoid the introduction of unjustified distortion to the crystal structure, which would likely mask the actual underlying microstructural contributions to the pattern. In those cases where the Bi-domain was close to its detection limit, the domain size was fixed to the last value that could be determined reliably to avoid overfitting.

Photocatalysis tests

For the photodegradation of the organic dyes, a 1 mM solution of MB or RhB was prepared in 20 mL of IPA, in 20 mL of methanol in the case of MO. Then, 2 mg of $Bi/Bi_{13}S_{18}Br_2$ NCs were mixed with 73 μL of the organic solution until a final volume of 2.5 mL of IPA in quartz cuvettes. Subsequently, the cuvettes were introduced in a photoreactor (λex=420 nm) until the complete photodegradation of the organic pollutants, measuring the UV-Vis spectra for following the process at different photoreaction times. The solution containing the photocatalyst and the organic molecule was centrifuged (7000 rpm for 5 minutes), and the spectra were collected from the supernatant. UV–visible absorption spectra were recorded on a spectrophotometer UV/VIS/NIR Lambda 1050, equipped with software PerkinElmer UV Winlab. Quartz cuvettes of 1 cm × 1 cm path length were used to acquire all the data. As photoreactor was used the PhotoreactorM2 from Penn PhD, adjusting the stirring at 400 rpm and the fan at 2800 rpm. For the study of the reaction mechanism, a 1 mM solution of benzoquinone (scavenger) was prepared in 1 mL of IPA. Then, 2 mg of $Bi/Bi_{13}S_{18}Br_2$ NCs were mixed with 73 μL of RhB solution and 100 μL of BZQ solution until a final volume of 2.5 mL of IPA in quartz cuvette. Before the irradiation, the mixture was stirred for 15 minutes in the dark to establish the adsorption-desorption equilibrium of RhB on the photocatalyst surface. The zeta (ζ) potential was determined by employing a Zetasizer Ultra (Malvern, UK).

Photoelectrochemical tests

Photoelectrodes preparation. 1x1 cm electrodes where crafted starting from the toluene suspensions of Bi HSs and Bi rods obtained from the synthesis. They were obtained by spin coating (Laurell WS-650MZ-23NPPB spin coater, equipped with a GAST 0523-101Q-G588NDX Vacuum Pump) on FTO glass. Optimal film homogeneity was obtained operating at 5000 RPM for 1 minute, with either 3x 50 μL (Bi HSs).

Photoelectrochemical setup. The photoelectrochemical characterization of the sample has been carried out in a single compartment quartz cell, purchased from PineResearch ("Low Volume Photoelectrochemical Three Electrode Quartz Cell"). Tests were performed under a typical three-electrode configuration, using the above-described photoelectrodes as working electrode (WE), a Pt coil as counter electrode (CE) and an Ag wire (sealed in a fritted glass tube, filled with the working electrolyte) as reference electrode (RE). Gas inlet and outlets were also implemented. The whole cell was gas-tight, with the gas outlet connected to an inline gas chromatograph (GC). The testing electrolyte was a 0.1 M $LiClO_4$ solution in ACN:H_2O (99:1 v/v). A THORLABS M415L4 - 415 nm, 1310 mW (Min) Mounted LED, 1500 mA was employed as illumination source and an Ivium Compact Stat.h as the potentiostat. The tests were performed feeding the cell by bubbling Ar (delivered by a Bronkhorst F-201CV-100-RGD-22-V mass flow controller) or CO_2 (delivered by a Bronkhorst F-201CV-100-RGD-22-V mass flow controller), depending on the nature of the test, with a flow rate set at 5.5 sccm. The gas outlet was connected in-line to a gas dryer (SRI Gas Stream Dryer, SRI part# 8670-5850), to a universal Mass Flow Meter (EL-Flow Prestige Bronkhorst, model FG-111B-AGD-22-V-DA-000) and then to the GC for the quantification of gaseous products.

Electrochemical tests. Three main electrochemical techniques have been used in the characterization of the CO_2RR photoelectroactivity of the samples under study. Open Circuit Potential (OCP) was measured under illumination and/or dark conditions, as to assess the interaction of the thin films with the incident radiation. Cyclic Voltammetry (CV) has been also operated under both illumination and dark conditions, in the presence and absence of CO_2, depending on the nature of the test, aiming at assessing the CO_2RR features of the materials. Finally, ChronoAmperometric scans (CA, 1 hour-long) have been recorded, again under both illumination and dark conditions, as to determine the CO_2RR product distribution yielded by the materials at definite potentials. Unless otherwise stated,

all the potentials reported in this work are measured versus the previously described RE. Blank tests were performed on the electrode support (*i.e.*, bare FTO, 1x1 cm).

Products quantification. Gaseous products were detected by an inline-connected SRI 8610C gas chromatograph (Multiple Gas Analyzer #5) equipped with a thermal conductivity detector (TCD) and flame ionization detector (FID) coupled with a methanizer. Argon has been used as gas carrier. Detectors response have been calibrated prior to experiments using a customized gas mixture containing the most typical CO_2RR gas phase products. Details on calibration and quantification methods can be found in our previous works. Liquid products were detected ex-situ, sampling the post-reaction electrolytes, by HPLC. All HPLC separations have been carried out on an Agilent Infinity 1260, equipped with a quaternary pump, standard autosampler, thermostatted column compartment, Diode Array Detector (DAD/UV-Vis) operating in the range between 190 to 950 nm and a Refractive Index Detector (RID). Possible CO_2RR liquid products (*e.g.*, formic acid/formate ions) have been separated on an Agilent Hi-Plex H (300 × 7.7 mm) operated at 50°C in 5 mM M $H_2SO_{4(aq)}$, isocratic mode, 0.6 mL min^{-1}, 25 µL injection volume. Chromatographic runs lasted for 30 minutes, allowing for the elution of all common CO_2RR products. Products were detected by either DAD/UV-Vis (210 and 280 nm) and/or RID (T = 40°C) depending on the nature of the analyte. A complete overview on the separation of liquid CO_2RR products according to this methodology can be found in literature.[61]

6.8 Appendix

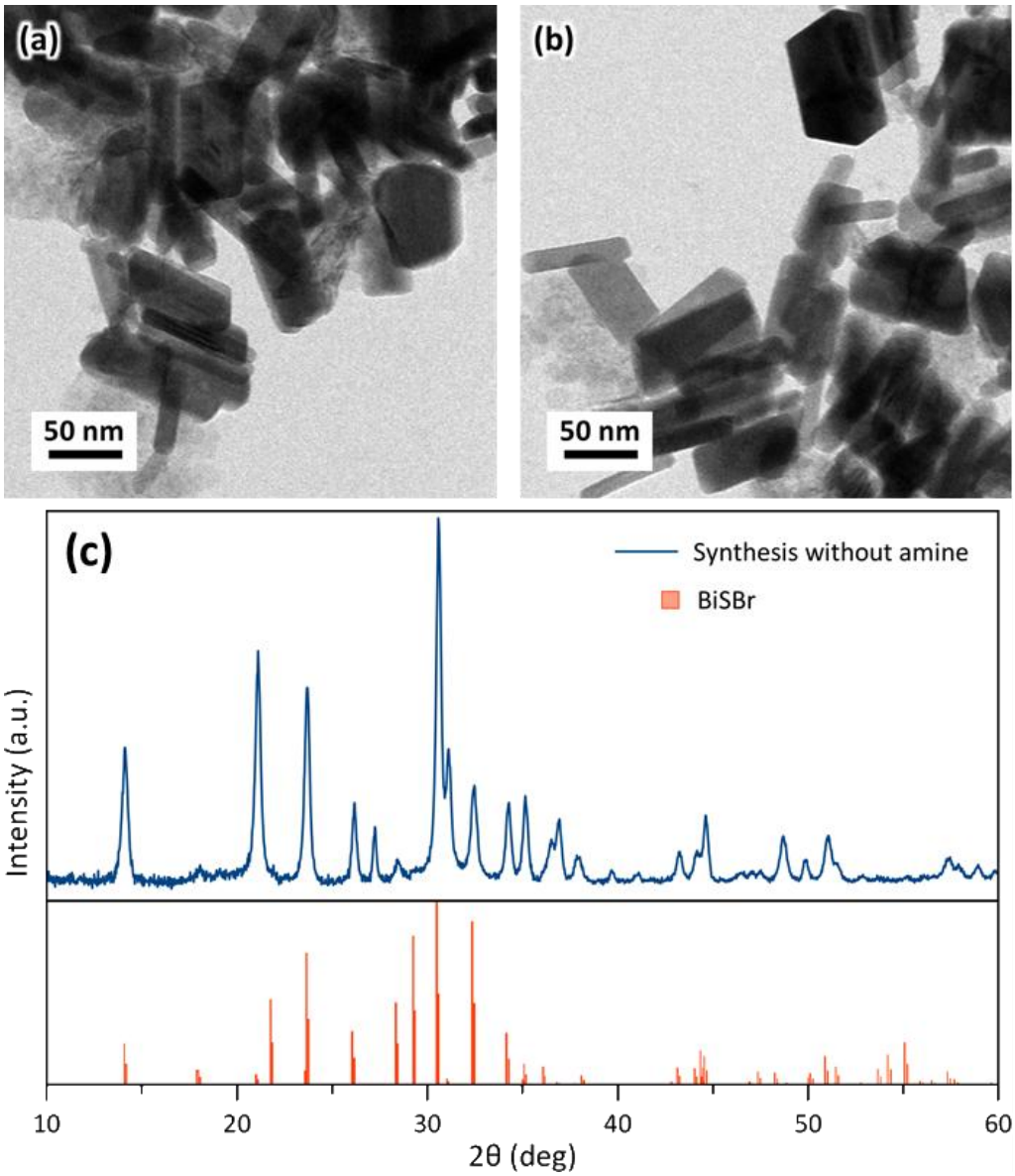

Figure 6.8. Control synthesis in the absence of amines. a-b) TEM images of colloidal BiSBr NCs synthetized in the absence of amines, following the procedure reported by Quarta *et al*. c) XRD pattern of colloidal BiSBr NCs synthetized in the absence of amine, confirming the phase attribution to BiSBr. Adapted with permission from ref 60. Licensed under CC-BY 4.0. Copyright © 2025 The Authors.

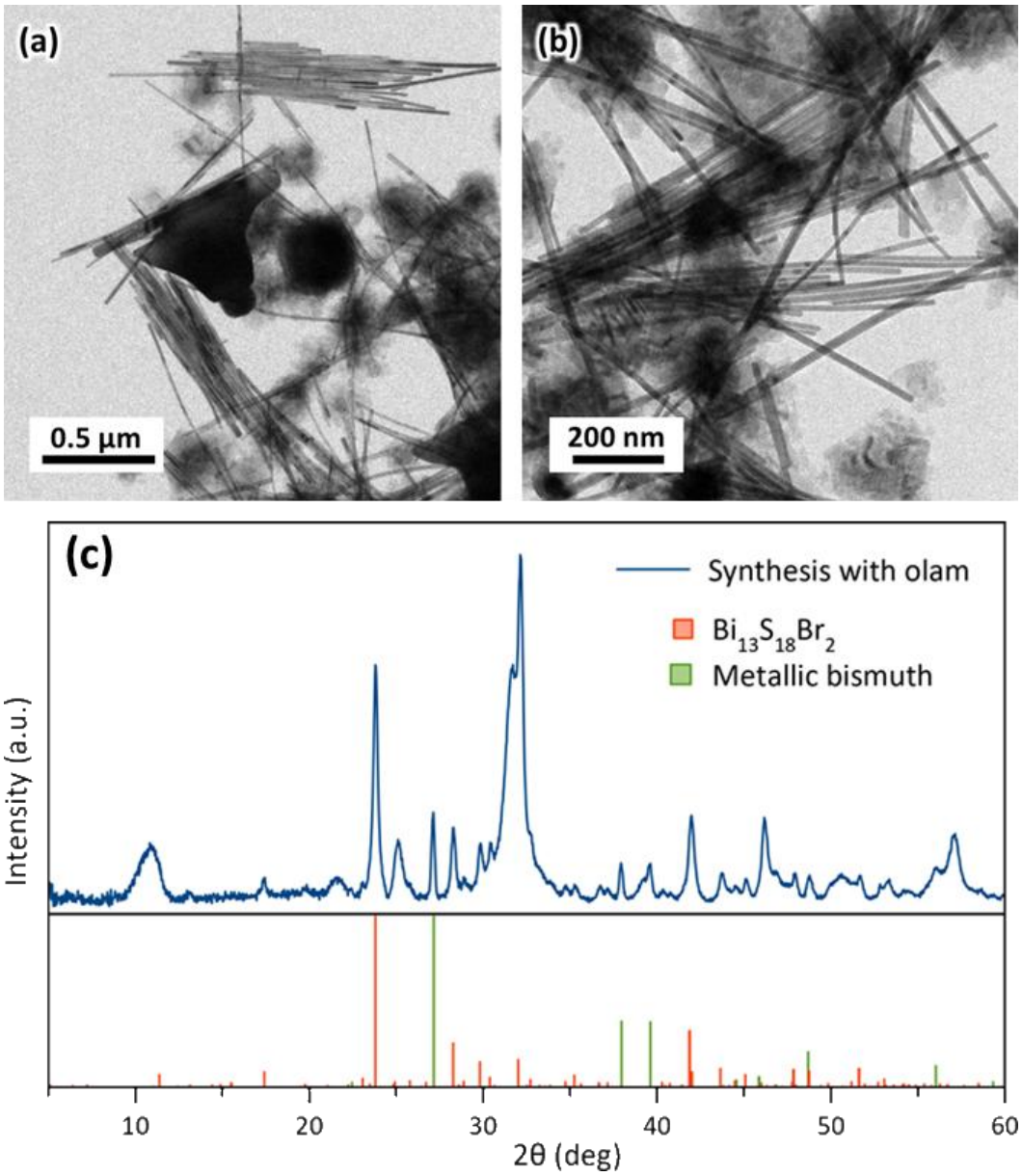

Figure 6.9. Synthesis performed with added oleylamine. a-b) TEM images of colloidal $Bi_{13}S_{18}Br_2$ obtained by adding 220 µL of oleylamine on top of the reagents used for Figure 6.8 while adopting identical reaction conditions. c) XRD pattern of the colloidal $Bi_{13}S_{18}Br_2$ nanorods obtained by adding oleylamine. Adapted with permission from ref 60. Licensed under CC-BY 4.0. Copyright © 2025 The Authors.

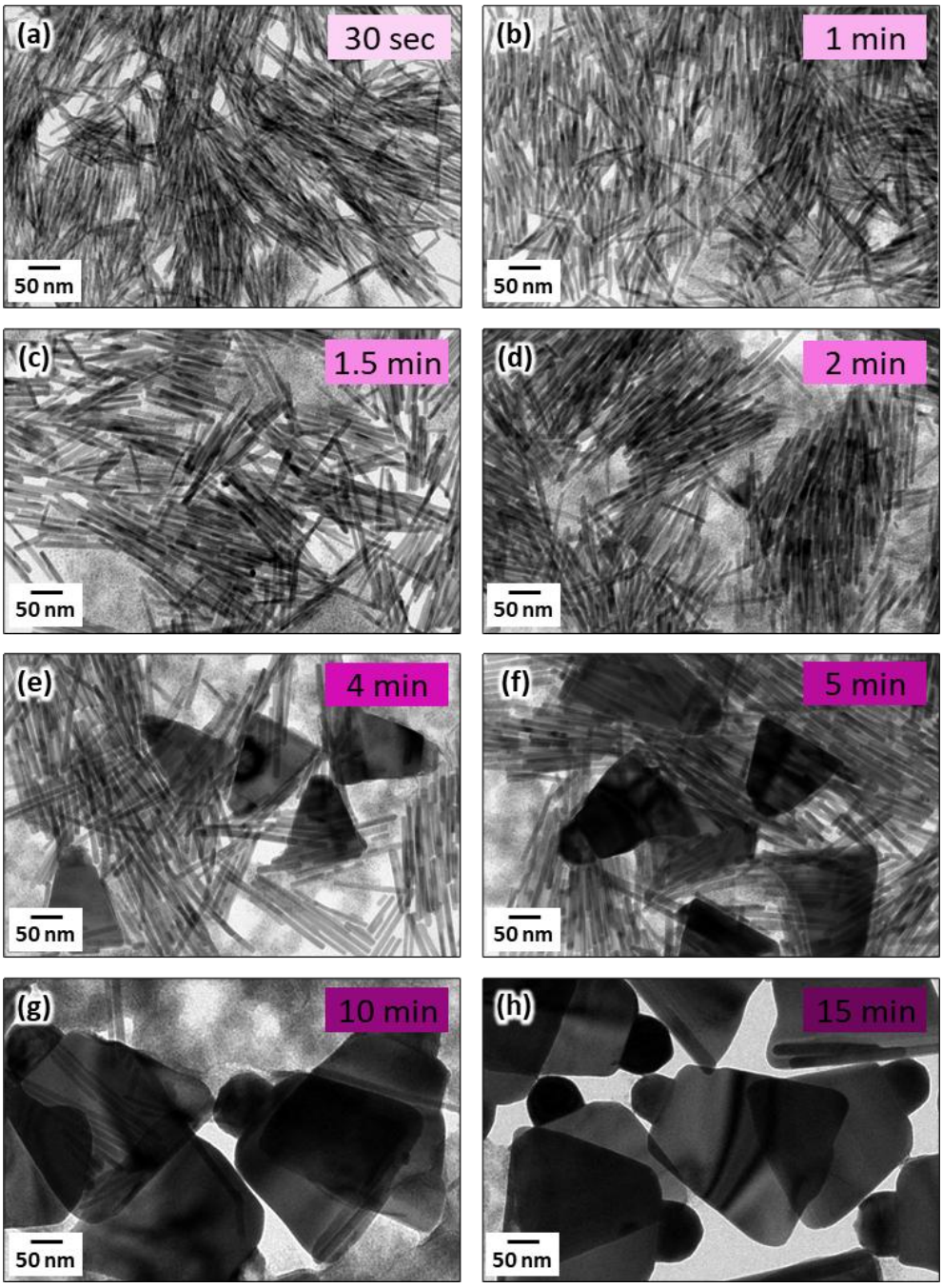

Figure 6.10. Morphology evolution of Bi/$Bi_{13}S_{18}Br_2$ nano-bells. TEM images of Bi/$Bi_{13}S_{18}Br_2$ solution aliquots taken at 30 s (a), 60 s (b), 1.5 min (c), 2 min (d), 4 min (e), 5 min (f), 10 min (g) and 15 min (h) after the start of the reaction. Adapted with permission from ref 60. Licensed under CC-BY 4.0. Copyright © 2025 The Authors.

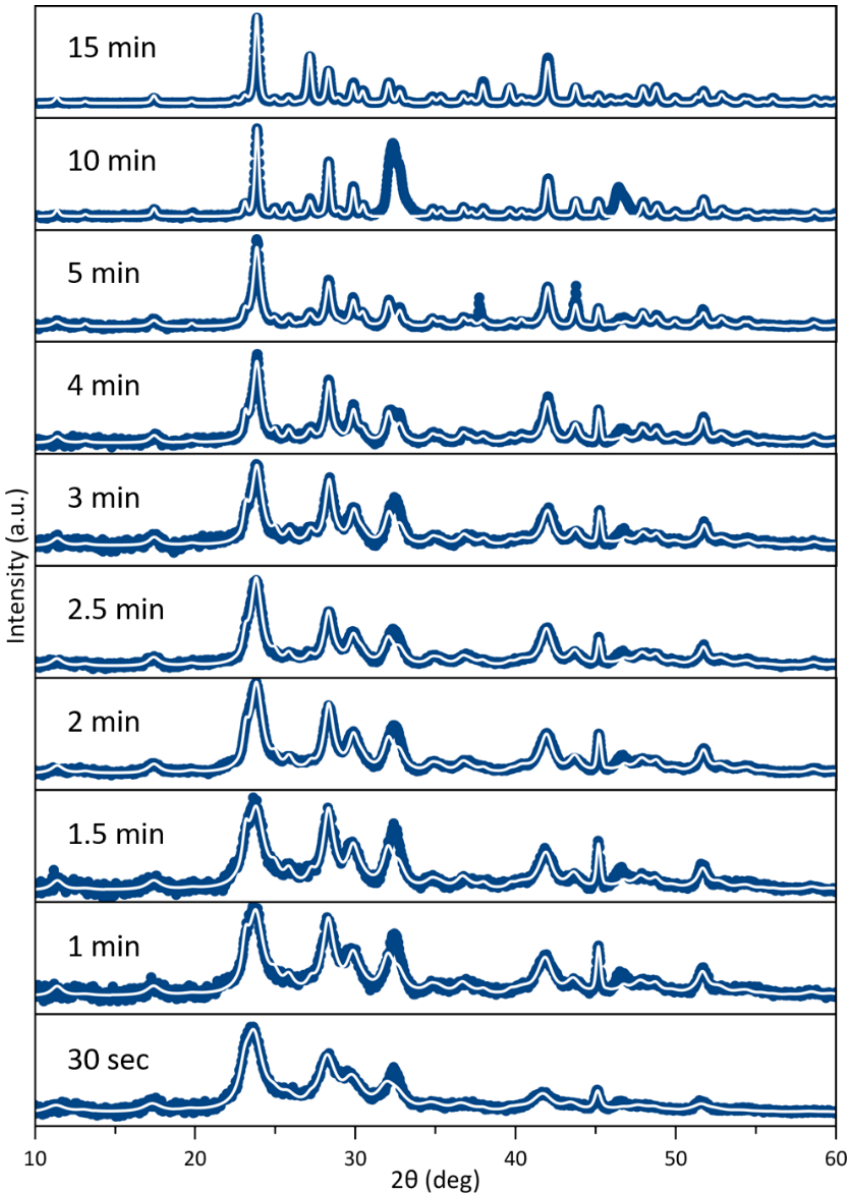

Figure 6.11. XRD Rietveld Fits. Rietveld fits of the XRD patterns collected from different reaction batch aliquots at various reaction times. Experimental patterns are shown in blue, while the fit traces are represented in white. To accurately capture the average dimensions of crystallites, we opted to exclude certain peaks (32.4° and 46.7°) from the fitting process when their significant preferential orientation and anisotropic broadening made it challenging to model their profiles accurately. This approach ensured that the fitting model reliably represented the remaining portions of the patterns. Reproduced with permission from ref 60. Licensed under CC-BY 4.0. Copyright © 2025 The Authors.

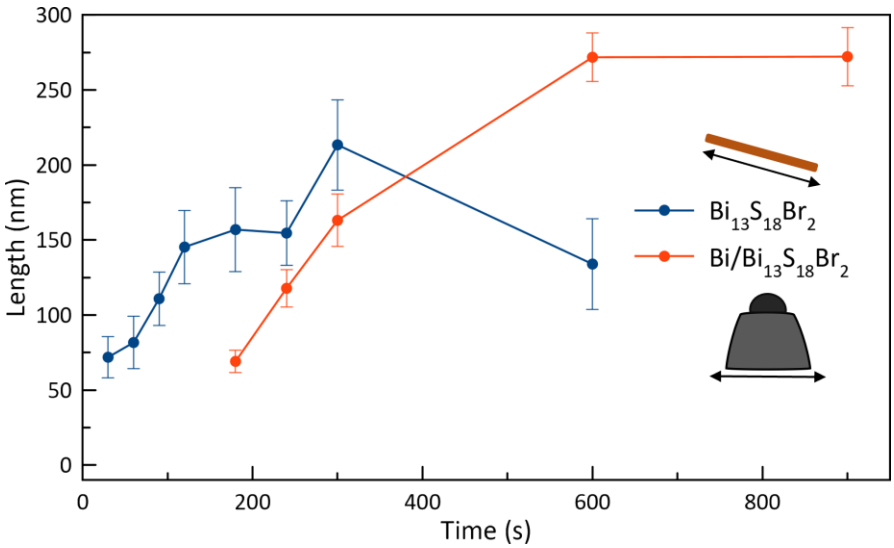

Figure 6.12. Size evolution of $Bi_{13}S_{18}Br_2$ by TEM. The length of free-standing $Bi_{13}S_{18}Br_2$ nanorods and of the $Bi_{13}S_{18}Br_2$ domains in $Bi/Bi_{13}S_{18}Br_2$ heterostructures was tracked by measuring 30 particles per time aliquot. Note note that there were not enough $Bi/Bi_{13}S_{18}Br_2$ heterostructures to obtain reliable statistics before the 200-seconds mark. Reproduced with permission from ref 60. Licensed under CC-BY 4.0. Copyright © 2025 The Authors.

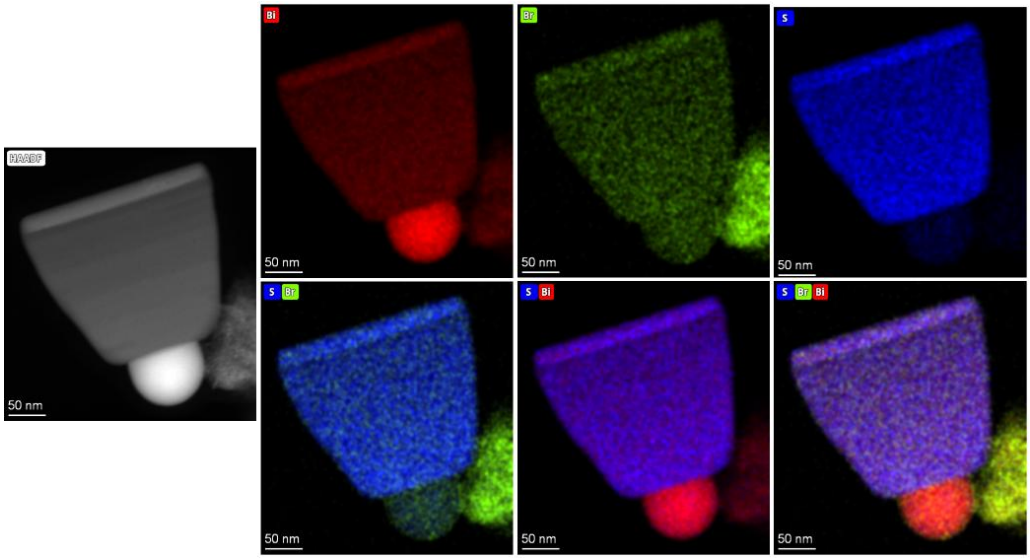

Figure 6.13. HAADF image and STEM-EDX compositional map. HAADF image and STEM-EDX compositional map of an individual nanobell, showing the presence of Bi, S and Br atoms. Reproduced with permission from ref 60. Licensed under CC-BY 4.0. Copyright © 2025 The Authors.

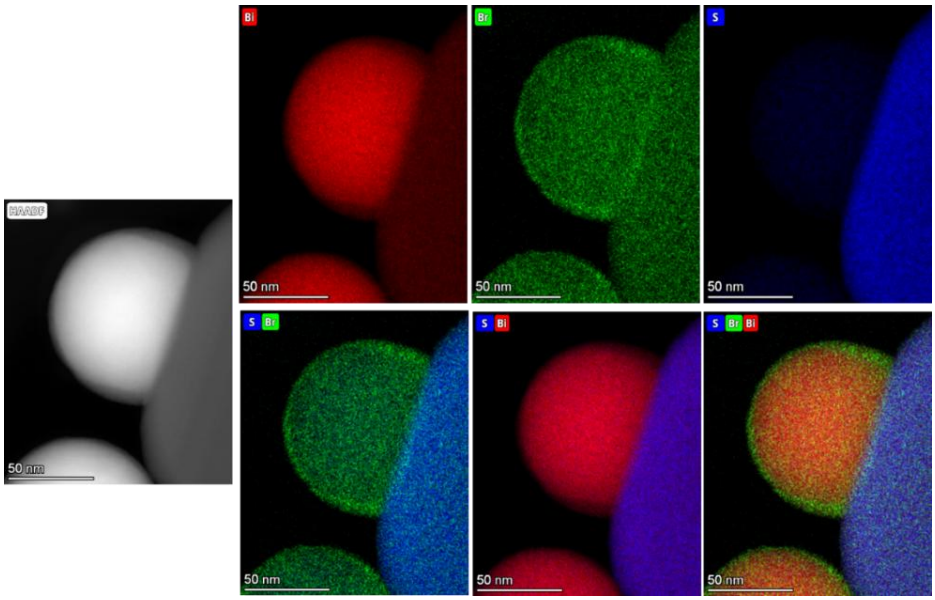

Figure 6.14. HAADF image and STEM-EDX compositional map metallic Bi. HAADF image and STEM-EDX compositional map of the Bi/chalcohalide contact region, showing the presence of a Br-rich shell surrounding the metal hemisphere. Reproduced with permission from ref 60. Licensed under CC-BY 4.0. Copyright © 2025 The Authors.

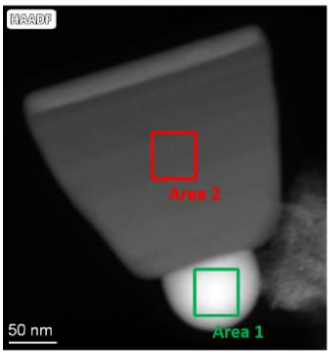

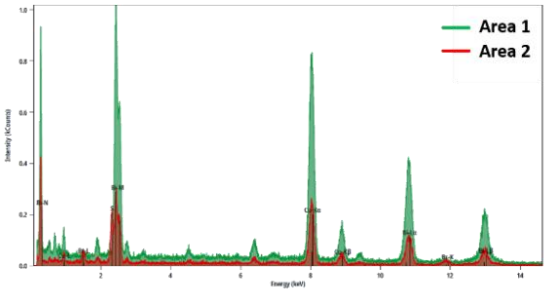

Area 1

Element	Atomic Fraction	Atomic Error	Mass Fraction	Mass Error
S	2.11	0.24	0.33	0.04
Br	0.66	0.13	0.26	0.05
Bi	97.24	0.33	99.41	0.08

Area 2

Element	Atomic Fraction	Atomic Error	Mass Fraction	Mass Error
S	47.44	2.40	13.44	1.22
Br	9.19	1.17	6.49	0.98
Bi	43.37	2.82	80.07	1.92

Figure 6.15. HAADF image and Energy-dispersive X-ray (EDX). HAADF image of an individual nanobell and Energy-dispersive X-ray (EDX) analysis. Reproduced with permission from ref 60. Licensed under CC-BY 4.0. Copyright © 2025 The Authors.

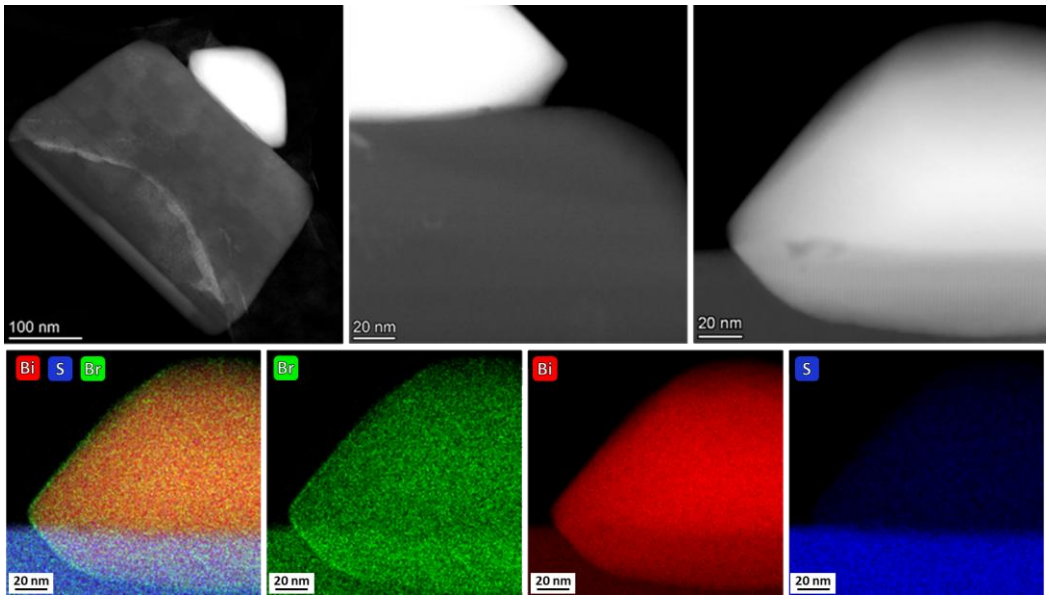

Figure 6.16. HAADF image and STEM-EDX compositional map. HAADF image and STEM-EDX compositional map .of an individual nanobell, showing the presence of Bi, S and Br atoms. Reproduced with permission from ref 60. Licensed under CC-BY 4.0. Copyright © 2025 The Authors.

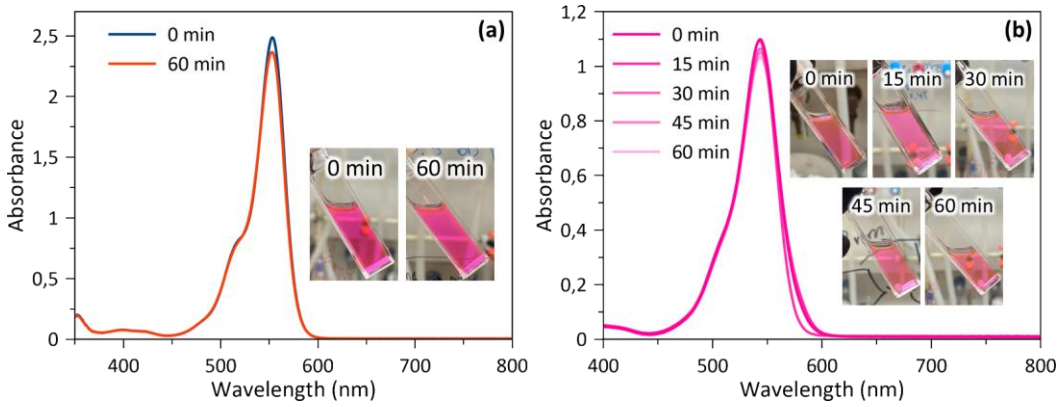

Figure 6.17. Rhodamine-B photostability test in the absence of photocatalyst and dark condition test. a) Absorbance spectra of the RhB solution before and after 1h of illumination at 420 nm in the absence of the photocatalyst. b) Cuvettes images during the reaction time in dark condition and absorbance spectra of the RhB during the reaction time in dark condition, the photocatalyst was removed by centrifugation. Adapted with permission from ref 60. Licensed under CC-BY 4.0. Copyright © 2025 The Authors.

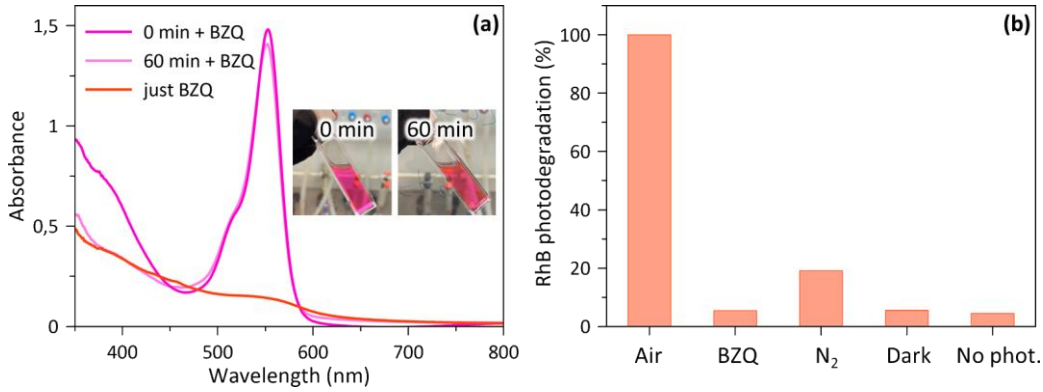

Figure 6.18. Rhodamine-B test in the presence of benzoquinone (BZQ) and RhB photodegradation percentage in different conditions. a) Cuvettes pictures before and after illumination with benzoquinone and absorbance spectra of RhB before and after illumination in the presence of benzoquinone, the photocatalyst was removed by centrifugation. b) Photodegradation activity of Bi/ $Bi_{13}S_{18}Br_2$ HSs in air condition, in the presence of benzoquinone, in nitrogen atmosphere, in dark conditions and without the use of the photocatalyst. Adapted with permission from ref 60. Licensed under CC-BY 4.0. Copyright © 2025 The Authors.

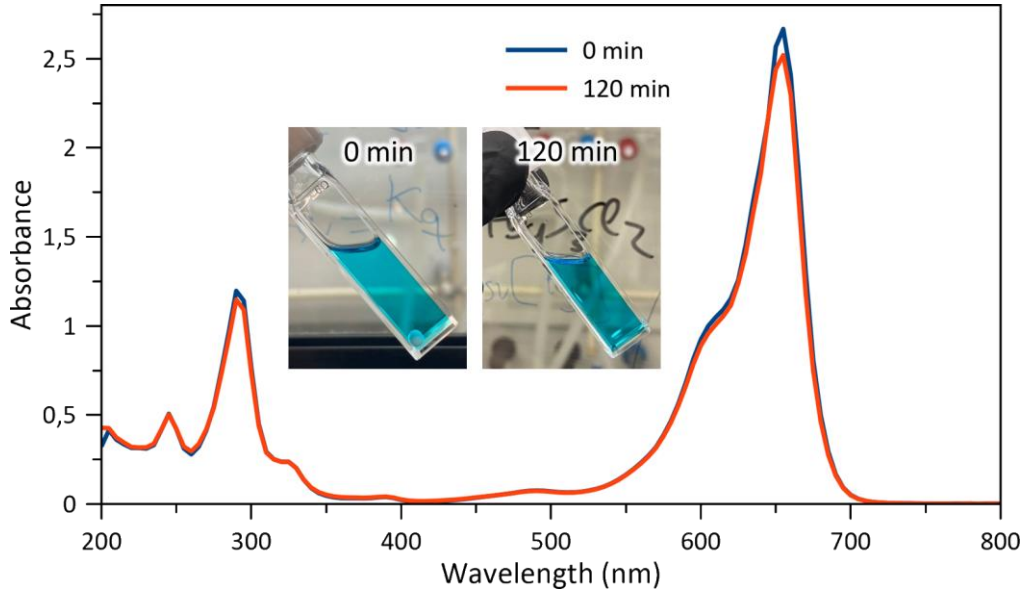

Figure 6.19. Methylene Blue photostability test in the absence of photocatalyst. Absorbance spectra of the MB solution before and after 2h of illumination at 420 nm in the absence of the photocatalyst. Adapted with permission from ref 60. Licensed under CC-BY 4.0. Copyright © 2025 The Authors.

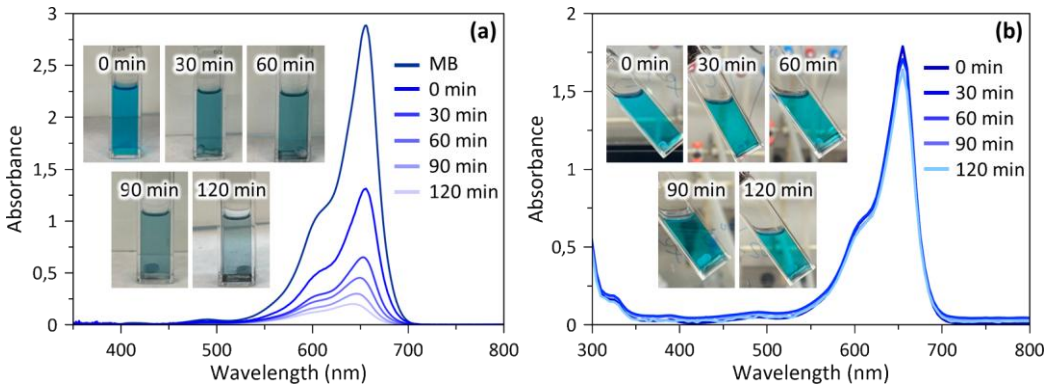

Figure 6.20. Methylene Blue photodegradation process and dark test. a) Cuvettes images during the reaction time in light condition and absorbance spectra of MB during the reaction time in light condition, the photocatalyst was removed by centrifugation. b) Cuvettes images during the reaction time in dark condition and absorbance spectra of the MB during the reaction time in dark condition, the photocatalyst was removed by centrifugation. Adapted with permission from ref 60. Licensed under CC-BY 4.0. Copyright © 2025 The Authors.

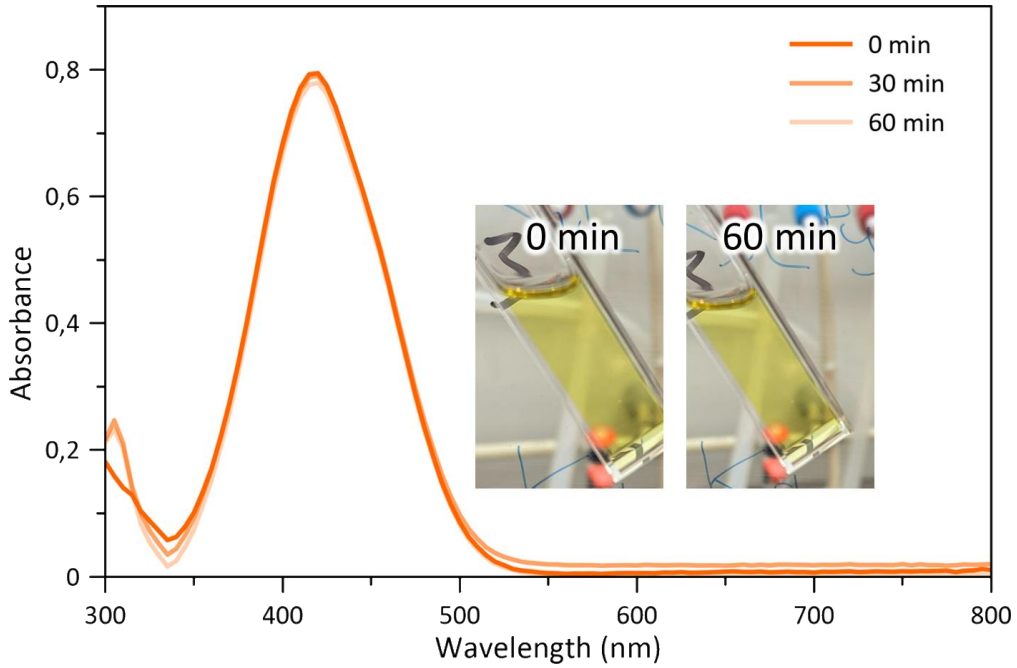

Figure 6.21. Methyl Orange photodegradation process. Absorbance spectra of MO during the reaction time in light condition, the photocatalyst was removed by centrifugation. Adapted with permission from ref 60. Licensed under CC-BY 4.0. Copyright © 2025 The Authors.

Table 6.1. Z potential of Bi/$Bi_{13}S_{18}Br_2$ nano-bells. Reproduced with permission from ref 60. Licensed under CC-BY 4.0. Copyright © 2025 The Authors.

Name	Mean
Zeta potential (mV)	-58,299
Conductivity (ms/cm)	0
Wall zeta potential (mV)	0
Quality factor	1,037
Zeta peak 1 mean (mV)	-53,796

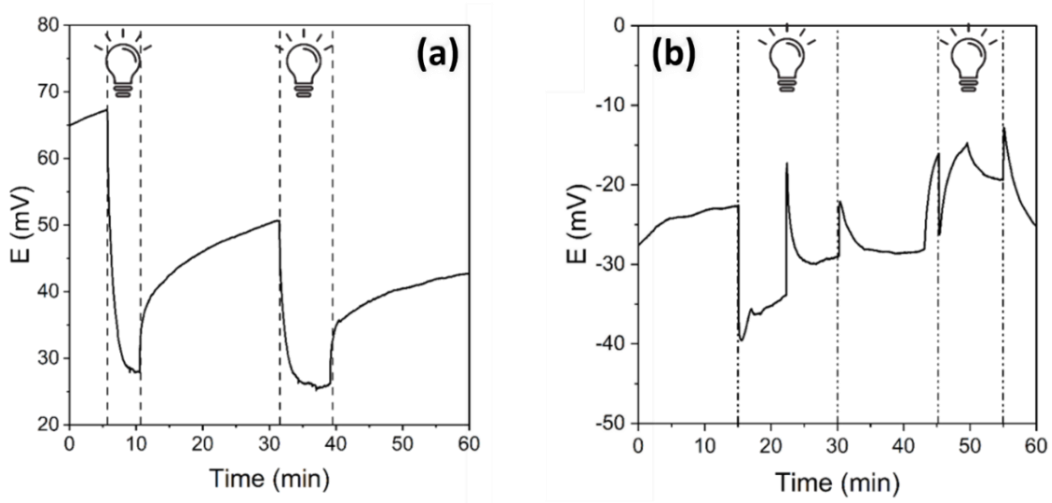

Figure 6.22. Open Circuit Voltage (OCP) traces. OCP traces recorded on (a) bare FTO, (b) Bi/ $Bi_{13}S_{18}Br_2$ HSs upon intermittent illumination with a 415 nm light source. Adapted with permission from ref 60. Licensed under CC-BY 4.0. Copyright © 2025 The Authors.

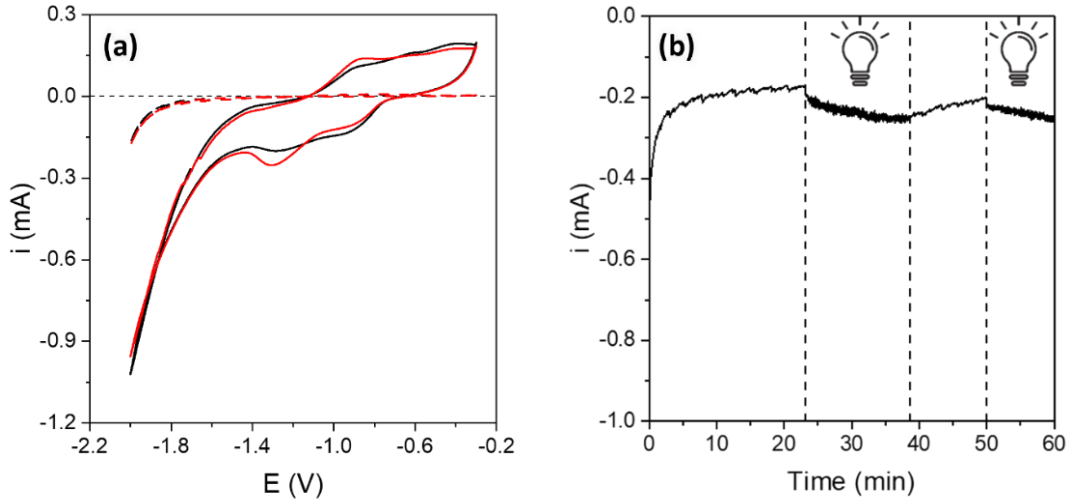

Figure 6.23. Cyclic Voltammetry (CV) traces and Chronoamperometry (CA). a) CV traces collected on bare FTO. (v = 100 mV s-1). Dotted curves have been collected under Ar bubbling (blank tests, only HER is possible), while full traces are related to CO_2RR tests. Black: dark conditions. Red: illumination (415 nm LED). b) CA scans collected on bare FTO (@ -2 V vs RE) under CO_2RR conditions. Adapted with permission from ref 60. Licensed under CC-BY 4.0. Copyright © 2025 The Authors.

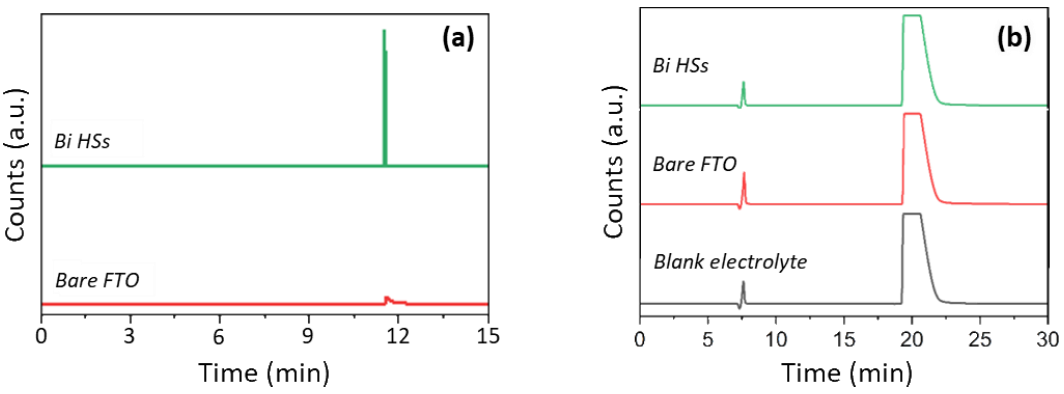

Figure 6.24. Gas chromatography and liquid chromatography. Sample chromatographic traces collected on the outlet gases and post-reaction electrolytes collected upon photoelectrochemical testing. (a) Typical FID (GC) and (b) RID (HPLC) traces. Adapted with permission from ref 60. Licensed under CC-BY 4.0. Copyright © 2025 The Authors.

6.9 Source Publications and Contributions

This chapter is based on the following publication:

Cabona, A.; Toso, S.; Griesi, A.; Rizzo, M.; Ferri, M.; Rusch, P.; Divitini, G.; Pérez-Prieto, J.; Galian, R. E.; Kriegel, I.; Manna, L. Synthesis, Growth Mechanism, and Photocatalytic Properties of Metallic-Bi/$Bi_{13}S_{18}Br_2$ Nano-Bell Heterostructures. *ACS Materials Lett.* **2025**, *7* (5), 1707–1716. https://doi.org/10.1021/acsmaterialslett.5c00043.

This article stemmed from the idea of synthesizing a new functional heterostructure that couples a metal domain with a semiconductor domain for photocatalytic applications. This work was made possible through collaboration with many colleagues. Andrea Griesi and Giorgio Divitini performed the advanced electron microscopy analyses and helped me to interpret the results. With the guidance of Stefano Toso, we successfully determine the epitaxial relationship between the two domains of the heterostructure. Michele Ferri and Martina Rizzo collaborated with me for the electrocatalysis tests. Raquel Galian guided me in the photocatalysis experiments. Finally, I would like to thank Liberato Manna, Ilka Kriegel and Raquel Galian for their guidance and assistance in preparing the manuscript.

6.9.1 Copyright

Some elements of this chapter were adapted from external source:

Figures:

- **Figure 6.1., Figure 6.11., Figure 6.12., Figure 6.13., Figure 6.14., Figure 6.15.**, **Figure 6.16.** Reproduced with permission from ACS Materials Lett. **2025**, 7 (5), 1707–1716. Licensed under CC-BY 4.0. Copyright © 2025 The Authors.

- **Figure 6.2., Figure 6.3., Figure 6.4., Figure 6.5., Figure 6.6., Figure 6.7., Figure 6.8., Figure 6.9., Figure 6.10., Figure 6.17., Figure 6.18., Figure 6.19., Figure 6.20., Figure 6.21., Figure 6.22., Figure 6.23., Figure 6.24.** Adapted with permission from ACS Materials Lett. **2025**, 7 (5), 1707–1716. Licensed under CC-BY 4.0. Copyright © 2025 The Authors.

Text (parts):

6.10 Bibliography

(1) Nowak, M.; Jesionek, M.; Mistewicz, K. Applications of Group 15 Ternary Chalcohalide Nanomaterials. In *Industrial Applications of Nanomaterials*; Elsevier, 2019; pp 225–282. https://doi.org/10.1016/B978-0-12-815749-7.00009-8.

(2) Nowak, M.; Jesionek, M.; Mistewicz, K. Fabrication Techniques of Group 15 Ternary Chalcohalide Nanomaterials. In ; Elsevier, 2019; pp 337–384. https://doi.org/10.1016/B978-0-12-815751-0.00010-9.

(3) Fatuzzo, E.; Harbeke, G.; Merz, W. J.; Nitsche, R.; Roetschi, H.; Ruppel, W. Ferroelectricity in SbSI. *Phys. Rev.* **1962**, *127* (6), 2036–2037. https://doi.org/10.1103/PhysRev.127.2036.

(4) Toroń, B.; Nowak, M.; Kępińska, M.; Szperlich, P. Mobility of Ferroelectric Domains in Antimony Sulfoiodide. *Acta Phys. Pol. A* **2014**, *126* (5), 1093–1095. https://doi.org/10.12693/APhysPolA.126.1093.

(5) Starczewska, A.; Solecka, B.; Nowak, M.; Szperlich, P. Dielectric Properties of SbSI in the Temperature Range of 292-475~K. *Acta Phys. Pol. A* **2014**, *126* (5), 1125–1127. https://doi.org/10.12693/APhysPolA.126.1125.

(6) Wlaźlak, E.; Blachecki, A.; Bisztyga-Szklarz, M.; Klejna, S.; Mazur, T.; Mech, K.; Pilarczyk, K.; Przyczyna, D.; Suchecki, M.; Zawal, P.; Szaciłowski, K. Heavy Pnictogen Chalcohalides: The Synthesis, Structure and Properties of These Rediscovered Semiconductors. *Chem. Commun.* **2018**, *54* (86), 12133–12162. https://doi.org/10.1039/C8CC05149F.

(7) He, J.; Hu, X.; Liu, Z.; Chen, W.; Longo, G. Prospect for Bismuth/Antimony Chalcohalides-Based Solar Cells. *Adv. Funct. Mater.* **2023**, *33* (48), 2306075. https://doi.org/10.1002/adfm.202306075.

(8) Nielsen, R. S.; Álvarez, Á. L.; Medaille, A. G.; Caño, I.; Navarro-Güell, A.; Álvarez, C. L.; Cazorla, C.; Ferrer, D. R.; Li-Kao, Z. J.; Saucedo, E.; Dimitrievska, M. Parallel Exploration of the Optoelectronic Properties of (Sb,Bi)(S,Se)(Br,I) Chalcohalides. *J. Mater. Chem. A* **2025**, *13* (37), 31727–31739. https://doi.org/10.1039/D5TA05011A.

(9) He, J.; Hu, X.; Liu, Z.; Chen, W.; Longo, G. Prospect for Bismuth/Antimony Chalcohalides-Based Solar Cells. *Adv. Funct. Mater.* **2023**, *33* (48), 2306075. https://doi.org/10.1002/adfm.202306075.

(10) Choi, Y. C.; Jung, K.-W. Recent Progress in Fabrication of Antimony/Bismuth Chalcohalides for Lead-Free Solar Cell Applications. *Nanomaterials* **2020**, *10* (11), 2284. https://doi.org/10.3390/nano10112284.

(11) Quarta, D.; Toso, S.; Fieramosca, A.; Dominici, L.; Caliandro, R.; Moliterni, A.; Tobaldi, D. M.; Saleh, G.; Gushchina, I.; Brescia, R.; Prato, M.; Infante, I.; Cola, A.; Giannini, C.; Manna, L.; Gigli, G.; Giansante, C. Direct Band Gap Chalcohalide Semiconductors: Quaternary $AgBiSCl_2$ Nanocrystals. *Chem. Mater.* **2023**, *35* (23), 9900–9906. https://doi.org/10.1021/acs.chemmater.3c01403.

(12) Kunioku, H.; Higashi, M.; Abe, R. Low-Temperature Synthesis of Bismuth Chalcohalides: Candidate Photovoltaic Materialswith Easily, Continuously Controllable Band Gap. *Sci. Rep.* **2016**, *6* (1), 32664. https://doi.org/10.1038/srep32664.

(13) Govindaraj, P.; Venugopal, K. Intrinsic Ultra-Low Lattice Thermal Conductivity in Orthorhombic BiSI: An Excellent Thermoelectric Material. *J. Alloys Compd.* **2022**, *929*, 167347. https://doi.org/10.1016/j.jallcom.2022.167347.

(14) Govindaraj, P.; Murugan, K.; Venugopal, K. Anisotropic Electron and Phonon Transport Properties in Pnictogen Chalcohalides: PnSI (Pn = Sb, Bi). *ACS Appl. Energy Mater.* **2023**, *6* (20), 10639–10651. https://doi.org/10.1021/acsaem.3c01811.

(15) Ghorpade, U. V.; Suryawanshi, M. P.; Green, M. A.; Wu, T.; Hao, X.; Ryan, K. M. Emerging Chalcohalide Materials for Energy Applications. *Chem. Rev.* **2023**, *123* (1), 327–378. https://doi.org/10.1021/acs.chemrev.2c00422.

(16) Wang, L.; Hung, Y.-C.; Hwu, S.-J.; Koo, H.-J.; Whangbo, M.-H. Synthesis, Structure, and Properties of a New Family of Mixed-Framework Chalcohalide Semiconductors: $CdSbS_2X$ (X = Cl, Br), $CdBiS_2X$ (X = Cl, Br), and $CdBiSe_2X$ (X = Br, I). *Chem. Mater.* **2006**, *18* (5), 1219–1225. https://doi.org/10.1021/cm0522230.

(17) Shyamal, S.; Pradhan, N. Nanostructured Metal Chalcohalide Photocatalysts: Crystal Structures, Synthesis, and Applications. *ACS Energy Lett.* **2023**, *8* (9), 3902–3926. https://doi.org/10.1021/acsenergylett.3c01236.

(18) Quarta, D.; Toso, S.; Giannuzzi, R.; Caliandro, R.; Moliterni, A.; Saleh, G.; Capodilupo, A.; Debellis, D.; Prato, M.; Nobile, C.; Maiorano, V.; Infante, I.; Gigli, G.; Giannini, C.; Manna, L.; Giansante, C. Colloidal Bismuth Chalcohalide Nanocrystals. *Angew. Chem.* **2022**, *134* (22), e202201747. https://doi.org/10.1002/ange.202201747.

(19) Quarta, D.; Toso, S.; Saleh, G.; Caliandro, R.; Moliterni, A.; Griesi, A.; Divitini, G.; Infante, I.; Gigli, G.; Giannini, C.; Manna, L.; Giansante, C. Mixed Valence of Bismuth in Hexagonal Chalcohalide Nanocrystals. *Chem. Mater.* **2023**, *35* (3), 1029–1036. https://doi.org/10.1021/acs.chemmater.2c02941.

(20) Bera, S.; Pradhan, N. Perovskite Nanocrystal Heterostructures: Synthesis, Optical Properties, and Applications. *ACS Energy Lett.* **2020**, *5* (9), 2858–2872. https://doi.org/10.1021/acsenergylett.0c01449.

(21) Carbone, L.; Cozzoli, P. D. Colloidal Heterostructured Nanocrystals: Synthesis and Growth Mechanisms. *Nano Today* **2010**, *5* (5), 449–493. https://doi.org/10.1016/j.nantod.2010.08.006.

(22) Liu, J.; Zhang, J. Nanointerface Chemistry: Lattice-Mismatch-Directed Synthesis and Application of Hybrid Nanocrystals. *Chem. Rev.* **2020**, *120* (4), 2123–2170. https://doi.org/10.1021/acs.chemrev.9b00443.

(23) Ha, M.; Kim, J.-H.; You, M.; Li, Q.; Fan, C.; Nam, J.-M. Multicomponent Plasmonic Nanoparticles: From Heterostructured Nanoparticles to Colloidal Composite Nanostructures. *Chem. Rev.* **2019**, *119* (24), 12208–12278. https://doi.org/10.1021/acs.chemrev.9b00234.

(24) Dutta, S. K.; Mehetor, S. K.; Pradhan, N. Metal Semiconductor Heterostructures for Photocatalytic Conversion of Light Energy. *J. Phys. Chem. Lett.*

(25) Ma, L.; Chen, S.; Shao, Y.; Chen, Y.-L.; Liu, M.-X.; Li, H.-X.; Mao, Y.-L.; Ding, S.-J. Recent Progress in Constructing Plasmonic Metal/Semiconductor Hetero-Nanostructures for Improved Photocatalysis. *Catalysts* **2018**, *8* (12), 634. https://doi.org/10.3390/catal8120634.

(26) Yuan, L.; Geng, Z.; Xu, J.; Guo, F.; Han, C. Metal-Semiconductor Heterostructures for Photoredox Catalysis: Where Are We Now and Where Do We Go? *Adv. Funct. Mater.* **2021**, *31* (27). https://doi.org/10.1002/adfm.202101103.

(27) Haldar, K. K.; Sinha, G.; Lahtinen, J.; Patra, A. Hybrid Colloidal Au-CdSe Pentapod Heterostructures Synthesis and Their Photocatalytic Properties. *ACS Appl. Mater. Interfaces* **2012**, *4* (11), 6266–6272. https://doi.org/10.1021/am301859b.

(28) Wu, K.; Zhu, H.; Liu, Z.; Rodríguez-Córdoba, W.; Lian, T. Ultrafast Charge Separation and Long-Lived Charge Separated State in Photocatalytic CdS–Pt Nanorod Heterostructures. *J. Am. Chem. Soc.* **2012**, *134* (25), 10337–10340. https://doi.org/10.1021/ja303306u.

(29) Pradhan, N. Design Strategies for Epitaxial Metal(0)–Halide Perovskite Nanocrystal Heterostructures. *ACS Energy Lett.* **2024**, *9* (5), 2378–2386. https://doi.org/10.1021/acsenergylett.4c00855.

(30) Huynh, W. U.; Dittmer, J. J.; Alivisatos, A. P. Hybrid Nanorod-Polymer Solar Cells. *Science* **2002**, *295* (5564), 2425–2427. https://doi.org/10.1126/science.1069156.

(31) Milliron, D. J.; Hughes, S. M.; Cui, Y.; Manna, L.; Li, J.; Wang, L.-W.; Paul Alivisatos, A. Colloidal Nanocrystal Heterostructures with Linear and Branched Topology. *Nature* **2004**, *430* (6996), 190–195. https://doi.org/10.1038/nature02695.

(32) Shim, M. Colloidal Nanorod Heterostructures for Photovoltaics and Optoelectronics. *J. Phys. D: Appl. Phys.* **2017**, *50* (17), 173002. https://doi.org/10.1088/1361-6463/aa65a5.

(33) Luo, J.; Selopal, G. S.; Tong, X.; Wang, Z. Colloidal Quantum Dots and Two-dimensional Material Heterostructures for Photodetector Applications. *Electron* **2024**, *2* (2), e30. https://doi.org/10.1002/elt2.30.

(34) Vaneski, A.; Susha, A. S.; Rodríguez-Fernández, J.; Berr, M.; Jäckel, F.; Feldmann, J.; Rogach, A. L. Hybrid Colloidal Heterostructures of Anisotropic Semiconductor Nanocrystals Decorated with Noble Metals: Synthesis and Function. *Adv. Funct. Mater.* **2011**, *21* (9), 1547–1556. https://doi.org/10.1002/adfm.201002444.

(35) Groom, R.; Jacobs, A.; Cepeda, M.; Drummey, R.; Latturner, S. E. $Bi_{13}S_{18}I_2$: (Re)Discovery of a Subvalent Bismuth Compound Featuring $[Bi_2]^{4+}$ Dimers Grown in Sulfur/Iodine Flux Mixtures. *Chem. Mater.* **2017**, *29* (7), 3314–3323. https://doi.org/10.1021/acs.chemmater.7b00702.

(36) Das, A.; Debnath, K.; Maria, I.; Das, S.; Dutta, P.; Swain, D.; Waghmare, U. V.; Biswas, K. Influence of Subvalent Twin-Rattler for High *n*-Type Thermoelectric Performance in $Bi_{13}S_{18}Br_2$ Chalcohalide. *J. Am. Chem. Soc.* **2024**, *146* (44), 30518–30528. https://doi.org/10.1021/jacs.4c11738.

(37) Bergmann, J.; Monecke, T.; Kleeberg, R. Alternative Algorithm for the Correction of Preferred Orientation in Rietveld Analysis. *J. Appl. Crystallogr.* **2001**, *34* (1), 16–19. https://doi.org/10.1107/S002188980001623X.

(38) Rodríguez-Carvajal, J. Recent Advances in Magnetic Structure Determination by Neutron Powder Diffraction. *Phys. B* **1993**, *192* (1), 55–69. https://doi.org/10.1016/0921-4526(93)90108-I.

(39) Alemayehu, A.; Zákutná, D.; Kohúteková, S.; Tyrpekl, V. Transition between Two Solid-solutions: Effective and Easy Way for Fine $Ce_{1-x}Gd_xO_{2-x/2}$ Powders Preparation. *J. Am. Ceram. Soc.* **2022**, *105*. https://doi.org/10.1111/jace.18443.

(40) Toso, S.; Dardzinski, D.; Manna, L.; Marom, N. Structure Prediction of Ionic Epitaxial Interfaces with Ogre Demonstrated for Colloidal Heterostructures of Lead Halide Perovskites. *ACS Nano* **2025**, *19* (5), 5326–5341. https://doi.org/10.1021/acsnano.4c12713.

(41) Toso, S.; Dardzinski, D.; Manna, L.; Marom, N. Fast Prediction of Ionic Epitaxial Interfaces with Ogre Demonstrated for Colloidal Heterostructures of Lead Halide Perovskites. Chemistry August 30, 2024. https://doi.org/10.26434/chemrxiv-2024-hwthh.

(42) Zhou, C.; Zheng, K.; Lu, Z.; Zhang, Z.; Liao, Z.; Chen, P.; Lu, W.; Zou, J. Quality Control of GaAs Nanowire Structures by Limiting As Flux in Molecular Beam Epitaxy. *J. Phys. Chem. C* **2015**, *119* (35), 20721–20727. https://doi.org/10.1021/acs.jpcc.5b05606.

(43) Leshchenko, E. D.; Sibirev, N. V. Recent Advances in the Growth and Compositional Modelling of III–V Nanowire Heterostructures. *Nanomaterials* **2024**, *14* (22), 1816. https://doi.org/10.3390/nano14221816.

(44) Johansson, J.; Dick, K. A. Recent Advances in Semiconductor Nanowire Heterostructures. *CrystEngComm* **2011**, *13* (24), 7175. https://doi.org/10.1039/c1ce05821e.

(45) Zhang, H.; Delikanli, S.; Qin, Y.; He, S.; Swihart, M.; Zeng, H. Synthesis of Monodisperse CdS Nanorods Catalyzed by Au Nanoparticles. *Nano Res.* **2008**, *1* (4), 314–320. https://doi.org/10.1007/s12274-008-8032-5.

(46) Savitzky, B. H.; Zeltmann, S. E.; Hughes, L. A.; Brown, H. G.; Zhao, S.; Pelz, P. M.; Pekin, T. C.; Barnard, E. S.; Donohue, J.; Rangel DaCosta, L.; Kennedy, E.; Xie, Y.; Janish, M. T.; Schneider, M. M.; Herring, P.; Gopal, C.; Anapolsky, A.; Dhall, R.; Bustillo, K. C.; Ercius, P.; Scott, M. C.; Ciston, J.; Minor, A. M.; Ophus, C. py4DSTEM: A Software Package for Four-Dimensional Scanning Transmission Electron Microscopy Data Analysis. *Microsc Microanal* **2021**, *27* (4), 712–743. https://doi.org/10.1017/S1431927621000477.

(47) Ai, L.; Jia, D.; Guo, N.; Xu, M.; Zhang, S.; Wang, L.; Jia, L. Controlled Growth of Single-Crystalline $Bi_{.333}(Bi_6S_9)Br$ Nanorods under Hydrothermal Conditions for Enhanced Photocatalytic Reduction of Cr (VI). *J. Alloys Compd.* **2020**, *842*, 155879. https://doi.org/10.1016/j.jallcom.2020.155879.

(48) Nguyen, V. H.; Lee, T.; Nguyen, T. D. Solvothermal Synthesis of Bismuth-Based Halide Perovskite Nanostructures for Photocatalytic Degradation of Organic Pollutants under LED Light Irradiation. *ACS Appl. Nano Mater.* **2023**, *6* (5), 3435–3445. https://doi.org/10.1021/acsanm.2c05218.

(49) Yu, Y.; Cao, C.; Liu, H.; Li, P.; Wei, F.; Jiang, Y.; Song, W. A Bi/BiOCl Heterojunction Photocatalyst with Enhanced Electron–Hole Separation and Excellent Visible Light Photodegrading Activity. *J. Mater. Chem. A* **2014**, *2* (6), 1677–1681. https://doi.org/10.1039/C3TA14494A.

(50) Fónagy, O.; Szabó-Bárdos, E.; Horváth, O. 1,4-Benzoquinone and 1,4-Hydroquinone Based Determination of Electron and Superoxide Radical Formed in Heterogeneous Photocatalytic Systems. *J. Photochem. Photobiol. A: Chem.* **2021**, *407*, 113057. https://doi.org/10.1016/j.jphotochem.2020.113057.

(51) Nguyen, T. T. D.; Nguyen, D.; Vo, P. P.; Doan, H. N.; Pham, H. T. N.; Hoang, V. H.; Tien Le, K.; Kinashi, K.; Huynh, V. T.; Nguyen, P. T. The Roles of Ethanol and Isopropanol as Hole Scavengers in the Photoreduction Reaction of Graphene Oxide by TiO2: A Competition of Oxygenated Groups Removal and Carbon Defects Invasion. *J. Mol. Liq.* **2023**, *381*, 121831. https://doi.org/10.1016/j.molliq.2023.121831.

(52) Gracien, E. B.; Jérémie, M. L.; Joseph, L. K.-K.; Omer, M. M.; Antoine, M. K.; Hercule, K. M.; Gerard, M. N. Role of Hydroxyl Radical Scavenger Agents in Preparing Silver Nanoparticles under γ-Irradiation. *SN Appl. Sci.* **2019**, *1* (9), 961. https://doi.org/10.1007/s42452-019-0973-7.

(53) Zhao, X.; Chen, H.; Chen, X.; Hu, J.; Wu, T.; Wu, L.; Li, M. Multiple Halide Anion Doped Layered Bismuth Terephthalate with Excellent Photocatalysis for Pollutant Removal. *RSC Adv.* **2018**, *8* (67), 38370–38375. https://doi.org/10.1039/c8ra08493a.

(54) Gao, F.; Zhao, Y.; Li, Y.; Wu, G.; Lu, Y.; Song, Y.; Huang, Z.; Li, N.; Zhao, J. Hierarchical Bi Based Nanobundles: An Excellent Photocatalyst for Visible-Light Degradation of Rhodamine B Dye. *J. Colloid Interface Sci.* **2015**, *448*, 564–572. https://doi.org/10.1016/j.jcis.2015.02.056.

(55) Percivalle, N. M.; Carofiglio, M.; Hernández, S.; Cauda, V. Ultra-Fast Photocatalytic Degradation of Rhodamine B Exploiting Oleate-Stabilized Zinc Oxide Nanoparticles. *Discover Nano* **2024**, *19* (1). https://doi.org/10.1186/s11671-024-04077-7.

(56) Denisov, N.; Yoo, J.; Schmuki, P. Effect of Different Hole Scavengers on the Photoelectrochemical Properties and Photocatalytic Hydrogen Evolution Performance of Pristine and Pt-Decorated TiO_2 Nanotubes. *Electrochim. Acta* **2019**, *319*, 61–71. https://doi.org/10.1016/j.electacta.2019.06.173.

(57) Bellato, F.; Ferri, M.; Zhu, D.; Le, T.-H.-H.; Annamalai, A.; Rizzo, M.; Martin, I.; Goldoni, L.; Brescia, R.; Prato, M.; De Trizio, L.; Kriegel, I.; Manna, L. Indium Arsenide Quantum Dot Derived Catalyst for Selective CO_2

Electrochemical Reduction to Formate. *ACS Energy Lett.* **2024**, *9* (3), 1097–1102. https://doi.org/10.1021/acsenergylett.4c00295.

(58) Elgrishi, N.; Rountree, K. J.; McCarthy, B. D.; Rountree, E. S.; Eisenhart, T. T.; Dempsey, J. L. A Practical Beginner's Guide to Cyclic Voltammetry. *J. Chem. Educ.* **2018**, *95* (2), 197–206. https://doi.org/10.1021/acs.jchemed.7b00361.

(59) Shyamal, S.; Patra, A.; Goyal, N.; Banerjee, S.; Dutta, S. K.; Ravishankar, N.; Pradhan, N. Tuning the Reaction Chemistry for the Sulfo-Bromination of Bismuth, Leading to Dual-Tapered Bi-Sulfobromide Platelet Nanocrystals and Their Heterostructures. *J. Am. Chem. Soc.* **2025**, *147* (20), 17260–17272. https://doi.org/10.1021/jacs.5c03518.

(60) Cabona, A.; Toso, S.; Griesi, A.; Rizzo, M.; Ferri, M.; Rusch, P.; Divitini, G.; Pérez-Prieto, J.; Galian, R. E.; Kriegel, I.; Manna, L. Synthesis, Growth Mechanism, and Photocatalytic Properties of Metallic-Bi/$Bi_{13}S_{18}Br_2$ Nano-Bell Heterostructures. *ACS Materials Lett.* **2025**, *7* (5), 1707–1716. https://doi.org/10.1021/acsmaterialslett.5c00043.

(61) Iglesias Van Montfort, H.-P.; Subramanian, S.; Irtem, E.; Sassenburg, M.; Li, M.; Kok, J.; Middelkoop, J.; Burdyny, T. An Advanced Guide to Assembly and Operation of CO_2 Electrolyzers. *ACS Energy Lett.* **2023**, *8* (10), 4156–4161. https://doi.org/10.1021/acsenergylett.3c01561.

CHAPTER 7

Conclusions

During this journey into the rational design by simulations, synthesis and characterization of novel nanostructured photocatalysts, it became clear that even a seemingly simple scientific question – how to speed up a reaction of interest – opens up a wide range of challenges. Already at the stage of selecting a general approach (**Chapter 2**), photocatalysis is just one of several possible routes. Its appeal as a model technology stems from its connection to current global challenges, such as the direct harvesting of sunlight to reduce our dependence on fossil fuels. And yet, even within this relatively specialized field, many questions remain open. Which material? For which reaction? Which morphology? How to produce it? How to maximize performance?

In this Thesis, we explored the full path from the conception of a new nanostructured photocatalyst to its design, synthesis, and characterization under operational conditions. Each chapter addressed multiple challenges, reflecting the layered and interconnected nature of the field. The solutions presented here advance the state of the art in small but concrete ways, and it is hoped that, taken together, they will contribute to a broader methodological effort toward the rational exploration of new functional nanomaterials in the future.

Starting at the ideation stage, the very first challenge is to identify an interesting target material, or in our case, a target heterojunction. Rather than following the predominant direction of the state of the art, where materials are combined primarily based on the matching of electronic properties, I chose to explore an orthogonal, structure-oriented approach, discussed in **Chapter 3**. This choice followed a simple philosophy: it is better to grow, and later improve, an average heterostructure than to be unable to ever obtain the best theoretical prediction because the constituent materials are structurally incompatible.

To this end, I adopted a tool developed by some of my colleagues: the Python library Ogre, which enables the rapid assessment of structural compatibility between candidate materials. By simulating electrostatic interactions, Ogre

provides a practical way to screen heterojunctions at an early stage, grounding the design process in realistic growth constraints rather than idealized assumptions. The capabilities of this approach are explored in **Chapter 4**, where we investigated the compatibility of the perovskite semiconductor $CsPbX_3$ with AgBr as a potential shell material to enhance chemical stability, and subsequently attempted its synthesis. This effort to translate prediction into chemical reality yielded an unexpected outcome, and a lesson in itself. While the full structural compatibility predicted by Ogre was indeed confirmed, it manifested in reverse: rather than obtaining a $CsPbX_3$ core surrounded by a protective AgBr shell, we unexpectedly synthesized the opposite architecture.

This result opened an interesting research direction toward hollow nanostructures, an architecture that remains relatively underexplored within the otherwise extremely rich literature on $CsPbX_3$ perovskites. More importantly, it provides an example of how even carefully designed prediction strategies must ultimately face the intrinsic complexity of nanochemistry, especially when multiple materials are brought together, and how mismatches between expectation and outcome can themselves generate meaningful scientific value.

Many questions remain still open, especially when heterostructures are employed as photocatalysts, where different band alignments can emerge, each with distinct implications for charge-carrier dynamics. In **Chapter 5**, I addressed this challenge by investigating $CsPbX_3/Pb_4S_3Y_2$ heterostructures as photocatalysts for the coupling of thiophenol. By optimizing the colloidal synthetic strategy, I achieved yields on tens-of-milligrams scale, exceeding typical literature reports, and thereby enabling broader photocatalytic applications. The coexistence of two independent semiconductor domains offered precise control over band alignment through halide composition, accessible via both direct synthesis and anion exchange. A combination of spectroscopic characterization allowed a detailed understanding of these alignments, guiding the choice the most effective configuration for photocatalytic applications. This led to the selection of the $CsPbBr_3/Pb_4S_3Br_2$ architecture with type II band alignment, which outperformed the corresponding single-component materials and delivered enhanced reaction yields. In this chapter, we directly demonstrated how the cooperative involvement of photogenerated electrons and holes, whose recombination is suppressed by the heterojunction, can be harnessed to improve photocatalytic efficiency.

After demonstrating that properly engineered semiconductor–semiconductor heterojunction directly enhances catalytic performance, a further question naturally

arises: what happens when a semiconductor is coupled with a metal? **Chapter 6** addressed this challenge through the development of a synthetic strategy for $Bi/Bi_{13}S_{18}Br_2$ heterostructures, where the controlled addition of a tertiary amine, serving as reducing agent, enabled the in-situ reduction of bismuth. During the reaction, the new metal/semiconductor interface evolved to deliver the final architecture, which exhibit a distinctive bell-shaped morphology arising from a complex, multistep growth mechanism. The well-defined interface of this heterostructure allowed its epitaxial relationship to be elucidated using Ogre, providing a clear structural understanding of the system. The functional advantages of combining a semiconductor and a metal within a single, engineered material were directly demonstrated through photo(electro)catalytic tests, including dyes degradation and CO_2 reduction. In this system, the synergy between heterojunction engineering and intrinsic stability of the hybrid architecture proved to be central for achieving enhanced catalytic performances.

Taken together, the findings presented in this Thesis highlight an important principle: whether coupling semiconductors or integrating metals, rational design guided by structural compatibility can translate theoretical predictions into functional materials. At the same time, careful considerations related to the electronic properties of the constituent compounds can give rise to architectures with superior performance in specific fields, in our case, photocatalysis. This work provides a framework for the design of next-generation hybrid photocatalysts and underscores the value of structure-driven strategies in advancing the field.